

CARBON NANOTUBE YARN ACTUATORS

by

Tissaphern Mirfakhrai

M.A.Sc., Simon Fraser University, 2002

B. Sc. Sharif University of Technology, 1998

A THESIS SUBMITTED IN PARTIAL FULFILLMENT OF
THE REQUIREMENTS FOR THE DEGREE OF

DOCTOR OF PHILOSOPHY

in

The Faculty of Graduate Studies
(Electrical and Computer Engineering)

THE UNIVERSITY OF BRITISH COLUMBIA
(Vancouver)

December 2009

© Tissaphern Mirfakhrai, 2009

ABSTRACT

The first demonstration of electromechanical actuation in carbon nanotubes (CNTs), aligned in the form of a twisted yarn, is presented in this thesis. Sheets of CNTs have been known to actuate when charged electrochemically. When an electric potential is applied between a sheet of CNTs and another electrode, both submersed in an electrolyte, the sheet expands. Actuation loads and stresses are low ($< 33 \text{ MPa}$); this is partly due to the random orientation of CNTs in those sheets. When actuated under similar conditions, the yarns show significantly higher stress ($2.0 \pm 0.4 \times 10^8 \text{ Pa}$) with similar strain (0.6 %). However, unlike the sheets, the yarns contract when the electric potential is applied; this is quite unexpected. The mechanism of this contraction is studied and is related to the insertion of ions in the yarn and the structural changes that take place in the yarn due to its helical twisted structure. A model is presented, relating the actuation strain with yarn geometry (diameter, twist rate, internal packing), electrolyte properties such as ion size, and applied potential. The actuation and mechanical properties of the yarn are studied in various electrolytes. Characterization techniques such as cyclic voltammetry and electrochemical impedance spectroscopy are employed to study the charge storage behaviour of the yarn, showing gravimetric capacitances between 10-60 F/g. It is also shown that the yarns can convert mechanical energy into electrical energy, and are thus capable of measuring mechanical forces. Their behaviour as mechanical force sensors is characterized, showing sensitivities about $2.0 \pm 0.6 \times 10^{-5} \text{ V/MPa}$. The yarns are superior in work density to piezoelectric actuators when normalized by active material. Creep, can still be an issue, while a tensile modulus of about $16 \pm 5 \text{ GPa}$ and a tensile strength of about 900 MPa mean that creep is much less than other types of artificial muscles at similar loads. Torsional actuation is also shown to take place if one end of the yarn is free to rotate. Thus, the CNT yarn actuators show the highest achieved stress among polymer artificial muscles and are the first to actuate torsionally, opening a wide range possibilities for applications.

TABLE OF CONTENTS

Abstract.....	ii
Table of Contents	iii
List of Tables	viii
List of Figures.....	ix
Acknowledgements	xx
Dedication	xxiii
Co-authorship Statement	xxv
1 INTRODUCTION, BACKGROUND AND GOALS.....	1
1.1. INTRODUCTION.....	1
1.2. ARTIFICIAL MUSCLES	2
1.2.1. <i>Electronic and ionic artificial muscles</i>	3
1.2.2. <i>Conducting polymer artificial muscles</i>	4
1.2.3. <i>Nanotube actuators</i>	8
1.3. CNT FIBRES AND YARNS	15
1.3.1. <i>Synthesizing CNT yarns</i>	16
1.4. CNT YARNS AS ACTUATORS.....	17
1.4.1. <i>Linear actuation</i>	17
1.4.2. <i>Torsional actuation</i>	18
1.5. ELECTROCHEMISTRY BACKGROUND AND TECHNIQUES	19
1.5.1. <i>Electrochemical charge storage: Gouy-Chapman model, double-layer, and diffuse layers</i> .19	19
1.5.2. <i>Cyclic Voltammetry (CV)</i>	21
1.5.3. <i>Electrochemical Impedance Spectroscopy (EIS)</i>	23
1.6. THESIS OVERVIEW	27
1.6.1. <i>Mechanical/electromechanical characterization (Chapters 2, 3)</i>	27
1.6.2. <i>Electrochemical characterization (Chapters 4 and 5)</i>	28

1.6.3. <i>Reverse/sensor mode characterization (Chapter 6)</i>	28
1.6.4. <i>Identifying possible actuation mechanisms (Chapter 7)</i>	29
1.7. CONCLUSIONS	30
REFERENCES.....	31
2 ELECTROCHEMICAL ACTUATION OF CARBON NANOTUBE YARNS.....	38
2.1. INTRODUCTION.....	38
2.2. METHODS.....	41
2.3. ACTUATION.....	45
2.4. THE YOUNG'S MODULUS AS A FUNCTION OF THE OXIDATION STATE	51
2.5. CONCLUSIONS	53
REFERENCES.....	55
3 CARBON NANOTUBE YARNS AS HIGH LOAD ACTUATORS AND SENSORS	57
3.1. INTRODUCTION.....	57
3.2. BACKGROUND.....	58
3.3. METHODS.....	65
3.4. ACTUATORS	67
3.5. FORCE SENSORS.....	71
3.6. CHALLENGES	74
3.7. SUMMARY	76
REFERENCES.....	77
4 CAPACITIVE CHARGING AND BACKGROUND PROCESSES IN CARBON NANOTUBE YARN ACTUATORS	80
4.1. INTRODUCTION.....	80
4.2. MODELING OF THE CAPACITIVE AND PARASITIC CURRENTS	82
4.3. DOUBLE LAYER CAPACITOR AND LEAKAGE RESISTANCE	82
4.4. PARALLEL AND SERIES RC MODEL	85
4.5. KINETICS-LIMITED PARASITIC REACTIONS AND DIODE MODEL	90

4.6.	DISCUSSION.....	94
4.7.	CONCLUSIONS	98
	REFERENCES	100

5 CARBON NANOTUBE YARN ACTUATORS: AN ELECTROCHEMICAL IMPEDANCE MODEL.....102

5.1.	INTRODUCTION.....	102
5.2.	THEORY	106
5.2.1.	<i>EIS of porous materials</i>	107
5.2.2.	<i>Finding the equivalent capacitance of a CPE</i>	112
5.3.	EXPERIMENTAL RESULTS AND DISCUSSION	114
5.3.1.	<i>Experiments in aqueous NaPF₆.....</i>	116
5.3.2.	<i>Experiments in acetonitrile.....</i>	121
5.4.	DISCUSSION.....	123
5.5.	CONCLUSIONS	127
	REFERENCES.....	129

6 CARBON NANOTUBE YARNS FOR FORCE SENSING AND ENERGY HARVESTING ..134

6.1.	INTRODUCTION.....	134
6.2.	METHODS.....	135
6.3.	RESULTS AND DISCUSSION	136
6.4.	CONCLUSIONS	146
	REFERENCES.....	147

7 IDENTIFICATION OF ACTUATION MECHANISMS.....149

7.1.	TWIST EFFECTS AS MECHANISM FOR CONTRACTILE ACTUATION	150
7.2.	POSSIBLE MECHANISMS FOR THE RADIAL EXPANSION	162
7.2.1.	<i>Pneumatic</i>	162
7.2.2.	<i>Double-layer forces</i>	164
7.2.3.	<i>Ions as physical barriers</i>	170

7.3.	POSSIBLE CAUSES OF THE OVERESTIMATION OF THE ACTUATION STRAIN.....	180
7.3.1.	<i>Non-uniform packing density and radial structure of the yarn.....</i>	180
7.3.2.	<i>Other possible causes of discrepancy.....</i>	187
7.4.	FULL MODEL FOR THE ACTUATOR	188
7.5.	COMPARISON WITH SENSOR	189
7.6.	CONCLUSIONS	192
	REFERENCES.....	193
8	CONTRIBUTIONS, CONCLUDING DISCUSSIONS AND FUTURE DIRECTIONS.....	197
8.1.	CONTRIBUTIONS.....	197
8.2.	ADVANTAGES AND CHALLENGES AS ACTUATORS.....	200
8.2.1.	<i>Actuation stress and strain</i>	200
8.2.2.	<i>Tensile modulus</i>	200
8.2.3.	<i>Strain rate and band width</i>	201
8.2.4.	<i>Work density and blocking load.....</i>	201
8.2.5.	<i>Coupling</i>	210
8.2.6.	<i>Creep</i>	212
8.2.7.	<i>Encapsulation and handling</i>	213
8.2.8.	<i>Repeatability.....</i>	213
8.3.	ADVANTAGES AND CHALLENGES AS MECHANICAL FORCE SENSOR:	214
8.3.1.	<i>Measurable stress levels.....</i>	214
8.3.2.	<i>Issues with parasitic currents and charges.....</i>	215
8.3.3.	<i>Issues with variable open-circuit cell potential</i>	215
8.4.	FUTURE WORK.....	216
8.4.1.	<i>Effect of load.....</i>	216
8.4.2.	<i>Viscoelastic modeling of the yarn.....</i>	216
8.4.3.	<i>Characterizing the actuation as a function of twist</i>	217
8.4.4.	<i>Studying the radial actuation under an atomic force microscope</i>	218
8.5.	POTENTIAL APPLICATIONS:	219

8.5.1. <i>High-load, high-temperature, light-weight actuator/sensor</i>	219
8.5.2. <i>Non-muscle application</i>	220
8.6. CONCLUDING REMARKS	220
REFERENCES.....	222
APPENDIX 1 : IMPEDANCE OF A PORE	226
REFERENCES.....	228
APPENDIX 2 : CALCULATION OF THE REPULSION BETWEEN TWO PARALLEL PLANAR ELECTRODES IN AN ELECTROLYTE	229
A2.1. CALCULATION OF THE POTENTIAL BETWEEN THE ELECTRODES.....	229
A2.2. CALCULATION OF THE REPULSION FORCE BETWEEN THE PLANAR ELECTRODES	232
A2.3. FINDING THE REPULSIVE STRESS AT LOW AND HIGH POTENTIALS:	235
REFERENCES.....	237
APPENDIX 3 : THE TENSILE MODULI OF THE DENSE AND SPARSE PARTS.....	238
A3.1. ACTUATION STRESS AND STRAIN FROM THE SPARSE PART OF THE YARN	238
A3.2. TENSILE MODULI OF THE SPARSE AND DENSE SECTIONS OF THE YARN	240
REFERENCES.....	245
APPENDIX 4 ATOMIC FORCE MICROSCOPY ON THE YARN SURFACE.....	246
A4.1. IMMOBILIZATION OF THE YARN FOR MICROSCOPY.....	246
A4.2. AFM IMAGING	249
A4.3. FORCE CURVES.....	252
A4.4. ESTIMATING THE RADIAL YOUNG'S MODULUS.....	254
A4.5. FUTURE DIRECTION	256
REFERENCES.....	257
APPENDIX 5 : UNDERSAMPLED SENSOR CURRENT ANALYSIS.....	258

LIST OF TABLES

Table 7.1 Rotation angle as a function of electrolyte concentration in torsional actuation experiments.....	162
Table 8.1: Comparison of the work density of CNT yarn actuators with other types of artificial muscles	209

LIST OF FIGURES

FIGURE 1.1: THE STRUCTURE OF TWO COMMON CONDUCTING POLYMERS: (A) POLYPYRROLE AND (B) POLYANILINE	5
FIGURE 1.2: STRUCTURE AND POSSIBLE MECHANISM OF ACTUATION VIA ION (YELLOW/PURPLE & A-) AND SOLVENT (RED/BLUE/GRAY) INSERTION BETWEEN CHAINS	6
FIGURE 1.3: THE STRUCTURAL TYPES OF NANOTUBES: (A) ZIGZAG, (B) ARMCHAIR (C) CHIRAL. (D) SHOWS A MULTIWALL CARBON NANOTUBE (MWNT).....	9
FIGURE 1.4: CHARGE INJECTION IN A CNT-BASED ELECTROMECHANICAL ACTUATOR: AN APPLIED POTENTIAL INJECTS CHARGES IN THE TWO NANOTUBE ELECTRODES IN SOLUTION [28] (RED SPHERES REPRESENT POSITIVE IONS AND YELLOW SPHERES REPRESENT NEGATIVE IONS).....	10
FIGURE 1.5: SCANNING ELECTRON MICROGRAPHS OF (A) A SHEET OF BUCKY PAPER AND (B) A FIBRE OF ALIGNED SWNTs.....	11
FIGURE 1.6: EXPERIMENTAL SETUP FOR ACTUATION OF A SHEET OF SWNT BUCKY PAPER FROM BAUGHMAN ET AL (1999)[26]	13
FIGURE 1.7: SEM IMAGES OF THE CNT YARNS USED IN OUR ACTUATION TESTS. (A) A SINGLE-PLY AND (B) A DOUBLE-PLY YARN. (IMAGES TAKEN USING THE UBC BIOIMAGING LABORATORY SEM).....	17
FIGURE 1.8: THE COMPACT (DOUBLE) LAYER OF CHARGE FOLLOWED BY THE DIFFUSE LAYER IN THE ELECTROLYTE NEAR A PLANAR ELECTRODE.....	21
FIGURE 1.9: THE CYCLIC VOLTAMMOGRAM OF A PURE IDEAL CAPACITOR, WHICH CAN MODEL THE CHARGE STORAGE BEHAVIOUR OF A CARBON NANOTUBE ACTUATOR TO FIRST ORDER AND A PARALLEL RC CIRCUIT, WHICH CAN MODEL THE CHARGE STORAGE IN THE ACTUATORS IN ADDITION TO SOME PARASITIC CURRENTS THAT MAY BE FLOW IN THE CELL.....	23
FIGURE 1.10: EXAMPLES OF EIS RESULTS FOR THE CNT YARN ACTUATOR: (A) THE NYQUIST (POLAR) PLOT AND (B) THE BODE PLOT FIT WITH THE RESPONSE FROM A PARALLEL-SERIES RC CIRCUIT (INSET IN A).	

THE SAME NYQUIST PLOT (C) AND BODE PLOT (D) FIT WITH THE RESPONSE OF A SIMILAR CIRCUIT (INSET IN C) WITH A CPE REPLACING THE CAPACITOR.....	26
FIGURE 2.1: IONS OF OPPOSITE CHARGES ARE ATTRACTED TO THE CNT ELECTRODES IN AN ELECTROLYTE WHEN A VOLTAGE IS APPLIED, RESULTING IN A CHANGE IN THE C-C BOND LENGTH AND ACTUATION .	39
FIGURE 2.2: SEM MICROGRAPH OF A TWIST-SPUN MWNT YARN	40
FIGURE 2.3: THE CNT YARN MOUNTED IN THE ASI MUSCLE ANALYZER CLAMP.....	41
FIGURE 2.4: THE EXPERIMENTAL SETUP FOR MEASURING ACTUATION OF THE YARNS.....	45
FIGURE 2.5: (A) STRAIN, (B) WORKING ELECTRODE VOLTAGE, (C) CELL CURRENT AND (D) TRANSFERRED CHARGE DURING CYCLIC VOLTAMMETRY OF THE MWNT YARN IN 0.2 M TBAP IN ACETONITRILE FOR AN APPLIED TENSILE LOAD OF 11 MPa.	46
FIGURE 2.6: STRAIN VS. NOMINAL CHARGE PER C ATOM DURING CV. THE ORIGIN OF THE HORIZONTAL AXIS IS ARBITRARY SINCE THE INITIAL CHARGE OF THE MWNTS IS UNKNOWN. THE DOTS REPRESENT STRAIN TO CHARGE OBSERVED IN MWNT SHEETS [9].	47
FIGURE 2.7: (A) CYCLIC VOLTAMMOGRAM FOR A 12MM-LONG SINGLE-PLY YARN SCANNED AT 1000 AND 100 MV/S. THE RECTANGLE SHOWS THE IDEAL CAPACITOR RESPONSE FOR A GRAVIMETRIC CAPACITANCE OF ~ 26 F/G AT 1000 MV/S. (B) CV OF AN 18 MM LONG YARN IN 0.5 M TETRABUTYLMONIUM TETRAFLUOROBORATE (TBATFB) IN ACETONITRILE (MeCN) AT A SCAN RATE OF 10 MV/s	48
FIGURE 2.8: APPLIED VOLTAGE PULSE TRAINS VS. Ag/Ag+ AND RESULTING ACTUATION STRAINS FOR ACTUATION IN 0.5 M TBATFB IN MeCN.....	50
FIGURE 2.9: THE STRAIN AMPLITUDE PLOTTED VS. THE APPLIED VOLTAGE AMPLITUDE.....	51
FIGURE 2.10: APPLIED STRAIN WAVEFORM AND THE RESULTING STRESS TO MEASURE THE YOUNG'S MODULUS OF THE YARNS.	52
FIGURE 2.11: THE YOUNG'S MODULUS OF THE CNT YARN AS A FUNCTION OF THE OXIDATION STATE UNDER THE LOADS OF (A) 35, (B) 60 AND (C) 70 MPa. THE HORIZONTAL AXES IN ALL THE PLOTS INDICATE A WORKING ELECTRODE VOLTAGE RANGING FROM -2V TO 2 V.	53

FIGURE 3.1: (A) SCANNING ELECTRON MICROGRAPH OF A CNT SHEET AND (B) CHARGE INJECTION IN A CNT-BASED ELECTROMECHANICAL ACTUATOR, WHERE AN APPLIED POTENTIAL INJECTS CHARGES IN THE TWO NANOTUBE ELECTRODES IN SOLUTION [4].....	60
FIGURE 3.2: CNT PAPER ACTUATOR STRAIN VS. (A) WORKING ELECTRODE (WE) VOLTAGE AND (B) NOMINAL CHARGE PER CARBON ATOM; THE RED LINE SHOWS THE PARABOLIC STRAIN-CHARGE RELATIONSHIP [10]. (COPYRIGHT 2001 SPIE--THE INTERNATIONAL SOCIETY FOR OPTICAL ENGINEERING).....	62
FIGURE 3.3: (A) THE SCANNING ELECTRON MICROGRAPH OF THE SPINNING PROCESS AND (B) THE SCHEMATIC OF THE SPINNING APPARATUS TO MAKE MWNT YARNS [11].	64
FIGURE 3.4: SCANNING ELECTRON MICROGRAPHS OF (A) A SINGLE-PLY YARN AND (B) A TWO-PLY YARN SPUN USING THE DRY TWIST-SPINNING TECHNIQUE. EXPERIMENTAL RESULTS PRESENTED ARE FROM A YARN SIMILAR TO (A).....	65
FIGURE 3.5: AN MWNT YARN MOUNTED IN THE ASI MUSCLE ANALYZER CLAMP, AND THE ELECTROCHEMICAL CELL SETUP USED FOR ACTUATION AND SENSING TESTS.	66
FIGURE 3.6: (A) ACTUATION STRAIN RESPONSE TO AN APPLIED SQUARE WAVE POTENTIAL OF -1.25 V AMPLITUDE PLOTTED IN (B) BETWEEN THE WORKING ELECTRODE (YARN) AND AN AG/AG ⁺ REFERENCE ELECTRODE. (C) ACTUATION STRAIN AS A FUNCTION OF THE APPLIED SQUARE-WAVE POTENTIAL AMPLITUDE. THE ELECTROLYTE WAS 0.1 M TETRABUTYLAMMONIUM HEXAFLUOROPHOSPHATE (TBAP) IN ACETONITRILE. (D) ACTUATION STRAIN OF THE CNT YARN ACTUATOR IN CYPHOS 101 IONIC LIQUID AS A FUNCTION OF APPLIED POTENTIAL (VS. CE) AT THREE LOADS OF 115, 168, AND 200 MPa.	69
FIGURE 3.7: (A) REPULSION BETWEEN THE LIKE CHARGES AND ATTRACTION BETWEEN THE OPPOSITE CHARGES PUSH THE MWNTs APART IN THE YARN, LEADING TO RADIAL EXPANSION. (B) RADIAL EXPANSION IN A TWISTED YARN RESULTS IN AXIAL CONTRACTION.....	70
FIGURE 3.8: (A) STRESS PROFILE APPLIED TO THE YARN UNDER CONSTANT POTENTIAL GENERATES A TRAIN OF CURRENT SPIKES SEEN IN (B). CURRENT SPIKE HEIGHT IS UNEVEN DUE TO UNDERSAMPLING.	72

FIGURE 3.9: SENSING CURRENT AS A FUNCTION OF THE APPLIED BIAS POTENTIAL AT THREE DIFFERENT LOADS.

72

FIGURE 3.10: DESIRED BLOCK DIAGRAMS OF MODELS FOR MWNT YARNS AS (A) ACTUATORS AND (B)

SENSORS.

75

FIGURE 4.1: SCANNING ELECTRON MICROGRAPH OF TWIST-SPUN MWNT YARNS80

FIGURE 4.2: (A) THE CYCLIC VOLTAMMOGRAM FOR THE CIRCUITS DRAWN IN (B) I. PURE CAPACITOR AND II.

PARALLEL COMBINATION OF A CAPACITOR AND A RESISTOR AND (C) CYCLIC VOLTAMMOGRAM FOR THE
CNT YARN ACTUATOR IN AN ELECTROLYTE MADE OF 0.2 M TETRABUTYLAMMONIUM
HEXAFLUOROPHOSPHATE IN ACETONITRILE, VIEWED OVER A POTENTIAL FOR COMPARISON84

FIGURE 4.3: (A) THE CYCLIC VOLTAMMOGRAM FOR THE CNT YARN ACTUATOR IN AN ELECTROLYTE MADE
OF 0.2 M TETRABUTYLAMMONIUM HEXAFLUOROPHOSPHITE IN ACETONITRILE VIEWED OVER A
POTENTIAL RANGE OF -0.5 TO 1.8 V(B) THE CAPACITIVE PART (C) THE LEAKAGE BACKGROUND
CURRENT AND (D) THE GRAVIMETRIC CAPACITANCE AS COMPUTED USING THE CAPACITIVE CURRENT IN
(B).....

89

FIGURE 4.4: (A) THE CYCLIC VOLTAMMOGRAM FOR THE CNT YARN ACTUATOR IN AN ELECTROLYTE MADE
OF 0.2 M TETRABUTYLAMMONIUM HEXAFLUOROPHOSPHATE IN ACETONITRILE, VIEWED OVER A
POTENTIAL RANGE OF -2.5 TO 2.5 V VERSUS REFERENCE (B) THE CAPACITIVE PART AND (C) THE
LEAKAGE BACKGROUND CURRENT.....

91

FIGURE 4.5: (A) EQUIVALENT CIRCUIT WITH POTENTIAL-DEPENDENT R_p TO MODEL FOR PARASITIC REACTIONS
AND (B) EQUIVALENT CIRCUIT MODEL FOR THE CNT YARN ELECTRODE IN THE CELL, ACCOUNTING FOR
CAPACITANCE, SOLUTION AND SERIES RESISTANCE, LEAKAGE AND BUTLER-VOLMER TYPE REACTIONS
.....

93

FIGURE 4.6: (A) THE CIRCUIT MODEL FOR THE SYSTEM STUDIED IN FIGURE 4.4 AND (B) THE COMPARISON OF
THE SIMULATION RESULTS FROM THE MODEL AND THE EXPERIMENTAL CV

93

FIGURE 4.7: COMPARISON OF THE CALCULATED $F(V)$ PARASITIC CURRENT FOR THE SAME CNT YARN SAMPLE
AS ABOVE AT 100 MV/S (THIN) AND 250 MV/S (BOLD).....

95

FIGURE 4.8: (A) STRAIN (COMPENSATED FOR CREEP) VS. TIME (B) TOTAL CHARGE VS. TIME (VERTICAL AXIS ORIGIN ARBITRARY) AND (C) STRAIN IN (A) VS. CHARGE IN (B), DURING A CV OF THE CNT YARN IN A 0.2 M SOLUTION OF TBAP IN ACETONITRILE UNDER A 20 MPa OF LOAD.....96

FIGURE 4.9: (A) STRAIN (COMPENSATED FOR CREEP) VS. TIME (B) STORED CHARGE VS. TIME (VERTICAL AXIS ORIGIN ARBITRARY) AND (C) STRAIN IN (A) VS. CHARGE IN (B), DURING A CV OF THE CNT YARN IN A 0.2 M SOLUTION OF TBAP IN ACETONITRILE UNDER A 20 MPa OF LOAD. THE PARABOLA IN (C) SHOWS A QUADRATIC FIT. NOTE THAT THE DIRECTIONS OF THE VALUES ON STRAIN AXES ARE IN REVERSE.98

FIGURE 5.1: SCANNING ELECTRON MICROGRAPHS OF (A) A TWIST-SPUN CARBON NANOTUBE YARN AND (B) A CLOSE-UP OF THE YARN SURFACE, SHOWING INDIVIDUAL MWNTs AND MWNT BUNDLES.104

FIGURE 5.2: A NARROW PORE IN A POROUS CONDUCTING ELECTRODE.107

FIGURE 5.3: THE NESTED ‘FRACTAL’ STRUCTURE OF TWIST-SPUN MWNT YARNS.109

FIGURE 5.4: VISUALISATION OF A MWNT BUNDLE WITHIN THE YARN (A) ELECTRIC FIELD LINES \mathbf{E} INITIALLY CONVERGE TOWARD THE EXPOSED FACE OF MWNT BUNDLE WHILE THE GAPS AROUND THE BUNDLE ARE PARTIALLY SHIELDED. (B) WITH ACCUMULATION OF IONS THAT FOLLOW THE ELECTRIC FIELD LINES TO THE OUTERMOST POINT OF THE BUNDLE, A CONCENTRATION GRADIENT IS ESTABLISHED (C) AN ARTIFICIAL BOUNDARY \boxed{B} IS DRAWN TO VISUALIZE THE PROCESS BY WHICH ACCUMULATED CHARGE IN THE OUTER AREAS \boxed{A} SPREADS TO THE VALLEY SIDES \boxed{C} UNDER THE FORCE OF THE TANGENTIAL ELECTRO-DIFFUSION GRADIENT. (D) THE RC LADDER CIRCUIT FORMED BY THE RESISTANCE OF THE MWNTs AND THE IONIC RESISTANCE OF THE ELECTROLYTE ALONG WITH THE DIFFUSION IMPEDANCE INTO THE YARN. EACH $Z_{\text{Diffusion}}$ IMPEDANCE BLOCK REPRESENTS AN RC LADDER CIRCUIT SIMILAR TO THE ONE IN FIGURE 5.2. THE CYLINDER REPRESENTS ANY OF THE BUNDLES IN (C), AND THE CAPACITORS LABELLED C_{Surface} ARE THE SAME AS THE SURFACE

CAPACITANCES IN (C), THIS TIME DRAWN ALONG THE LENGTH OF THE BUNDLE.....111

FIGURE 5.5: PROPOSED CIRCUIT MODELS FOR THE ELECTROCHEMICAL BEHAVIOUR OF THE MWNT YARN

ELECTRODE, USING (A) A CPE AND (B) AN IDEAL CAPACITOR. THE SERIES RESISTOR R_1 MODELS THE

SOLUTION AND CONTACT RESISTANCE AND THE PARALLEL RESISTOR R_2 MODELS THE PROCESSES RESULTING IN A LOSS OF THE STORED CHARGE.....	115
---	-----

FIGURE 5.6: CYCLIC VOLTAMMOGRAMS OF THE YARN IN (A) 1 M AQUEOUS SOLUTION OF SODIUM HEXAFLUOROPHOSPHATE, AND (B) 0.2 M SOLUTION OF TBAPF ₆ IN ACETONITRILE.....	117
--	-----

FIGURE 5.7: NYQUIST PLOTS OF THE YARN IMPEDANCE IN A 1 M AQUEOUS SOLUTION OF SODIUM HEXAFLUOROPHOSPHATE AT VARIOUS BIAS POTENTIALS: (A) -0.75 V (B) -0.50 V (C) 0 V (D) +0.25 V (E) +0.50 V (F) +0.75 V AND (G) 1.00 V VS. AG/AGCl IN 3 M NaCl RE. THE FIT LINES SHOW THE IMPEDANCE RESPONSE OF THE CIRCUIT MODEL IN FIGURE 5.5A. THE CHI-SQUARE ERRORS ARE 0.304, 0.039, 0.128, 0.103, 0.017, 0.025, AND 0.039, RESPECTIVELY.....	118
--	-----

FIGURE 5.8: BEST FIT CIRCUIT PARAMETER VALUES FOR THE CELL CONTAINING THE YARN IN AN AQUEOUS NaPF ₆ SOLUTION (A) Y_0 , (B) P , (C) R_2 BASED ON DIRECTLY FITTING THE CIRCUIT IN FIGURE 5.5A AND BASED ON EQN. 5.3 (D) THE GRAVIMETRIC CAPACITANCE BASED ON EQN. 5.4 COMPARED TO THE GRAVIMETRIC CAPACITANCE FOUND BY FITTING THE CIRCUIT IN FIGURE 5.5B.....	119
--	-----

FIGURE 5.9: NYQUIST PLOTS OF THE IMPEDANCE OF THE MWNT YARN ELECTRODE IN A 0.2 M SOLUTION OF TBAPF ₆ IN ACETONITRILE AT VARIOUS POTENTIALS. THE CHI-SQUARE ERRORS ARE 0.065, 0.018, 0.038, 0.036, 0.042, 0.027, 0.018, AND 0.037, RESPECTIVELY.....	122
--	-----

FIGURE 5.10: BEST FIT CIRCUIT PARAMETER VALUES FOR THE CELL CONTAINING THE YARN IN A SOLUTION OF 0.2 M TBAPF ₆ IN ACETONITRILE. (A) Y_0 , (B) P , (C) R_2 BASED ON DIRECTLY FITTING THE CIRCUIT IN FIGURE 5.5A AND BASED ON EQN. 5.3, (D) THE GRAVIMETRIC CAPACITANCE BASED ON EQN. 5.4 COMPARED TO THE GRAVIMETRIC CAPACITANCE FOUND BY FITTING THE CIRCUIT IN FIGURE 5.5B....	123
---	-----

FIGURE 5.11: SURFACE CAPACITANCE (F/m^2) OF THE MWNT BUNDLES CALCULATED BASED ON THE MEASURED CAPACITANCES AND THE SURFACE AREA OF THE BUNDLES AS MODELED IN FIGURE 5.4 (A) IN AQUEOUS 1 M NaPF ₆ AND (B) IN 0.2 M TBAPF ₆ IN ACETONITRILE.....	127
---	-----

FIGURE 6.1: (A) STRESS PROFILE APPLIED TO THE YARN UNDER CONSTANT POTENTIAL OF 0.50 V VS. RE GENERATES A TRAIN OF CURRENT SPIKES (A CONSTANT BACKGROUND CURRENT OF 0.08 mA SUBTRACTED) SHOWN IN (B). (C) SENSOR PEAK CURRENT AS A FUNCTION OF THE APPLIED BIAS	
--	--

POTENTIAL AT THREE DIFFERENT LOADS. FIGURE REPEATED FROM CHAPTER 3 FOR THE READER'S CONVIENIENCE.....	138
---	-----

FIGURE 6.2: PROPOSED SENSING MECHANISM: (A) STRETCHING A TWISTED YARN RESULTS IN RADIAL COMPACTION. (B) THE RADIAL COMPACTION BRINGS ADJACENT MWNTs CLOSER TO ONE ANOTHER, DECREASING THE CHARGE STORAGE CAPACITY OF THE YARN. (C) SINCE THE CAPACITANCE HAS DECREASED AND THE POTENTIAL IS CONSTANT, SOME IONS MUST LEAVE THE YARN, THUS GENERATING THE SENSING CURRENT. BLUE AND RED SPHERES REPRESENT NEGATIVE AND POSITIVE IONS, RESPECTIVELY. THE PLOTTED POTENTIALS ARE FOR DEMONSTRATION PURPOSES.

139

FIGURE 6.3: CHARGE TRANSFERRED FORM THE YARN IN RESPONSE TO TENSION (A) AS A FUNCTION OF THE APPLIED BIAS POTENTIAL AT THREE LOADS. (B) CHARGE TRANSFERRED AT TWO BIAS POTENTIALS OF +/- 1 V AS A FUNCTION OF THE APPLIED STRAIN. THE STRAIN VALUES IN (B) CORRESPOND TO THE STRESS VALUES IN (A).....

141

FIGURE 6.4: (A) EXAMPLE OF THE SENSOR VOLTAGE RESPONSE TO THE APPLIED STRESS (B) SENSING VOLTAGE AS A FUNCTION OF BIAS AT VARIOUS LOADS. THE LINES INTERCONNECTING POINTS ARE TO AID WITH THE IDENTIFICATION OF TRENDS.

143

FIGURE 6.5: SENSOR VOLTAGE AS A FUNCTION OF LOAD AT VARIOUS BIAS POTENTIALS. INSET SHOWS THE SLOPES OF FIT LINES FOR THOSE FIVE POTENTIALS AS A FUNCTION OF THE APPLIED POTENTIAL.

144

FIGURE 6.6: TRANSDUCTION EFFICIENCY IN CHARGED CNT YARNS USED AS SENSORS.....

145

FIGURE 7.1: IDEALIZED HELICAL YARN GEOMETRY: (A) IDEALIZED GEOMETRY (B) "OPENED-OUT" DIAGRAM OF CYLINDER AT RADIUS r , AND (C) "OPENED-OUT" DIAGRAM OF THE CYLINDER AT RADIUS R (YARN SURFACE).....

152

FIGURE 7.2: AXIAL CONTRACTION INDUCED IN AN IDEALIZED TWIST YARN INDUCED DUE TO RADIAL EXPANSION.

154

FIGURE 7.3: THE RADIAL-AXIAL POISSON'S RATIO OF THE YARN, CONNECTED BLACK DIAMONDS SHOW THE EXPERIMENTAL RESULTS FROM [5] AND THE RED DASHED LINE SHOWS THE PREDICTION ASSUMING AN IDEALIZED TWISTED FIBRE YARN.

156

FIGURE 7.4: LOAD PADDLE HANGING FROM THE YARN WITHIN THE EXPERIMENTAL CELL	158
FIGURE 7.5: THE CAMERA VIEW OF THE CELL FROM UNDERNEATH, SHOWING THE RECTANGULAR PADDLE WITH ITS PAINTED CORNER, AND THE PROTRACTOR (A) AT THE BEGINNING OF ROTATION AND (B) DURING ROTATION. THE PAINTED CORNER ROTATES IN THE CCW DIRECTION AS THE ARROW SHOWS.	159
FIGURE 7.6: UNWINDING AND REWINDING ANGLES FOR 12 TORSIONAL ACTUATION CYCLES IN RESPONSE TO A SQUARE WAVE POTENTIAL BETWEEN 0 V AND +1 V VS. AG/AGCl IN 3 M NaCl REFERENCE ELECTRODE, IN A 1M AQUEOUS SOLUTION OF NaCl.	160
FIGURE 7.7: POTENTIAL PROFILE BETWEEN AND OUTSIDE TWO PLANAR ELECTRODES SEPARATED BY A DISTANCE OF D IN AN ELECTROLYTE WITH THEIR DOUBLE-LAYERS INTERACTING.	166
FIGURE 7.8: PREDICTED ACTUATION STRAIN IN THE AXIAL DIRECTION AS A FUNCTION OF THE APPLIED POTENTIAL BASED ON THE CLASSIC DLVO THEORY. THE POTENTIAL OF ZERO CHARGE IS TAKEN AS ZERO.	168
FIGURE 7.9: GRAVIMETRIC CAPACITANCE OF THE YARN SAMPLE AS A FUNCTION OF THE APPLIED BIAS POTENTIAL. THE RED SQUARES AND BLUE CIRCLES SHOW THE CAPACITANCE ESTIMATES BASED ON THE TWO METHODS DISCUSSED IN CHAPTER 6, AND ARE THE SAME AS IN FIGURE 6.10D. THE TRIANGLES SHOW THE AVERAGES BETWEEN THE GRAVIMETRIC CAPACITANCES FOUND USING THE TWO METHODS.	173
FIGURE 7.10: STRAIN TO CHARGE RELATIONSHIP IN THE YARN FOR VARIOUS IONS. TBA^+ AND PF_6^- WERE MEASURED IN ACETONITRILE AS SOLVENT, WHILE Na^+ AND Cl^- WERE MEASURED IN WATER.	175
FIGURE 7.11: ACTUATION STRAIN VERSUS VOLUME OF UNSOLVATED IONS TRANSFERRED DURING ACTUATION. DASHED LINES SHOW LINEAR FITS TO THE DATA.....	176
FIGURE 7.12: ACTUATION STRAIN VERSUS THE VOLUME OF SOLVATED IONS TRANSFERRED DURING ACTUATION.....	177
FIGURE 7.13: ACTUATION STRAIN AS A FUNCTION OF THE APPLIED BIAS POTENTIAL. THE PRESUMED PZC IS THE ZERO OF THE POTENTIAL AXIS.....	180

FIGURE 7.14: (A) SCANNING ELECTRON MICROGRAPH OF THE CROSS-SECTION OF A TWISTED CNT YARN WITH A DIAMETER OF ABOUT 20 μm , SHOWING A DENSE CORE AND A SPARSE OUTER RING. (B) CLOSE- UP MICROGRAPHS OF THE SPARSE AND DENSE PARTS OF THE SAME YARN (IMAGES COURTESY OF KEN ATKINSON, CISRO).....	182
FIGURE 7.15: (A) STEP POTENTIAL APPLIED TO A YARN SAMPLE IN 0.2 M TBAP IN MeCN ELECTROLYTE AND (B) THE YARN ACTUATION STRAIN RESPONSE TO THE POTENTIAL PROFILE IN (A), WHICH SHOWS A FAST CONTRACTION, FOLLOWED BY A SLOW CONTRACTION. THE RED LINES IN (B) SHOW LINEAR FITS TO THE TWO SEGMENTS OF THE STRAIN RESPONSE, THE FIT EQUATIONS FOR WHICH ARE PRESENTED.	185
FIGURE 7.16: ACTUATION STRAIN VS. APPLIED POTENTIAL AFTER THE DENSE-SPARSE RADIAL STRUCTURE OF THE YARN ARE TAKEN INTO ACCOUNT (BLUE CIRCLES), COMPARED WITH EXPERIMENTALLY MEASURED RESPONSE (RED TRIANGLES), FROM CHAPTER 2.	187
FIGURE 7.17: A REPRODUCTION OF FIGURE 5.4B (SQUARES AND CIRCLES), WITH THE RESULTS OF THE MODEL PREDICTION (LINES) SUPERIMPOSED. THE BLUE CIRCLES INDICATE THE EXPERIMENTAL RESULTS USING THE TBA^+ ION AT -1 V BIAS AND THE RED SQUARES ARE EXPERIMENTAL RESULTS FOR PF_6^- ION AT +1 V BIAS.	192
FIGURE 8.1: CNT YARN ACTUATOR (REPRESENTED BY THE GRAY LINE) WORK CYCLE UNDER A CONSTANT LOAD: ΔL_{AB} , EFFECT OF INITIAL LOADING; ΔL_{BC} , (CONTRACTILE) EFFECT OF ACTUATION; ΔL_{CD} (EXPANSIVE) EFFECT OF THE (DECREASING) CHANGE IN THE YOUNG'S MODULUS OF THE YARN; ΔL_0 FREE STROKE STRAIN OF THE ACTUATOR.....	203
FIGURE 8.2: STRAIN GENERATED AS A FUNCTION OF LOAD FOR ACTUATION OF A YARN WITH A 18 MM DIAMETER AND A LENGTH OF 12.9 MM IN A 0.2 M SOLUTION OF TETRABUTYLAMMONIUM HEXAFLUOROPHOSPHATE IN RESPONSE TO A STEP VOLTAGE BETWEEN 0 AND 2 V VS. Ag/Ag+.	205
FIGURE 8.3: ACTUATOR WORK CYCLE WHEN WORKING AGAINST A SPRING.	208
FIGURE A1.1: (A) AN INFINITE RC LADDER NETWORK WITH THE IMPEDANCE, Z AND (B) ITS CIRCUIT EQUIVALENT.....	226

FIGURE A2.1: POTENTIAL PROFILE BETWEEN AND OUTSIDE TWO PLANAR ELECTRODES SEPARATED BY A DISTANCE OF D IN AN ELECTROLYTE WITH THEIR DOUBLE-LAYERS INTERACTING.	229
FIGURE A3.1: (A) SCANNING ELECTRON MICROGRAPH OF THE CROSS SECTION OF THE YARN, SHOWING ITS DENSE CORE AND SPARSE OUTER RING AND (B) CLOSE UP SEMs OF THE SPARSE AND DENSE PARTS; REPEATED FROM CHAPTER 7 FOR THE READER'S CONVENIENCE.	239
FIGURE A4.1: SCHEMATIC DRAWING OF IMMOBILIZATION OF THE YARN ON A GLASS SLIDE BY GOLD ELECTRODEPOSITION	248
FIGURE A4.2: OPTICAL MICROSCOPE IMAGE OF THE YARN, IMMOBILIZED ON A GLASS SLIDE USING A THIN LAYER OF UV-CURED POLYURETHANE AS ADHESIVE.....	249
FIGURE A4.3: A THREE DIMENSIONAL RENDITION OF THE SURFACE OF THE YARN, IMAGED USING AN ATOMIC FORCE MICROSCOPE.	250
FIGURE A4.4: ATOMIC FORCE MICROSCOPE IMAGE OF THE YARN SURFACE, SHOWING AREAS TO THE RIGHT AND LEFT EXTREMES, SMOOTHED POSSIBLY DUE TO THE DIFFUSION OF POLYURETHANE INTO THE YARN.	251
FIGURE A4.5: POSITION OF THE THREE POINTS SELECTED FOR FORCE-CURVE MEASUREMENTS ON THE YARN, INDICATED ON AN AFM IMAGE OF THE YARN SURFACE.	253
FIGURE A4.6: FORCE CURVE AT (A) POINT 0, (B) POINT 1, AND (C) POINT 2	254
FIGURE A4.7: HERTZ MODEL FIT TO A FORCE CURVE DATA TO ESTIMATE THE RADIAL MODULUS	256
FIGURE A4.8: SCHEMATIC DESIGN FOR A SUGGESTED SETUP TO MEASURE RADIAL ACTUATION OF THE YARN WHILE IT IS IMMOBILIZED.....	257
FIGURE A5.1: HISTOGRAM OF THE MAGNITUDE OF THE CURRENT PEAKS AT A LOAD OF 45 MPa AND BIAS POTENTIAL OF +0.5 V VS. AG/AG+. IT CUTS-OFF ABOVE THE 65 nA BIN, IMPLYING THE VALUE OF THE PEAK TO FALL IN THAT BIN.....	259
FIGURE A5.2: HISTOGRAM FOR A FORCE SENSING EXPERIMENT AT A PRELOAD OF ABOUT 120 MPa AND A CHANGE IN THE LOAD OF ABOUT 100 MPa IN THE FORM OF A SQUARE-WAVE. THE BIAS POTENTIAL WAS +0.75 V VS. AG/AG+.	260

FIGURE A5.3: SENSOR CURRENTS FROM FIGURE 6.2C, NORMALIZED BY LOAD, AT VARIOUS BIAS POTENTIALS.

.....261

ACKNOWLEDGEMENTS

First and foremost, I owe particular thanks to my advisor, Prof. John D. W. Madden, from whom I have learned a lot and whose penetrating questions have taught me to question everything more deeply. John has provided me with great projects and guided me in my research, while at the same time allowing me the freedom to explore other areas. He supported me to attend several conferences and workshops, and thus provided opportunities for me to interact with others in the field; I have learned a great deal through such interactions and they particularly helped my scientific self-esteem to grow. Whether it was during the frustrating hours in the lab, or while body-surfing on the sandy beaches of Wollongong, John has always been a great and very positive presence in my life, and I have always looked up to him.

I would like to thank Prof. Dan Bizzotto for providing coherent answers to my endless questions about electrochemistry, and Prof. Joseph Yan, for his intelligent advice about mechanical properties and apparatus, especially in the earlier stages of my research. Special thanks are owed to my parents, who have supported me throughout my years of education, both morally and financially. I wouldn't have become the person I am without my father's constant constructive criticism and my mother's perpetual love. Professors Frank Ko, David Pulfrey, Michael Wolf, and Boris Stoeber have made me grateful by accepting to be on my examination committees and by enriching me with their knowledge through our past interactions. I would like to thank the Natural Sciences and Engineering Research Council of Canada for supporting my work through a Discovery Grant, and the Institute for Computing, Information and Cognitive Systems (ICICS) and the Graduate Student Society of the University of British Columbia for providing conference travel funding. I would also like to thank the following people:

- Professor Ray H. Baughman for honouring me by including me in his group's amazing research on CNT yarns and sheets and actuators in general and allowing me to spend several enjoyable months at his lab at UT Dallas
- Professor Alireza Nojeh for his unwavering support throughout the years and for providing me with his wealth of knowledge about quantum chemical simulation of CNTs

- Dr. Mikhail E. Kozlov for his valuable feedback on my manuscript drafts and his always supportive presence, especially during my months at UT Dallas
- Professors Shaoli Fang and Mei Zhang, for fabricating the yarns on which my experiments are based, and also for their feedback on my manuscript drafts
- Professor George Sawatsky for his time and valuable advice about quantum mechanical problems in single CNT actuation
- Professors Geoffrey M. Spinks and Gordon G. Wallace for the valuable discussions about actuation mechanisms in conducting polymer actuators and CNT artificial muscles, and for kindly allowing me to spend some time in their great laboratories
- Professors Elisabeth Smela and Toribio Hernandez Otero for valuable discussions about actuation mechanisms in conducting polymers
- Dr. Ken Atkinson of CISRO, the coinventor of the CNT spinning technology, for discussions about the mechanical properties and the structure of the yarn
- Professor Konrad Walus for allowing me to use his COMSOL Multiphysics ® license for some of my simulations
- Drs. Jiyoung Oh, Javad Foroughi, and J. Norman Barisci for giving me the pleasure of working with them on some of the experiments mentioned in this thesis
- Dr. Michael J. Higgins for supporting me with his seemingly unlimited knowledge and expertise with atomic force microscopy
- Dr. Philippe Poulin for his generous advice regarding CNT fibre spinning techniques
- Dr. Martin Kendig for kindly going out of his way to expose me to his in-depth knowledge about surface phenomena in electrochemistry and constant phase elements
- Dr. Konstantinos Dassios for his help with the experiments about viscoelastic properties of yarns and for the valuable discussions afterwards
- Professor John Hearle for guiding me towards his most informative papers and books about yarn mechanics, and providing me with an unpublished manuscript of his about CNT fibres
- Drs. Johannes Riemenschneider and Lucie Viry for valuable discussions about CNT actuation
- The staff at the UBC Bioimaging Laboratory, especially Derrick Horne and Garnet Martens, for their help with SEM imaging

- Professor Mahbod M. Bassir for introducing me to the beauties of chemistry before I was 10 years old
- Professor Mark J. MacLachlan for reviving my love for chemistry through his enthusiastic teaching and advice
- Drs. Aya Sode and Robin Stoodly for always answering my stupid questions about electrochemistry with kind smiles
- Rahul Krishna-Prasad for implementing a number of the simulations of single CNT actuation and for helping me with the technicalities of Gaussian 03, and Erik Miehling for his help with wet-spinning of CNT fibres. Interactions with both of them have been educating experiences for me
- Arash, Tina, Bahar, Mya, Eddie, Alex, Joanna, Ali ($\times 2 !$), Paul, and Dan, for being great collaborators and friends. Especial thanks to Niloofar, for being a very valuable and supportive friend for me, and also for proofreading a version of this thesis at short notice.
- Drs. Azadeh Faridi, Elham Farahani, Bijan Afsari, Mohammad Nariman and Pedram Hovareshti for being such great friends despite the gaping geographical distances
- Shirin and Wayne, for the great musical moments I spent in their company in the longest partnership of my life to date
- Dr. Ali Parsa for recommending and providing great music for me to listen to throughout my PhD year.
- Drs. Terry Estrin, Ramona Luengen, and Bernard Duerksen, for helping me keep my sanity during these difficult years through their artistic and psychological support.
- The technical and administrative staff at UBC department of electrical and computer engineering, and the Advanced Materials and Process Engineering Laboratory (AMPEL)
- The undergraduate students who worked with me throughout my years at UBC, a list of whom is posted on my website.

DEDICATION

*To my parents,
and my grandmother*

"Could you not hold a hempen fibre so tightly between your fingers that I, pulling by the other end, would break it before drawing it away from you? Certainly you can. ... but at the point where a yarn parts the fibres are very short...as they would be if the parting of the yarn occurred not by breaking of the filaments, but by their slipping one over the other."

Galileo (1638)

CO-AUTHORSHIP STATEMENT

- Identification and design of research program

Following the invention of the CNT yarn dry-spinning technology by our collaborators at UT Dallas, they suggested that we tested those yarns for electromechanical actuation. After our preliminary measurements confirmed the presence of actuation in the yarns, the author proposed this research program as his PhD thesis to Professor Madden, with the aim of measuring their properties and determining their potential. We received the approval and support of the UT Dallas group, who made the yarns for us.

- Performing the research

All experiments presented in this thesis have been performed by the author. The only exceptions are the experiments in chapter 2, identified as having been performed using “setup 2”, which were done by our collaborators at UT Dallas, in particular Drs. Mikhail Kozlov and Jiyoung Oh. Professors Mei Zhang and Shaoli Fang spun all the yarns for the experiments mentioned in this thesis using their dry-spinning setup, with the exception of the wet-spun yarns mentioned in chapter 1, which were my own work.

- Data analyses

The data analyses presented in this thesis is principally the author’s. I have strongly benefitted from extensive discussions and guidance with my advisor, Professor John D. W. Madden, and from comments made during phone conversations and occasional meetings with Professor Ray Baughman and Dr. Mikhail Kozlov of the UT Dallas group.

- Manuscript preparation

All manuscripts included in this thesis have been written by the author as the first and principal author. I have benefited from the comments of my coauthors on my manuscripts, which have improved the presentation and helped refine the interpretations.

Chapter 1

1 Introduction, background and goals

1.1. Introduction

The goal of this research has been to characterize twisted yarns of carbon nanotube (CNT) as electromechanical systems, such as actuators and mechanical force sensors, and to determine the mechanism of actuation and sensing in these novel materials. As in most mechanical sensors and actuators, either the input or the output of the system is a mechanical quantity, and the other is an electrical signal. The characterization will thus include determining the relationships between the input and output of the system, which can be electrical or mechanical quantities. Since actuation and sensing in CNT yarns takes place as they are electrochemically charged, their characterization also involves employing techniques from electrochemistry. Gaining knowledge about the passive mechanical properties of the yarns is another step towards determining the actuation mechanism in these novel actuators.

In this chapter, the background information is provided about artificial muscles in general and ionic artificial muscles in particular. Since CNT yarn actuation is based on electrical charging and the yarns can most effectively be charged ionically in an electrolyte, some background information from physical chemistry and electrochemistry are also provided to describe the ionic charging phenomena. Spinning techniques employed to produce

fibres and yarns from CNTs are briefly discussed. This information is later used in other chapters to characterize the yarns.

1.2. Artificial muscles

Our most common actuators are combustion engines, electric motors and piezoelectrics. Combustion engines are generally most efficient when operated continuously and are therefore not ideal for applications in which motion is frequently interrupted, such as in valves or walking robots [1]. Electric motors are low in torque to mass compared to muscle making them very bulky for medical, robotic and fluidic applications. Like combustion engines they also operate best at constant speed. Piezoceramics achieve very high power densities but strain is small (0.1 %), making massive mechanical amplification necessary if significant displacements are needed. There is currently no technology that is widely used to replace or simulate muscle, providing a strong motivation for research and development.

A variety of polymers have emerged that exhibit substantial deformations in response to applied voltage. These materials reversibly contract and expand in length and volume, which is the primary similarity with muscle. The performance of the emerging polymer actuators exceeds that of natural muscle in many respects, making them particularly attractive for use anywhere where a muscle-like response is desirable, including in medical devices, prostheses, robotics, toys, bio-mimetic devices and micro/nano-electromechanical systems [2, 3]. Commercial application of these materials is at an early stage [4]. A few properties of interest in artificial muscles are listed below.

- **Stress:** typical or maximum force per cross-sectional area that a given material is able to work against.

- **Strain:** displacement normalized by the original material length in the direction of actuation.
- **Strain rate:** average rate of change in strain per unit time during an actuator stroke.
- **Elastic Modulus** (Young's modulus): material stiffness normalized by sample length and cross-sectional area.
- **Work Density:** work generated in one actuator cycle per unit volume of actuator.
- **Coupling:** the proportion of input energy that is transformed into external work.
- **Efficiency:** the ratio of work generated to input energy expended. It can be higher than the coupling as sometimes electrical and thermal energy can be recovered from the actuator e.g. during capacitive discharge.
- **Cycle Life:** number of useful strokes the material is able to undergo before the actuator performance is significantly degraded.
- **Charge storage capacitance:** the amount of electric charge stored in the actuator per applied potential. In many cases there is a direct relationship between the amount of stored charge and the actuation strain/stress.

1.2.1. Electronic and ionic artificial muscles

Artificial muscles have been divided into two major groups [5]. In the first group dimensional change (actuation) is in response to electric field. These are commonly known as electronic or electric electroactive polymers. Some of the technologies that fall under this category are dielectric elastomer actuators (DEAs), relaxor ferroelectric

polymers, and liquid crystal elastomers. Although DEAs are lately becoming commercially available for certain applications, there are a number of general disadvantages with electronic electroactive polymers. The materials in this group typically require high voltages applied to create the electric field required to actuate. This is not acceptable or desirable in many applications. Also, due to the low tensile moduli, the actuation stresses by materials in this group are typically low, especially for dielectric and liquid crystal elastomers. Artificial muscles that operate at low voltages and are capable of applying large stresses are therefore of prime interest.

The second group is a class of materials in which the presence and movement of ions is necessary to make actuation possible. This group is referred to as ionic electroactive polymers. For the ions to be able to move an electrolyte phase is necessary, which is often liquid; so these actuators are also known as wet electroactive polymers. Actuators in this group include conducting polymers, and ionic polymer metal composites (IPMC). Carbon nanotube actuators typically fall into this category, although they are not technically polymers, and thus we hereby discuss in more detail the actuation mechanism in ionic artificial muscles by studying actuation in conducting polymer actuators before turning our attention to CNT actuators. Conducting polymers are particularly relevant as the actuation mechanisms for CNT yarns, discussed in Chapter 7, appear to be very similar to those in conducting polymer actuators.

1.2.2. Conducting polymer artificial muscles

Conducting polymers are polymeric materials that are typically semiconducting when undoped and highly conducting when doped with donor or acceptor ions [6]. Doping is typically achieved chemically or electrochemically. Some applications that have long

been of interest include polymer light emitting diodes, electrochromic windows, energy storage, sensing and actuation [6]. Polypyrrole and polyaniline are two common conducting polymers (Figure 1.1)

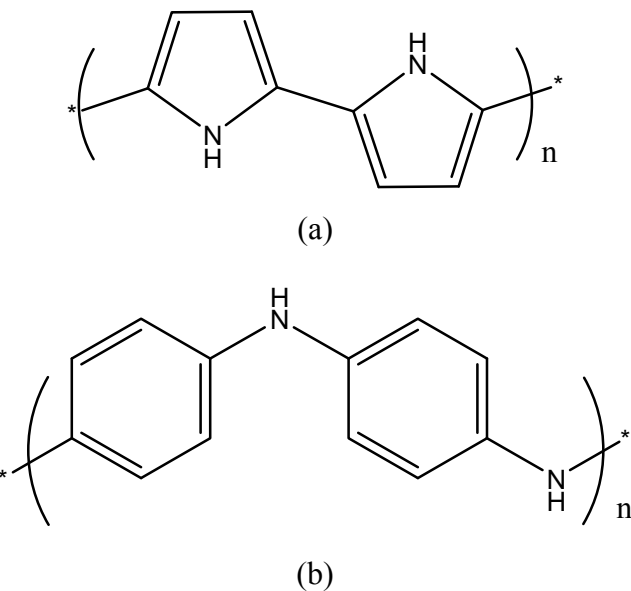


Figure 1.1: The structure of two common conducting polymers: (a) polypyrrole and (b) polyaniline

Though the use of conducting polymers as artificial muscles was first published by Baughman and coworkers in 1990 [7], advances in performance have been continuously made up to the present and further improvements are both desirable and achievable. These conducting polymer artificial muscles use the dimensional changes resulting from electrochemical ion insertion and deinsertion, possibly along with associated solvating species. Typically a conducting polymer strip is used as one electrode in an electrochemical cell. When a potential is applied between the muscle and another (counter) electrode, ions with charge of opposite (same) sign to the potential applied to the artificial muscle are attracted to and enter (leave) the porous muscle, causing it to expand (contract). Since both electrodes can be comprised of conducting polymers, both

can be used as artificial muscles. Depending upon the conducting polymer/electrolyte system used, the initial state, and the rate of potential change used for actuation, electron insertion into one electrode can be accompanied by a volume increase as cations are inserted or a volume decrease as anions are removed and similar processes can occur at the counter-electrode [8, 9]. Expansion appears to be primarily perpendicular to the polymer chain orientation for oriented polymers, suggesting to first order that ions and accompanying solvent are slotted between chains [10-12], as depicted in Figure 1.2, which shows the structure of polypyrrole doped with PF_6^- [13, 14]. The polymers most often used in actuation are polypyrrole, polyaniline and polythiophene derivatives.

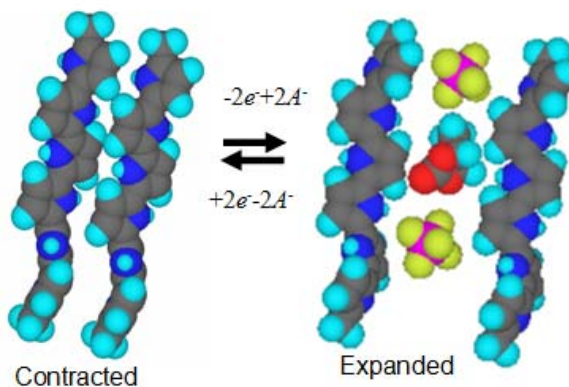


Figure 1.2: Structure and possible mechanism of actuation via ion (yellow/purple & A-) and solvent (red/blue/gray) insertion between chains

Strains are typically between 2 and 10 %, though recent work by Kaneto and coworkers show that actuator strokes can reach 30 % [15]. High quality electrochemically grown films and solution spun fibres have tensile strengths on the order of 100 MPa or higher, and added carbon nanotubes can further increase strength and reduce problematic creep [16]. Small strains (< 0.2 %) are achieved at loads of 100 MPa [16], with operating

stresses being more typically 1-34 MPa [9]. These can be compared with $\sim 20\%$ strain and 0.2 MPa for mammalian skeletal muscle [17]. Work densities approach 100 kJ/m³ [18]. Operating voltages are ~ 2 V, though higher voltages of up to 10 V are sometimes used to increase actuation rate.

Due to the porous structure of conducting polymers, charge, in the form of ion-electron pairs can be stored throughout their volume, leading to huge charge storage capacitance. As we shall show in Chapters 4 and 5, CNT yarns are similarly porous, and also exhibit very high capacitance. It has been shown that the actuation strain generated in conducting polymer actuators is proportional to the amount of charge stored in the polymer. Techniques from electrochemistry, such as cyclic voltammetry (CV) and electrochemical impedance spectroscopy (EIS), described later in this chapter, are thus sometimes used to measure the charge storage capacitance to estimate the amount of charge, and to predict the actuation strain. The charge storage capacitance is typically expressed as a gravimetric capacitance, with units of Farads per gram.

The advantage of conducting polymers over electronic EAPs is their low operating voltage. Much of the input electrical energy can be recovered, but the need to shunt relatively large amounts of electrical charge can slow actuation and push the limits of power supplies, making large scale applications (e.g. robotic arms) challenging. Applications being considered include blood vessel reconnection, dynamic Braille displays, valves and actuated catheters [19, 20].

As will be discussed in the following section, the basic requirements for the operation of carbon nanotube actuators are very similar to those for the conducting polymer actuators. In both cases, the charging of a conducting backbone is key to the actuation, and this

charging leads to a structural change in the backbone. It is known that the intercalation of ions balancing the backbone charge within the conducting polymer actuators is their main actuation mechanism. It shall be shown that intercalation likely contribute to the actuation, at least in some forms of nanotube-based actuators.

1.2.3. Nanotube actuators

Another group of ionic artificial muscles are the carbon nanotube actuators. Carbon single-wall nanotubes (SWNTs) can be thought of as a single layer of graphite (graphene) rolled into a cylinder of nanometer diameter (Figure 1.3a-c). Carbon multi-wall nanotubes (MWNTs) are nested SWNTs (Figure 1.3d). Although the rolled-up graphene provides a good understanding of CNT structure, CNTs are typically grown directly by creating carbon radicals that then bond to form CNTs. The main methods of CNT growth include chemical vapour deposition (CVD), laser ablation, joule heating, and arc discharge[21]. Almost all SWNT growth methods require a catalyst, while MWNTs can be made in the absence of catalyst [21].

Individual CNTs are materials with exceptional mechanical properties. The tensile modulus of single-wall carbon nanotubes (~ 1 TPa) is among the highest measured [21], while their tensile strength is thought to be between 20 and 40 GPa, about ten times higher than for continuous fibres of any type [22]. These great properties sound more impressive in light of the intrinsically low-density structure of CNTs as compared with other materials exhibiting similar properties, such as metal nanowires. SWNTs may be either metallic or semiconducting, depending on the direction around which the graphite sheet is rolled to form the nanotube [22].

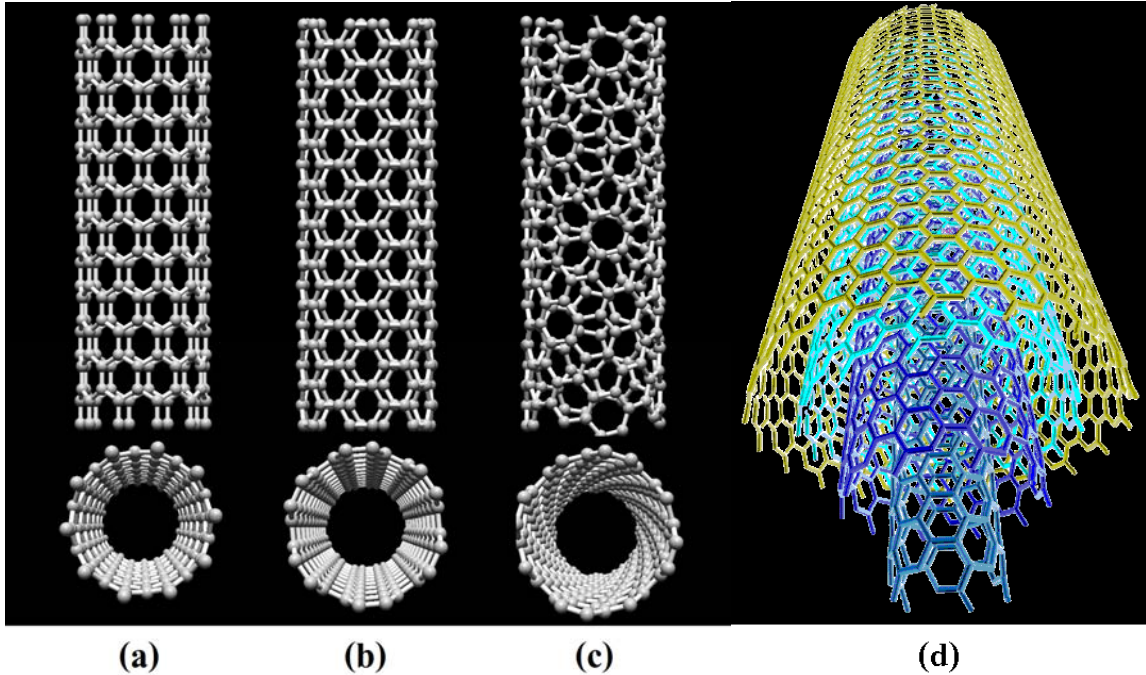


Figure 1.3: The structural types of nanotubes: (a) zigzag, (b) armchair (c) chiral. (d) shows a Multiwall Carbon Nanotube (MWNT)

At high levels of charge injection into individual carbon nanotubes, the predominant cause of actuation is believed to be electrostatic [23, 24]. The electrostatic forces are repulsive interactions between like charges injected into the nanotubes (rather than between two electrodes). A voltage is applied between an actuating nanotube electrode and a counter electrode, through an ion containing solution, as depicted in Figure 1.4 (where the counter-electrode is another CNT), leading to charging. Electrostatic repulsive forces between like charges on the carbon nanotubes work against the stiff carbon-carbon bonds in the nanotubes to elongate and expand the nanotubes, though quantum mechanical effects can predominate over electrostatic forces at low levels of charge injection, resulting in a non-monotonic strain-charge dependence [25-27]. The strains are low (< 2 % [22]) since carbon nanotubes are extremely stiff.

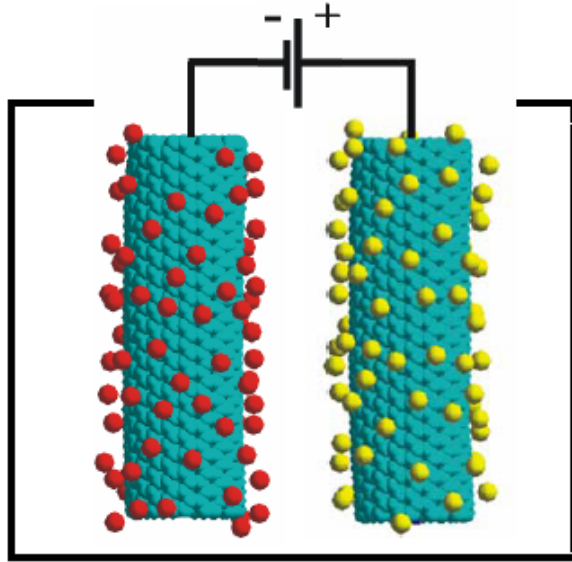


Figure 1.4: Charge injection in a CNT-based electromechanical actuator: an applied potential injects charges in the two nanotube electrodes in solution [28] (red spheres represent positive ions and yellow spheres represent negative ions)

Actuation in individual CNTs is difficult to measure [29]. The bulk of the literature on CNT actuators is about actuation in films ('Bucky paper'), or CNT fibres (Figure 1.5) composed of many nanotubes [26, 28, 30, 31]. While individual SWNTs exhibit superb mechanical properties, observed properties are much poorer for assemblies of trillions of these nanotubes in nanotube yarns and sheets, and this restricts the performance of actuators based on nanotube yarns or sheets.

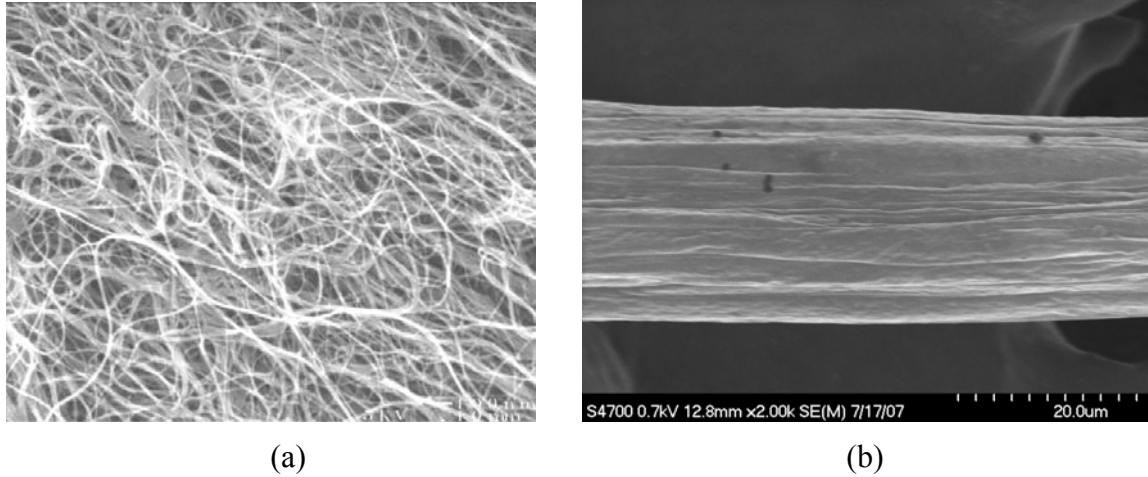


Figure 1.5: Scanning electron micrographs of (a) a sheet of Bucky paper and (b) a fibre of aligned SWNTs.

Baughman et al. first showed actuation in sheets of Bucky paper in 1999 [26]. They used two sheets of SWNT paper as the working and counter electrodes in an electrochemical cell. The change in the length of the working electrode SWNT sheet was monitored using an optical sensor (Figure 1.6). The resulting actuation strain when the potential difference between the electrodes was changed showed a somewhat parabolic expansion with increasing charge regardless of the sign of the applied potential. Baughman et al. interpreted this data to suggest that actuation strain in sheets of CNTs was a result of expansion in individual CNTs upon charging. In light of our findings about actuation in CNT yarns, presented in Chapter 7 of this thesis, it is likely that the actuation in Bucky paper is in fact due to interaction between adjacent charged CNTs that manifest themselves in the form of expansion due to random orientation of the CNTs. Baughman went on to suggest that by using longer CNTs and aligning them, it would be possible to create actuators that can actuate by about 1-2 % under huge loads up to the tensile strength of the CNTs (~ 63 GPa), and thus create actuators with unprecedented load and

work densities. Indeed, this suggestion by Baughman was one of the inspirations for the present work.

The porous nature of the CNT films and fibres enables fast ion transport with response times of < 10 ms, with the maximum effective strain rate to date shown to be about 19 %/s, and effective power to mass ratios of 270 W/kg (half that of a high revving electric motor). The achievable response rate is expected to decrease with increasing nanotube sheet thickness, increasing inter-electrode separation, and decreasing ionic conductivity of the electrolyte [32] since rate is expected to be ion and electron transport limited.

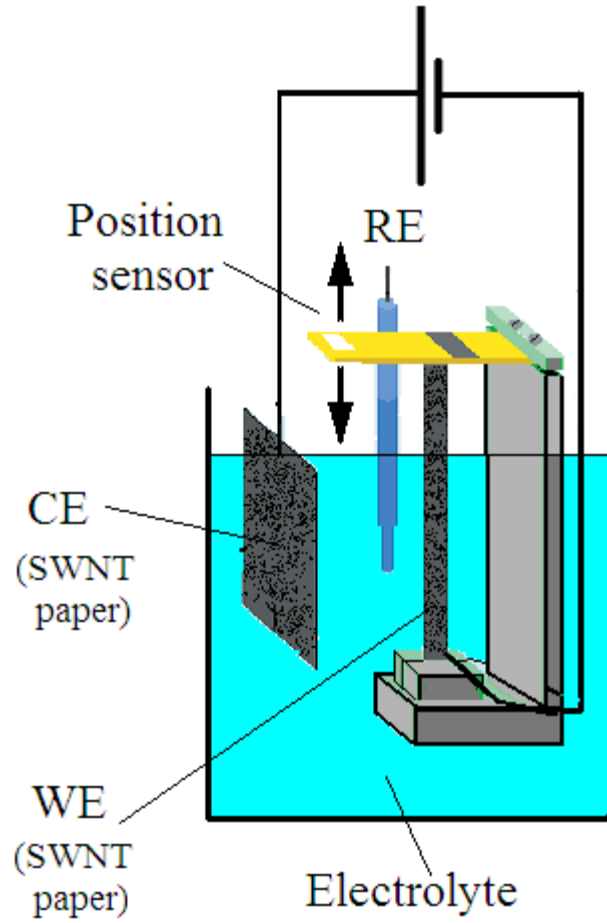


Figure 1.6: Experimental setup for actuation of a sheet of SWNT Bucky paper from Baughman et al (1999)[26]

Beside Bucky paper, actuation has been reported in fibres of CNTs. These usually have the advantage of having higher tensile strengths and moduli [33, 34]. The ultimate work densities thought achievable for individual nanotube actuators are unmatched by any

actuator technology, perhaps reaching 108 J/m^3 ¹. Achieving such incredible work densities in a bulk material will require using extremely long nanotubes, or ones that are cross-linked together, so that the mechanical properties of nanotube yarns and sheets approach those of the individual SWNTs. These approaches should lead to high electromechanical coupling. The maximum coupling achieved before the work of the present author was less than 1 %, likely the result of the tremendously large energy needed to deform individual nanotubes ($E=640 \text{ GPa}$) and the fact that this energy cannot presently be effectively utilized for actuation because of low bulk modulus ($E \sim 15 \text{ GPa}$) compared with the individual nanotube modulus [35]. The mechanical energy is thus small at present compared to stored electrical energy.

High work density combined with good temperature stability ($> 450 \text{ }^\circ\text{C}$ in air, $> 1000 \text{ }^\circ\text{C}$ inert environment) make CNT actuators prime candidates for use in situations where weight and temperature are important, as in aerospace applications. Strains are relatively small compared to other polymer actuators (but up to an order of magnitude larger than is found in typical piezoceramics). Strain might be increased by employing electrolytes such as highly purified ionic liquids that can withstand larger potentials without creating significant parasitic electrochemical reactions.

¹ The ultimate work density can be calculated as $W = \frac{1}{2} Y \varepsilon^2$. The Young's modulus, Y , of CNTs is

estimated to be about 1 TPa , and the maximum measured strain is about 1 %.

$$\text{Therefore, } W = \frac{1}{2} Y \varepsilon^2 = \frac{1}{2} \times 10^{12} \times 10^{-4} = 0.5 \times 10^8 \frac{\text{J}}{\text{m}^3}.$$

CNT actuators have recently been shown to actuate when used as electrodes in a fuel-cell-like geometry [36]. In such a setup, the energy from the fuel is used directly to charge and actuate the CNT artificial muscle. This possibility is exciting because it allows creating fuel-powered artificial muscles. The energy density of fuel cells is much higher than that of batteries, allowing for smaller, easily rechargeable power sources for the actuator, and thus helping enable autonomous applications of CNTs and possibly other artificial muscle technologies [37].

1.3. CNT fibres and yarns

The mechanical and actuation properties of CNT papers are quite inferior to those of individual CNTs. For example, CNT paper has considerably smaller tensile strength (between 6-33 MPa [38]) compared to the individual nanotubes (~37 GPa [22]). In order to improve mechanical properties, researchers are working to create highly aligned macroscopic structures of CNTs that can maintain the marvellous mechanical and actuation properties of individual CNTs to a larger extent. Ropes or strings made of nanotubes became a new center of attraction for researchers and several groups developed their own method of creating such ropes. Carbon nanotube actuators also benefit from improvements in the mechanical properties of nanotube sheets and fibres, which should enable actuation at higher loads, and the creation of stiffer actuators. A key contribution of this thesis work is the demonstration of greatly improved actuation in structures containing aligned nanotubes (and in particular in yarns).

1.3.1. Synthesizing CNT yarns

Several methods to spin fibres and yarns made of aligned CNT were being investigated at the time this research was started. These included wet-spun fibres, such as those made by Vigolo et al. [30, 39] using a bath of Poly(Vinyl Alcohol) (PVA) to bind CNTs together, and fibres spun directly from Chemical Vapour Deposition (CVD) furnace as shown by Li et al. [19].

The CNT yarns - used in all the actuation experiments described in this thesis - are made at the Alan G. MacDiarmid NanoTech Institute of the University of Texas in Dallas, using motor-assisted drawing of the yarn [20]. These yarns were selected for actuation tests over the other types discussed in the previous paragraph for the following reasons:

1. Unlike the wet-spun fibres, the yarns are highly porous, and the large pores make the inner surface area of the yarn highly accessible (See Chapters 2 and 5).
2. At about 800-900 MPa, their tensile strength is similar or higher than those of the other fibre types [40]. This strength represents a dramatic advance over the tensile strength of Bucky paper which is only a few MPa [32].
3. The alignment of the CNTs in the yarn seems to be better compared to the other fibre types and the CNTs are quite long. This may result in actuation properties closer to what has been expected from individual CNTs.

The yarns are directly spun from a forest of MWNTs, grown by CVD. The details of the spinning process can be found in Chapter 3. The electrical conductivity of the yarn is

about $300 \pm 5 \frac{S}{m}^2$. This value is found using the average diameter of the yarn as found by SEM. As shall be shown in Chapter 2, the Young's modulus of the yarns is about 15-20 GPa. This value can be compared with the modulus of Bucky paper that is about 1 GPa [32]. Thermal properties of the yarns can be found in [41]. The CNT yarn shown in Figure 1.7a has a diameter of 10 μm with a twist angle of about 30° . It is possible to twist two of these yarns together to make a two-ply yarn (Figure 1.7b).

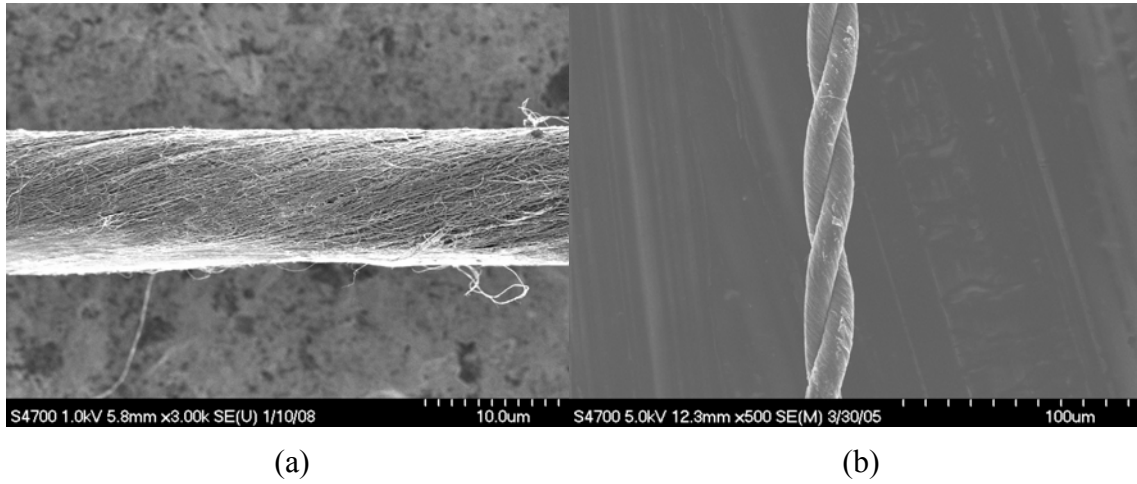


Figure 1.7: SEM images of the CNT yarns used in our actuation tests. (a) a single-ply and (b) a double-ply yarn. (Images taken using the UBC Bioimaging laboratory SEM).

1.4. CNT yarns as actuators

1.4.1. Linear actuation

Upon obtaining the first samples of yarns from UTD collaborators, we tested the samples for actuation. Our early results showed that there was an increase in tensile stress in the yarns when the yarn was clamped at both ends and a voltage was applied between the

² The reported uncertainty is the standard deviation of measurements from various samples

yarn and the counter electrode. This implied that the length of the yarn would be decreasing when the yarn was charged. Performing isotonic actuation tests confirmed this, showing that the yarn contracted when it was charged and expanded again almost to its initial length when discharged. This result contradicted all previous experimental results about actuation in CNT-based materials, all of which had shown expansion in the material upon being charged³. In fact, many types of artificial muscles, such as dielectric elastomers, expand when activated. Natural muscle contracts upon being activated, and creating artificial muscles that contract in the active state like natural muscle has been a challenge pursued by other groups (see [43] and references therein). Identifying possible mechanisms for the contractile actuation became one of the main goals of this thesis and studies were conducted to test for their existence. Another goal was to see whether the properties of CNT actuators can be dramatically improved by using these yarns with their higher tensile strength and modulus.

1.4.2. Torsional actuation

The axial contraction described above is observed if both ends of the yarn are prevented from freely rotating by being clamped. If one end of the yarn is anchored instead, and is otherwise free to rotate, the yarn unwinds upon being charged and winds back when discharged, resulting in a visible rotation of the anchor, which can exceed several turns. However, the yarn tends to unwind more than it winds back every time the potential goes

³ Contraction in CNT sheets had been reported at potentials beyond the breakdown potential limits of the electrolyte, but not at potentials within those limits. This contractile actuation has been shown to be due to gas evolution within the electrode and not due to ionic charging [42].

back to zero, resulting in a gradual net untwisting of the yarn. Since the amount of actuation is a function of the twist rate, this net untwisting leads to a gradual loss of actuation. Torsional actuation provides valuable information about actuation mechanisms that are also behind the tensile actuation, and as shall be seen in Chapter 7, enables us to confirm the mechanism of actuation and relate the actuation strains to the twisted structure of the yarn.

1.5. Electrochemistry background and techniques

Since the yarns actuate when charged electrochemically, it is necessary to discuss the origins and theory of electrochemical charge storage along with the two most important techniques used for electrochemical characterization. Here the Gouy-Chapman model for electrochemical charge storage is described, followed by the descriptions of cyclic voltammetry (CV) and electrochemical impedance spectroscopy (EIS), two techniques frequently used to study the electrochemical charge storage and charge loss behaviour of materials, and employed later in the thesis to study and characterize the yarn.

1.5.1. Electrochemical charge storage: Gouy-Chapman model, double-layer, and diffuse layers

When a conducting material is placed in an electrolyte and a potential is applied to it, ions of opposite charge are attracted to it. This leads to the build-up of a layer of charge close to the surface, known as the double-layer [44]. The double layer is usually followed by an exponential decrease in charge concentration at larger distances from the electrode surface (Figure 1.8). This second layer of charge is referred to as the diffuse layer. In standard electroanalytical chemistry, where low electrolyte concentrations are of interest,

the interactions between the ions are typically ignored and they are assumed to be point charges following a Boltzmann distribution. These assumptions lead into the Gouy-Chapman model, which describes some of the basic properties of double layers, such as the surface capacitance of electrodes and the dependence of that capacitance on the applied potential⁴ [44].

The charges on the electrode surface along with the counter-ions in the double-layer and the diffuse layers can be considered as a capacitor (Figure 1.8), which due to the small separation between the opposite charges (on the order of a solvated ion radius, ~ 1 nm), can have a very large capacitance (~ 0.1 F/m² in concentrated solutions [44]) compared to what is achievable in parallel-plate capacitors. If the electrode surface is porous or rough, counter-ions can find their way into the pores and allow the inner surfaces of the pores to charge, thus increasing the capacitance even further by increasing the available surface area. Since there is plenty of space between the polymer strands in conducting polymer actuators, and between individual CNTs and bundles in CNT actuators, a large amount of electrical charge will be stored inside the electrode (actuator) volume when a potential is applied between the actuator and another counter-electrode, leading to actuation. Thus, if the effective capacitance of the actuator electrode is known, the amount of charge stored in it can be estimated at a given potential, and the actuation can be related to the applied potential.

⁴ For a detailed description of the GC model, see Bard and Falkner pp. 546-54

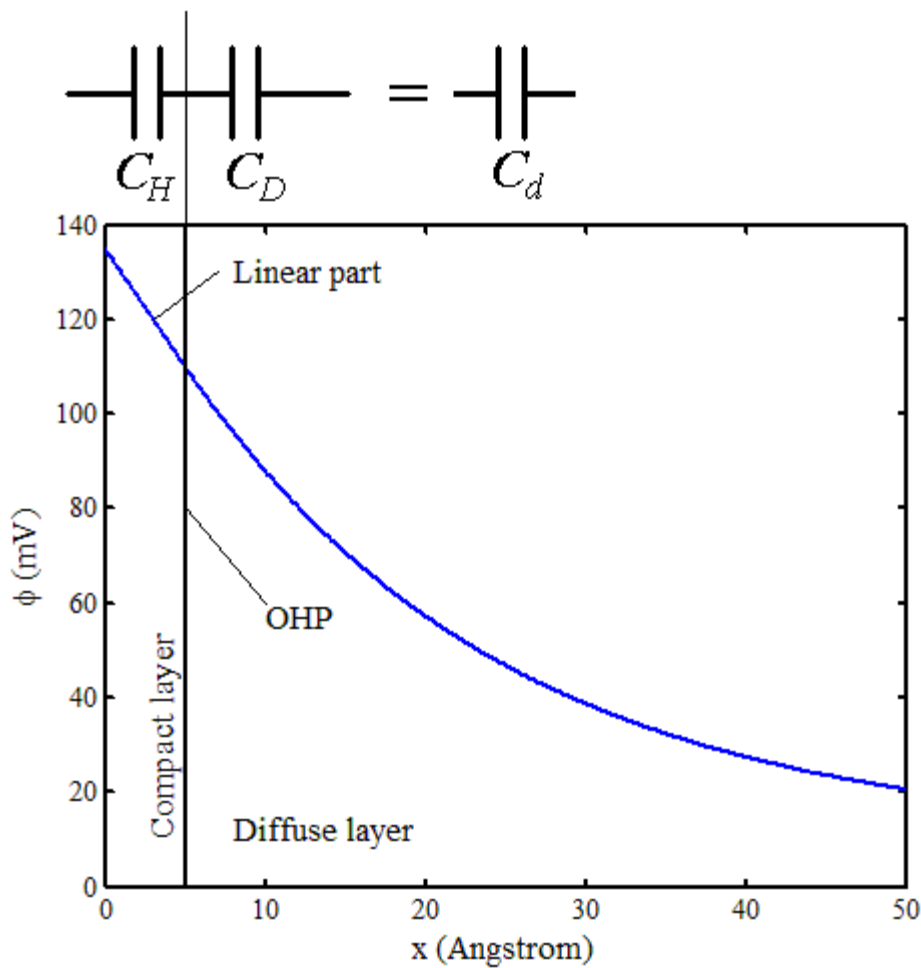


Figure 1.8: The compact (double) layer of charge followed by the diffuse layer in the electrolyte near a planar electrode

1.5.2. Cyclic Voltammetry (CV)

In cyclic voltammetry the potential applied between the working electrode (i.e. the artificial muscle) and the counter electrode is swept back and forth at a constant rate within the desired range of potentials, forming a triangular potential waveform, while the cell current is measured. Typically, the current is plotted vs. the applied potential, forming a diagram known as a cyclic voltammogram. For a purely capacitive material,

this diagram should resemble a rectangle⁵ (Figure 1.9) [45]. The vertical width of such a rectangle is proportional to the capacitance of the electrode⁶. Any peaks in the cyclic voltammogram of a cell can imply electrochemical reactions taking place in the cell. Such reactions can lead to a loss of charge that would be transferred through the interface due to Faradaic electrochemical reactions. Currents due to Faradaic reactions can sometimes be modelled by adding a parallel resistor to the capacitor model. Such a resistor shows that some charge flows in the cell without being stored in the actuator, and thus without contributing to the actuation. Since the magnitude of the parasitic current can depend nonlinearly on the applied potential, the resistance of the resistor in question can also depend on the potential. When studying artificial muscles such loss of charge can hinder achieving a good understanding of the actuation mechanisms, since part of the charge entering the cell would not be contributing to actuation. Therefore, it is important to study and identify charge storage and charge loss processes and mechanisms. Cyclic voltammetry provides a useful tool for such studies, as will be discussed in Chapters 4 and 5.

⁵ $i = C \frac{dV}{dt}$, $\frac{dV}{dt} = \pm \alpha \Rightarrow i = \pm \alpha C$, forming a line parallel with the horizontal axis with a positive offset at upsweep and with a negative offset at downsweep, resulting in a rectangular shape.

⁶ $2\alpha C$, as is evident from the previous footnote.

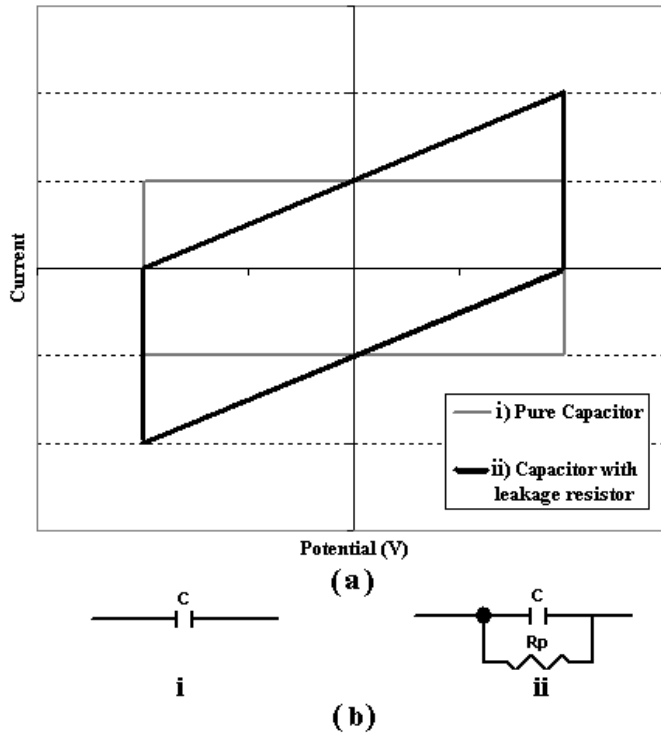


Figure 1.9: The cyclic voltammogram of a pure ideal capacitor, which can model the charge storage behaviour of a carbon nanotube actuator to first order and a parallel RC circuit, which can model the charge storage in the actuators in addition to some parasitic currents that may be flow in the cell.

1.5.3. Electrochemical Impedance Spectroscopy (EIS)

Electrochemical Impedance Spectroscopy is another method employed to study the charge storage properties of the CNT yarn artificial muscles. In this method a small sinusoidal voltage is superimposed on a bias potential applied to the cell. The frequency of the sinusoidal signal is then varied within a desired range and the impedance of the cell is measured by measuring the resulting current at various frequencies. The Bode plot and a polar plot of the impedance are made, and a fitting routine can be used to find an equivalent circuit whose impedance has a similar dependence on frequency as the measured impedance response (Figure 1.10). Typically, engineers think in terms of

capacitance when charge storage is involved. So by fitting the response of a circuit including a capacitor, such as the inset in Figure 1.10a, the equivalent capacitance of the electrode can be estimated. However, as can be seen from Figure 1.10a and b, the response of a circuit including one capacitor is not a very good fit and exhibits deviations from the experimentally measured response, particularly in the Nyquist plot and the phase response in the Bode plot. Alternative equivalent circuits can be used to improve the fit. One such circuit is shown in the inset in Figure 1.10c, and includes a circuit element with an impedance of

$$Z = \frac{1}{Y_0(j\omega)^P}, \quad (1.1)$$

where P is a real number between zero and one, usually close to unity [46]. Depending on the structure and properties of the materials used for the electrode, the value of P may vary. Y_0 is a real constant combining the resistive and capacitive properties of the electrode. If Y_0 is independent of frequency, the impedance, Z will have a constant phase angle. Therefore, the circuit element is known as a Constant Phase Element (CPE). If P is 1, then the element acts as a capacitor. As can be seen from comparing Figure 1.10a and b with Figure 1.10c and d, the CPE-based circuit model results in response that fits the system response more closely. However, the fractional values of P required to provide a good fit in experiments like these make it more difficult to relate the model to physical phenomena. That is why it is sometimes preferred to use the capacitor-based circuit depicted in Figure 1.10a inset. In some situations, physical interpretations of CPEs can be generated using transmission line models. In Chapter 5 both types of fit are used to describe the electrochemical response of the yarns, and to extract capacitance, which is

then used in Chapter 7 to help understand the actuation mechanism. A Solatron 1260 impedance/gain-phase analyzer was used in our EIS measurements. Some of the results obtained using EIS are presented in Chapter 5.

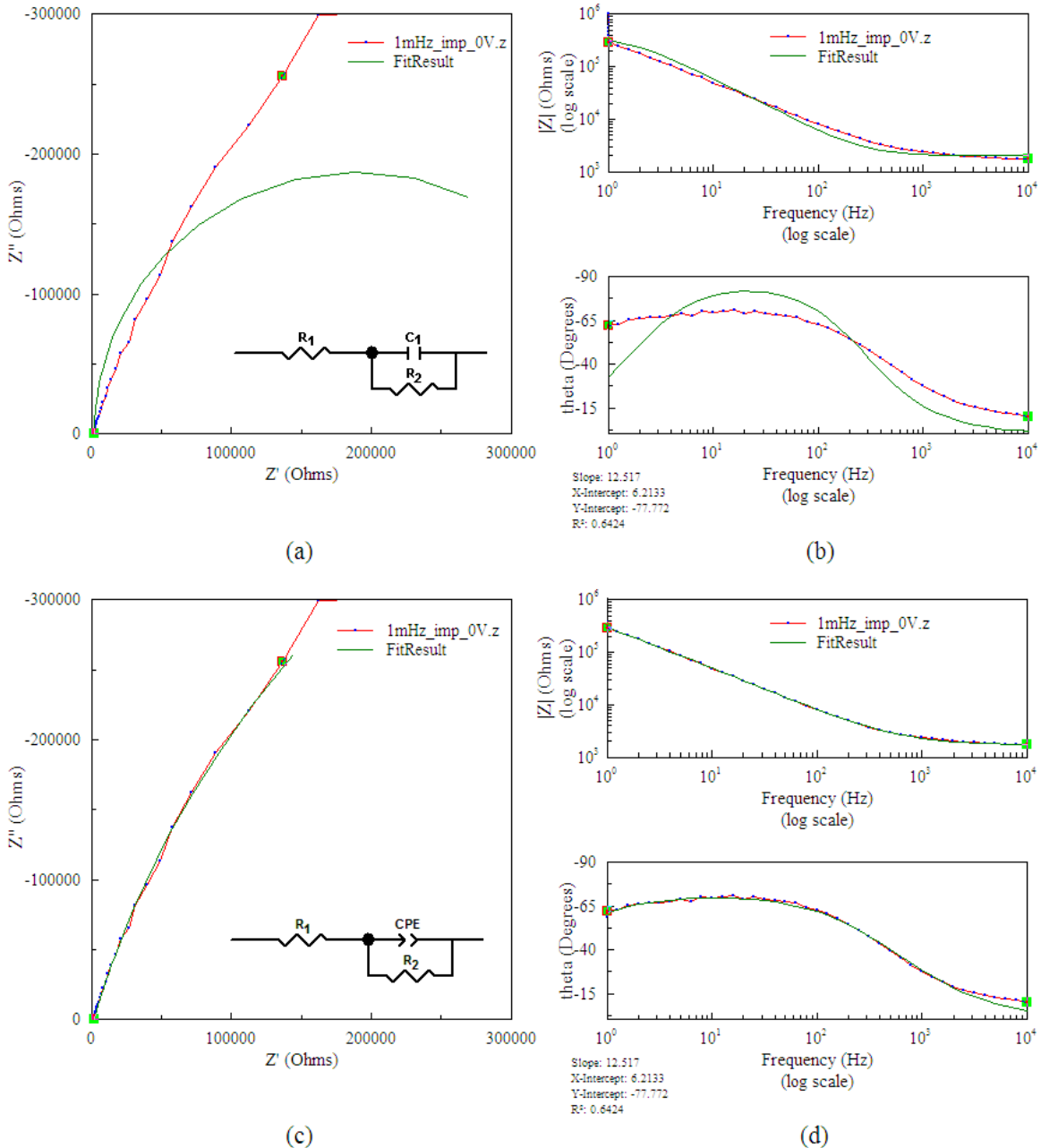


Figure 1.10: Examples of EIS results for the CNT yarn actuator: (a) the Nyquist (polar) plot and (b) the Bode plot fit with the response from a parallel-series RC circuit (inset in a). The same Nyquist plot (c) and Bode plot (d) fit with the response of a similar circuit (inset in c) with a CPE replacing the capacitor.

1.6. Thesis overview

To better understand that actuation in the yarns and to pave the way toward their engineering applications it is necessary to characterize them from various points of view. Below is an overview of the most important measurements needed to understand the actuation properties of the yarn. The description of each characteristic is accompanied by a summary of the most important techniques used to characterize that aspect of performance. The results of these measurements are described in Chapters 2-7, which are followed by discussion and conclusions in Chapter 8.

1.6.1. Mechanical/electromechanical characterization (Chapters 2, 3)

1.6.1.1. Actuation tests

By definition an actuator must be capable of producing movement. How much motion, and how does this depend on the charge and voltage, in the case of electrically driven actuators, are fundamental questions. If the effective capacitance of the artificial muscle is known, the amount of the stored charge can be related to the applied voltage. The relationship between the stress or strain generated in the artificial muscle, and the stored charge or the applied voltage can be considered as the characteristic equation of the artificial muscle.

An electromechanical apparatus is needed to find the relationship between stress/strain and charge/voltage. For most of the experiments in this thesis the electromechanical “muscle analyzer” made by Aurora Scientific Inc. was used to measure stresses and strains as described in Chapter 2. A Solatron 1287 electrochemical interface was used to

control the applied potentials and currents. More details of electromechanical actuation tests can be found in Chapters 2 and 3.

1.6.1.2. Tensile tests

It is important to know if and how the tensile properties of an artificial muscle depend on the electrical quantities such as voltage and charge. A stiffer material deforms less under the same force compared to a more compliant material. Thus, if the stiffness of an artificial muscle under load changes with its oxidation state, a strain will be induced because of the change in the modulus itself. It is therefore important to measure the tensile modulus of the yarn at various applied potentials. Measurements of tensile properties are presented in Chapter 2.

1.6.2. Electrochemical characterization (Chapters 4 and 5)

The CNT yarn actuator is an ionic actuator and is actuated in an electrolyte. As mentioned, the amount of actuation in ionic artificial muscles usually depends on the amount of ionic charge stored in their volume, and so in order to understand the actuation behaviour, it is important to know how much charge is stored in the yarn under various electrical and mechanical conditions. For this purpose, cyclic voltammetry (CV) and electrochemical impedance spectroscopy (EIS), discussed above, are used to study the charge storage and loss behaviour of the yarns.

1.6.3. Reverse/sensor mode characterization (Chapter 6)

Most actuators can work in reverse mode to convert mechanical energy to electrical energy. An example of this is the electric motor, which, if turned by external mechanical

power, can work as a generator. In the paper adopted here as Chapter 6 it is shown that the CNT yarn actuators are no exception and can generate an electric voltage or current in response to a change in the applied mechanical tension force. The experimental setup for this measurement is similar to those used in actuation tests. The main difference is that the “muscle analyzer” electromechanical apparatus applies a time varying tension force or displacement (rather than holding one of these constant), and the electrical quantities are now the outputs for this sensor/system. Results show that the CNT yarns can convert the mechanical energy to electrical energy. At constant potential, the application of an external force results in a current being generated in the cell. At open circuit, the application of an external force results in a change in the open-circuit potential of the cell. The magnitude of the generated current and the induced change in the open-circuit potential corresponds to the magnitude of the applied force.

1.6.4. Identifying possible actuation mechanisms (Chapter 7)

Identifying possible actuation mechanisms in CNT yarn artificial muscles was one of the main goals of this thesis. Chapter 7 is dedicated to identifying possible mechanisms and presenting experimental and theoretical evidence for and against each. A model is presented based on the system geometry and physical parameters that can predict the actuation behaviour with good accuracy.

We suggest that a possible and likely explanation for contractile actuation in the yarns is a structural change within the yarn, leading to an axial contraction due to the yarn geometry. Literature on yarn mechanics predicts that if a twisted yarn swelled, it would contract due to an effective change in its twist rate [47]. Therefore, any mechanism that would lead to a radial swelling in the yarn could potentially explain the axial contraction.

All evidence is consistent with the assumption that such structural change indeed takes place in the yarn, leading to actuation. Three possible mechanisms for the radial swelling were identified and investigated. These three mechanisms are:

1. Pneumatics and gas evolution, due to the formation of a gas from the breakdown of the electrolyte within the CNT structure;
2. Double-layer forces, as predicted by DLVO theory [48, 49], due to a repulsion between the charged double-layers around CNTs within the yarn;
3. Ion insertion and intercalation, due to the extra volume of ions and solvent that are inserted into the yarn structure.

All three mechanisms will lead to radial strain, which in turn leads to an axial contraction if the ends of the yarn are prevented from twisting. As suggested and discussed in Chapter 7, ion insertion is likely responsible for CNT yarn actuation.

1.7. Conclusions

The goal of this chapter was to provide the context and background about CNT yarn actuators that are the focus of this thesis. An overview of artificial muscles in general and ionic artificial muscles in particular was presented. The fibre spinning process that is used to spin the yarns used in our experiments is introduced and compared with two alternative techniques. Some of the main techniques used to characterize the yarn actuators are introduced, such as cyclic voltammetry and electrochemical impedance spectroscopy. An overview of the proceeding chapters, which are based on previous publications, was presented.

References

- [1] J. D. Madden, "Mobile robots: Motor challenges and materials solutions," *Science*, vol. 318, pp. 1094-7, 2007.
- [2] J. D. W. Madden, B. Schmid, M. Hechinger, S. R. Lafontaine, P. G. A. Madden, F. S. Hover, R. Kimball, and I. W. Hunter, "Application of polypyrrole actuators: Feasibility of variable camber foils," *IEEE Journal of Oceanic Engineering*, vol. 29, pp. 738-749, 2004.
- [3] J. D. W. Madden, N. A. Vandesteeg, P. A. Anquetil, P. G. A. Madden, A. Takshi, R. Z. Pytel, S. R. Lafontaine, P. A. Wieringa, and I. W. Hunter, "Artificial muscle technology: Physical principles and naval prospects," *IEEE Journal of Oceanic Engineering*, vol. 29, pp. 706-728, 2004.
- [4] Y. Bar-Cohen, "World-Wide EAP: EAP Materials and Product Manufacturers," vol. 2006, 2006.
- [5] Y. Bar-Cohen, *Electroactive polymer (EAP) actuators as artificial muscle*, 2nd ed. Bellingham, WA: SPIE, 2004.
- [6] T. A. Skotheim, R. L. Elsenbaumer, and J. R. Reynolds, *Handbook of Conducting Polymers*. New York: Marcel Dekker, 1998.
- [7] R. H. Baughman, "Conducting polymer artificial muscles," *Synthetic Metals*, vol. 78, pp. 339-353, 1996.
- [8] Q. Pei and O. Inganäs, "Electrochemical applications of the beam bending method; a novel way to study ion transport in electroactive polymers," *Solid State Ionics*, vol. 60, pp. 161-166, 1993.

- [9] J. D. Madden, P. G. Madden, P. A. Anquetil, and I. W. Hunter, "Load and time dependence of displacement in a conducting polymer actuator," *Materials Research Society Proceedings*, vol. 698, pp. 137-144, 2002.
- [10] R. H. Baughman, R. L. Shacklette, and R. L. Elsenbaumer, "Micro electromechanical actuators based on conducting polymers.," in *Topics in Molecular Organization and Engineering, Vol.7: Molecular Electronics*, , P. I. Lazarev, Ed. Dordrecht: Kluwer, 1991, pp. 267
- [11] T. E. Herod and J. B. Schlenoff, "Doping induced strain in polyaniline: stretchoelectrochemistry," *Chemistry of Materials*, vol. 5, pp. 951-955, 1993.
- [12] R. Z. Pytel, E. L. Thomas, Y. Chen, and I. W. Hunter, "Anisotropic actuation of mechanically textured polypyrrole films," *Polymer* vol. 49, pp. 1338-1349, 2008.
- [13] M. R. Warren and J. D. Madden, "A structural and electrochemical study of polypyrrole as a function of oxidation state," *Syntehtic Metals*, vol. 156, pp. 724-730, 2006.
- [14] Y. Nogami, J.-P. Pouget, and T. Ishiguro, "Structure of highly conducting PF6--doped polypyrrole," *Synthetic Metals*, vol. 62, pp. 257-263, 1994.
- [15] S. Hara, T. Zama, W. Takashima, and K. Kaneto, "TFSI-doped polypyrrole actuator with 26% strain," *Journal of Materials Chemistry*, vol. 14, pp. 1516-1517, 2004.
- [16] G. M. Spinks, V. Mottaghitalab, M. Bahrami-Saniani, P. G. Whitten, and G. G. Wallace, "Carbon-nanotube-reinforced polyaniline fibers for high-strength artificial muscles," *Advanced Materials*, vol. 18, pp. 637-40, 2006.
- [17] T. Mirfakhrai, J. D. Madden, and R. H. Baughman, "Polymer Artificial Muscles," *Materials Today*, vol. 10, pp. 30-38, 2007.

- [18] G. M. Spinks and V.-T. Truong, "Work-per-cycle analysis for electromechanical actuators," *Sensors and Actuators A-Physical*, vol. 119 pp. 455–461, 2005.
- [19] A. DellaSanta, A. Mazzoldi, and D. DeRossi, "Steerable microcatheters actuated by embedded conducting polymer structures," *Journal of intelligent material systems and structures*, vol. 7, pp. 292-300, 1996.
- [20] P. F. Pettersson, E. W. H. Jager, and O. Inganas, "Surface micromachined polymer actuators as valves in PDMS microfluidic system," *Proc. Microtechnologies in Medicine and Biology, 1st Annual International Conference On., Lyon, France*, pp. 334-335, 2000.
- [21] B. W. Smith and D. E. Luzzi, "Carbon Nanotubes," in *Introduction to Nanoscale Science and Technology*, S. E. a. J. R. H. Massimiliano Di Ventra, Jr., Ed. USA: Springer, 2004.
- [22] R. H. Baughman, A. A. Zakhidov, and W. A. de Heer, "Carbon nanotubes - the route toward applications," *Science*, vol. 297, pp. 787-792, 2002.
- [23] G. M. Spinks, G. G. Wallace, R. H. Baughman, and L. Dai, "Carbon Nanotube Actuators: Synthesis, Properties, and Performance," in *Electroactive Polymers (EAP) Actuators as Artificial Muscles, Reality, Potential and Challenges* Y. Bar-Cohen, Ed. Bellingham WA: SPIE press, 2004 pp. 261-95.
- [24] L. Pietronero and S. Strässler, "Bond-length Change as a Tool to Determine Charge Transfer and Electron-Phonon Coupling in Graphite Intercalation Compounds " *Physical Review Letters*, vol. 47, pp. 593-96, 1981.

- [25] T. Mirfakhrai, R. Krishna-Prasad, A. Nojeh, and J. D. W. Madden, "Electromechanical actuation of single-walled carbon nanotubes: an ab initio study," *Nanotechnology*, vol. 19, pp. 315706 2008.
- [26] R. H. Baughman, C. X. Cui, A. A. Zakhidov, Z. Iqbal, J. N. Barisci, G. M. Spinks, G. G. Wallace, A. Mazzoldi, D. De Rossi, A. G. Rinzler, O. Jaschinski, S. Roth, and M. Kertesz, "Carbon nanotube actuators," *Science*, vol. 284, pp. 1340-1344, 1999.
- [27] T. Mirfakhrai, R. Krishna-Prasad, A. Nojeh, and J. D. W. Madden, "Bond Order Effects in Electromechanical Actuation of Single-Walled Carbon Nanotubes," *Journal of Chemical Physics, accpeted (A09.05.0110)*, 2009.
- [28] T. Mirfakhrai, J. Oh, M. Kozlov, E. C. W. Fok, M. Zhang, S. Fang, R. H. Baughman, and J. D. W. Madden, "Electrochemical actuation of carbon nanotube yarns," *Smart Materials and Structures*, vol. 16, pp. S243, 2007.
- [29] J. A. Sippel-Oakley, Charge-Induced Actuation in Carbon Nanotubes and Resistance Changes in Carbon Nanotube Networks, Doctor of Philosophy Thesis, 2005, Physics, University of Florida,
- [30] P. Poulin, B. Vigolo, and P. Launois, "Films and fibers of oriented single wall nanotubes," *Carbon*, vol. 40, pp. 1741-1749, 2002.
- [31] J. Riemschneider, H. Temmen, and H. P. Monner, "CNT Based Actuators: Experimental and Theoretical Investigation of the In-Plain Strain Generation," *Journal of Nanoscience and Nanotechnology*, vol. 7, pp. 3359-3364, 2007
- [32] J. D. W. Madden, J. N. Barisci, P. A. Anquetil, G. M. Spinks, G. G. Wallace, R. H. Baughtnan, and I. W. Hunter, "Fast carbon nanotube charging and actuation," *Advanced Materials*, vol. 18, pp. 870-+, 2006.

- [33] M. Lucas, B. Vigolo, S. Badaire, D. L. Bolloc'h, A. Marucci, D. Durand, M. Hamilton, C. Zakri, P. Poulin, and P. Launois, "Alignment of Carbon Nanotubes in Macroscopic Fibers," in *Structural and Electronic Properties of Molecular Nanostructures*, H. K. e. al., Ed., 2002.
- [34] M. Kozlov, J. Oh, V. Seker, E. Kozlov, M. Zhang, S. Fang, R. Capps, E. Munoz, R. Baughman, T. Mirfakhrai, and J. Madden, "Electro-Mechanical Actuation of Carbon Nanotube Yarns, Sheets and Composites," presented at Materials Research Society fall meeting, 2005.
- [35] T. Mirfakhrai, J. Oh, M. Kozlov, E. C. W. Fok, M. Zhang, S. Fang, R. H. Baughman, and J. D. W. Madden, "Electrochemical actuation of carbon nanotube yarns," *Smart Materials and Structures*, vol. 16, 2006.
- [36] V. H. Ebron, Z. W. Yang, D. J. Seyer, M. E. Kozlov, J. Y. Oh, H. Xie, J. Razal, L. J. Hall, J. P. Ferraris, A. G. MacDiarmid, and R. H. Baughman, "Fuel-powered artificial muscles," *Science*, vol. 311, pp. 1580-1583, 2006.
- [37] J. D. Madden, "Materials science - Artificial muscle begins to breathe," *Science*, vol. 311, pp. 1559-1560, 2006.
- [38] P. G. Whitten, G. M. Spinks, and G. G. Wallace, "Mechanical properties of carbon nanotube paper in ionic liquid and aqueous electrolytes," *Carbon*, vol. 43, pp. 1891-1896, 2005.
- [39] B. Vigolo, A. Penicaud, C. Coulon, C. Sauder, R. Pailler, C. Journet, P. Bernier, and P. Poulin, "Macroscopic Fibers and Ribbons of Oriented Carbon Nanotubes," *Science*, vol. 290 pp. 1331-4, 2000.

- [40] K. R. Atkinson, S. C. Hawkins, C. Huynh, C. Skourtis, J. Dai, M. Zhang, S. Fang, A. A. Zakhidov, S. B. Lee, A. E. Aliev, C. D. Williams, and R. H. Baughman, "Multifunctional carbon nanotube yarns and transparent sheets: Fabrication, properties, and applications," *Physica B: Condensed Matter*, vol. 394, pp. 339-343, 2007.
- [41] A. E. Aliev, C. Guthy, M. Zhang, S. Fang, A. A. Zakhidov, J. E. Fischer, and R. H. Baughman, "Thermal transport in MWCNT sheets and yarns," *Carbon*, vol. 45, pp. 2880-2888, 2007.
- [42] G. M. Spinks, G. G. Wallace, L. S. Fifield, L. R. Dalton, A. Mazzoldi, D. De Rossi, Khayrullin, II, and R. H. Baughman, "Pneumatic carbon nanotube actuators," *Advanced Materials*, vol. 14, pp. 1728-32, 2002.
- [43] F. Carpi, C. Salaris, and D. D. Rossi, "Folded dielectric elastomer actuators," *Smart Materials and Structures*, vol. 16 pp. S300-S305, 2007.
- [44] A. J. Bard and L. R. Faulkner, *Electrochemical Methods, Fundamentals and Applications*, Second ed. New York: Wiley, 2001.
- [45] T. Mirfakhrai, M. Kozlov, M. Zhang, S. Fang, R. H. Baughman, and J. D. W. Madden, "Capacitive charging and background processes in carbon nanotube yarn actuators," *Proc. SPIE Smart Materials and Structures/NDE*, vol. 6524, pp. 65241H1-12, 2007.
- [46] J. R. Macdonald and W. R. Kenan, *Impedance Spectroscopy: Emphasizing Solid Materials and Systems*: Wiley-Interscience 1987.
- [47] J. W. S. Hearle, P. Grossberg, and S. Backer, *Structural Mechanics of Fibers, Yarns and Fabrics*, vol. 1. New York: Wiley-Interscience, 1969.

- [48] E. J. W. Verwey and J. T. G. Overbeek, *Theory of the stability of lyophobic colloids: The interaction of sol particles having an electric double layer*. Amsterdam: Elsevier Publishing Company, 1948.
- [49] B. V. Derjaguin and L. D. Landau, "Theory of stability of strongly charged lyophobic sols and of the adhesion of strongly charged particles in solutions of electrolytes," *Acta Physicochimica URSS*, vol. 14, pp. 633-62, 1941.

Chapter 2:

2 Electrochemical actuation of carbon nanotube yarns¹

In this chapter, the experimental evidence for electromechanical actuation in twisted yarns of carbon nanotubes is presented. The experimental apparatus used for most experiments in this thesis is also described. The actuation strain behaviour in response to triangular and square wave potentiostatic input is studied. The change in the elastic modulus of the yarn as a function of the oxidation state is also investigated. These results will be referred to later in the thesis and compared to the predictions of the proposed model for the actuation mechanisms.

2.1. *Introduction*

Individual carbon nanotubes (CNTs) offer exceptional properties. The tensile modulus of single-wall carbon nanotubes (640 GPa) approaches that of diamond, while their tensile strength of approximately 20-40 GPa is about ten times higher than of continuous yarns or fibres of any type [1]. Many research groups have been working to make bulk

¹ A version of this chapter has been published. Mirfakhrai, T.; Oh, J.; Kozlov, M.; Fok, E. C. W.; Zhang, M.; Fang, S.; Baughman, R. H. and Madden, J. D., “Electrochemical actuation of carbon nanotube yarns”, Smart Materials and Structures, vol. 16, No. 2, pp. S243-249, April 2007

assemblies or yarns that can approach the modulus and tensile strength of individual CNTs. Interest in nanotube assemblies expanded in a new direction when it was found that sheets of nanotubes (Bucky paper) actuate when used as an electrode in an electrochemical cell [2]. Since then actuation strains of up to 0.4 % [3] have been reported at effective strain rates of as high as 19 %/s [4].

Electrochemical double layer charge injection in nanotubes is believed to induce actuation via quantum mechanical and electrostatic effects that dominate for small and large degrees of charge injection, respectively [2, 5]. This double layer charge injection, shown in Figure 2.1, is a non-Faradaic process in which changing the charge on the carbon atoms results in changes of C-C bond lengths [6, 7]. The excess charge on the nanotubes is compensated at the nanotube-electrolyte interface by ions (cations or anions). The nanotubes act as double layer capacitors that are charged and discharged during actuation cycles.

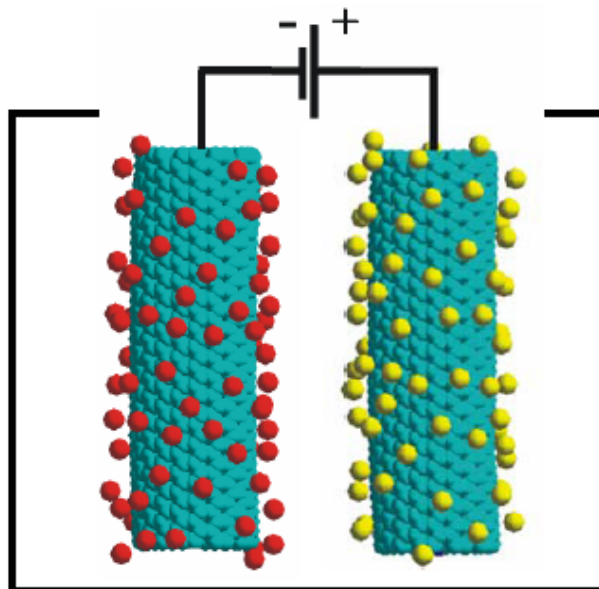


Figure 2.1: Ions of opposite charges are attracted to the CNT electrodes in an electrolyte when a voltage is applied, resulting in a change in the C-C bond length and actuation

Because the Young's modulus of individual CNTs is extremely high, a relatively small strain of actuation can result in high stress generation, producing unprecedented work densities per cycle [8]. The actuation process can be potentially fast if charge can be injected quickly, leading to high power to mass ratios [4]. CNTs are stable at temperatures as high as 1000°C if sealed from oxygen, making them appropriate for high-temperature actuation. However, before any of this can be realized it is necessary to make macroscopic structures out of CNTs that preserve the superb mechanical and electronic properties of the component CNTs. Actuation of sheets of multi-wall carbon nanotubes (MWNTs) has been reported [9], showing reasonable strain but having only moderate tensile strength. Another approach is to spin fibres of aligned nanotubes. The present paper reports the first actuation measurements made on MWNT yarns that have been recently developed by the NanoTech Institute of the University of Texas at Dallas [10]. A scanning electron micrograph of such a yarn is show in Figure 2.2.

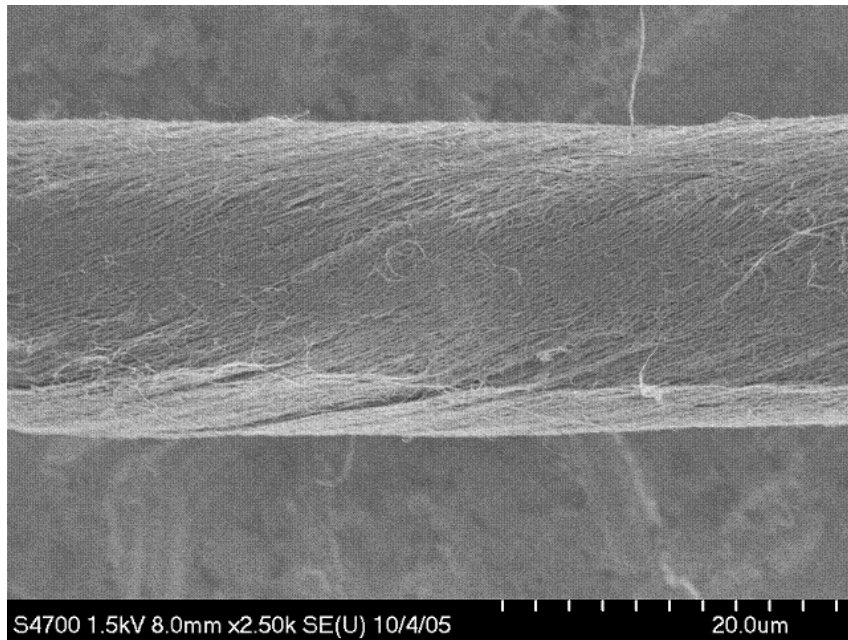


Figure 2.2: SEM micrograph of a twist-spun MWNT yarn

2.2. Methods

MWNT yarns were prepared by a dry spinning method [10], i.e., by drawing and twisting tubes from a forest. The MWNT forest was synthesized by catalytic CVD using acetylene gas as the carbon source. MWNTs, which are about 10 nm in diameter, are simultaneously drawn from the MWNT forest and twisted. The nanotube length in the forest is about 300 μm , resulting in yarn diameters between 1 and 60 μm , depending upon the forest width used for spinning. The twist is characterized by the helix angle (α), which depends directly upon the degree of twist and inversely on the yarn diameter. The degree of twist is typically 15,000 turns/m.

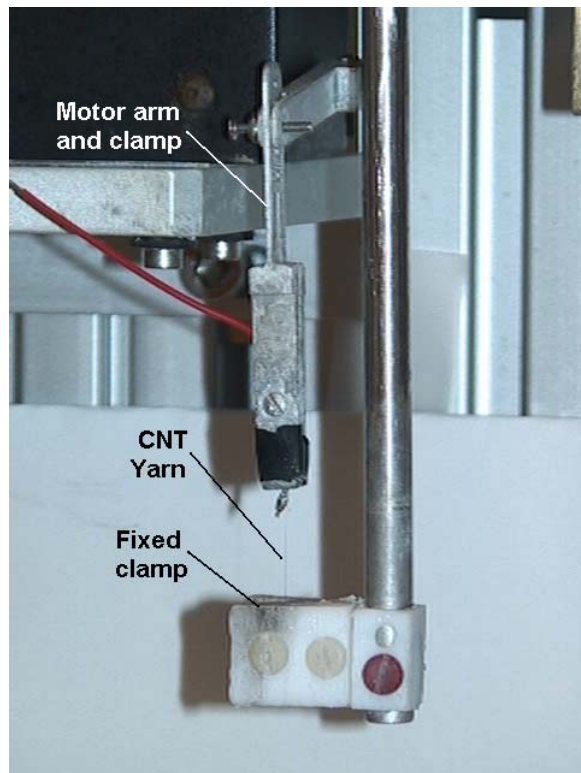


Figure 2.3: The CNT yarn mounted in the ASI muscle analyzer clamp.

In order to apply forces and record actuation forces and displacements generated by the CNT yarns, an Aurora Scientific ASI 300 muscle analyzer and its LabView-based software (www.aurorascientific.com) have been employed. Figure 2.3 is a photo of the apparatus used to apply force and of the yarn and clamping mechanism. The fibre is mounted between a lower fixed clamp and an upper movable motor arm. A computer-controlled potentiostat, similar to the one described in [11], is used to apply potentials. A data acquisition card (National Instruments 6036E) gathers the force and displacement data from the muscle analyzer and also logs the applied voltage and current. Figure 2.4 is a block diagram of the measurement setup with the yarn as one of the electrodes in the actuation cell. This configuration is referred to as Setup 1.

For some of the strain measurements a Perkin-Elmer DMA 7e with a custom sample holder and electrochemical cell was employed. The voltage was applied and current recorded via a Gamry Instruments potentiostat. This setup is referred to as Setup 2. All observed dimensional changes were normalized by sample length and are reported in percent.

As in any other measurements, uncertainties exist. The largest uncertainty comes from the measurement in the diameter of the yarn, which is taken to be equal to the average values measured by the SEM. There is about $\pm 10\%$ variation in the diameter of the yarn. This leads to a 20 % uncertainty in stress and load measurements. The uncertainty in the measurement of the length of the yarn is 0.5 mm. The lengths of the samples used for the reports in this thesis range from 12 mm and 18 mm (Chapter 2); 9 mm, 21 mm, and 16.2 mm (Chapter 3); 18.2 mm (Chapter 4); 5 mm and, 15 mm (Chapter 5); and 16.2 (Chapter 6). Therefore the uncertainty in the length of the yarn is between 2.4 % to 10 %. Since

this has the same value for all measurements of strain in an experiment, it leads to a shift or scaling of all strain values up or down, but does not affect the observed trends.

There are also uncertainties from measurement instruments. The precision resolution for displacement using the ASI setup is 1 μm . At low actuation strains the uncertainty from the precision resolution dominates the uncertainty in the reported strain values, while at higher strains, the uncertainty in the measurement of the sample length dominate the uncertainty of reported strain value. The uncertainty in the force measurement of the instrument is $\pm 0.3 \text{ mN}$ or $\pm 0.03 \text{ g}$. For a yarn with a diameter of 10 μm , this corresponds to a stress level of $\pm 3.8 \text{ MPa}$. Similar to the uncertainty for the strain measurements, the uncertainty due to the precision of the force sensor is comparable with the uncertainty from measuring the sample diameter at low loads. At higher loads, the uncertainty in the yarn diameter dominates.

The resolution in measurement of current and potential from the Solatron potentiostat is practically about 100 pA and 5 μV , respectively. In practice, there are fluctuating background currents in the order of $\pm 1 \text{ nA}$ in most of our experiments that induce the uncertainty. The uncertainty values and the number of significant figures for the quantities reported in this thesis are based on the above considerations, unless otherwise noted.

Two control experiments were performed to ensure that the observed electromechanical actuation is not due to signal interference or noise. In one experiment the

electromechanical “actuation” of a hair² was tested under conditions similar to those used for the yarn. No actuation or cell current was observed. This experiment suggests that the observed actuation strain is not due to crosstalk between channels, ground loops, etc. In another experiment, the actuation of the yarn itself was also tested in DI water, to ensure that actuation was in fact due to the presence of the ions. An initial contraction is observed when the yarn is submersed in water with no external potentials applied, but the length of the yarn stabilizes after about 300 seconds. Afterwards, very small strains close to the measurement uncertainty were observed when actuation potentials were applied. These strains can be probably attributed to the presence of some ions in the DI water, or residual contamination on the yarn surface or the glassware.

² Thanks Mya!

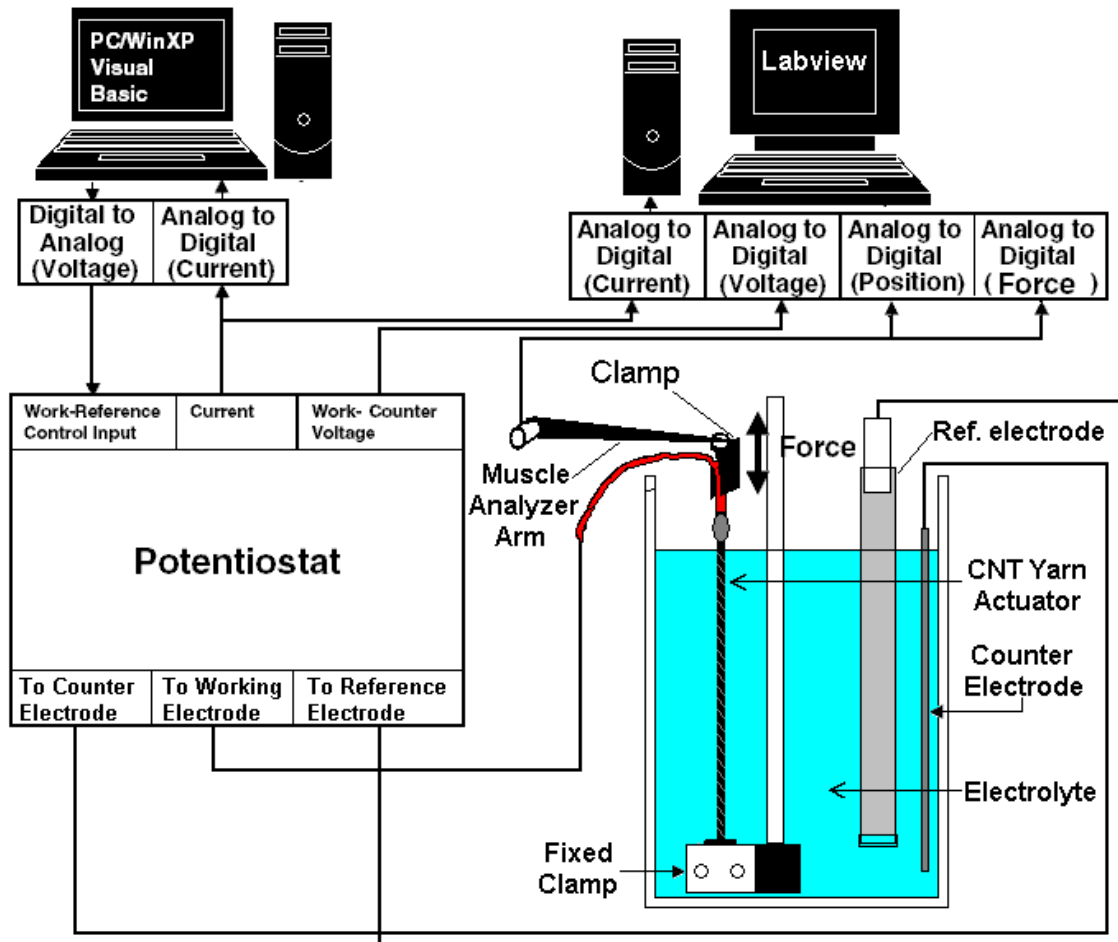


Figure 2.4: The experimental setup for measuring actuation of the yarns

2.3. Actuation

A 12 mm length of single-ply yarn with a diameter of 18 μm was loaded to 11 MPa using Setup 1 and was left in the electrolyte to relax for 30 minutes. The electrolyte used is 0.2 M tetrabutylammonium hexafluorophosphate (TBAP) in acetonitrile (MeCN). Afterwards a triangular voltage input was applied at a scan rate of 1000 mV/s, and the resulting currents and strains were measured (Figures 2.5b, a, and c, respectively). The reference electrode was aqueous Ag/AgCl in 3 M NaCl, and the counter electrode was a sheet of polypyrrole. The charge transferred (Figure 2.5d) was calculated by numerically integrating the current.

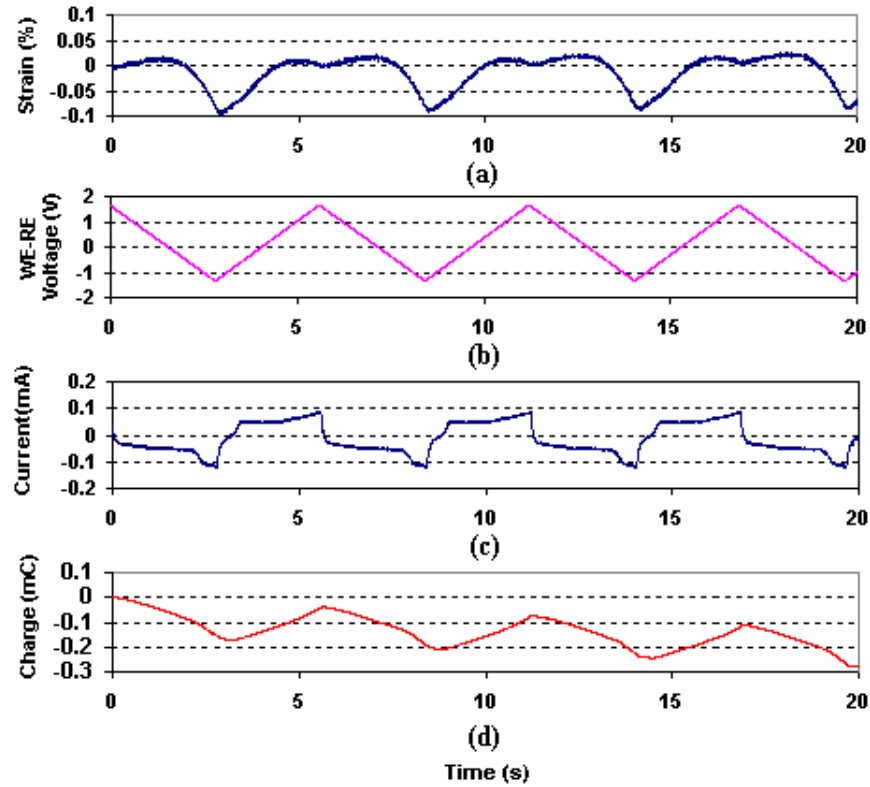


Figure 2.5: (a) Strain, (b) working electrode voltage, (c) cell current and (d) transferred charge during cyclic voltammetry of the MWNT yarn in 0.2 M TBAP in acetonitrile for an applied tensile load of 11 MPa.

The absolute value of the strain during the cyclic voltammetry (CV) is plotted vs. nominal charge per C atom (including atoms on the interior of the tubes) in Figure 2.6 for charging and discharging half-cycles. The number of atoms is calculated using the measured density of the yarns (0.8 g/cm^3) and the molar weight of carbon (12 g/mol). The magnitudes of strain match those obtained using sheets of carbon single-wall nanotubes (SWNTs) [5] over the same range of nominal charge per atom. However, the direction of the actuation in yarns is in the form of a contraction instead of an expansion. That is why the absolute value of the yarn strain is plotted to make the results readily comparable with those of Hughes and Spinks [9] in MWNT sheets (bold dots with error bars). It can be seen that the strain in yarns and sheets is similar in magnitude. However, the much larger

tensile strengths of the yarns makes them far more suitable for application. The similarity in actuation magnitude and its dependence on the charge implies that while the structure of the yarn actuator is different with the MWNT sheet, similar actuation mechanism may be at work in both. In chapter 7, we show that the actuation of the yarns is unlikely to be due to the expansion of individual CNTs, and depends on size of the ions entering the yarn. Further investigation is needed to determine if the same mechanism is also responsible for actuation in CNT sheets.

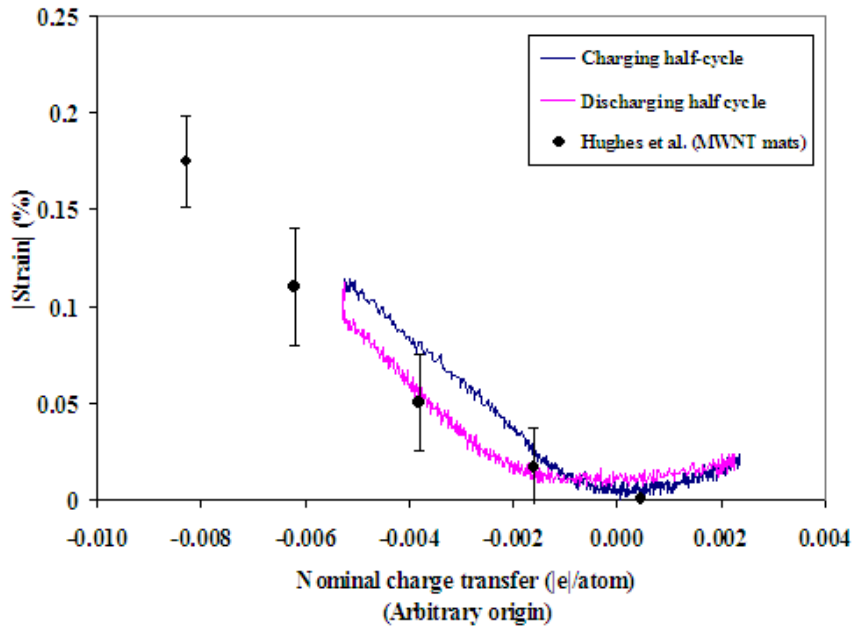


Figure 2.6: Strain vs. nominal charge per C atom during CV. The origin of the horizontal axis is arbitrary since the initial charge of the MWNTs is unknown. The dots represent strain to charge observed in MWNT sheets [9].

The experiment was repeated at a scan rate of 100 mV/s. The resulting currents for 1000 mV/s and 100 mV/s are plotted vs. the applied voltage (Figure 2.7a). The gravimetric capacitance of the yarn in TBAP in acetonitrile was estimated using the CVs to be 26 ± 5 F/g over a potential range of -0.7 V to $+0.7$ V, as shown by the square response of an ideal capacitor in Figure 2.7a. This high capacitance is very similar in magnitude to the

capacitance observed in single-wall carbon nanotubes [9], and suggests that the external surfaces of the MWNTs are largely accessible to electrolyte. The double layer capacitance of the nanotubes is estimated to be 0.17 F/m^2 . This result is derived from the measured capacitance and an estimate for the surface area per mass of MWNTs having an outer diameter of 10 nm and 8 inner layers, where the MWNT geometry was measured by transmission electron microscopy. It has been assumed that charge injection is only to outer walls and that all outer walls are accessible for charge injection. The capacitance drops by about 20 % as the scan rate is increased from 100 to 1000 mV/s. This can be due to the existence of fast and slow charging processes in the yarn similar to those described in [12] or may be limited by the mass transport. This non-ideal capacitive behaviour is further discussed in chapter 5, where we show that it may better be described as a constant phase element rather than a capacitor.

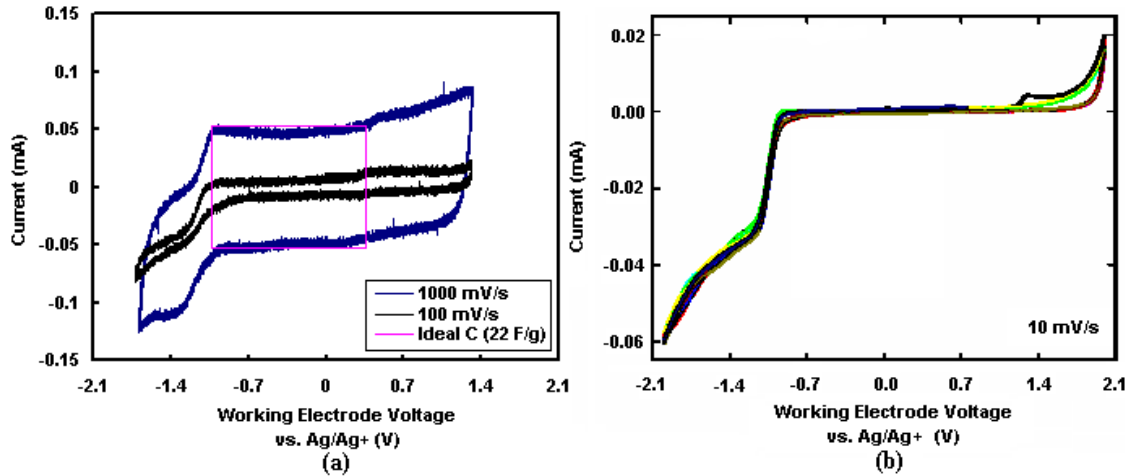


Figure 2.7: (a) Cyclic voltammogram for a 12mm-long single-ply yarn scanned at 1000 and 100 mV/s. The rectangle shows the ideal capacitor response for a gravimetric capacitance of $\sim 26 \text{ F/g}$ at 1000 mV/s. (b) CV of an 18 mm long yarn in 0.5 M tetrabutylammonium tetrafluoroborate (TBATFB) in acetonitrile (MeCN) at a scan rate of 10 mV/s

A similar experiment was performed using Setup 2 in 0.5 M tetrabutylammonium tetrafluoroborate (TBATFB) in acetonitrile (MeCN) again vs. Ag/Ag⁺ and with a Pt mesh/CNT counter electrode. The potential window was -2.50 to +2.50 V. The response to a triangular potential input scanned at 10 mV/s is shown in Figure 2.7b. The voltammetry results suggest a capacitive response due to double-layer charging of the nanotubes over a voltage range of approximately -0.7 V to +0.7 V vs. Ag/Ag⁺. The capacitance at 10 mV/s scan rate in TBATFB in acetonitrile is estimated at 22±2 F/g. Beyond this potential range a kinetics-limited reaction appears to be contributing to the current. It may be the result of electrolyte degradation. These reactions are further discussed in chapter 5.

The CV plots are considerably less resistive compared to those of MWNT sheets reported in [9]. Better axial alignment of the nanotubes in the yarns and fewer defects in the MWNTs used in the yarns are likely causes of the better conductivity along the yarn axis, resulting in a much less resistive response. This makes the yarns a much better candidate to be used as a supercapacitor compared to the MWNT sheets.

Figure 2.8 shows the actuation strain and the current in response to a series of voltage pulses with amplitudes between -2.50 V and +2.50 V. The electrolyte was 0.5 M TBATFB in MeCN. The maximum actuation strain achieved was measured to be 0.5 % using Setup 2. A similar experiment was performed using Setup 1. The voltages were applied using a Solartron SI 1287 electrochemical interface. The electrolyte was 0.2 M TBAP in MeCN, the reference electrode was aqueous Ag/AgCl and the counter electrode was a sheet of polypyrrole. The potential of the reference electrode stayed the same before and after the experiment. The pulses in each train had the same voltage amplitude.

The experiment was repeated for voltage pulses relative to 0 V vs. Ag/AgCl of -2.5V, -2V, -1.5V, -1V, -0.5V, 0V, 0.5V, 1 V and 2 V. The maximum strain achieved is about 0.5 %.

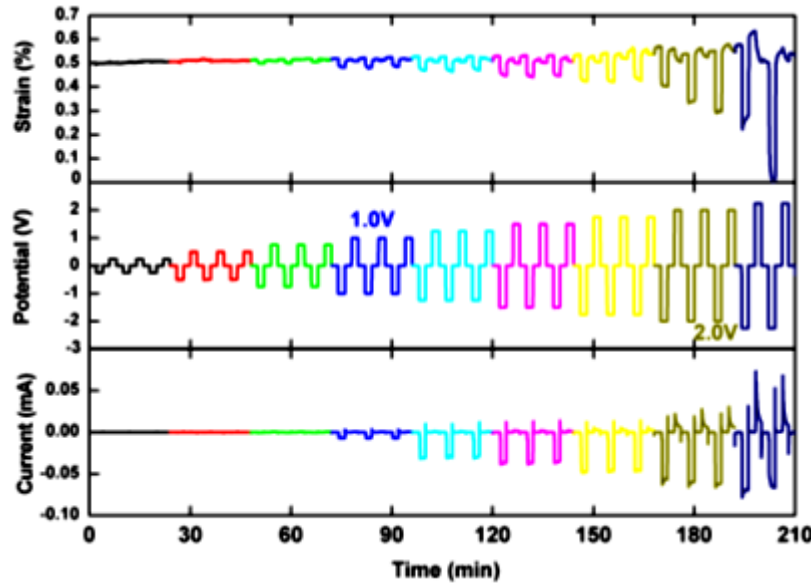


Figure 2.8: Applied voltage pulse trains vs. Ag/Ag⁺ and resulting actuation strains for actuation in 0.5 M TBATFB in MeCN

Some creep is observed during actuation in both cases similar to what has been reported before [9, 13]. The creep seems to depend on the voltage amplitude and the actuation rate, but the nature of this dependence has not yet been studied. The creep rate is very close to the rate in [9], which is about $1.6 \times 10^{-4} \text{ \%}/\text{s}$, but the creep itself is smaller in this case over the same number of actuation cycles than the creep reported in [9]. This becomes more significant if we consider that actuation in this case takes place under up to 30 MPa of load as opposed to 200 kPa in [9], demonstrating one of the benefits of employing the yarns.

The amplitude of the resulting actuation strain is plotted vs. the applied voltage pulse amplitude in Figure 2.9. For comparison, the voltages are all plotted versus Ag/Ag⁺ by adjusting the voltages measured against Ag/AgCl by 0.335 V [14]. Error bars are about the same size or smaller as the icons and are therefore hard to see on the plot.

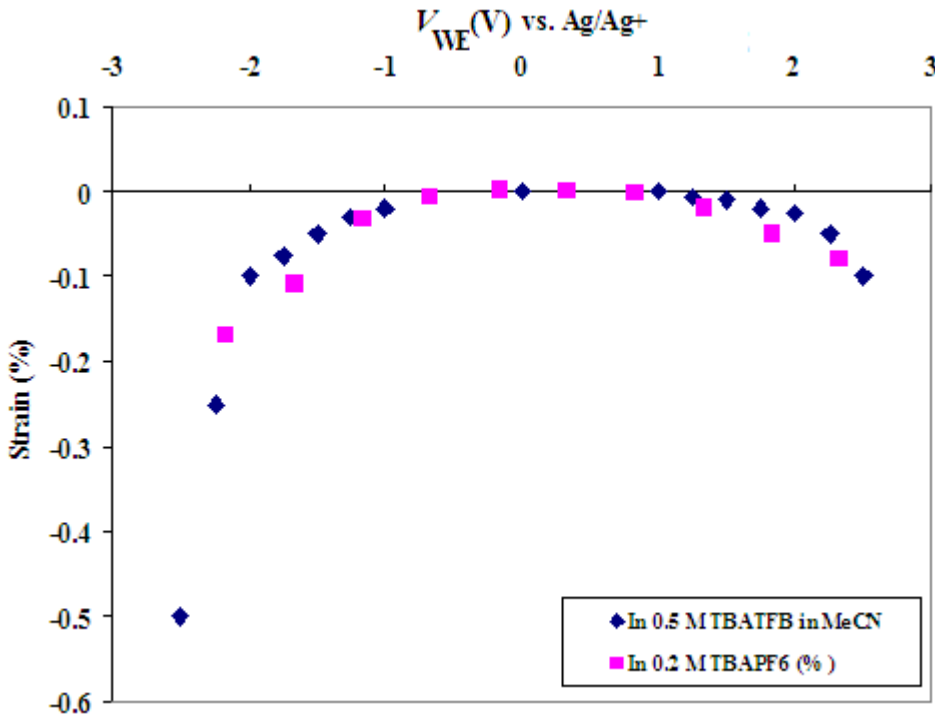


Figure 2.9: The strain amplitude plotted vs. the applied voltage amplitude.

2.4. The Young's modulus as a function of the oxidation state

The magnitude of isotonic actuation strain (i.e., for fixed load) can be influenced by potential-induced changes in modulus, as seen in polypyrrole [15]. It can also be a function of the tensile load applied on the yarn. The dependence of the Young's modulus on the charge state of the yarn and load was therefore studied.

The ASI 300 muscle analyzer was used to obtain stress/strain curves at a number of fixed potentials. The yarn was elongated by 0.1 % over 0.5 s and then brought back to its original length. The applied strain waveform and the resulting stresses are plotted in

Figure 2.10. Lines were fit to the resulting stress vs. strain curves for loading and unloading half-cycles. The relative slopes of these lines provide the effective Young's moduli of the yarn during loading and unloading.

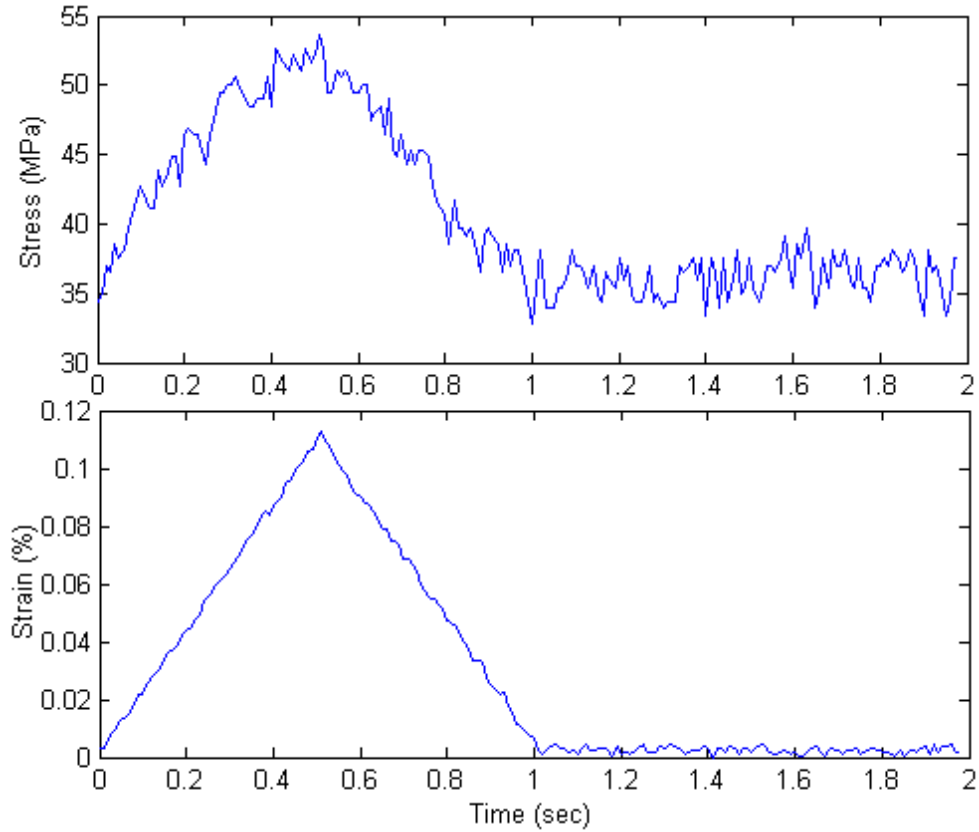


Figure 2.10: Applied strain waveform and the resulting stress to measure the Young's modulus of the yarns.

The measured Young's moduli under the loads of 35, 60 and 70 MPa are plotted in Figure 2.11. Within experimental error, no significant change in modulus is observed as the oxidation state is changed between -1.5 V to 1.5 V. The modulus in that range of voltages is 16 ± 5 GPa, but it seems to drop at the two extremes of voltage (-2 V and 2 V). This variation is within the range of experimental uncertainty, however. Nevertheless the uncertainty in modulus is large enough that it could induce a strain comparable to the actuation strains in Figure 2.9. The present results provide a first bound on the variation.

If modulus is changing at extreme voltages, it could have been a factor affecting the strains observed in Figure 2.9.

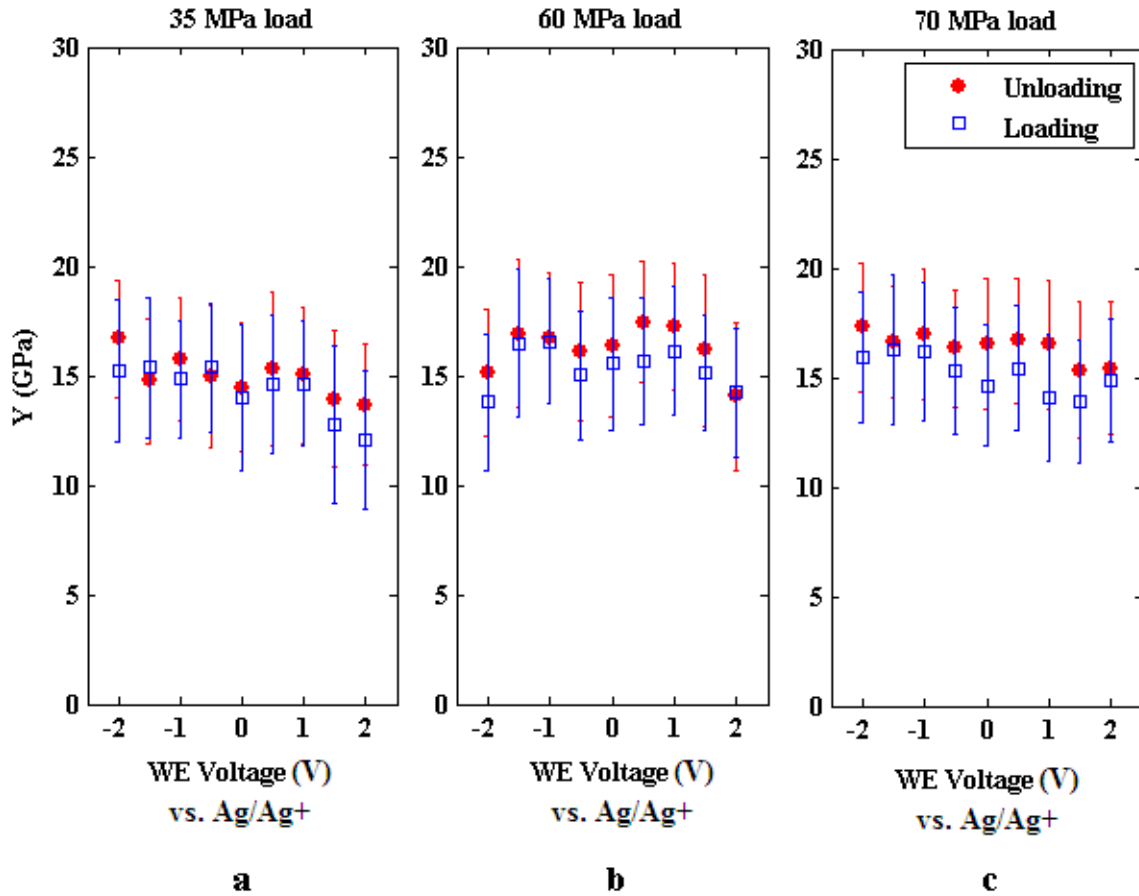


Figure 2.11: The Young's modulus of the CNT yarn as a function of the oxidation state under the loads of (a) 35, (b) 60 and (c) 70 MPa. The horizontal axes in all the plots indicate a working electrode voltage ranging from -2V to 2 V.

2.5. Conclusions

The actuation behaviour of yarns spun from multi-wall carbon nanotubes was studied. The yarns were found to contract as a result of applied voltage, unlike what had been previously reported for sheets of CNTs. The actuation strain increases nonlinearly with applied voltage, as has been observed in single-wall nanotubes. Maximum actuation strain of 0.5 % is reported at an applied voltage of -2.50 V. The gravimetric capacitance

of the yarn is found to be about 26 ± 5 F/g. The dependence of the tensile modulus on oxidation state has been studied and it is concluded that the Young's modulus about 16 ± 5 GPa and decreases at higher applied potential.

References

- [1] R. H. Baughman, A. A. Zakhidov, and W. A. de Heer, "Carbon nanotubes - the route toward applications," *Science*, vol. 297, pp. 787-792, 2002.
- [2] R. H. Baughman, C. X. Cui, A. A. Zakhidov, Z. Iqbal, J. N. Barisci, G. M. Spinks, G. G. Wallace, A. Mazzoldi, D. De Rossi, A. G. Rinzler, O. Jaschinski, S. Roth, and M. Kertesz, "Carbon nanotube actuators," *Science*, vol. 284, pp. 1340-1344, 1999.
- [3] J. N. Barisci, G. M. Spinks, G. G. Wallace, J. D. Madden, and R. H. Baughman, "Increased actuation rate of electromechanical carbon nanotube actuators using potential pulses with resistance compensation," *Smart Materials and Structures*, vol. 12, pp. 549-55, 2003.
- [4] J. D. W. Madden, J. N. Barisci, P. A. Anquetil, G. M. Spinks, G. G. Wallace, R. H. Baughnan, and I. W. Hunter, "Fast carbon nanotube charging and actuation," *Advanced Materials*, vol. 18, pp. 870-873, 2006.
- [5] G. M. Spinks, G. G. Wallace, R. H. Baughman, and L. Dai, "Carbon Nanotube Actuators: Synthesis, Properties, and Performance," in *Electroactive Polymers (EAP) Actuators as Artificial Muscles, Reality, Potential and Challenges* Y. Bar-Cohen, Ed. Bellingham WA: SPIE press, 2004 pp. 261-95.
- [6] C. T. Chan, W. A. Kamitakahara, K. M. Hoand, and P. C. Eklund, "Charge-transfer effects in graphite intercalates: ab initio calculations and neutron-diffraction experiment" *Physical Review Letters* vol. 58 pp. 1528-31 1987.
- [7] L. Pietronero and S. Strässler, "Bond-length Change as a Tool to Determine Charge Transfer and Electron-Phonon Coupling in Graphite Intercalation Compounds" *Physical Review Letters*, vol. 47, pp. 593-596, 1981.

- [8] J. D. W. Madden, N. A. Vandesteeg, P. A. Anquetil, P. G. A. Madden, A. Takshi, R. Z. Pytel, S. R. Lafontaine, P. A. Wieringa, and I. W. Hunter, "Artificial muscle technology: Physical principles and naval prospects," *IEEE Journal of Oceanic Engineering*, vol. 29, pp. 706-728, 2004.
- [9] M. Hughes and G. M. Spinks, "Multiwalled carbon-nanotube actuators," *Advanced Materials* vol. 17, pp. 443-46, 2005.
- [10] M. Zhang, K. R. Atkinson, and R. H. Baughman, "Multifunctional carbon nanotube yarns by downsizing an ancient technology," *Science*, vol. 306, pp. 1358-1361, 2004.
- [11] J. D. Madden, R. A. Cush, T. S. Kanigan, and I. W. Hunter, "Fast contracting polypyrrole actuators," *Synthetic Metals*, vol. 113, pp. 185-193, 2000.
- [12] Y. Oren and A. Soffer, "The electrical double layer of carbon and graphite electrolodes. Part II. Fast and slow charging processes," *Journal of Electroanalytical Chemistry*, vol. 186, pp. 63-77, 1985.
- [13] M. H. Haque, K. Hying, I. Kolaric, T. Wallmersperger, and B. Kroplin, "Theoretical and experimental investigations of fundamental effects in carbon nanotube sheet actuators," presented at EAPAD: Smart Structures and Materials 2006: Electroactive Polymer Q.3 Actuators and Devices; , San Diego CA, 2006.
- [14] L. Meites, "Handbook of Analytical Chemistry, Sect. 5.." New York, NY: McGraw Hill, 1963.
- [15] G. M. Spinks, L. Liu, G. G. Wallace, and D. Zhou, "Strain response from polypyrrole actuators under load," *Advanced Functional Materials*, vol. 12, 2002.

Chapter 3

3 Carbon Nanotube Yarns as High Load Actuators and Sensors¹

3.1. *Introduction*

Individual carbon nanotubes (CNTs) have been shown to have high modulus (0.7 TPa), and high strength (30 GPa), while also displaying high electrical (10–30 kS/cm) and thermal (2000 W/mK) conductivities [1]. The low density of CNTs makes the specific properties even more useful, hence the interest of technologists in developing applications. A difficulty delaying commercial applications has been the absence of methods for controlling the arrangement of trillions of CNTs as they are being assembled into yarns and sheets. A main method of assembling CNTs has been to disperse them into a liquid and then use a coagulation-based process to spin the dispersions into fibres. Alternatively, the CNTs in these dispersions can also be filtered out of solution to make nanotube sheets called Bucky paper [1].

¹ A version of this chapter has been published as Mirfakhrai, T.; Oh, J.; Kozlov, M.; Fok, E. C. W.; Zhang, M.; Fang, S., Baughman, R. H. and Madden, J. D., “Carbon Nanotube Yarns as High Load Actuators and Sensors”, *Advances in Science and Technology* 61, pp. 65-74, 2008

A recently demonstrated alternative to solution-based methods is to create twist-spun yarns of multi-walled nanotubes (MWNTs) by drawing from aligned forests of nanotubes [2]. The MWNTs in these yarns are held together by the combination of twist-based lateral forces and van der Waals interactions between bundled nanotubes, whose effect is enhanced by long MWNT lengths and incorporation of individual MWNTs in more than one bundle. These yarns offer attractive mechanical properties, including tensile strengths that can exceed a GPa and a toughness close to that of the Kevlar used for antiballistic vests [3]. It has been shown that a dimensional change takes place in the yarns when a voltage is applied to them in an electrolyte [4]. Due to the high tensile strength and Young's modulus of the yarns, the yarns can operate at high forces and produce useful work densities.

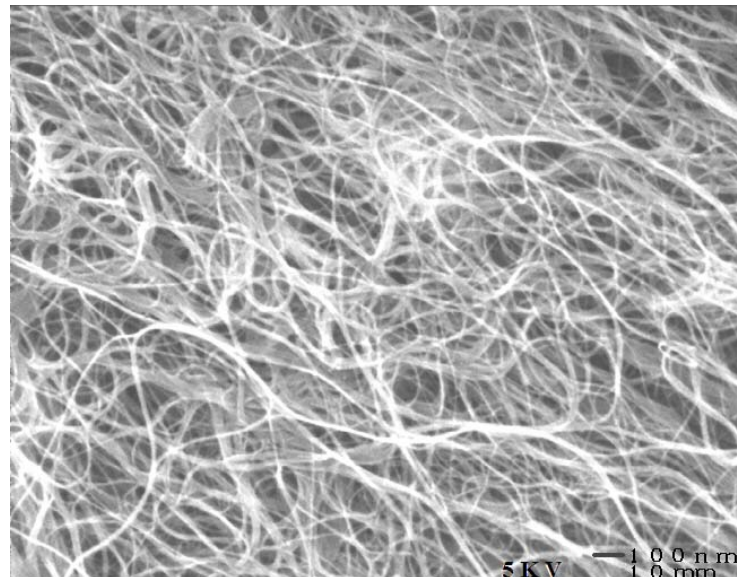
Piezoelectrics, electric motors, conducting polymers [5] and many other actuators can be operated as sensors or generators as well as actuators. We report that if a force is applied to a charged yarn in an electrolyte, it also can generate a change in its potential or short-circuit current. Therefore, the yarn can be used as a force sensor. Because their density is quite low (0.8 g/cm^3) they are potentially suited to be used in aerospace applications where the weight of the equipment is a major concern.

In following sections, we first briefly discuss the history of CNT actuators, followed by a description of the experimental methods and then a discussion of the application of MWNT yarns as actuators and sensors.

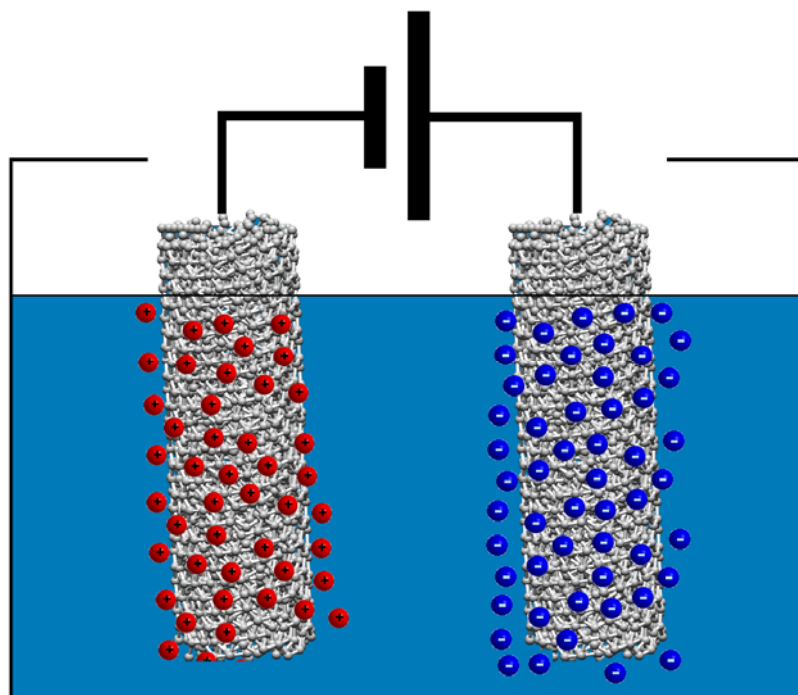
3.2. Background

As early as 1969, it was realized that the carbon-carbon bond length in graphite expands when potassium is intercalated between graphene sheets in graphite [6]. In this process,

potassium atoms transfer about one electron each to the graphite structure. The graphite sheets will become negatively charged and the positive potassium ions will rest between the graphite sheets. The overall structure is therefore neutral and is sometimes referred to as a 'graphite salt'. Quantum mechanical effects cause an expansion when electrons are added to a graphite sheet and a contraction when electrons are removed, due to the electron-hole symmetry breaking effect of second neighbour antibonding interactions[7]. Quantum mechanical effects are more complicated for carbon nanotubes, and highly dependent on the nanotube type, adding electrons causes a contraction of some bonds and an expansion of others depending upon the location of bonding and antibonding nearest neighbour orbitals[8]. On the other hand, coulombic repulsion of like charges causes expansion of all bonds, and this coulombic effect dominates over quantum mechanical effects for carbon nanotubes when charge injection is large [8]. Due to the combination of quantum mechanical and coulombic effects, dimensional changes are generally asymmetric with respect to charge sign when the amount of injected charge is small, but the dependence of dimensional change on injected charge approaches quadratic for carbon nanotubes when charge injection is large [9].



(a)



(b)

Figure 3.1: (a) Scanning electron micrograph of a CNT sheet and (b) Charge injection in a CNT-based electromechanical actuator, where an applied potential injects charges in the two nanotube electrodes in solution [4].

The actuation of a single nanotube may be of interest in nano-manipulation. However, if macroscopic actuation is desired, large-scale structures of CNTs must be built to transfer the desirable characteristics of an individual CNT actuator to the macroscopic world. In 1999, Baughman et al. [10] described the actuation of a bending bilayer composed of two pieces of carbon nanotube paper. A scanning electron micrograph of a sheet of CNT paper can be seen in Figure 3.1a, which consists of numerous entangled CNTs. Two sheets of CNT paper are submerged in an electrolyte. An applied potential from a voltage source injects charges of opposite signs in the two nanotube electrodes. These charges in each electrode are completely balanced by ions from the electrolyte (denoted by the charged spheres on each nanotube cylinder in Figure 3.1). The electrodes in Figure 3.1 resembling a single nanotube but can also represent what is happening to an arbitrary number of nanotubes in each electrode. Depending on the electrochemical potential of each electrode and the relative number of nanotubes in each electrode, the opposite electrodes can provide in-phase or out-of-phase mechanical deformations. In other words, depending on how the two electrodes are charged in the beginning, they can either elongate simultaneously, resulting in a linear actuator, or one can elongate while the other contracts, resulting in a bending bilayer actuator. Charge injection at the surface of a nanotube bundle is balanced by the surface layer of electrolyte cations. Initially 0.1% actuation was observed from CNT paper (Figure 3.2); thus demonstrating the first charge induced deformation using carbon nanotubes.

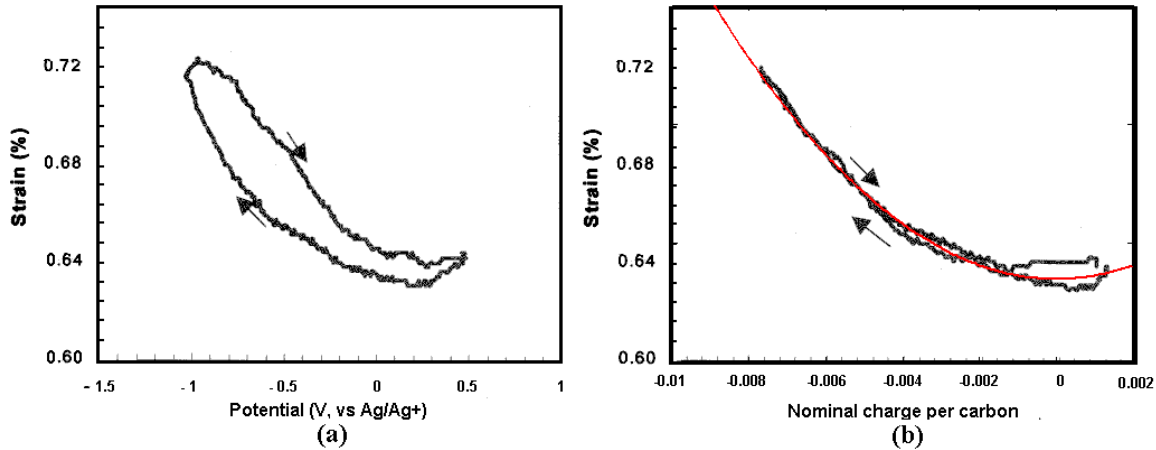
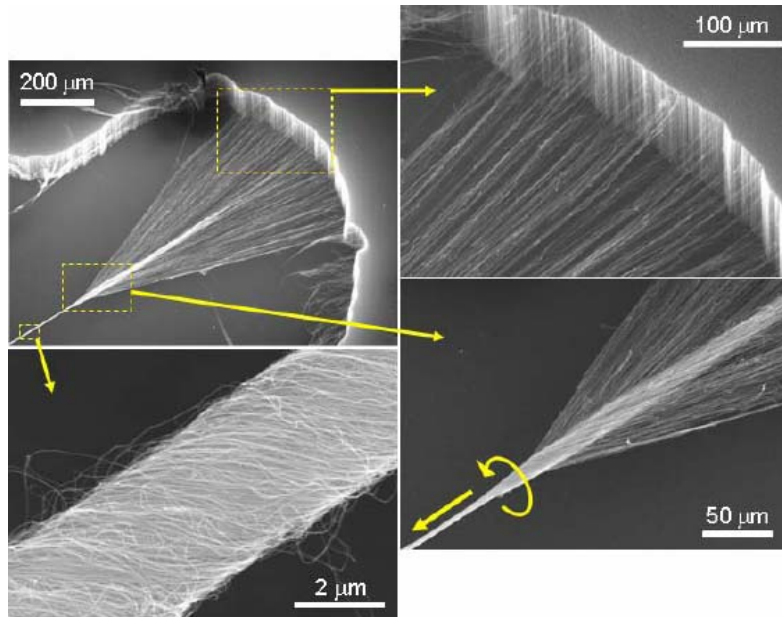


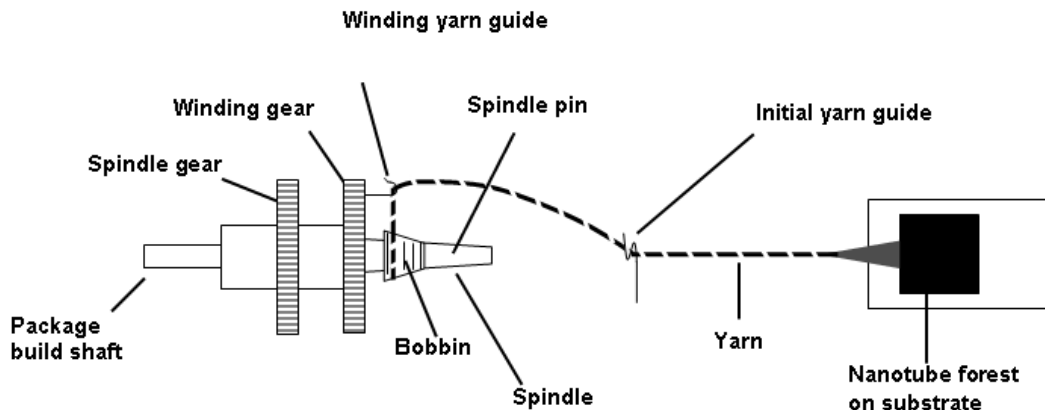
Figure 3.2: CNT paper actuator strain vs. (a) Working Electrode (WE) voltage and (b) nominal charge per carbon atom; the red line shows the parabolic strain-charge relationship [10]. (Copyright 2001 SPIE--The International Society for Optical Engineering).

In principle it should be possible to achieve higher strains and stresses than were observed in the initial results. The theoretically predicted actuation strain for a single nanotube is up to about 1%, while that of the nanotube paper has been less than 0.1% so far. CNT paper has considerably lower tensile strength compared to the individual nanotubes (~37GPa). Therefore researchers tried creating highly aligned macroscopic structures of CNTs that can maintain the marvellous mechanical and actuation properties of individual CNTs to a larger extent. It became obvious that the success of actuator technology based on carbon nanotubes will depend on improvements in the mechanical properties of nanotube sheets and fibres with a high surface area by increasing nanotube alignment and the binding between nanotubes. Ropes or strings made of nanotubes became a new center of attraction for researchers and several groups developed their own method of creating such ropes.

A spinning method was developed at the NanoTech Institute of the University of Texas in Dallas, which allows the dry-spinning of twisted yarns of CNTs directly from a forest of CNTs [2]. The mechanical and electrical properties of these macroscopic yarn structures are closer to those of the underlying CNTs than any macroscopic structure made up to that time. The spinning process can be summarized as follows. An MWNT forest is grown on an iron catalyst-coated Si substrate by CVD of ethane at 680°C. The yarn is started by pulling MWNTs from a side of the forest of nanotubes using a cylindrical sharp spindle. Each nanotube picks up those around it due to van der Waals forces (Figure 3.3a). The diameter of the resulting twisted yarn is proportional to the forest sidewall area used for this initial draw. A continuous spinning apparatus introduces twist as it winds the twist-spun yarn onto a bobbin and builds a yarn package (Figure 3.3b). The spinning apparatus comprises a spindle and a winding gear with an associated winding yarn guide, and a driving mechanism for yarn. The spindle and the winding gear are driven by two independent variable-speed motors (not shown in the figure). A removable bobbin is driven by a translation mechanism, which travels back and forth during spinning for yarn. The advantage of the system is the precise control of twist level. Electronic interfaces enable real-time adjustment during spinning. This apparatus can also be used to continuously make multi-ply yarns. In such a case, the nanotube forest is replaced by reels of unplied singles yarn. All the control parameters can be conveniently adjusted in real time.



(a)



(b)

Figure 3.3: (a) the Scanning electron micrograph of the spinning process and (b) the schematic of the spinning apparatus to make MWNT yarns [11].

An MWNT yarn is shown in Figure 3.4a, and has been used in the experiments presented.

This one has a diameter of $10 \mu\text{m}$ with a twist angle of about 23° . It is possible to twist two of these yarns together to make a two-ply yarn (Figure 3.4b). The experiments

described in this paper only show the results for a single-ply yarn such as the one in Figure 3.4. The testing methods are now described.

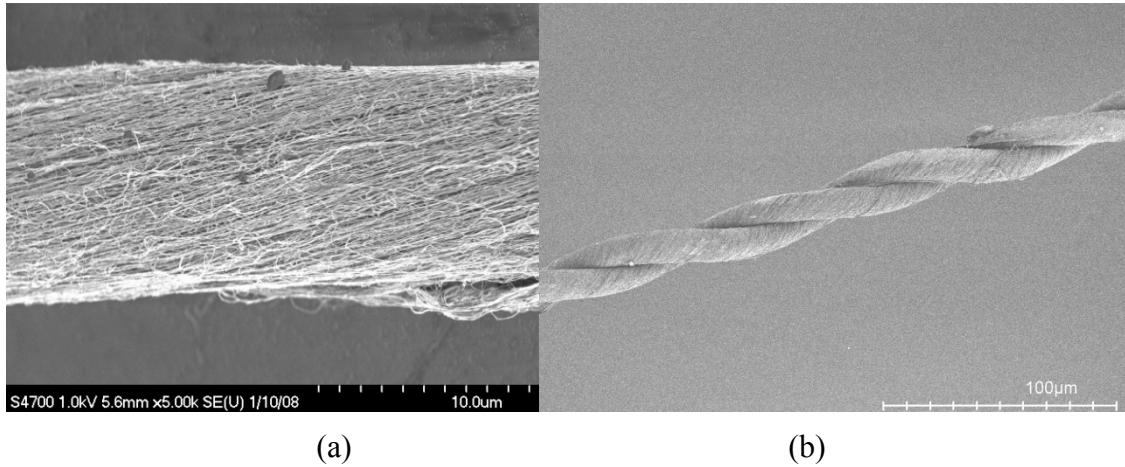


Figure 3.4: Scanning electron micrographs of (a) a single-ply yarn and (b) a two-ply yarn spun using the dry twist-spinning technique. Experimental results presented are from a yarn similar to (a)

3.3. Methods

MWNT yarns were prepared by a dry spinning method [2], in which they are drawn from a forest and twisted into yarns. The MWNT forest was synthesized by catalytic CVD using acetylene gas as the carbon source. MWNTs, which are about 10 nm in diameter, are simultaneously drawn from the MWNT forest and twisted. The diameter of the samples used was about 10 μm . The length of the sample used for the high load actuation experiments (Figure 3.6d) was 21 mm. The sample used for the results in Figure 3.6a-c was 9 mm long. The twist is characterized by the helix angle (α), which depends directly upon the degree of twist and inversely on the yarn diameter. The degree of twist is typically 13500 turns/m, which produces a twist angle of 23 degrees for a typical diameter yarn.

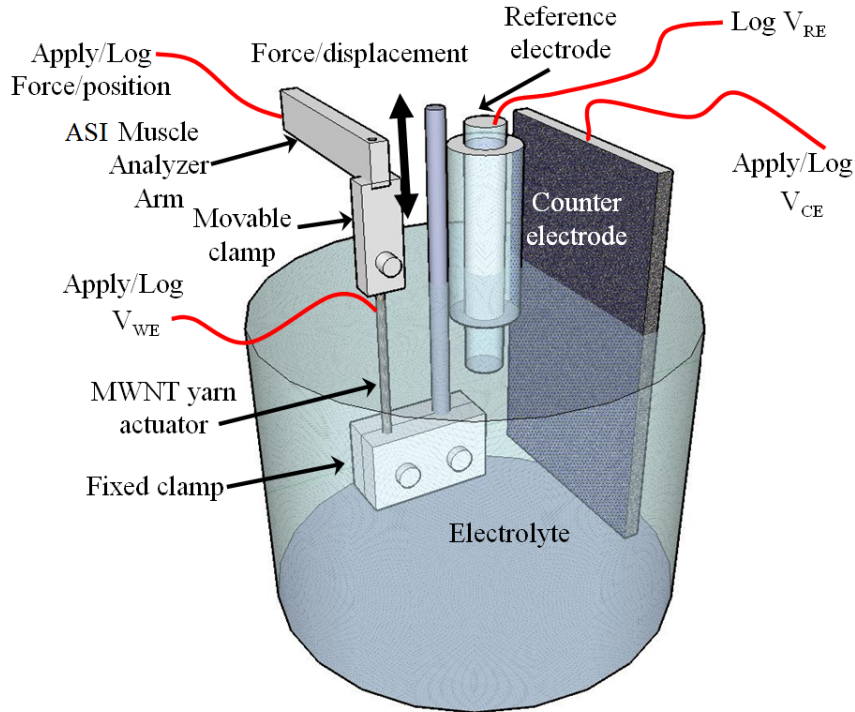


Figure 3.5: An MWNT yarn mounted in the ASI muscle analyzer clamp, and the electrochemical cell setup used for actuation and sensing tests.

In order to apply forces and record actuation forces and displacements generated by the MWNT yarns, an Aurora Scientific ASI 300 muscle analyzer and its LabView-based software (www.aurorascientific.com) have been employed. Figure 3.5 shows a diagram of the apparatus used to apply force and of the yarn and clamping mechanism. The fibre is mounted between a lower fixed clamp and an upper movable motor arm. A computer-controlled potentiostat is used to apply potentials. A data acquisition card (National Instruments 6036E) gathers the force and displacement data from the muscle analyzer and also logs the applied voltage and current. The ASI 300 instrument can be programmed to keep the load on the yarn constant and to measure the displacement generated by the yarn, or it can keep the length of the yarn constant and measure the tension change in the yarn due to actuation. Finally, it can also be used to apply a desired

force profile as a function of time and measure the resulting changes in the length of the sample.

To study actuation, the potentiostat is used to apply a voltage between the yarn, which is the working electrode (WE) and a piece of porous carbon fibre paper acting as the counter electrode (CE). The capacitance of the CE is much larger than that of the yarn. The potential of the WE is measured relative to an Ag^+ reference electrode (RE). The potential between WE and CE is controlled by the potentiostat such that the potential between WE and RE follows the desired values and profiles

3.4. Actuators

It is observed that when a potential is applied and varied under constant load, the length of the yarn starts to change. Figure 3.6a shows the strain (adjusted for creep) generated in the yarn when the potential between the WE and RE is changed as shown in Figure 3.6b. A series of voltage pulses with various amplitudes were applied to the yarn and the resulting actuation strains under a load of 100 MPa are plotted in Figure 3.6c. Strains up to 0.6 % have been obtained at higher applied potentials achievable in ionic liquids, at loads as high as 200 MPa (Figure 3.6d). This is a world record for actuation load of artificial muscles, established by using the yarn (which has exceptionally high tensile strength) with the right electrolyte (Cyphos 101 ionic liquid). Creep is one factor limiting the maximum load achievable with artificial muscles. The previous electrolytes tried typically facilitate the creep by reducing the interaction between CNTs in the yarn, while the viscous, honey-like ionic liquid electrolyte seems to slow down the creep to about 3.6×10^{-8} %/s per MPa of load. This is two orders of magnitude smaller than the

1.6×10^{-4} %/s reported in chapter 2, which at a load of 35 MPa applied in that experiment, is equivalent to 4.6×10^{-6} %/s per MPa.

Since the Young's modulus of the yarn is about 20 GPa, these relatively small strains translate to stresses of more than 14 MPa. The tensile strength of the yarn is about 1 GPa, and we have previously shown that actuation strain does not diminish when the load is increased [4]. Therefore in principle loads potentially as large as 1 GPa can be displaced by as much as 0.6 % by the yarn actuators, resulting in high coupling [12].

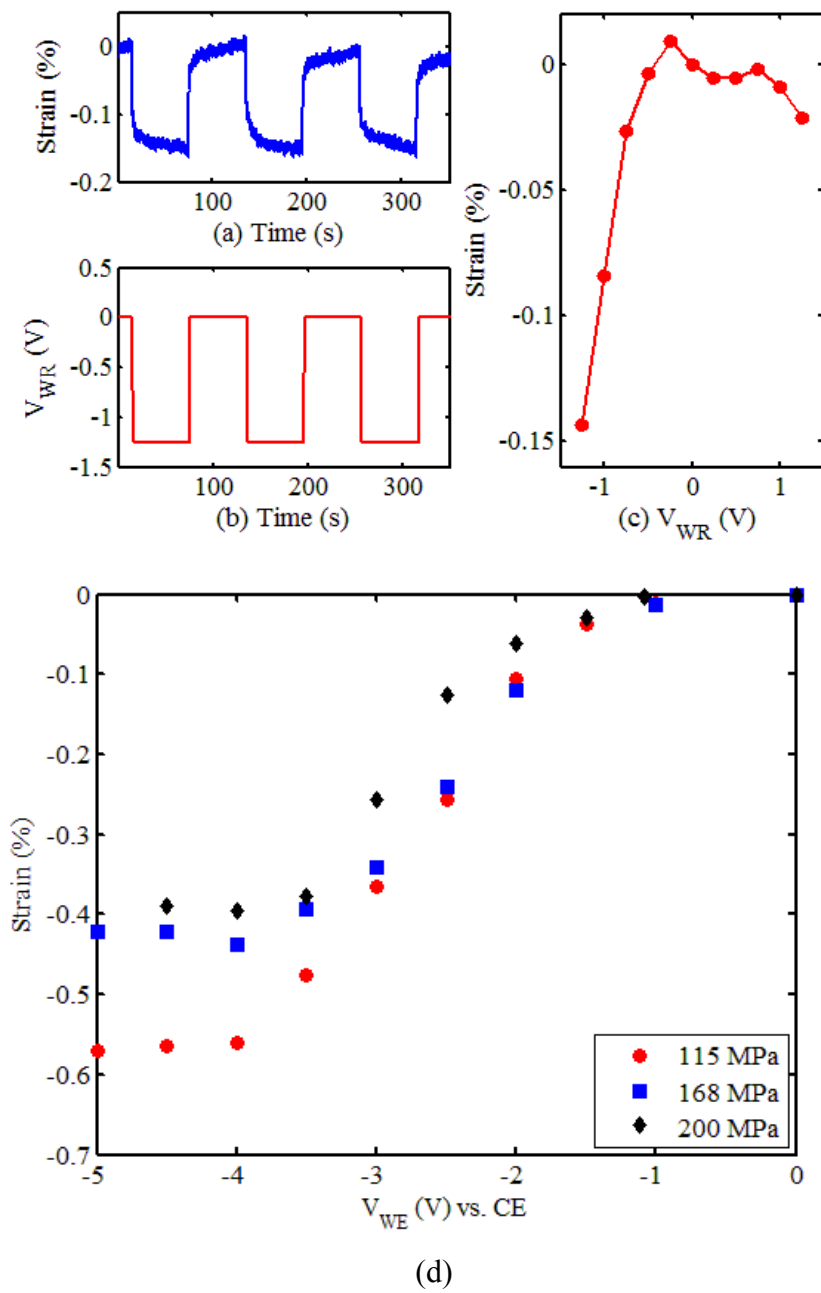


Figure 3.6: (a) Actuation strain response to an applied square wave potential of -1.25 V amplitude plotted in (b) between the working electrode (yarn) and an Ag/Ag⁺ reference electrode. (c) Actuation strain as a function of the applied square-wave potential amplitude. The electrolyte was 0.1 M tetrabutylammonium hexafluorophosphate (TBAP) in acetonitrile. (d) Actuation strain of the CNT yarn actuator in Cyphos 101 ionic liquid as a function of applied potential (vs. CE) at three loads of 115, 168, and 200 MPa.

This actuation is in the form of contraction upon the application of the voltage. The charging of the nanotubes may lead to deformation of individual tubes via a combination of quantum mechanical and Coulombic effects [10, 13]. However, the fact that the strain is in the form of axial contraction suggests that Coulombic repulsion between the adjacent MWNTs or MWNT bundles are primarily responsible for the actuation. When the yarn is charged, ions of opposite charge are attracted to the yarn and find their way inside, resulting in a build-up of like charges in the small space between the MWNTs. The repulsion between these like charges as well as the attraction between the ions and the oppositely-charged carriers on the MWNT backbones may push the MWNTs apart resulting in a radial expansion of the yarn (Figure 3.7a). As known from yarn mechanics [14], radial expansion in a twisted yarn results in axial contraction (Figure 3.7b).

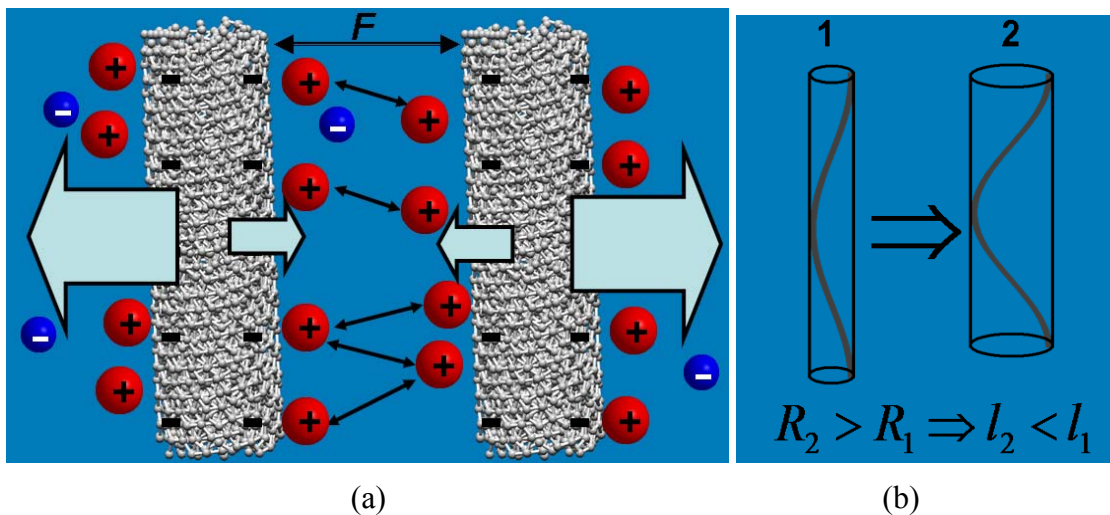


Figure 3.7: (a) Repulsion between the like charges and attraction between the opposite charges push the MWNTs apart in the yarn, leading to radial expansion. (b) Radial expansion in a twisted yarn results in axial contraction

3.5. Force Sensors

Many actuators can also act as generators and sensors if a force is applied to them. For example, an electric motor can also act as a generator. It has also been shown that conducting polymers act as sensors [5, 15]. Here we report the results of investigating generation of electric current/voltage in a yarn. When a force is applied to the yarn biased to a given voltage in an electrolyte, a spike is observed in the current (Figure 3.8). Figure 3.9 shows the amplitude of these current spikes plotted as a function of the applied bias potential between the WE and RE. The sensor peak current output is plotted at three different levels of the amplitude of the stress pulse at 15, 30, and 45 MPa, at a prestress of 30 MPa. The example in Figure 3.8 is at +0.50 V, while the stress is changed by 45 MPa. As can be seen in Figure 3.9, the peak sensor current can reach 75 nA.

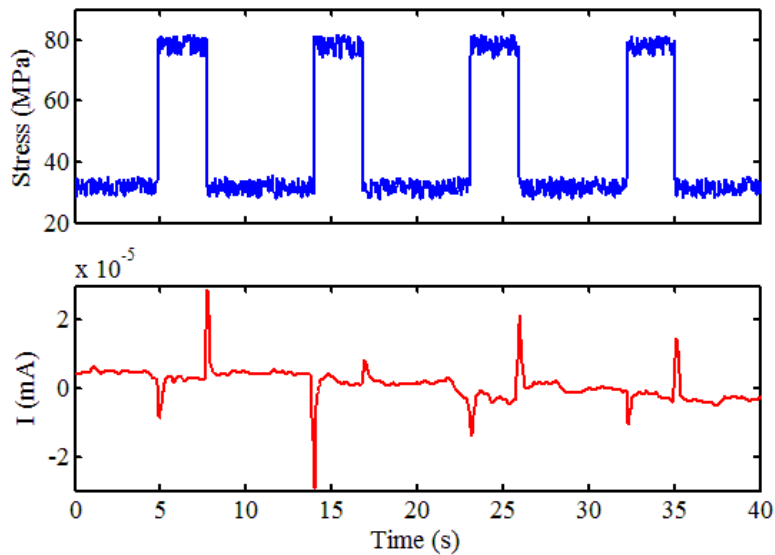


Figure 3.8: (a) Stress profile applied to the yarn under constant potential generates a train of current spikes seen in (b). Current spike height is uneven due to undersampling.

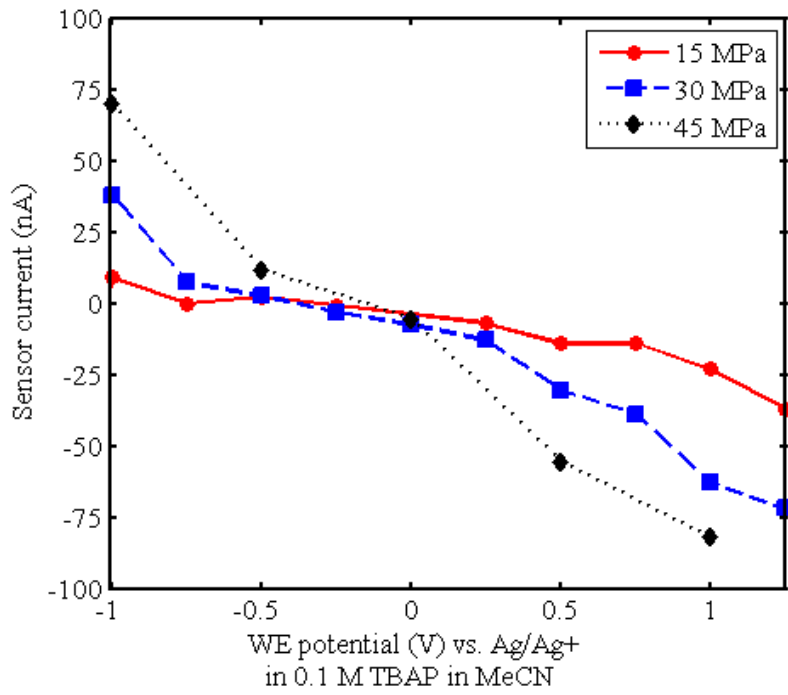


Figure 3.9: Sensing current as a function of the applied bias potential at three different loads.

It is tempting to suggest that by pulling on the yarn, the individual MWNTs are being stretched, and thus varying the capacitance as their size changes. However, considering

that the Poisson's ratio of MWNTs is about 0.2 to 0.3 [16], applying strains in the range used in our experiments will result in an expansion of the surface area of the MWNTs. An increase in surface of a conductor would likely increase its capacitance. If the yarn is biased to a fixed positive potential, stretching will lead to more charging and the incorporation of extra *negative* ions from the electrolyte, resulting in a *positive* current spike by convention. Since this prediction is contradicted by the experiments, we must assume that a different mechanism is at work. Moreover, the changes in surface area of individual nanotubes are expected to be negligible, since the modulus of individual nanotubes is so high.

One possibility is that ions are squeezed out of the nanotubes, producing a change due to charge expulsion, similar to the mechanism that has been proposed to explain similar sensor behaviour in conducting polymers [5]. When a positive bias potential is applied to the yarn, negative ions are absorbed at the surface of the yarn due to Coulomb forces and penetrate the yarn. When a force is applied to the yarn, the axial tension compacts the yarn radially [14]. This radial compaction reduces the inner surface area available for interaction with the ions, thus expelling the negative ions that have been inside. The eviction of the negative ions results in an inward current into the yarn. A current flowing into the yarn working electrode is negative (by convention). The current is reversed when a negative bias potential is applied to the yarn, resulting in a flux of negative ions into the yarn, and a positive current flowing outward from the yarn. This model is in accord with the proposed actuation model and can explain the sensing behaviour of the yarns well. The characteristic properties of the yarn as a mechanical force sensor are further discussed in Chapter 6.

The fact that carbon nanotube yarns can act as both sensors and actuators is an exciting observation. More investigation is needed to understand their behaviour and a theory to quantitatively account for the sensory effects will be discussed in Chapter 6. We have already demonstrated that the yarns can work as actuators at loads of up to 200 MPa and we see no reason that they cannot operate as sensors up to at least the same load levels [12]. If they can operate at close to their tensile strength of about 1 GPa, it will result in a mechanical stress sensor operating at unprecedented load levels. Since MWNTs are stable at temperatures of up to 450 °C in air and to above 2000 °C in the absence of oxygen, applications such as high-temperature force sensors can be contemplated. In such circumstances the electrolyte has to be stable at high temperatures. Molten salts are one class of electrolyte that may be appropriate.

3.6. Challenges

Before CNT yarns can be adopted by engineers as actuators and sensors, it is necessary to develop a predictive model to relate the actuation strain to the applied voltage and the sensor voltage/current to the applied strain. Due to the nonlinear behaviour of these actuators/sensors a simple strain-to-charge ratio model (in which strain is linearly proportional to charge density) will not provide a good description. It will be important to develop physical models or at least black-box type models that predict the system behaviour under typical conditions required for engineering applications (Figure 3.10).

The actuation and sensing models are expected to be the inverses of each other.

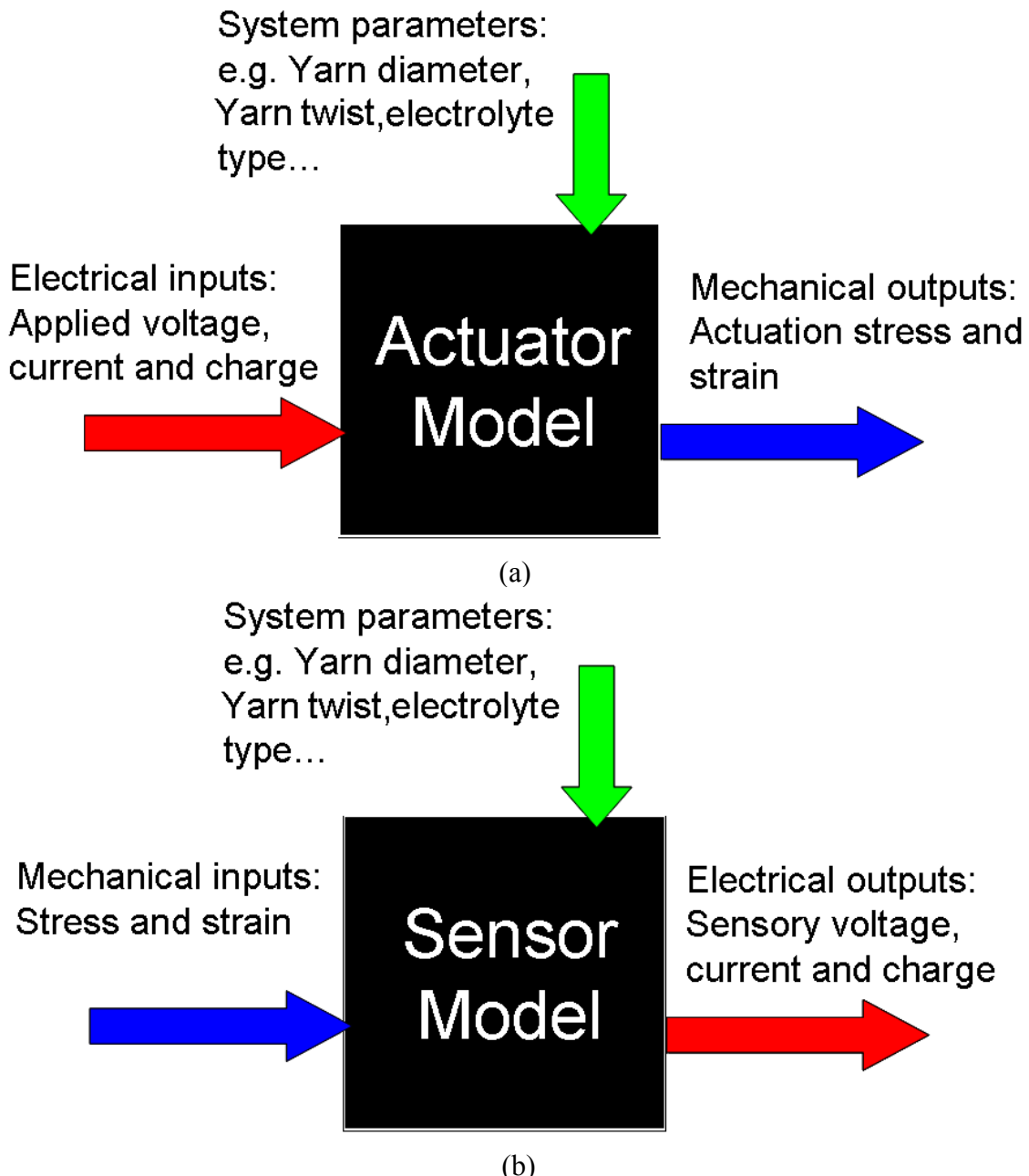


Figure 3.10: Desired block diagrams of models for MWNT yarns as (a) actuators and (b) sensors.

A practical challenge in the application of the yarns arises because of the existence of a potential-related “creep” phenomenon. When a relatively large potential is applied to the

yarn, it not only results in a large actuation, but also seems to speed up the creep. If the double-layer repulsion theory is correct, it is conceivable that the same forces that result in the actuation of the yarn by repelling the individual MWNTs from one another, work against the forces that hold the MWNTs together in the yarn. With these forces reduced, the MWNTs become more likely to slip, resulting in accelerated creep. The creep is highly dependent on electrolyte composition, so it may be possible to operate at high loads while minimizing its effect.

3.7. Summary

Twist-spun yarns of multi-walled carbon nanotubes were shown to work as electromechanical actuators and force sensors. Strains of up to $0.60\pm0.02\%$ at loads of up to $2.0\pm0.4 \times 10^8$ Pa have been achieved in actuation mode, while sharp and easily detectable current spikes of up to 75 ± 1 nA are generated in force sensory mode. Their very low density of 0.8 g/cm³ makes them very promising for many applications, especially in situations like aerospace applications where cargo weight is an issue.

References

- [1] R. H. Baughman, A. A. Zakhidov, and W. A. de Heer, "Carbon nanotubes - the route toward applications," *Science*, vol. 297, pp. 787-792, 2002.
- [2] M. Zhang, K. R. Atkinson, and R. H. Baughman, "Multifunctional carbon nanotube yarns by downsizing an ancient technology," *Science*, vol. 306, pp. 1358-1361, 2004.
- [3] K. R. Atkinson, S. C. Hawkins, C. Huynh, C. Skourtis, J. Dai, M. Zhang, S. Fang, A. A. Zakhidov, S. B. Lee, A. E. Aliev, C. D. Williams, and R. H. Baughman, "Multifunctional carbon nanotube yarns and transparent sheets: Fabrication, properties, and applications," *Physica B: Condensed Matter*, vol. 394, pp. 339-343, 2007.
- [4] T. Mirfakhrai, J. Oh, M. Kozlov, E. C. W. Fok, M. Zhang, S. Fang, R. H. Baughman, and J. D. W. Madden, "Electrochemical actuation of carbon nanotube yarns," *Smart Materials and Structures*, vol. 16, pp. S243, 2007.
- [5] Y. Wu, G. Alici, J. D. W. Madden, G. M. Spinks, and G. G. Wallace, "Soft mechanical sensors through reverse actuation in polypyrrole," *Advanced functional materials*, vol. 17, pp. 3216-22, 2007.
- [6] D. E. Nixon and G. S. Parry, "The expansion of the carbon-carbon bond length in potassium graphites," *Journal of Physics C: Solid State Physics*, pp. 1732, 1969.
- [7] M. Verissimo-Alves, B. Koiller, H. Chacham, and R. B. Capaz, "Electromechanical effects in carbon nanotubes: Ab initio and analytical tight-binding calculations," *Physical Review B*, vol. 67, pp. 161401, 2003.

- [8] G. Sun, J. Kurti, M. Kertesz, and R. H. Baughman, "Dimensional Changes as a Function of Charge Injection in Single-Walled Carbon Nanotubes," *Journal of the American Chemical Society*, vol. 124, pp. 15076-15080, 2002.
- [9] R. H. Baughman, "Conducting polymer artificial muscles," *Synthetic Metals*, vol. 78, pp. 339-353, 1996.
- [10] R. H. Baughman, C. X. Cui, A. A. Zakhidov, Z. Iqbal, J. N. Barisci, G. M. Spinks, G. G. Wallace, A. Mazzoldi, D. De Rossi, A. G. Rinzler, O. Jaschinski, S. Roth, and M. Kertesz, "Carbon nanotube actuators," *Science*, vol. 284, pp. 1340-1344, 1999.
- [11] M. Zhang, S. Fang, R. H. Baughman, A. A. Zakhidov, K. R. Atkinson, A. E. Aliev, S. Li, and C. Williams, "Fabrication and Application of Nanofiber Ribbons and Sheets and Twisted and Non-Twisted Nanofiber Yarns," in *PCT Int. Application P. I. Application*, Ed., 2007, pp. 425
- [12] T. Mirfakhrai, J. Oh, M. Kozlov, S. Fang, M. Zhang, R. H. Baughman, and J. D. W. Madden, "Actuation of Carbon Nanotube Yarns in Ionic Liquids," *In preparation*, In preparation.
- [13] T. Mirfakhrai, R. Krishna-Prasad, A. Nojeh, and J. D. W. Madden, "Electromechanical actuation of single-walled carbon nanotubes: an ab initio study," *Nanotechnology*, vol. 19, pp. 315706 2008.
- [14] J. W. S. Hearle, P. Grossberg, and S. Backer, *Structural Mechanics of Fibers, Yarns and Fabrics*, vol. 1. New York: Wiley-Interscience, 1969.

- [15] W. Takashima, T. Uesugi, M. Fukui, M. Kaneko, and K. Kaneto, "Mechanochemoelectrical effect of polyaniline film," *Synthetic Metals*, vol. 85, pp. 1395-1396, 1997.
- [16] Z.-c. Tu and Z.-c. Ou-Yang, "Single-walled and multiwalled carbon nanotubes viewed as elastic tubes with the effective Young's moduli dependent on layer number," *Physical Review B*, vol. 65, pp. 233407, 2002.

Chapter 4

4 Capacitive charging and background processes in carbon nanotube yarn actuators¹

4.1. Introduction

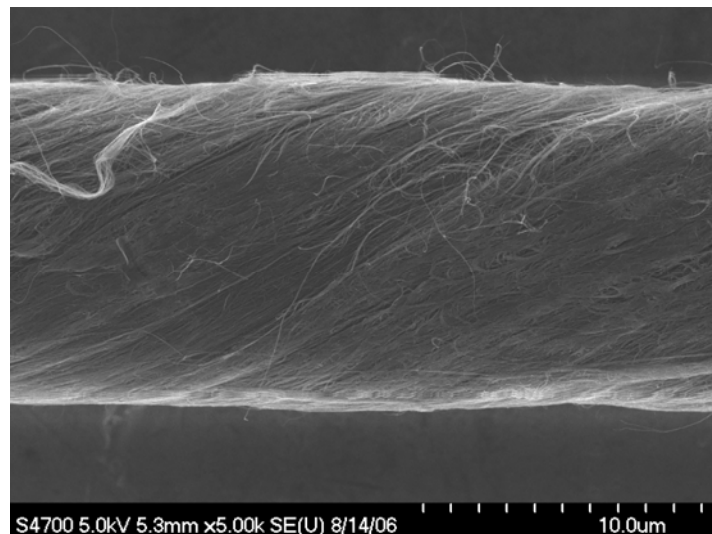


Figure 4.1: Scanning electron micrograph of twist-spun MWNT yarns

Following on from seminal work demonstrating the electrochemically driven actuation of single walled carbon nanotubes, yarns made through spinning multi-wall carbon

¹ A version of this chapter has been published as Mirfakhrai, T.; Kozlov, M.; Zhang, M.; Fang, S.; Baughman, R. H. and Madden, J. D. W., "Capacitive charging and background processes in carbon nanotube yarn actuators", Proceedings of SPIE Smart Structures / NDE, 2007 [6524-54]

nanotubes (MWNTs) [1] have been shown to act as artificial muscles [2]. The CNT yarns used in our experiments are made at the 'NanoTech Institute of the University of Texas in Dallas, [1]. An MWNT forest is grown on an iron catalyst-coated Si substrate by chemical vapor deposition of acetylene at 680°C. The yarn is started by pulling MWNTs from a side of the nanotube forest. Each nanotube picks up those around it due to van der Waals forces. The spindle and the winding gear are driven by two independent variable-speed motors allowing for the precise control of twist level. The resulting CNT yarn is shown in Figure 4.1, similar to those used in the experiments presented in the present article. The yarn imaged here has a diameter of 11.67 μm with a twist angle of about 30°.

We have previously reported the electrochemical actuation of these yarns, which are of particular interest because their tensile strengths and Young's moduli are high and rapidly improving [2], enabling increases in actuator work density and efficiency [1]. They have also been operated as fuel-powered artificial muscles [3, 4]. During electrochemical or fuel-powered actuation the yarn is the working electrode (WE) in an electrochemical cell and the presence of an electrolyte is necessary to allow for ion transport required for actuation. The ions that are inserted or removed act to charge or discharge nanotubes within the yarn, and this charging is believed to result in actuation via electrostatic and quantum chemical mechanisms [1]. The electrochemical behaviour of the yarns is key to understanding mechanisms and determining performance. In the sections that follow the current and actuation in response to input triangular waves in potential are studied and a method to separate charging and kinetics limited currents demonstrated. The length of the yarn sample used in the experiments, the results of which are shown in this chapter was

18.2 mm, with a diameter of approximately 10 μm as measured with scanning electron microscope. The uncertainty values are the same as those discussed in Chapter 2.

4.2. Modeling of the capacitive and parasitic currents

One way of studying the electrochemical behaviour of a material is Cyclic Voltammetry (CV). In a CV experiment the current passing through an electrochemical cell, containing the material of interest as the working electrode, is measured while the working electrode potential is swept cyclically over a range. CVs are powerful because substantial information is collected in a short time. However it is often difficult to extract quantitative data from them because of the simultaneous operation of many processes (e.g. mass transport, electron transfer kinetics, double layer charging, solution resistance). We begin with the premise that CNT systems are relatively simple in their electrochemical characteristics, being mostly described by double layer charging reactions and kinetics-limited parasitics (e.g. degradation of the electrolyte). It is expected that the actuation of the yarn is the result of double-layer charging for example [5]. Therefore a capacitor, representing the double-layer capacitance, can be considered as a first order approximation for the equivalent circuit for the yarn. Series and parallel resistances and ultimately non-linear elements are added to flesh out this model.

4.3. Double layer Capacitor and leakage resistance

If the potential applied to an ideal capacitor is swept in a cyclic linear fashion, the current versus potential plot is a perfect rectangle spanning the potential range over which the experiment is conducted. However, in general the charge stored in the double-layer may be drained through kinetics or diffusion-limited Faradaic reactions, potentially modeled using Butler-Volmer or diffusion-limited behaviours. In this work, it is assumed that the

experiments are conducted in clean environments such that currents due to Nernstian reactions are negligible. For now, let us assume that the potential drop across the yarn electrode is sufficiently small such that the leakage due to the reactions can be modeled by a resistor R_P , itself a function of the working electrode (WE) potential, V . If a resistor is included in parallel with the capacitor to represent leakage, the original rectangular CV will be tilted into a parallelogram with a tilt angle that is a function of the resistance of the leakage resistor. Figure 4.2a shows the calculated CV for a pure capacitor and a parallel R-C circuit.

The experimental CV of the CNT yarn actuator in its middle potential range (Figure 4.2c) resembles the parallelogram in Figure 4.2a, suggesting that it too may be viewed as a superposition of capacitive and leakage currents. We therefore propose to break down the total measured cell current i_T as:

$$i_T = i_C + i_P .$$

The current i_C is the capacitive part of the current and can be expressed as $i_C = C \frac{dV}{dt}$, where V is the working electrode potential versus the reference. The current i_P is the leakage current flowing through the resistor and for now we assume it to be only a function of the working electrode potential, i.e. $i_P = f(V)$, which is expected in a kinetics-limited parasitic reaction but not for mass transport limited cases. Assuming this model the cell current i_T can be expressed as:

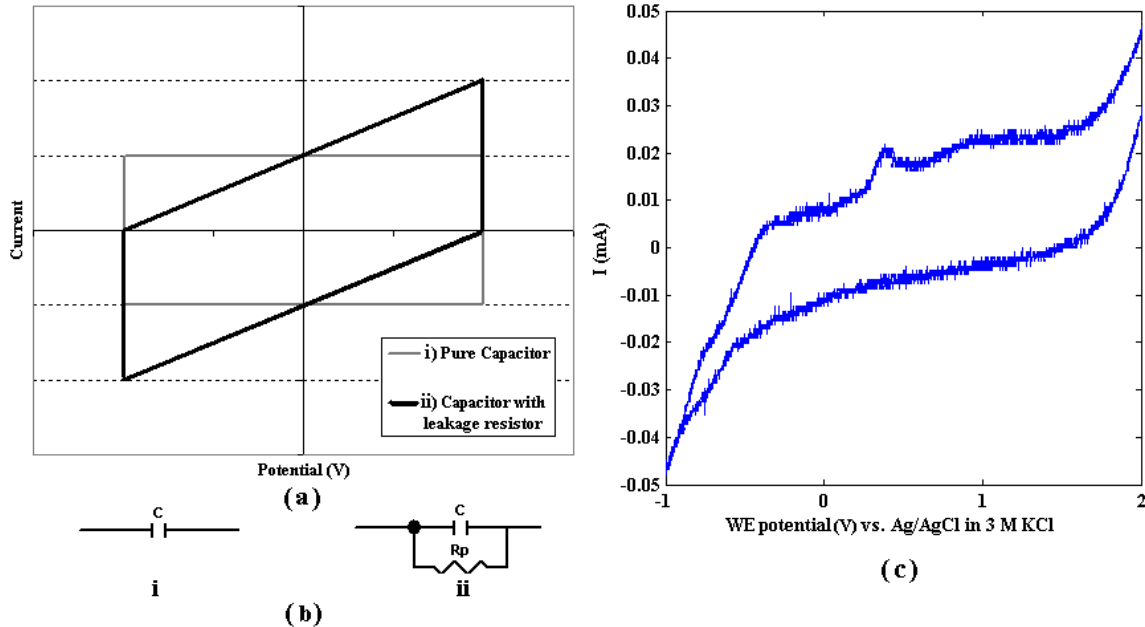


Figure 4.2: (a) The cyclic voltammogram for the circuits drawn in (b) i. pure capacitor and ii. parallel combination of a capacitor and a resistor and (c) cyclic voltammogram for the CNT yarn actuator in an electrolyte made of 0.2 M tetrabutylammonium hexafluorophosphate in acetonitrile, viewed over a potential for comparison

$$i_T = C \frac{dV}{dt} + f(V)$$

When the WE potential sweep is in the positive direction, $\frac{dV}{dt} = +\alpha$, where α is the

CV scan rate. So $i_T^+ = +\alpha C + f(V)$. During the potential sweep in the negative

direction, $\frac{dV}{dt} = -\alpha$ and so $i_T^- = -\alpha C + f(V)$. Therefore: $i_T^+ + i_T^- = 2f(V)$ and

$i_T^+ - i_T^- = 2\alpha C$. The capacitance and the leakage current can be estimated as a function of the current by:

$$C = \frac{i_T^+ - i_T^-}{2\alpha}, \quad f(V) = \frac{i_T^+ + i_T^-}{2}$$

The current is thus divided between a capacitive part proportional to the scan-rate and a rate-independent current, $f(V)$. The accuracy of the model depends on this condition being satisfied and we shall test for it later.

4.4. Parallel and series RC model

In most cases, unless the electrodes are close to each other, the resistance of the solution and the contacts cannot be neglected. Therefore we need to introduce a resistance in series with the above parallel RC to model these resistances. When a series resistance is included to account for the solution and contact resistances, matters become more complicated. The differential equations governing the system are now:

$$\begin{cases} i(t) = C \frac{dv_c(t)}{dt} + \frac{v_c(t)}{R_p} \\ v(t) = v_c(t) + R_s i(t) \end{cases}$$

Solving for $i(t)$:

$$i(t) = \frac{v(t) - v_c(0)e^{\frac{-t}{RC}}}{R_s} - \frac{e^{\frac{-t}{RC}}}{R_s^2 C} \int_{\tau=0}^t v(\tau) e^{\frac{\tau}{RC}} d\tau$$

During the rising cycle of a CV, $v(t) = V_L + \alpha t$, where V_L is the lower bound of the potential at which we start the cycle and α is the scan rate. Substituting in the above equation we obtain

$$i_+(t) = \frac{V_L + \alpha t - v_c(0)e^{\frac{-t}{RC}}}{R_s} - \frac{e^{\frac{-t}{RC}}}{R_s^2 C} \int_{\tau=0}^t (V_L + \alpha \tau) e^{\frac{\tau}{RC}} d\tau$$

where $R = R_s \parallel R_p = \frac{R_s R_p}{R_s + R_p}$. After calculating the integral:

$$i_+(t) = \frac{V_L + \alpha t}{R_s} - \frac{R}{R_s^2} (V_L + \alpha t) + \frac{\alpha C R^2}{R_s^2} + \frac{e^{\frac{-t}{RC}}}{R_s} \left(-v_c(0) + \frac{R V_L}{R_s^2} - \frac{\alpha C R^2}{R_s^2} \right)$$

If $t_+ \gg RC$, i.e. the time passed is considerably longer than the system's time constant (or the scan rate is very slow and we are away from the turning points of the CV), the

terms including $e^{\frac{-t}{RC}}$ become negligibly small and the above result can be simplified to

$$i_+(t) = \frac{V_L + \alpha t}{R_s + R_p} + \frac{\alpha R^2 C}{R_s^2}$$

Similarly, during the down-sweep of a CV, (i.e. $t > T$), $v(t) = V_H - \alpha(t - T)$, where V_H is the upper bound of the potential during the CV and T is the point of time when the potential has reached V_H and is beginning to decrease.

$$i_-(t) = \frac{V_H - \alpha(t - T) - v_c(0)e^{\frac{T-t}{RC}}}{R_s} - \frac{e^{\frac{-t}{RC}}}{R_s^2 C} \int_{\tau=0}^t (V_0 - \alpha(\tau - T)) e^{\frac{\tau}{RC}} d\tau$$

where $R = R_s \parallel R_p = \frac{R_s R_p}{R_s + R_p}$. After integration:

$$i_-(t) = \frac{V_H - \alpha(t-T) - v_c(0)e^{-\frac{t-T}{RC}}}{R_s} - \frac{R}{R_s^2}(V_H - \alpha(t-T) + \alpha RC) - \\ - \frac{R}{R_s^2}e^{\frac{-t}{RC}}(V_L(e^{\frac{T}{RC}} - 1) - V_H e^{\frac{T}{RC}} + \alpha Te^{\frac{T}{RC}} + 2\alpha RC(1 - e^{\frac{T}{RC}}))$$

If $t_- > T \gg RC$, i.e. during the down-sweep and assuming that the time passed before switching the sweep direction is considerably longer than the system's time constant, the above result can be simplified to

$$i_-(t) = \frac{V_H - \alpha(t-T)}{R_s + R_p} - \frac{\alpha R^2 C}{R_s^2}$$

So far we have found that:

$$\begin{cases} i_+(t) = \frac{V_L + \alpha t}{R_s + R_p} + \frac{\alpha R^2 C}{R_s^2} & t \leq T \\ i_-(t) = \frac{V_H - \alpha(t-T)}{R_s + R_p} - \frac{\alpha R^2 C}{R_s^2} & t > T \end{cases} \Rightarrow \begin{cases} i_+(t_+) = \frac{V_+}{R_s + R_p} + \frac{\alpha R^2 C}{R_s^2} \\ i_-(t_-) = \frac{V_-}{R_s + R_p} - \frac{\alpha R^2 C}{R_s^2} \end{cases},$$

where $V_+ = V_L + \alpha t_+$ and $V_- = V_H - \alpha(t_- - T)$ and t_+, t_- are the times during one cycle at which the potential reaches V_+, V_- respectively. Looking at the currents i_+ and i_- at a given potential, $V_+ = V_- = V$ and we can say that

$$\frac{i_+ + i_-}{2} = \frac{V_+ + V_-}{2(R_s + R_p)} + \frac{\alpha R^2 S}{R_s^2} - \frac{\alpha R^2 S}{R_s^2} = \frac{V}{R_s + R_p},$$

which is only a function of the potential at that point V . Therefore we call it $f(V)$:

$$\Rightarrow f(V) = \frac{V}{R_s + R_p} \quad (4.1)$$

If $R_p >> R_s$, then $\Rightarrow f(V) \cong \frac{V}{R_p}$, i.e. the slope of $f(V)$ versus V is $\frac{1}{R_p}$ and R_p can be

determined by measuring that slope. The capacitive current is given by:

$$\begin{aligned} i_{cap} &= \frac{i_+|_V - i_-|_V}{2} = \frac{\left(\frac{V_+}{R_s + R_p} + \frac{\alpha R^2 C}{R_s^2}\right) - \left(\frac{V_-}{R_s + R_p} - \frac{\alpha R^2 C}{R_s^2}\right)}{2} \\ &= \frac{\frac{V}{R_s + R_p} - \frac{V}{R_s + R_p} + \frac{2\alpha R^2 C}{R_s^2}}{2} = \frac{\alpha R^2 C}{R_s^2} \\ \Rightarrow i_{cap} &= \frac{\alpha R^2 C}{R_s^2} = \frac{\alpha R_s^2 R_p^2 C}{R_s^2 (R_s + R_p)^2} = \frac{\alpha C}{\left(1 + \frac{R_s}{R_p}\right)^2}. \end{aligned}$$

If $R_p >> R_s$ then $\Rightarrow i_{cap} \cong \alpha C \Rightarrow C = \frac{i_{cap}}{\alpha}$. (4.2)

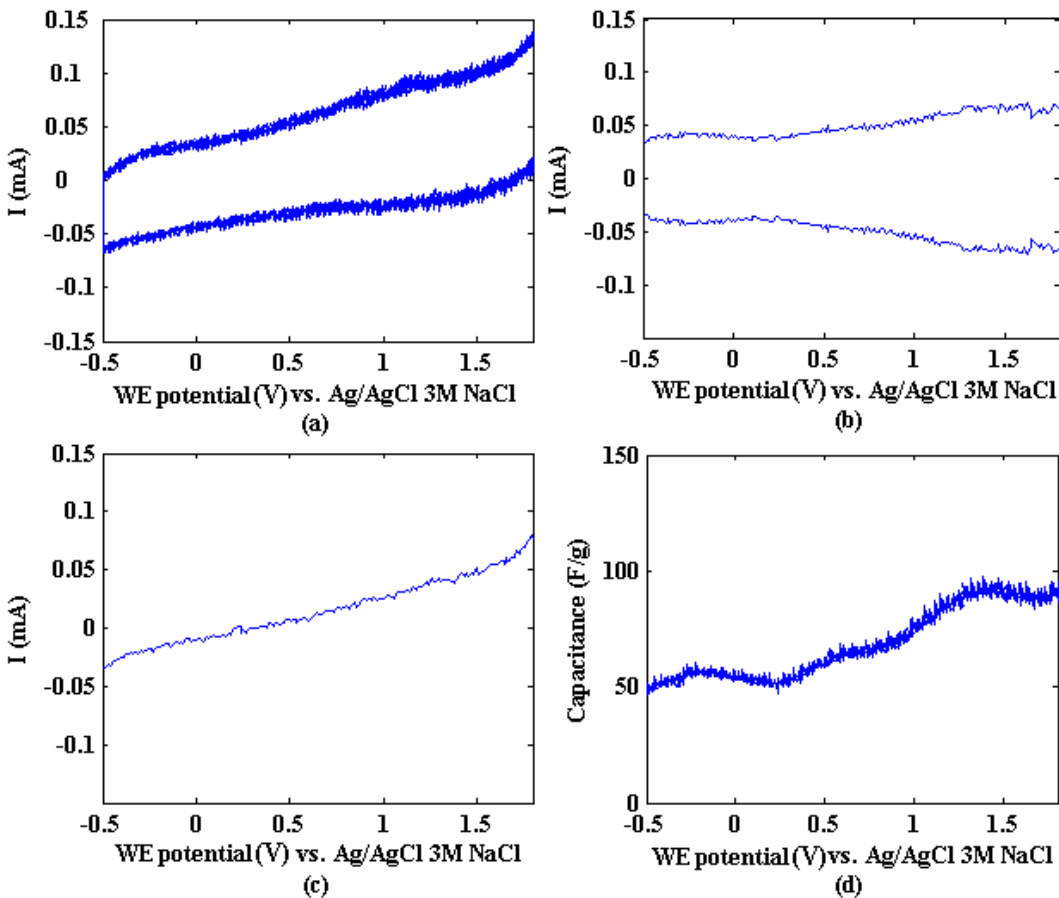


Figure 4.3: (a) The cyclic voltammogram for the CNT yarn actuator in an electrolyte made of 0.2 M tetrabutylammonium hexafluorophosphate in acetonitrile viewed over a potential range of -0.5 to 1.8 V(b) the capacitive part (c) the leakage background current and (d) the gravimetric capacitance as computed using the capacitive current in (b)

Figure 4.3a shows the experimental CV for the actuation of CNT yarn with a diameter of 18 μm and length of 18.2 mm during a CV in a 0.2 M solution of tetrabutylammonium hexafluorophosphate (TBAP) in acetonitrile under a constant 20 MPa of stress. The counter electrode was a piece of carbon fibre paper (Ballard AvCarb P-50T). The same counter electrode has been used for all experiments in this paper. The respective capacitive and leakage currents computed using the $R_s - R_p - C$ model (equations 4.1

and 4.2) are plotted Figure 4.3b and c as a function of the working electrode potential. The capacitance as a function of potential, calculated for this sample based on the above method is plotted in Figure 4.3d. $R_s + R_p$ is estimated from the slope of the line in Figure 4.3b to be about $48 \text{ k}\Omega$. R_s is measured to be approximately $1.5 \text{ k}\Omega$ by studying the step response of the system. Thus the condition that $R_p \gg R_s$ seems to have been satisfied. C_g at $V=0 \text{ V}$ is estimated to be $55 \pm 1.5 \text{ F/g}$.

4.5. Kinetics-limited parasitic reactions and diode model

Beyond certain potentials in both positive and negative directions the magnitudes and contributions of these component currents seem to change as a function of the applied WE potential. This can be seen from the irregular shape of the CV in Figure 4.4a, which is exactly the same as those in Figure 4.3 except viewed over a larger potential range.

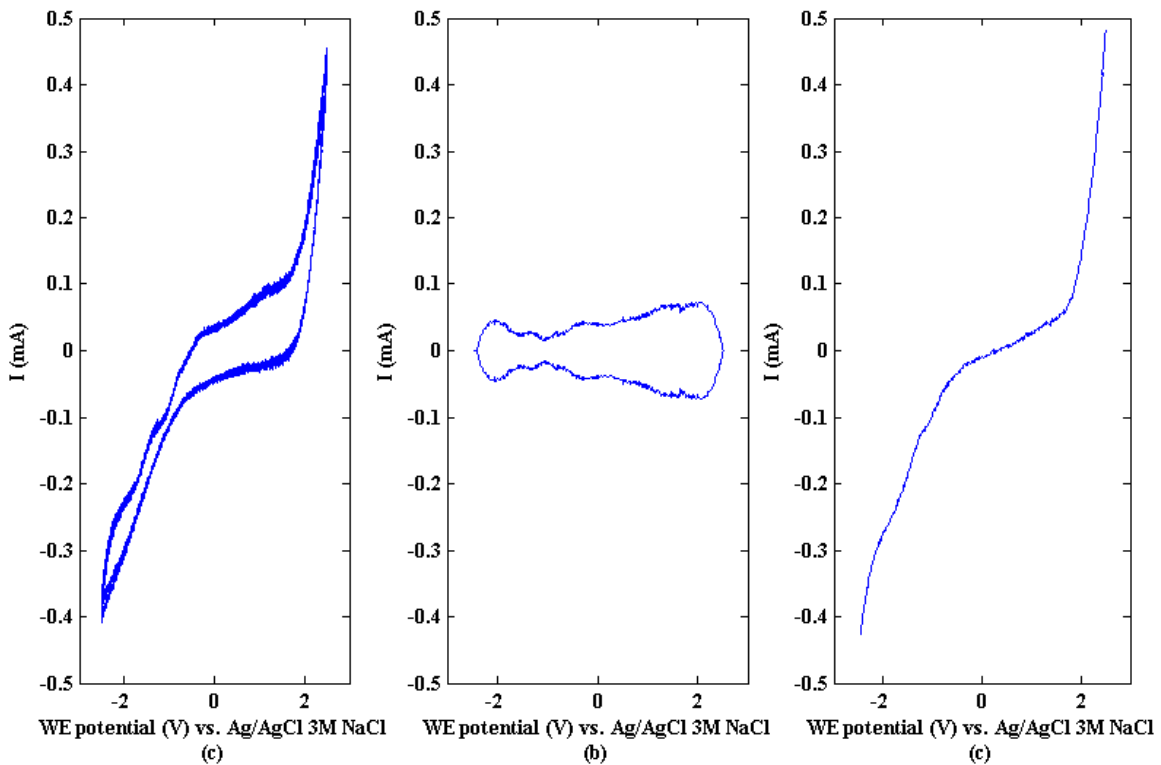


Figure 4.4: (a) The cyclic voltammogram for the CNT yarn actuator in an electrolyte made of 0.2 M tetrabutylammonium hexafluorophosphate in acetonitrile, viewed over a potential range of -2.5 to 2.5 V versus reference (b) the capacitive part and (c) the leakage background current

As can be seen from Figure 4.4c, there is a significant and abrupt rise in the parasitic current below -1 V and above +1.5 V. This suggests that the reaction modeled by RP might best be modeled using a non-linear relationship such as the Butler-Volmer equation [6]. With this assumption the governing differential equations for the circuit in Figure

4.5a will be $V(t) = v_c(t) + i_{bv}R_s + R_sC \frac{dv_c}{dt}$ resulting in

$$\frac{d\eta}{dt} + \frac{\eta}{R_sC} + \frac{i_0}{C} (e^{(1-\beta)\eta} - e^{-\beta\eta}) = \frac{V(t) - E_0}{R_sC} \quad (4.3).$$

Here R_s and C are defined as before, η is the overpotential across the electrode, β is the transfer coefficient, $f = F/RT$ (where F is Faraday's constant, R is the molar gas constant and T is the absolute temperature) and E_0 is the standard potential of the reaction considered. The three terms to the left of equation 4.3 behave as a capacitance, a resistance and two diodes ($i = i_0 e^{\frac{nV}{RT}}$ behaviour²) respectively in terms of equivalent circuit elements. The difference in the signs of the two exponential terms indicates that the two diodes must be mounted in opposite directions to model the reaction in the forward and the reverse directions. Therefore we propose to model the system with the circuit in Figure 4.5b. In general, there may be more than one reaction happening in either positive or negative potentials, therefore more than one diode branch may exist in parallel in each direction to model different reactions. Figure 4.6a shows the model with parameters calculated for the CV in Figure 4.4a. Circuit simulation results using *Electronics Workbench 5.12* and the experimental CV are in close agreement (Figure 4.6b). The CV fits nicely with one assuming a capacitance of 180 μF (equivalent of 55 F/g , the capacitance at 0 V) parallel with a Butler-Volmer branch with standard potential of 1.9 V versus reference and $i_0 = 1.5 \mu\text{A}$. R_s is again found to be around $1.5k\Omega$.

² This must not be mistaken for an ideal diode whose i-V characteristic would consist of two line segments instead of the exponential.

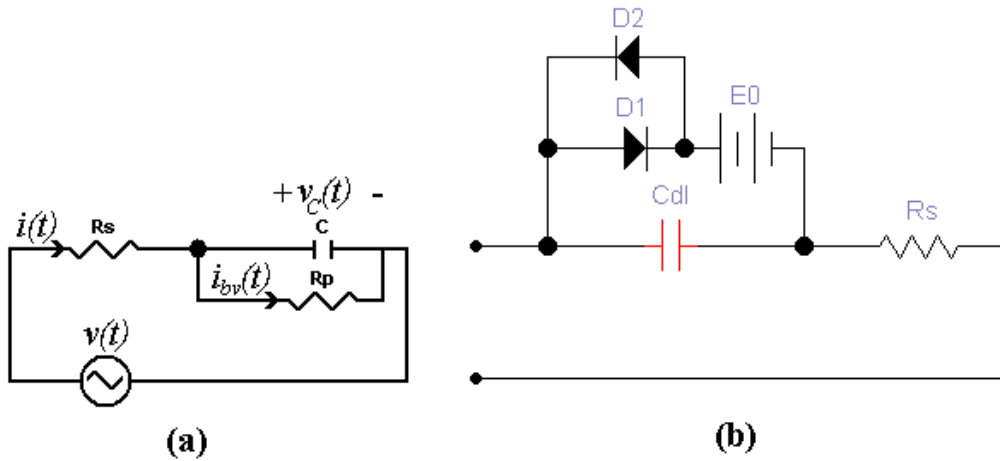


Figure 4.5: (a) Equivalent circuit with potential-dependent R_p to model for parasitic reactions and (b) equivalent circuit model for the CNT yarn electrode in the cell, accounting for capacitance, solution and series resistance, leakage and Butler-Volmer type reactions

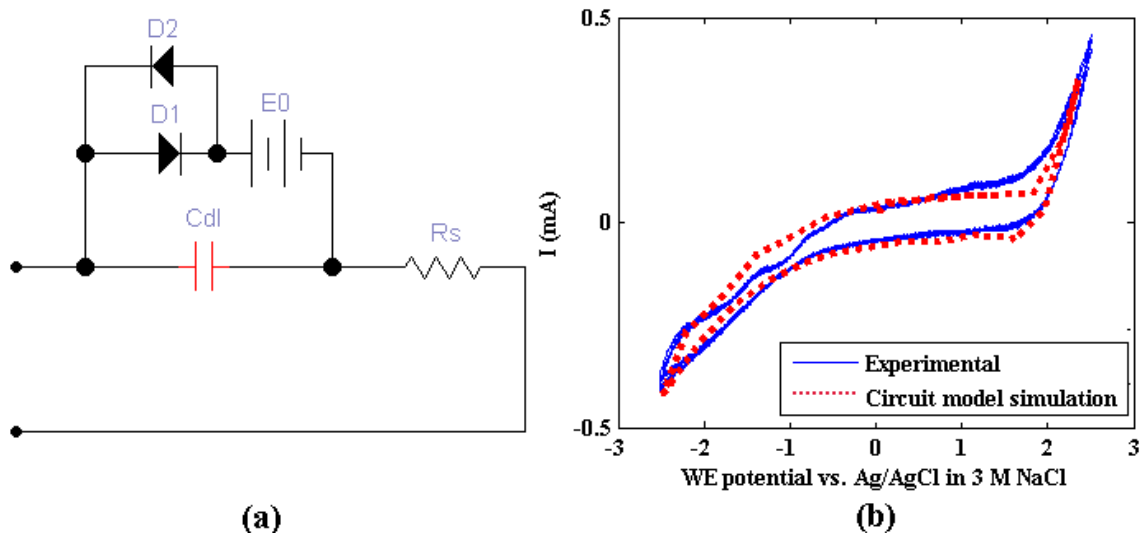


Figure 4.6: (a) The circuit model for the system studied in Figure 4.4 and (b) the comparison of the simulation results from the model and the experimental CV

4.6. Discussion

In order for the model to be accurate, it is important to prove that the parasitic current $f(V)$ does not depend on the scan rate. The model was applied to the experimental data for the same sample at scan rates of 100 and 250 mV/s. The computed parasitic currents are plotted in Figure 4.7. As can be seen, even though the scan rate is 2.5 times larger, the computed parasitic currents are virtually the same. This will be the case as long as currents from diffusion-limited Faradaic processes are negligible. Currents from diffusion-limited processes such as those due to contamination are neither independent of rate nor proportional to it (e.g. they could be proportional to the square root of the rate). Therefore the assumptions of our model will no longer be satisfied and the accuracy of the model decreases. In such cases part of the current due to Faradaic processes will erroneously appear in both computed capacitive and parasitic currents unless the corresponding peaks in the original CV are detected and removed before computing i_{cap} and $f(V)$. It is also evident from Figure 4.7 that the slopes of the two kinetics-limited tails of the plot are different in the positive and negative directions. This implies either the existence of multiple reactions in different directions or a kinetics-limited reaction that flows more easily in one direction than the other. Preliminary analysis of the data from the fitting predicts that the capacitance may depend on the scan rate of the CV. The change in capacitance in response to a 100-fold change in the scan rate in an aqueous electrolyte is estimated at about 30 %, closer to those measured for porous carbon electrodes by Oren and Soffer for in [7] than those measured for carbon single-walled nanotubes in [8].

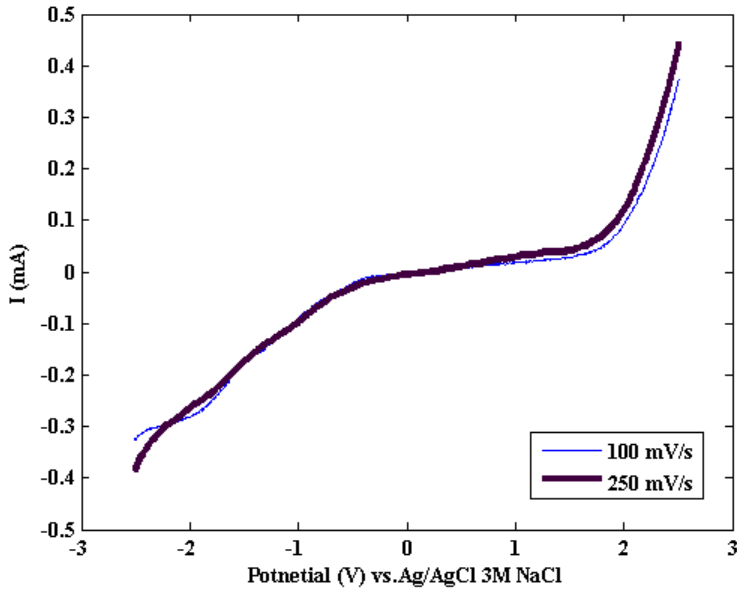


Figure 4.7: Comparison of the calculated $f(V)$ parasitic current for the same CNT yarn sample as above at 100 mV/s (thin) and 250 mV/s (bold)

As an example for the application of the model, let us consider the strain response of the CNT yarn actuator to a cyclic voltammogram. A general relationship is expected to exist between the actuation strain and the charge stored in the actuator. If the actuator charge is taken as the integral of the total cell current, the charge contributing to parasitic reactions will be included. Such parasitic reactions are especially problematic at very positive or very negative potentials, where the currents due to those reactions increase almost exponentially. The model promises to allow the separation of these components.

Figure 4.8 shows the strain in response to the potentials and currents shown in Figure 4.3. The strain (compensated for creep by subtracting a line) and the total charge are plotted in (a) and (b) versus time. The origin of the charge axis is arbitrary as we don't know the initial charge of the yarn. In Figure 4.8c the strain in (a) is plotted versus the total charge

in (b). The resulting plot is confusing and it is hard to extract any information about the relationship between strain and charge out of it. The model is now applied to the CV for this experiment (Figure 4.3a) by dividing the current into the rate-independent $f(V)$ (Figure 4.3c) and the capacitive current i_{cap} (Figure 4.3b). The stored charge is calculated by integrating the capacitive current.

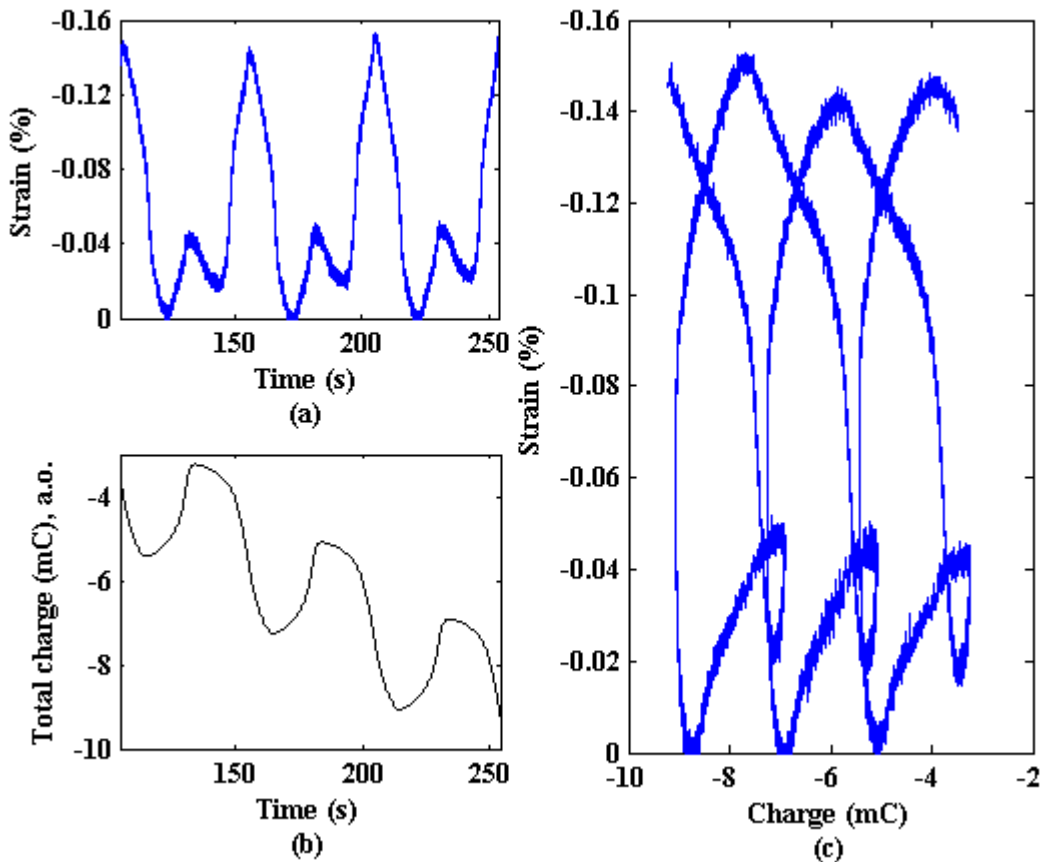


Figure 4.8: (a) Strain (compensated for creep) vs. time (b) total charge vs. time (vertical axis origin arbitrary) and (c) strain in (a) vs. charge in (b) , during a CV of the CNT yarn in a 0.2 M solution of TBAP in acetonitrile under a 20 MPa of load

Figure 4.9a shows the same strain as in Figure 4.8a. Figure 4.9b shows the stored charge versus time as found by integrating the capacitive part of the current in Figure 4.3b. The strain and the stored charge are plotted versus each other in Figure 4.9c. This plot is comparable with the results reported in [9] for carbon single-walled nanotubes. The dotted red line shows a quadratic fit. The hysteretic effect may be due to the charge consumed in diffusion-limited reactions that had been counted as part of the capacitive current and other anomalies in the CVs due to effects other than capacitance or Butler-Volmer type reactions or to the nonlinear nature of the creep which has been assumed to be linear. Some reactions due to contaminations seem to contribute to the current in the shape of some Nernstian peaks (e.g. the small peak in Figure 4.4a around -1 V). This means that if such peaks were accounted for before computing i_{cap} and $f(V)$, the stored charge profile in Figure 4.9b would probably exhibit an asymmetric behaviour corresponding to the asymmetric behaviour of the strain profile in Figure 4.9a. Under such circumstances the strain-charge plot of Figure 4.9c is expected to retrace itself without the hysteresis. The presence of impurities (redox mediators) in the electrolyte that act to shuttle charge between electrodes can dissipate charge under open-circuit conditions. Also, Faradaic processes occurring at only one electrode can result in differences in the amount of capacitively-stored charge in the two electrodes. Further study and modeling is needed in order to diagnose the nature of the anomalies in the CV to obtain the true relationship between the strain and the stored charge.

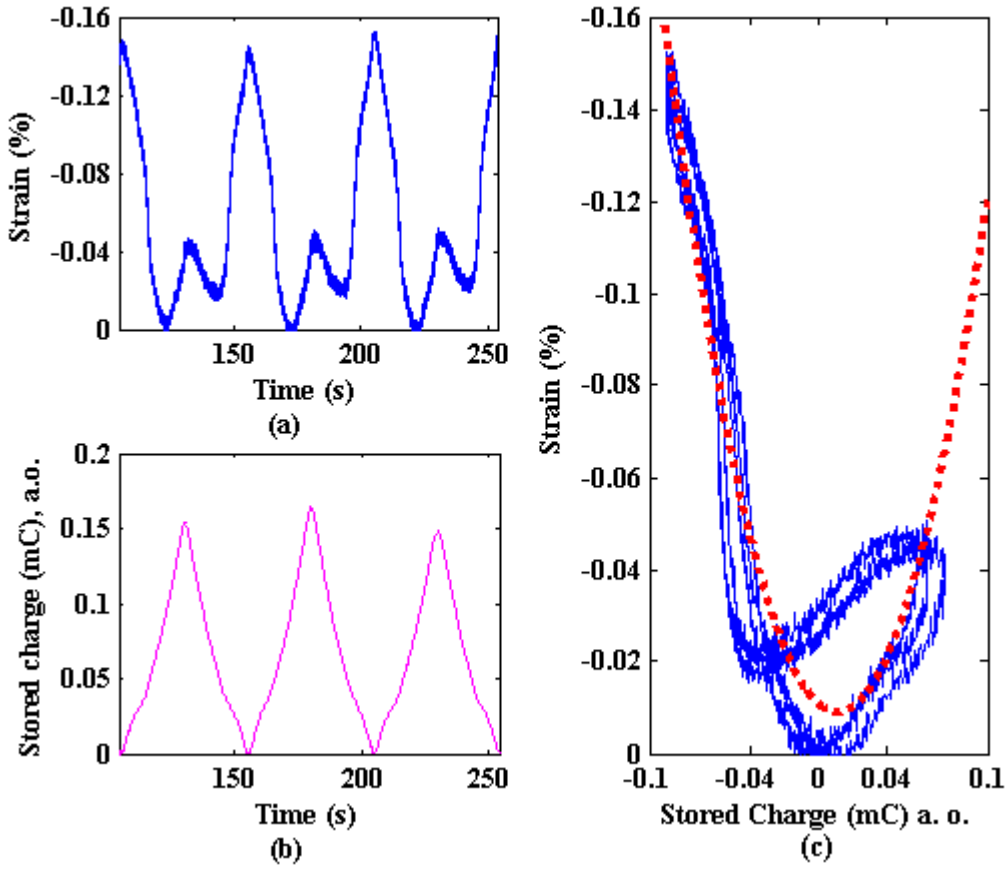


Figure 4.9: (a) Strain (compensated for creep) vs. time (b) stored charge vs. time (vertical axis origin arbitrary) and (c) strain in (a) vs. charge in (b) , during a CV of the CNT yarn in a 0.2 M solution of TBAP in acetonitrile under a 20 MPa of load. The parabola in (c) shows a quadratic fit. Note that the directions of the values on strain axes are in reverse.

4.7. Conclusions

A nonlinear circuit is presented to model the electrochemical charge storage behaviour of a carbon nanotube yarn actuator and its large-signal i - V characteristics. This model simplifies the computation of the capacitance and leakage resistances of the yarn and paves the way for a better understanding of the strain-charge relationship in ionic artificial muscles especially yarns and actuators made of carbon nanotubes. It is shown that the parasitic and background currents do not significantly depend on the scan rate and can be

assumed to be only a function of the potential applied, at least within the range of scan rates tested.

REFERENCES

- [1] M. Zhang, K. R. Atkinson, and R. H. Baughman, "Multifunctional carbon nanotube yarns by downsizing an ancient technology," *Science*, vol. 306, pp. 1358-1361, 2004.
- [2] T. Mirfakhrai, J. Oh, M. Kozlov, E. C. W. Fok, M. Zhang, S. Fang, R. H. Baughman, and J. D. W. Madden, "Electrochemical actuation of carbon nanotube yarns," *Smart Materials and Structures*, vol. 16, 2007.
- [3] M. Kozlov, J. Oh, T. Mirfakhrai, V. H. Ebron, Z. Yang, D. J. Seyer, H. Xie, J. Razal, L. J. Hall, M. Zhang, S. Fang, J. P. Ferraris, A. G. MacDiarmid, J. D. W. Madden, and R. H. Baughman, "From electrical to fuel-powered artificial muscles," presented at EAPAD: Smart Structures and Materials 2007: Electroactive Polymer Q.3 Actuators and Devices; , San Diego, CA, 2007.
- [4] V. H. Ebron, Z. W. Yang, D. J. Seyer, M. E. Kozlov, J. Y. Oh, H. Xie, J. Razal, L. J. Hall, J. P. Ferraris, A. G. MacDiarmid, and R. H. Baughman, "Fuel-powered artificial muscles," *Science*, vol. 311, pp. 1580-1583, 2006.
- [5] R. H. Baughman, C. X. Cui, A. A. Zakhidov, Z. Iqbal, J. N. Barisci, G. M. Spinks, G. G. Wallace, A. Mazzoldi, D. De Rossi, A. G. Rinzler, O. Jaschinski, S. Roth, and M. Kertesz, "Carbon nanotube actuators," *Science*, vol. 284, pp. 1340-1344, 1999.
- [6] A. J. Bard and L. R. Faulkner, *Electrochemical Methods, Fundamentals and Application*, 2nd ed. New York: Wiley, 2001.
- [7] Y. Oren and A. Soffer, "The electrical double layer of carbon and graphite electrolodes. Part II. Fast and slow charging processes," *Journal of Electroanalytical Chemistry*, vol. 186, pp. 63-77, 1985.

- [8] J. N. Barisci, G. G. Wallace, and R. H. Baughman, "Electrochemical studies of single-wall carbon nanotubes in aqueous solutions," *Electrochemistry Communications*, vol. 488, pp. 92-98, 2000.
- [9] G. M. Spinks, G. G. Wallace, R. H. Baughman, and L. Dai, "Carbon Nanotube Actuators: Synthesis, Properties, and Performance," in *Electroactive Polymers (EAP) Actuators as Artificial Muscles, Reality, Potential and Challenges* Y. Bar-Cohen, Ed. Bellingham WA: SPIE press, 2004 pp. 261-295.

Chapter 5

5 Carbon Nanotube Yarn Actuators: An Electrochemical Impedance Model¹

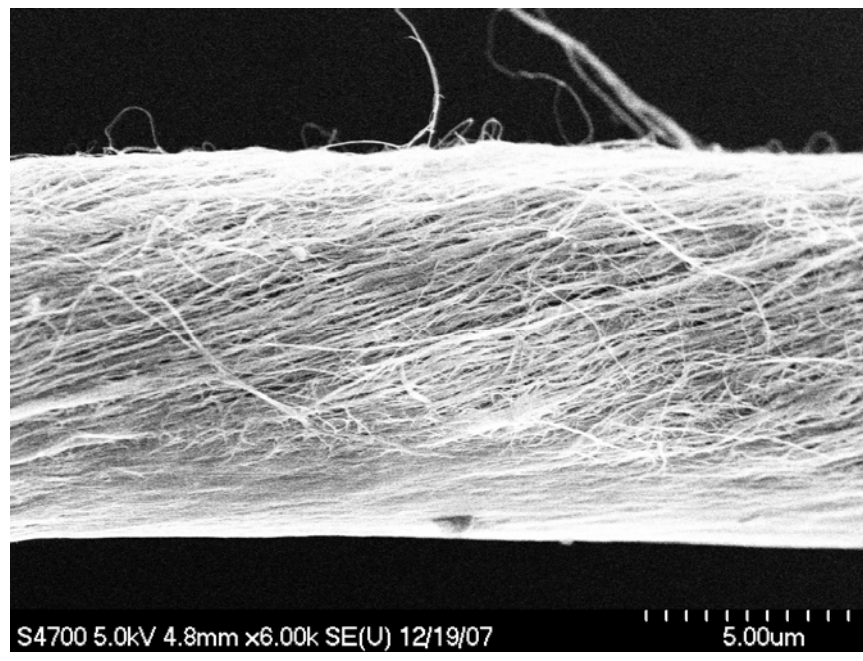
5.1. *Introduction*

Individual carbon nanotubes (CNTs) have been shown to have high modulus (0.7 TPa), and high strength (30 GPa), while also displaying high electrical (10–30 kS/cm) and thermal ($2000 \frac{W}{m \cdot ^\circ K}$) conductivities [1]. The low density of CNTs makes their gravimetric properties even more useful, hence the interest of technologists in developing applications. Commercial applications have been delayed by the absence of methods for controlling the arrangement of typically over a trillion CNTs as they are being assembled into fibres and textiles, and accomplishing this assembly at industrially useful rates.

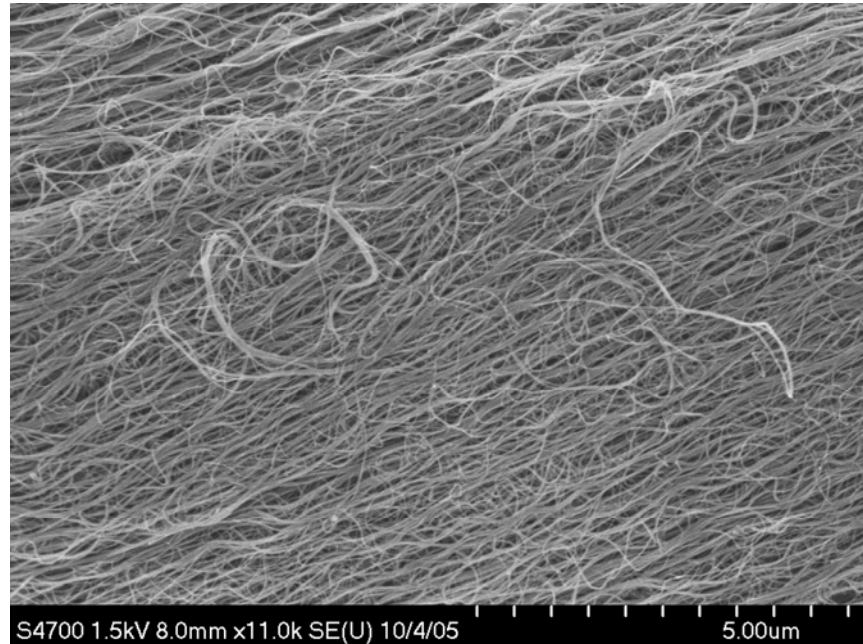
A recently demonstrated assembly method is to create twist-spun yarns of multi-walled nanotubes (MWNTs) by drawing yarns from aligned forests of nanotubes [2]. A scanning

¹ A version of this chapter has been published as Mirfakhrai, T.; Oh, J. Kozlov, M.; Zhang, M.; Fang, S.; Baughman, R. H. and Madden, J. D., “Carbon Nanotube Yarn Actuators: An Electrochemical Impedance Model”, Journal of the Electrochemical Society, 156 (6) K97-K103, 2009.

electron micrograph of such a yarn is shown in Figure 5.1a. The MWNTs in these yarns are likely held together by the combination of twist-based lateral forces and van der Waals interactions between bundled nanotubes, whose effect is enhanced by long MWNT lengths and incorporation of individual MWNTs in more than one bundle. We have previously shown that a dimensional change takes place in the yarns when a voltage is applied to them in an electrolyte [3]. Due to the high tensile strength (1 GPa) and Young's modulus (20 GPa) of the yarns [4], the yarns can operate under high loads to produce useful work output. Like many other actuators, they can also operate in reverse to convert mechanical energy to electrical energy, thereby acting as mechanical force sensors and electrical energy generators [5, 6].



(a)



(b)

Figure 5.1: Scanning electron micrographs of (a) a twist-spun carbon nanotube yarn and (b) a close-up of the yarn surface, showing individual MWNTs and MWNT bundles.

Both actuation and sensing effects are most evident when the yarn is used as an electrode in an electrochemical cell and is thus electrochemically charged. This means that in order to fully characterize the yarn as an actuator and sensor, its electrochemical behaviour needs to be studied. A number of works have used Electrochemical Impedance Spectroscopy (EIS) to characterize the electrochemical behaviour of CNTs. Yang and Wu [7] compared the EIS response of capped and uncapped CNTs created by arc discharge. They used a non-aqueous electrolyte and reported a difference between the response of open- and closed-ended CNTs. Yang *et al.* [8] attempted to fit a circuit model to the EIS data of a mixture of MWNTs, carbon black and polyvinylidene fluoride (PVDF) and to relate the changes in the values of the circuit model parameters to the variations of the diffusion constants with applied bias. Zhang *et al.* [9] compared the EIS response of entangled CNTs with that of aligned CNT arrays and found a lower series resistance and higher gravimetric capacitance for the aligned CNT arrays. Liu *et al.* [10] studied the effect of electrochemical oxidation on the EIS response of CNTs. They use the EIS data to show that the oxidative purification treatments on CNTs open their ends, shorten their lengths, make defects on the tube walls, and therefore enlarge their specific surface area. Therefore, the electrical double-layer capacitance of the CNTs is greatly increased. Barisci *et al.* [11] used EIS to study and model sheets of Bucky paper and also fit a circuit model. They showed that both the effective capacitance and electrode resistance were functions of the oxidation state of the Bucky paper. All these studies show the usefulness of using EIS in studying the electrochemical properties of nanotube-based structures and the application of circuit models to gain a better understanding of the electrochemical processes involved.

A close-up image of the yarn surface (Figure 5.1b) shows that there are large gaps between the constituent MWNTs in the yarn and that the yarn surface is very rough on a nanoscopic scale. This means that models for rough and porous electrodes geometries may be needed to account for the electrochemical behaviour of the yarn. In this paper, we employ EIS and cyclic voltammetry to characterize the yarn. In the sections that follow, we first present the theoretical background needed to analyze the EIS data and to model the electrochemical behaviour of the yarns and then present the experimental results and discussion.

5.2. Theory

EIS can be used to study many electrochemical phenomena. Circuit models having similar response to that of the electrochemical cell under study are often employed to relate the EIS behaviour to physical phenomena. In many electrochemical applications, the values of the circuit parameters in such models are of prime importance in understanding the system. For example, in energy storage devices the capacitance of the electrode surface is the main quantity of interest, which can be estimated using EIS. EIS data is used to better understand corrosion [12] and to estimate the thickness of an electrochemically deposited layer [13]. Since the actuation of the yarns depends on the charge stored in them [3], EIS may be a useful tool to study their behaviour. Because of the porous structure of our yarns, we concentrate our discussion on the information that can be obtained from EIS data for porous electrodes.

5.2.1. EIS of porous materials

Porosity or roughness of the electrode surface is expected to change the frequency dependence of the interfacial impedance. A simple approach to the problem of porous and rough interfaces is based on the use of transmission line analogies [14]. Consider a cylindrical pore in a conducting electrode as depicted in Figure 5.2. If the series resistance of the electrolyte per unit length is R_0 , and the interfacial capacitance per unit length is C_0 , then the pore behaves as a transmission line and has an impedance given by

$$Z = \sqrt{\frac{R_0}{j\omega C_0}}, \quad (5.1)$$

where $j = \sqrt{-1}$, $\omega = 2\pi f$, and f is the frequency of the electrical excitation.

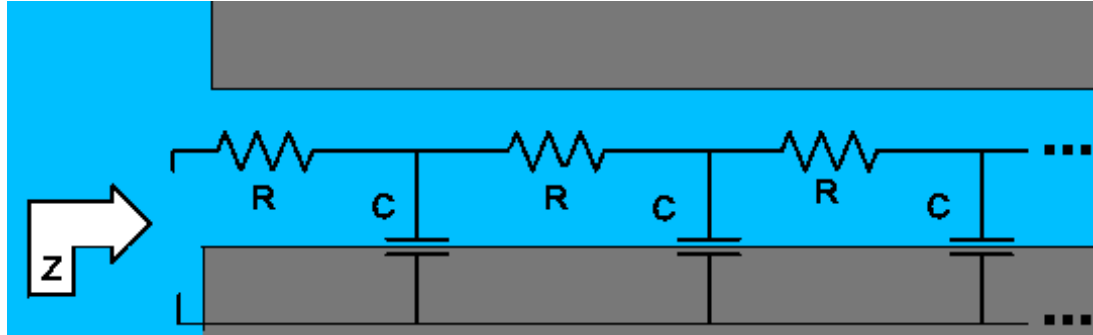


Figure 5.2: A narrow pore in a porous conducting electrode.

A derivation of Eqn. 5.1 can be found in appendix 1. This approach can be extended to more complex situations that include pores of finite depth, non-uniform pores, and situations where the interfacial capacitance is replaced by a complex admittance, corresponding to electrochemical reactions taking place down the depth of the pore [15]. It is also possible to include finite electrode resistance.

In practice, the frequency dependence of the electrochemical response is often neither purely capacitive nor proportional to $\frac{1}{\sqrt{j\omega}}$. More generally, the impedance can take the form of

$$Z = \frac{1}{Y_0(j\omega)^P}, \quad (5.2)$$

where P is a real number between zero and one, usually close to unity [15]. Depending on the structure of the porous electrode, the value of P may vary. Y_0 is a constant combining the resistive and capacitive properties of the electrode. If Y_0 is a real number independent of frequency, the impedance, Z will have a constant phase angle. It is, therefore, known as a Constant Phase Element (CPE). Y_0 can be related to the thickness of the double-layer, since it include the effect of the size of the double-layer capacitance. If P is 1, then the element acts as a capacitor. If it is $\frac{1}{2}$, then it will represent a pore impedance, as depicted in Figure 5.2 and if it is 0, then we have a pure resistor. Often other values of P appear in experiments, which make it more difficult to relate to physical phenomena.

Some attempts have been made in relating the parameters of a CPE model to the electrode properties and geometry. Le Mehaute [16, 17] represented a rough or porous electrode-electrolyte interface as a fractal and proposed that the exponent P of the CPE is related to the fractal dimension D . Sapoval and Chazalviel studied cases where Faradaic and diffusion processes coexist in fractal electrodes. They proposed a number of equivalent circuit networks for particular fractal geometries and suggested a relationship between the fractal dimension and the model network parameters [18]. Scheider showed how almost any arbitrary value of exponent P can be modeled by replacing some

branches in the circuit in Figure 5.2 with transmission lines themselves [19]. He also presented an argument in an attempt to relate the branched network configurations to the physical realities of the electrode-electrolyte interface.

In the case of our yarns, individual MWNTs having diameters of about 10 nm form into more or less cylindrical bundles that have diameters ranging from 50 nm to 100 nm. Combinations of these bundles form the twisted yarn, which is again cylindrical. It can therefore be approximated that the yarn is formed of nested self-similar objects of variable dimensions and can qualify as a ‘fractal’ electrode (Figure 5.3). It is therefore not unexpected if the impedance of the yarn behaves like a CPE. However, proof of existence of a universal relationship between the fractal dimension and the CPE parameters, as well as its exact form and quantitative nature, are subjects open to investigation [18, 20].

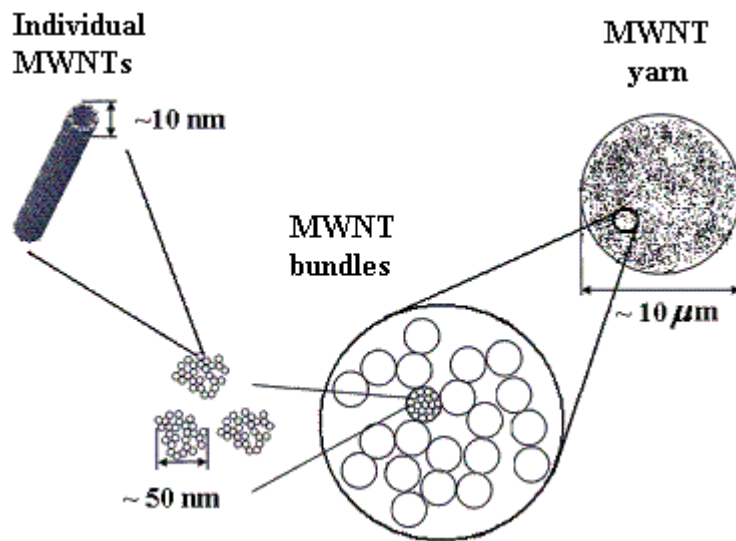


Figure 5.3: The nested ‘fractal’ structure of twist-spun MWNT yarns.

A parallel way of studying the impedance behaviour of the yarn is to consider diffusion and field effects, which can both contribute to the charging process of an electrode-electrolyte interface. For planar electrodes, diffusion gradients are perpendicular to the electrode surface and opposed to the field direction. However, on a rough surface, like that of our yarns, roughness can cause uneven charging of the double-layer. In such situations, considerable diffusion gradients tangential to the electrode surface may exist [19]. The relative magnitude of the charge moving due to the lateral diffusion gradients compared to the charge moving in the direction of the electric field depends on the radius of curvature and the roughness of the surface.

As discussed in reference [19], let us visualize diffusion over the surface of a MWNT bundle near the yarn surface. Figure 5.4 shows what happens to bundles of MWNTs in the yarn when a potential is applied to the yarn. Red spheres represent ions of opposite charge to the charge accumulated on the MWNT bundle surface and (smaller) blue spheres represent ions with the same charge type as on the MWNTs. Imagine that a step in galvanostatic current is applied at $t = 0$. Initially, no concentration gradients are present and ions (red spheres in Figure 5.4) flow along the electric field lines (Figure 5.4a) to the exposed side of the MWNT bundle. As charge accumulates in the double layer on the exposed side of the bundle, the folding down of the equipotential lines and the lateral concentration gradient cause tangential spreading of ions to the space around the bundle (Figure 5.4b). The line of constant electric potential (Φ) moves closer and folds around the bundle. At the outermost point, the concentration gradient vector \mathbf{N} opposes the electric field, while at the side the concentration gradient has a tangential component

which acts in the same direction as the electric field. As time passes, larger parts of the surface become accessible to charge and the effective capacitance increases.

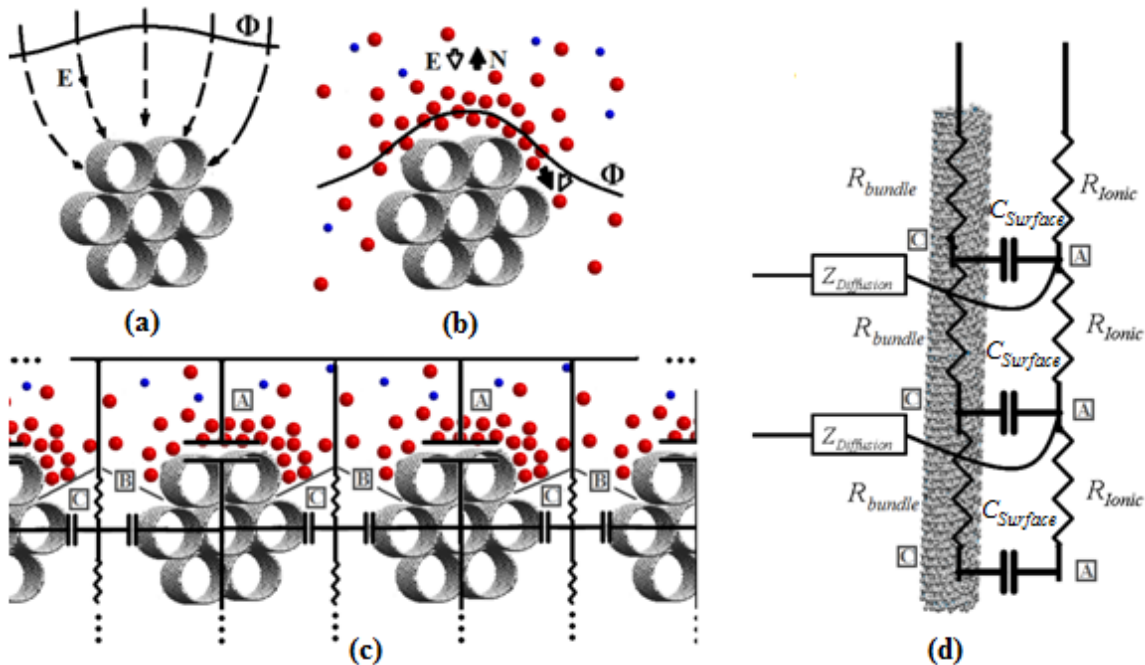


Figure 5.4: Visualisation of a MWNT bundle within the yarn (a) Electric field lines \mathbf{E} initially converge toward the exposed face of MWNT bundle while the gaps around the bundle are partially shielded. (b) With accumulation of ions that follow the electric field lines to the outermost point of the bundle, a concentration gradient is established (c) An artificial boundary \boxed{B} is drawn to visualize the process by which accumulated charge in the outer areas \boxed{A} spreads to the valley sides \boxed{C} under the force of the tangential electro-diffusion gradient. (d) The RC ladder circuit formed by the resistance of the MWNTs and the ionic resistance of the electrolyte along with the diffusion impedance into the yarn. Each $Z_{Diffusion}$ impedance block represents an RC ladder circuit similar to the one in Figure 5.2. The cylinder represents any of the bundles in (c), and the capacitors labelled $C_{Surface}$ are the same as the surface capacitances in (c), this time drawn along the length of the bundle.

To estimate the orders of magnitude involved in this process, it can be supposed that an artificial boundary \boxed{B} may be drawn (Figure 5.4c) dividing the surface into the exposed side, \boxed{A} , and a valley side, \boxed{C} . The exposed side, \boxed{A} , is assumed to charge uniformly as if it were a segment of a perfectly smooth parallel plane electrode, while the valley side \boxed{C} is assumed to be completely shielded from the bulk electrolyte. The double layer in the valley is thus charged exclusively from the input at \boxed{B} by ions moving under the lateral electro-diffusion potential gradient. This movement along the surface \boxed{C} is described mathematically by the branched network shown. This branched network forms a first order series-series network with another RC ladder formed along the length of the yarn due to the surface capacitance and the resistance along the length of the MWNT bundles and the resistance of the electrolyte (Figure 5.4d). It is assumed that the ladder circuits along the length of the MWNT bundles are connected together at the ends of the yarn. Scheider [19] showed that the frequency response of such a first order series-series branched RC ladder network corresponds to a phase exponent of 0.75. He also showed that including a third level of branching in the circuit model can lead into a CPE exponent of 0.875. We shall use this theory to compare the frequency response of the MWNT yarns with that of a CPE and to find a circuit model employing a CPE to describe the response of MWNT yarn electrodes.

5.2.2. Finding the equivalent capacitance of a CPE

It is often desirable to have an estimate of the ‘capacitance’ of an electrode surface. Since the actuation of the MWNT yarns depends on the charge stored in them, it is useful to find an estimate of their capacitance. One way of finding such a capacitance is to fit an

RC circuit model to the impedance of the cell. However, if such a fit is not very good, the value of the capacitance obtained this way may not be very useful. Several attempts have been made to find the ‘capacitance’ of a CPE [21]. Hsu and Mansfeld [13] proposed a method to estimate the capacitance of a CPE. Their method is based on the fact that in a circuit consisting of a CPE in parallel with a resistor, the real part of the impedance becomes independent of the exponent P at the frequency where the imaginary part of the impedance has a maximum (ω_m). At that frequency, all the energy loss in the cell can be assumed to be in the resistor and the CPE can be set equivalent to a capacitor. Based on Kramers-Kronig theorem the resistance of the parallel resistor can then be calculated [22] using

$$R = 2.3 \times \frac{4}{\pi} \int_{\omega_m}^{\infty} Z''(\omega) d(\log \omega), \quad (5.3)$$

where Z'' is the imaginary part of the measured impedance. If Z'' varies monotonically with frequency, it has no clear maximum point and so Eqn. 5.3 can only provide a lower limit for the resistance. Since the above equation is independent of the CPE exponent P , it will also apply for a pure capacitor, which is a CPE with $P=1$. Using the value of R from the above equation, the equivalent capacitance can be found as

$$C = \frac{1}{\omega_m R}. \quad (5.4)$$

We shall use this equation to determine the capacitance of the CPE element representing the MWNT yarn and compare it with the capacitance value obtained from fitting a simple RC model to the same impedance response.

5.3. Experimental results and discussion

A twist-spun yarn of carbon nanotubes with a diameter of about 10 µm was used as the working electrode (WE) in an electrochemical cell. In the case of aqueous electrolyte, the length of the yarn immersed in the electrolyte was 15 mm, and in the case of acetonitrile, it was 5 mm. In both cases the yarn was held in place in the electrolyte using a Teflon clamp. The other end of the yarn was held outside the electrolyte where electronic contact was made to it. The yarn was otherwise exposed to the solution all around. Images and diagrams of the cell setup can be found in chapter 2 and chapter 3. The counter-electrode (CE) was a piece of carbon fibre paper (avCarbTM, Ballard Materials), whose surface area was substantially larger than that of the yarn. The electrochemical impedance of the cell was measured in a 1 M aqueous solution of sodium hexafluorophosphate (NaPF_6), as well as in a 0.2 M solution of tetrabutylammonium hexafluorophosphate (TBAPF₆) in acetonitrile, at various bias potentials applied between the WE and CE. In the case of the aqueous electrolyte, the reference electrode (RE) was Ag/AgCl in 3 M NaCl and in the case of the acetonitrile-based electrolyte, it was 0.1 M AgNO_3 in acetonitrile, hereby referred to as Ag/Ag⁺. The impedance of the cell was measured over a range of frequencies spanning from 10 mHz to 10 kHz using a Solatron SI 1260 Impedance/Gain-Phase Analyzer equipped with a SI 1287 Electrochemical Interface. The amplitude of the AC signal was 20 mV in all cases. Data recording and fitting were performed using the Zview 3.0a software package with Calc-Modulus data weighing, which means each data point's weight is normalized by its magnitude during the fitting process. Cyclic voltammograms were also performed on both cells at a scan rate of 40 mV/s over the

ranges of -1.00 V to +1.00 V vs. Ag/AgCl in 3 M NaCl in the aqueous electrolyte and -1.40 V to +0.60 V vs. Ag/Ag⁺ in the acetonitrile-based electrolyte.

The impedance was found to have a real value at high frequencies. This is equivalent to a series resistance, which can be due to the solution and contact resistances. It was also found that as potential across the interface was increased to large positive or negative values, some parasitic reactions started occurring at the interface. These reactions resulted in some charge being transmitted from the electrode to the ions in the electrolyte, thus effectively shunting the capacitor. It was therefore decided to model the cell impedance as a circuit consisting of a resistor in series with the parallel combination of a CPE and a resistor (Figure 5.5a). The resistor R_1 represents the electrolyte and contact resistance and R_2 represents the charge transfer resistance across the interface, leading to partially discharging the capacitor. For comparison, an alternative circuit model was also used replacing the CPE with an ideal capacitor (Figure 5.5b). Variations of these equivalent circuits were tested, but the minimal RMS error compared with the experimental data was only observed when the proposed model was applied.

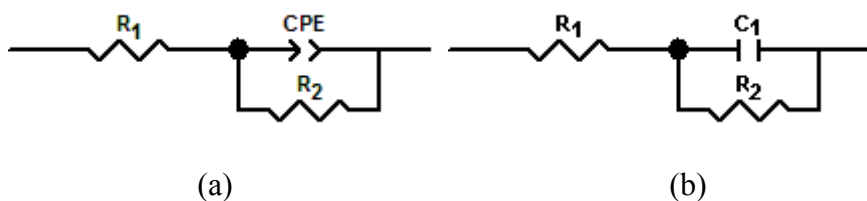
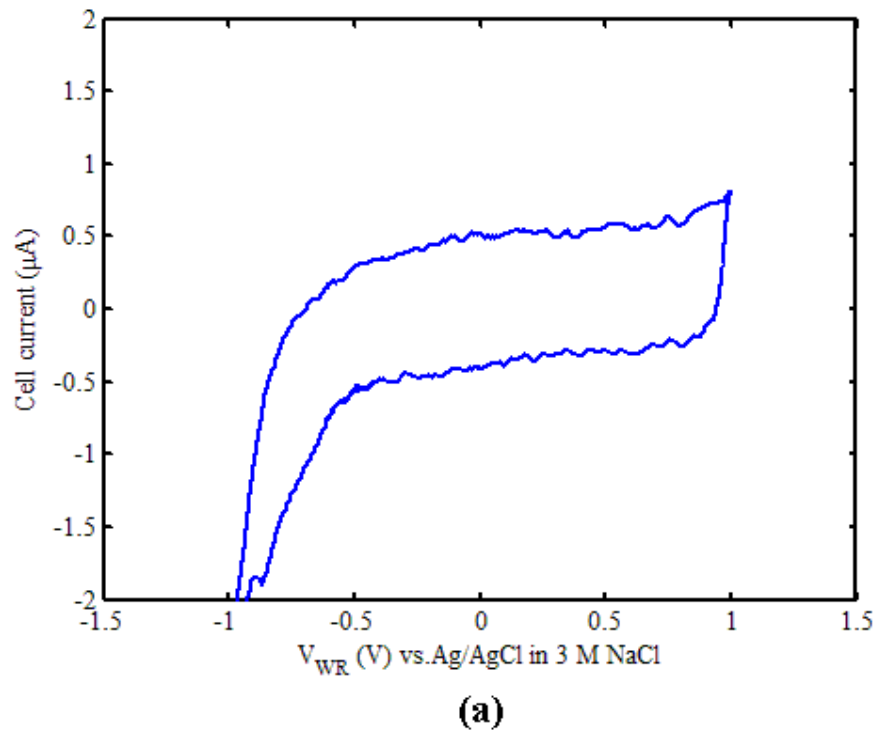


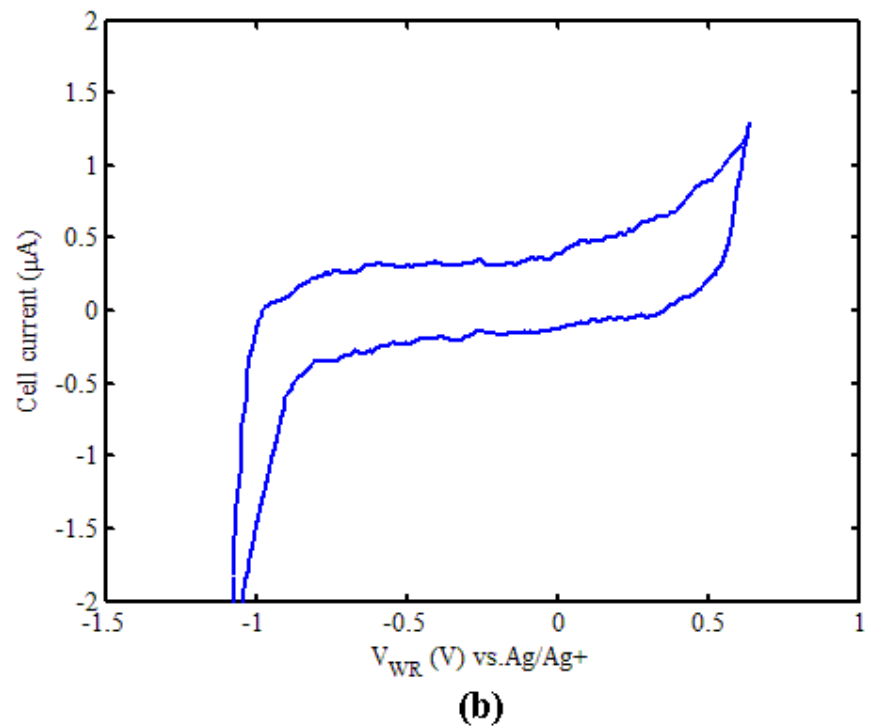
Figure 5.5: Proposed circuit models for the electrochemical behaviour of the MWNT yarn electrode, using (a) a CPE and (b) an ideal capacitor. The series resistor R_1 models the solution and contact resistance and the parallel resistor R_2 models the processes resulting in a loss of the stored charge.

5.3.1. Experiments in aqueous NaPF₆

Figure 5.6a shows the CV results for the experiment in aqueous electrolyte. The results of the EIS measurements in a 1 M aqueous solution of sodium hexafluorophosphate at various potentials ranging from -0.75 V to +1.00 V vs. RE are plotted in Figure 5.7. The circuit in Figure 5.5a was fitted to the impedance response and the best fit circuit parameter values are plotted as a function of the bias potential in Figure 5.8. The simulated frequency responses of the best fit circuits are shown as continuous lines along with the experimentally-measured cell responses (dots) in Figure 5.7. The error bars in Figures. 5.8b and 5.8c refer to the average error between the fit and the experimental data. The error in Figure 5.8a is too small to be visible on the plot. The Chi-Squared error is the square of the standard deviation between the original data and the calculated model spectrum. The Chi-Squared error values are indicated below Figure 5.7.



(a)



(b)

Figure 5.6: Cyclic voltammograms of the yarn in (a) 1 M aqueous solution of sodium hexafluorophosphate, and (b) 0.2 M solution of TBAPF₆ in acetonitrile.

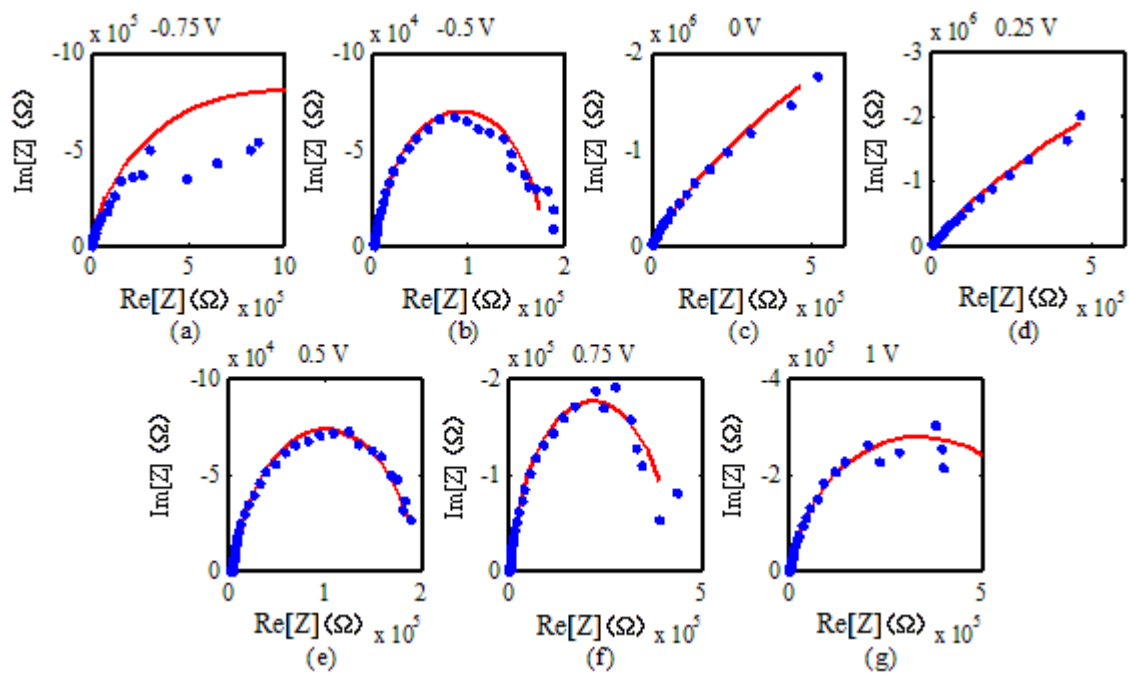


Figure 5.7: Nyquist plots of the yarn impedance in a 1 M aqueous solution of sodium hexafluorophosphate at various bias potentials: (a) -0.75 V (b) -0.50 V (c) 0 V (d) +0.25 V (e) +0.50 V (f) +0.75 V and (g) 1.00 V vs. Ag/AgCl in 3 M NaCl RE. The fit lines show the impedance response of the circuit model in Figure 5.5a. The Chi-Square errors are 0.304, 0.039, 0.128, 0.103, 0.017, 0.025, and 0.039, respectively.

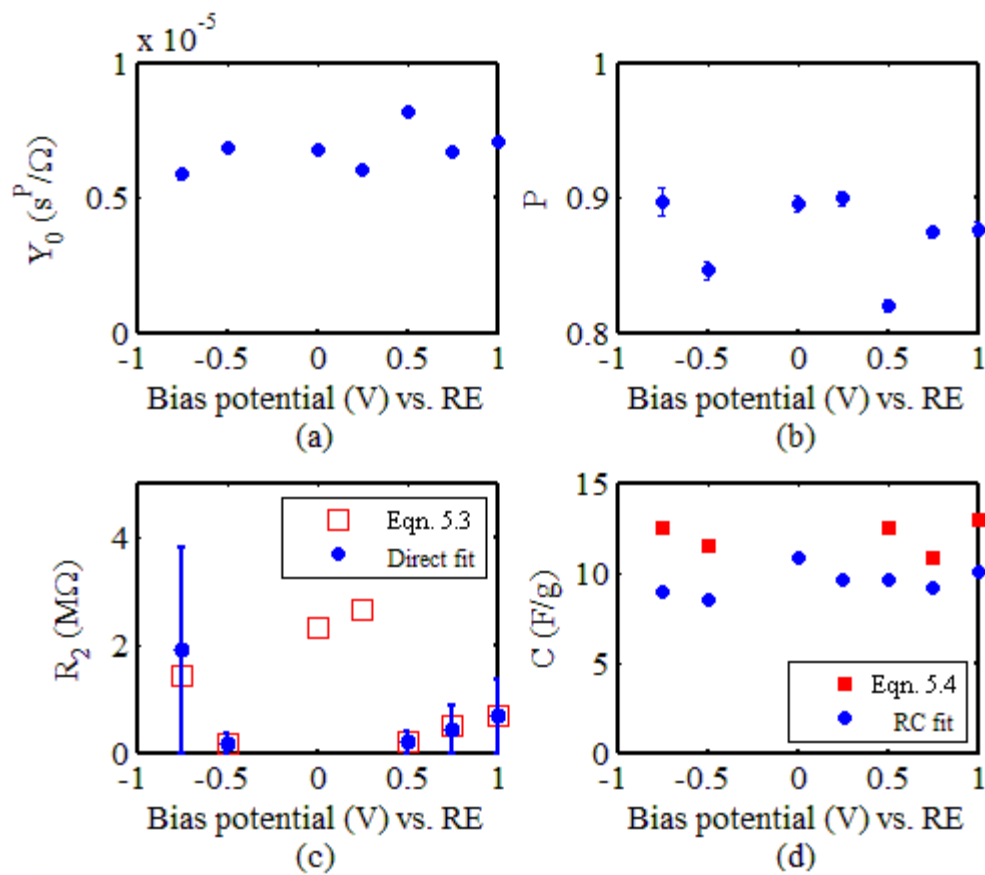


Figure 5.8: Best fit circuit parameter values for the cell containing the yarn in an aqueous NaPF_6 solution (a) Y_0 , (b) P , (c) R_2 based on directly fitting the circuit in Figure 5.5a and based on Eqn. 5.3 (d) the gravimetric capacitance based on Eqn. 5.4 compared to the gravimetric capacitance found by fitting the circuit in Figure 5.5b.

Figure 5.8c shows the dependence of the parallel resistor R_2 on the bias potential. At bias potentials close to 0 V, the value of the resistance R_2 becomes very large and has little effect on the overall fitting error. This implies that this circuit parameter is unnecessary. The values for R_2 at those two points are therefore not shown in Figure 5.8c. Looking at the CV plot (Figure 5.6a), this behaviour is expected, since almost no parasitic reactions should occur at low electrode potentials and therefore R_2 should act as open circuit at

low potentials. As the potential is increased, the form of the CV implies that parasitic reactions are substantial at potentials beyond +0.8 V vs. RE and below -0.5 V vs. RE. The intervening potential window of about 1.3 V in width is consistent with the electrolysis potentials of water, and therefore it is likely that the parasitic reactions, which increase as the potential limits are approached, are the result of decomposition of the water. The values of the parallel resistance R_2 from Eqn. 5.3 are also plotted as a function of the applied bias potential (squares). As can be seen in Figure 5.7c and Figure 5.7d, at potentials close to zero, the impedance spectra are quite linear-looking, and therefore the imaginary part of the impedance does not reach a visible maximum as it does at other potentials. Therefore Eqn. 5.3 can only provide us with a lower limit on the resistance. This is consistent with the result of the direct fitting method, which predicted that R_2 was so large that the parallel resistor was found to be unnecessary to provide a good fit. At other potentials, where the imaginary part of the impedance first increases and then decreases as the frequency is increased, ω_m can be found and R_2 can be calculated using Eqn. 5.3. In Figure 5.8c the resistance values found in this way virtually coincide with those found using direct fitting of the RC circuit. At higher potentials R_2 becomes much smaller and the fitting uncertainty decreases significantly compared with the two aforementioned points, indicating that parasitic reactions start to happen at the WE. Figure 5.8b shows the dependence of the phase exponent P on bias potential. It can be seen that P varies only between 0.82 and 0.9. Figure 5.8d shows the gravimetric capacitance based on direct fitting of the circuit in Figure 5.5b along with the value computed using Eqn. 5.4 at the potentials where that equation is applicable. It can be seen that while the EIS results of the yarn show a clear CPE behaviour, if an effective

capacitance is needed equations 5.3 and 5.4 can be used to relate the CPE results to a close estimate of the effective capacitance.

5.3.2. Experiments in acetonitrile

Similar measurements were performed in a 0.2 M solution of tetrabutylammonium hexafluorophosphate (TBAPF₆) at various potentials ranging from -1.40 to +0.60 V vs. Ag/Ag⁺. The results of EIS measurements are plotted in Figure 5.9. The circuit in Figure 5.5a was fit to the impedance response and the best fit circuit parameter values are plotted as a function of the bias potential in Figure 5.10. The simulated frequency responses of the best fit circuits are shown along with the experimentally-measured cell responses in Figure 5.9. Figure 5.10b shows the dependence of the phase exponent *P* on bias potential. It can be seen that *P* varies only between 0.82 and 0.94. Figure 5.10d compares the capacitance found based on Eqn. 5.4 and the best fit capacitance value using the circuit in Figure 5.5b. As can be seen in Figure 5.10c, as was the case with the aqueous electrolyte, when the bias potential is not close to the extremes of the studied range, the fitting uncertainty for the parallel resistor *R*₂ becomes very large, implying that this circuit parameter is irrelevant as no charge transfer should occur at low electrode potentials. The values of *R*₂ at those two points, that are deemed irrelevant, are not shown in Figure 5.10c. At higher potentials *R*₂ once again becomes much smaller and its fitting uncertainty decreases significantly compared to the two points mentioned above, indicating that parasitic reactions start to happen at the WE. Judging by the CV (Figure 5.6b), reactions are significant above +0.5 V and below -0.8 V. These numbers are once again consistent with breakdown potentials of water, implying that some water or

moisture contamination must have entered the cell during the measurements. At potentials where Eqn. 5.3 is applicable, the values found for R_2 are very close to those obtained through direct fitting (squares). At $V = -0.65$ V and $V = -0.40$ V vs. Ag/Ag⁺, the imaginary part of the impedance has no clear maximum and hence Eqn. 5.3 and 5.4 are not applicable.

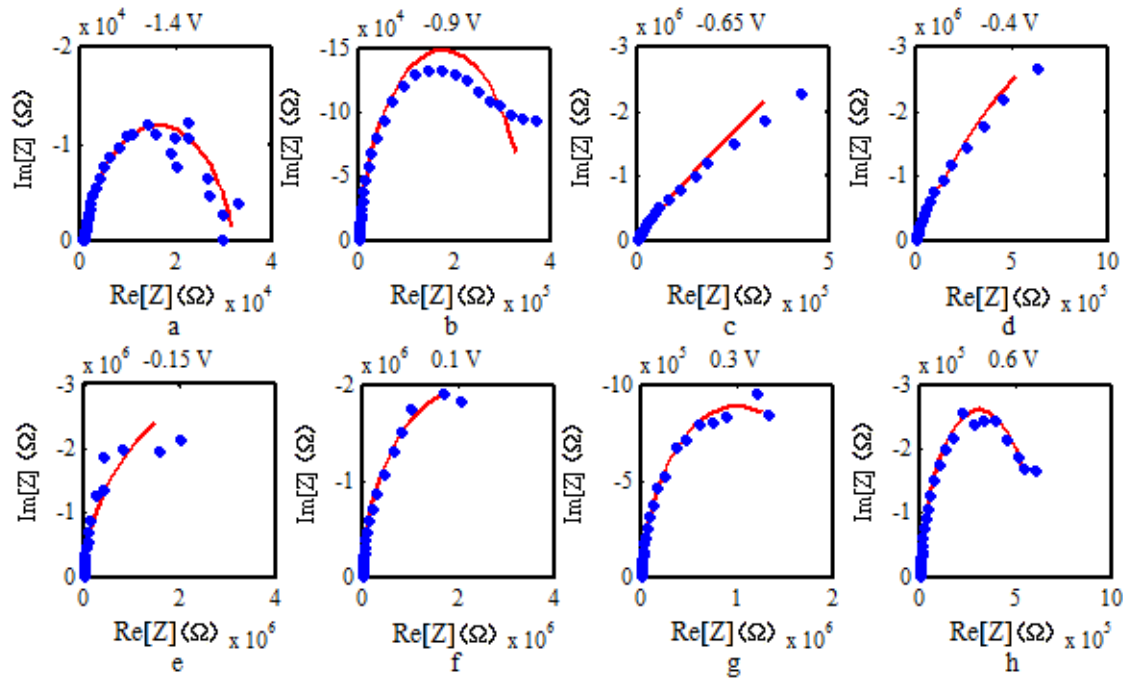


Figure 5.9: Nyquist plots of the impedance of the MWNT yarn electrode in a 0.2 M solution of TBAPF₆ in acetonitrile at various potentials. The Chi-Square errors are 0.065, 0.018, 0.038, 0.036, 0.042, 0.027, 0.018, and 0.037, respectively.

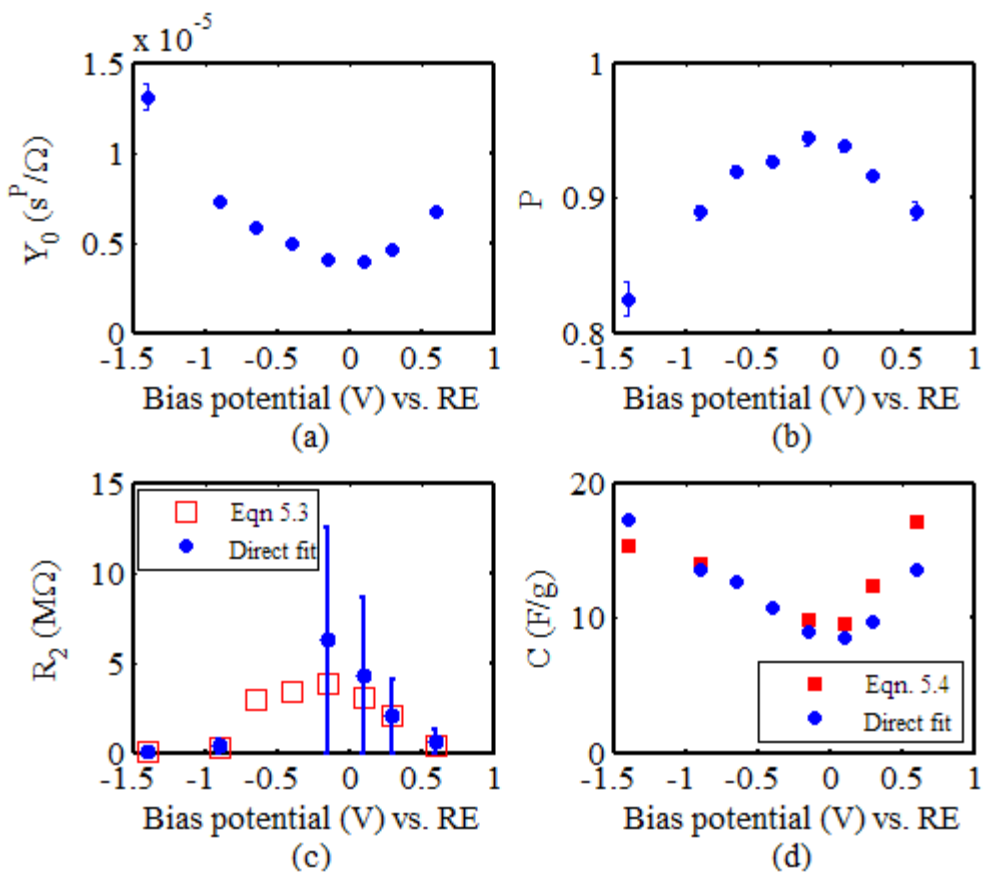


Figure 5.10: Best fit circuit parameter values for the cell containing the yarn in a solution of 0.2 M TBAPF₆ in acetonitrile. (a) Y_0 , (b) P , (c) R_2 based on directly fitting the circuit in Figure 5.5a and based on Eqn. 5.3, (d) the gravimetric capacitance based on Eqn. 5.4 compared to the gravimetric capacitance found by fitting the circuit in Figure 5.5b.

5.4. Discussion

Comparison between the plots in Figure 5.8 and Figure 5.10, shows that the gravimetric capacitance value in acetonitrile and water at low potentials is in the same range. However, while the gravimetric capacitance in the aqueous electrolyte is relatively independent of the bias potential, the gravimetric capacitance in acetonitrile seems to increase as the absolute value of the applied voltage is increased. One possible explanation is that the number of pores filled with electrolyte depends on potential

because of the change in surface stress due to charging [23, 24]. Another possibility is the partial desolvation of ions as they enter into the pores of the yarn [25-27]. In the process the ions get partially deprived of their solvation spheres at higher potentials, resulting in a smaller distance between the charge layer and the electrode surface, and a higher capacitance. Small ions can penetrate deeper into the pores of the yarn, increasing the effective surface area. This is consistent with the observation of increased Y_0 at extreme potentials in acetonitrile (Figure 5.10a). This increase in capacitance is not observed in the aqueous electrolyte. This may be because water molecules are smaller and more polar compared to acetonitrile, and therefore the solvation shell is not lost at potentials under study. It is also possible that the contaminating water in the acetonitrile electrolyte is partially contributing to the formation of solvation spheres, thus changing the capacitance of the Helmholtz layer in the acetonitrile electrolyte, and making its size comparable to that of aqueous electrolyte. The estimated value of the capacitance from Eqn. 5.4 is almost always larger than the value estimated by fitting the parallel-series RC circuit in Figure 5.5b. Since the CPE provides a better fit than the RC circuit (whose fits are not shown here), the ‘real’ capacitance value found from Eqn. 5.4 is expected to be a better estimate of the capacitive behaviour of the interface since it is based on a better fit.

In both model fits, the parallel resistor R_2 becomes irrelevant at smaller potentials, where no electron transfer is expected to take place across the electrode-electrolyte interface. The value of R_2 drops significantly as the potential difference across the electrode is increased and as charge starts to transfer through the interface. The solution of TBAP in acetonitrile is known to be stable over a large potential range of -2.9 V to +3.4 V vs. SCE (equivalent to about -3.26 V to 3.04 V vs. Ag/Ag⁺ 0.1 M) [28]. Considering the

potentials at which parasitic reactions occur according to the CV, it is likely that water (as a contaminant in the case of acetonitrile solvent) is the prime suspect for the parasitic reactions. The capacitive voltage range could be extended by employing anhydrous solvents. The electrochemical behaviour of the yarn outside its purely-capacitive range is still of great interest since in electro-chemo-mechanical actuators like this it is occasionally necessary to apply large potentials to the actuator [29], and it is important to have electrochemical models that describe the behaviour of the actuator at such potentials [30].

Comparing Figure 5.8a with Figure 5.10a shows that the CPE coefficient Y_0 has smaller variation in water compared to acetonitrile. If the value of Y_0 is indeed related to the thickness of the double layer, then it can be said that the double-layer thickness in the non-aqueous electrolyte changes more drastically compared to the aqueous electrolyte.

The phase exponent P has average values of about 0.88 in the aqueous electrolyte and about 0.89 in the non-aqueous electrolyte. The similarity of these two numbers supports our assumption that the CPE behaviour is rooted in the structure of the MWNT yarn electrode. Based on the branched RC circuits discussed in [19], such an exponent can be explained by the existence of third level of branching. Indeed if ions can diffuse between individual MWNTs in a bundle, a model employing a third level of branching physically justifies an exponent of 0.875, which is close to the estimated value.

The results for the gravimetric capacitance are consistent with the results found for CNT paper electrodes in acetonitrile by Barisci et al. [11]. We did not observe a linear tail in the Nyquist plots at low frequencies as reported in [7, 8] even though the lower frequency limit in our measurements was the same (0.01 Hz), except at 0 V and 0.25 V in the

aqueous electrolyte and at -0.65 V and -0.40 V in the acetonitrile-based electrolyte. This may imply that electron transfer effects dominate at the rest of the applied potentials in our measurements; a suggestion that is consistent with the parasitic currents evident in the CVs. The Nyquist plots in [9] are measured only at 1.00 V vs. Pt in an ionic liquid and it is therefore hard to compare the dependence of the behaviour of their CNTs on the applied bias. Nevertheless the larger phase angle of their electrodes implies a more capacitive behaviour than that of our yarns, which is consistent with the CPE behaviour in our yarns being determined by the self-similar structure of the yarns rather than the porous structure which is common in both materials.

Based on the magnitude of the current observed in the CVs, the capacitance in the acetonitrile electrolyte is about 17 F/g, which is consistent with the values of capacitance reported in Figure 5.10d. Similarly, the capacitance of the yarn in the aqueous electrolyte is estimated using the CV to be about 14 F/g, which is again quite close to the range of capacitances in Figure 5.8d.

The capacitance per surface area of the bundles was calculated assuming that the yarn consists of parallel bundles of MWNTs with diameters of about 50 nm, and using the capacitance values found above. The results for aqueous and acetonitrile-based electrolyte are plotted in Figure 5.11. The estimated surface capacitance values are consistent with the range expected for MWNT sheets based on surface area measurement (using BET [31]).

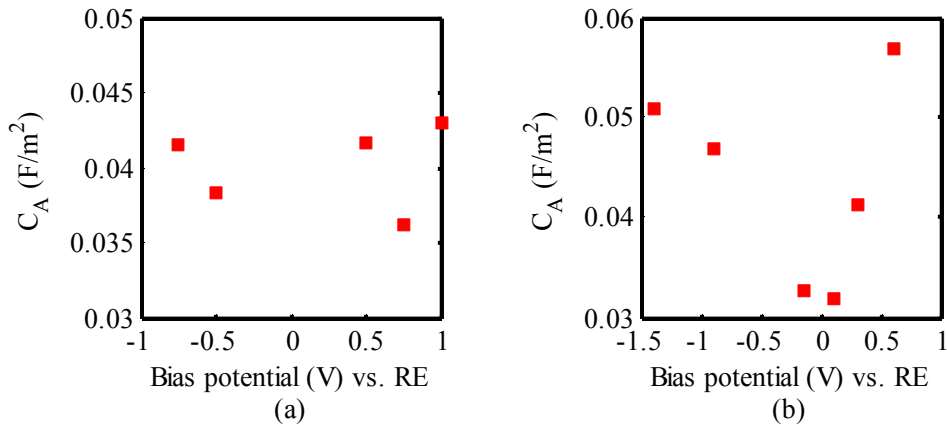


Figure 5.11: Surface capacitance (F/m^2) of the MWNT bundles calculated based on the measured capacitances and the surface area of the bundles as modeled in Figure 5.4 (a) in aqueous 1 M NaPF_6 and (b) in 0.2 M TBAPF_6 in acetonitrile.

5.5. Conclusions

The electrochemical response of a twist-spun yarn made of MWNTs was studied in aqueous and non-aqueous electrolytes using EIS. The frequency dependence of the impedance of the yarn is found to comply with that of a model containing a CPE with a phase exponent close to 0.88, in parallel with a resistor modeling charge transfer across the interface. This parallel combination of the CPE and resistor is placed in series with another resistor, which can model the solution and contact resistance. An attempt has been made to relate the exponent of the CPE to the physical structure of the yarn, which has self-similar structure at length scales from 10 nm to 10 μm . Since the yarns show phase exponents of about 0.88, while similar MWNT structures with random orientations of nanotubes exhibit exponents closer to 1, it is possible that the CPE behaviour of the yarns is related to nested transmission lines that are related to the underlying physical structure, and to their self-similar (“fractal”) nature. The gravimetric capacitance of the yarn is estimated based on the CPE parameters. The capacitance per surface area of the

MWNT bundles is estimated using the model, which is found to be consistent with previous reports.

References

- [1] R. H. Baughman, A. A. Zakhidov, and W. A. de Heer, "Carbon nanotubes - the route toward applications," *Science*, vol. 297, pp. 787-792, 2002.
- [2] M. Zhang, K. R. Atkinson, and R. H. Baughman, "Multifunctional carbon nanotube yarns by downsizing an ancient technology," *Science*, vol. 306, pp. 1358-1361, 2004.
- [3] T. Mirfakhrai, J. Oh, M. Kozlov, E. C. W. Fok, M. Zhang, S. Fang, R. H. Baughman, and J. D. W. Madden, "Electrochemical actuation of carbon nanotube yarns," *Smart Materials and Structures*, vol. 16, pp. S243, 2007.
- [4] K. R. Atkinson, S. C. Hawkins, C. Huynh, C. Skourtis, J. Dai, M. Zhang, S. Fang, A. A. Zakhidov, S. B. Lee, A. E. Aliev, C. D. Williams, and R. H. Baughman, "Multifunctional carbon nanotube yarns and transparent sheets: Fabrication, properties, and applications," *Physica B: Condensed Matter*, vol. 394, pp. 339-343, 2007.
- [5] T. Mirfakhrai, J. Oh, M. Kozlov, S. Fang, M. Zhang, R. H. Baughman, and J. D. W. Madden, "Mechanical force sensors using twisted yarns of carbon nanotubes," In preparation.
- [6] T. Mirfakhrai, M. Kozlov, M. Zhang, S. Fang, R. H. Baughman, and J. D. W. Madden, "Carbon nanotube yarns: Sensors, actuators and current carriers," presented at SPIE Smart Materials and Structures/NDE, San Diego, CA, 2008.
- [7] Z.-h. Yang and H.-q. Wu, "The electrochemical impedance measurements of carbon nanotubes," *Chemical Physics Letters*, vol. 343, pp. 235-240, 2001.

- [8] Z.-h. Yang, S. Sang, Y. Feng, Y. Zhou, K. Huang, and H. Wu, "Electrochemical impedance study of Li-ion insertion into the raw acid-oxidized carbon nanotubes," *Diamond and Related Materials*, vol. 14, pp. 1302-1310, 2005.
- [9] H. Zhang, G. Cao, Y. Yang, and Z. Guo, "Comparison Between Electrochemical Properties of Aligned Carbon Nanotube Array and Entangled Carbon Nanotube Electrodes," *Journal of The Electrochemical Society*, vol. 155 pp. K19-K22, 2008.
- [10] C.-M. Liu, H.-B. Cao, Y.-P. Li, H.-B. Xu, and Y. Zhang, "The effect of electrolytic oxidation on the electrochemical properties of multi-walled carbon nanotubes," *Carbon*, vol. 44, pp. 2919-2924, 2006.
- [11] J. N. Barisci, G. G. Wallace, D. Chattopadhyay, F. Papadimitrakopoulos, and R. H. Baughman, "Electrochemical Properties of Single-Wall Carbon Nanotube Electrodes," *Journal of The Electrochemical Society*, vol. 150, pp. E409-E415, 2003.
- [12] R. de Levie, "The influence of surface roughness of solid electrodes on electrochemical measurements," *Electrochimica Acta*, vol. 10, pp. 113-130, 1965.
- [13] C. H. Hsu and F. Mansfeld, "Concerning the Conversion of the Constant Phase Element Parameter Y₀ into a Capacitance," *Corrosion*, vol. 57, pp. 747-748, 2001.
- [14] R. de Levie, "Electrochemical Response of Porous and Rough Electrodes," in *Advances in Electrochemistry and Electrochemical Engineering*, vol. 6, P. Delahay and C. W. Tobias, Eds. New York: Interscience, 1967.
- [15] J. R. Macdonald and W. R. Kenan, *Impedance Spectroscopy: Emphasizing Solid Materials and Systems*: Wiley-Interscience 1987.

- [16] A. Le Mehaute, "Transfer processes in fractal media," *Journal of Statistical Physics*, vol. 36, pp. 665-676, 1984.
- [17] A. Le Mehaute and G. Crepy, "Introduction to transfer and motion in fractal media: The geometry of kinetics," *Solid State Ionics*, vol. 9-10, pp. 17-30, 1983.
- [18] B. Sapoval and J.-N. Chazalviel, "Electrical response of fractal and porous interfaces," *Physical Review A*, vol. 38, pp. 5867-5887, 1988.
- [19] W. Scheider, "Theory of Frequency Dispersion of Electrode Polarization. Topology of Networks with Fractional Power Frequency Dependence," *Journal of Physical Chemistry*, vol. 79, pp. 127-136, 1975.
- [20] R. Kant, R. Kumar, and V. K. Yadav, "Theory of Anomalous Diffusion Impedance of Realistic Fractal Electrode," *The Journal of Physical Chemistry C*, vol. 112, pp. 4019-4023, 2008.
- [21] S. F. Mertens, C. Xhoffer, B. C. De Cooman, and E. Temmerman, *Corrosion*, vol. 53, pp. 381, 1997.
- [22] F. Mansfeld and M. W. Kendig, "Discussion of the paper "The application of the transform of Kramers-Kronig for computing the polarization resistance"," *Materials and Corrosion*, vol. 50, pp. 475, 1999.
- [23] J. Weissmüller and J. W. Cahn, "Mean stresses in microstructures due to interface stresses: A generalization of a capillary equation for solids," *Acta Materialia*, vol. 45, pp. 1899-1906, 1997.

- [24] J. Weissmüller, H. L. Duan, and D. Farkas, "Deformation of solids with nanoscale pores by the action of capillary forces," *Acta Materialia*, vol. In Press, Corrected Proof, 2009.
- [25] J. Chmiola, G. Yushin, Y. Gogotsi, C. Portet, P. Simon, and P. L. Taberna, "Anomalous Increase in Carbon Capacitance at Pore Sizes Less Than 1 Nanometer," *Science* vol. 313, pp. 1760-1763, 2006.
- [26] R. Lin, P. L. Taberna, J. Chmiola, D. Guay, Y. Gogotsi, and P. Simona, "Microelectrode Study of Pore Size, Ion Size, and Solvent Effects on the Charge/Discharge Behavior of Microporous Carbons for Electrical Double-Layer Capacitors," *Journal of The Electrochemical Society*, vol. 156 pp. A7-A12, 2009.
- [27] P. Simon and Y. Gogotsi, "Materials for electrochemical capacitors," *Nature Material*, vol. 7, pp. 845 - 854, 2008
- [28] A. J. Fry, "Solvents and Supporting Electrolytes," in *Laboratory Techniques in Electrochemistry*.
- [29] J. D. W. Madden, J. N. Barisci, P. A. Anquetil, G. M. Spinks, G. G. Wallace, R. H. Baughnan, and I. W. Hunter, "Fast carbon nanotube charging and actuation," *Advanced Materials*, vol. 18, pp. 870-873, 2006.
- [30] T. Mirfakhrai, M. Kozlov, M. Zhang, S. Fang, R. H. Baughman, and J. D. W. Madden, "Capacitive charging and background processes in carbon nanotube yarn actuators," *Proc. SPIE Smart Materials and Structures/NDE*, vol. 6524, pp. 65241H1-12, 2007.

[31] S. Shiraishi, M. Kibe, T. Yokoyama, H. Kurihara, N. Patel, A. Oya, Y. Kaburagi, and Y. Hishiyama, "Electric double layer capacitance of multi-walled carbon nanotubes and B-doping effect," *Applied Physics A*, vol. 82, pp. 585-591, 2006.

Chapter 6

6 Carbon Nanotube Yarns for Force Sensing and Energy Harvesting¹

6.1. Introduction

Twist-spun yarns of multi-walled carbon nanotubes are drawn from aligned forests of nanotubes [1]. The MWNTs in these yarns may be held together by strong van der Waals forces that arise due to the interactions on the long and smooth surfaces of the MWNTs, and perhaps also by intertwined bundles. These yarns offer exceptional mechanical properties such as very high gravimetric modulus and tensile strengths of about 1 GPa [2]. It has been shown that a dimensional change (actuation) takes place in the yarns when a voltage is applied to them in an electrolyte [3]. Due to the very high tensile strength and Young's modulus of the yarns, the yarn actuators generate high forces per cross-sectional area. Many other actuators can also act as generators and sensors if a force is applied to

¹ A version of this chapter has been submitted for publication. Mirfakhrai, T.; Kozlov, M.; Zhang, M.; Fang, S.; Baughman, R. H. and Madden, J. D., "Mechanical Force Sensors Using Twisted Yarns of Carbon Nanotubes", 2009

them. For example, electric motors and generators work under identical principles. Here it is shown that yarns can generate an electric current/voltage when a mechanical force is applied. In the sections that follow, we first present the results of experiments in which loads are applied to the yarn at various constant potentials, and also at open circuit. The yarns do in fact act as sensors and generators.

6.2. Methods

MWNT yarns were prepared by a dry spinning method [1], i.e., by drawing and twisting tubes from a forest. The MWNT forest was synthesized by catalytic CVD using acetylene gas as the carbon source. MWNTs, which are about 10 nm in diameter, are simultaneously drawn from the MWNT forest and twisted. The length and the diameter of the sample used were about 16 mm and 10 μm , respectively. The diameter was measured using a scanning electron microscope. The twist is characterized by the helix angle (α), which depends directly upon the degree of twist and inversely on the yarn diameter. The degree of twist is typically 15,000 turns/m, corresponding to a twist angle of about 23 degrees.

In order to apply forces and record actuation forces and displacements generated by the CNT yarns, an Aurora Scientific ASI 300 muscle analyzer and its LabView-based software (www.aurorascientific.com) have been employed (see chapter 2 for a more detailed description of this setup). The ASI 300 instrument can be programmed to keep the load on the yarn constant and to measure the displacement generated by the yarn, or it can keep the length of the yarn constant and measure the tension change in the yarn due to actuation. Finally, it can also be used to apply a desired force profile as a function of time and measure the resulting changes in the length of the sample. The fibre is mounted

between a lower fixed clamp and an upper movable motor arm. Photograph and diagram of the apparatus used to apply force and of the yarn and clamping mechanism can be found in [3, 4]. A computer-controlled potentiostat is used to apply potentials. A data acquisition card (National Instruments 6036E) gathers the force and displacement data from the muscle analyzer and also logs the applied voltage and current.

6.3. Results and discussion

When a force is applied to the yarn biased to a given voltage in an electrolyte, a spike is observed in the current going through the cell (Figure 6.1a and b). Figure 6.1c shows the amplitude of these sensor current spikes plotted as a function of the applied bias potential between the WE and RE. We believe that the unequal magnitude of the sensor current response during various cycles is due to the measured signal being undersampled. This assumption is supported by the fact that the largest peak at every load level occurs several times and consistently with the same magnitude during the course of an experiment, which could be hundreds of cycles, and is attested by the statistical analysis in Appendix 5. The amplitude of this peak current is plotted at for stress pulses of 15, 30 and 45 MPa in amplitude. The example in Figure 6.1b is at +0.5 V, while the stress is changed by 45 MPa.

One possible reason for the change in capacitance can be that the surface area of the individual CNTs is changed when a force pulls on the yarn. However, it is known that the Poisson's ratio of MWNTs is about 0.2-0.3 [5]. Therefore, applying strains in the range used in our experiments will expand the surface area of the individual MWNTs, leading to an increase in their capacitance. If the yarn is biased to a positive potential such that the MWNTs are positively charged when the yarn is stretched, an increase in

the capacitance would attract additional negative ions from the electrolyte, inducing a positive (by convention) current. This prediction is contradicted by our experimental data, and we must therefore look for a different mechanism.

Our proposed theory is as follows. When a positive bias potential is applied to the yarn in electrolyte, negative ions are attracted to the surface of the yarn due to Coulomb forces and gradually penetrate the yarn. When a force is applied to the yarn, the axial tension radially compacts the yarn [6] (Figure 6.2a). This radial compaction reduces the inner volume available for interaction with the ions, limiting the extent of the diffuse layer, and expelling negative ions that have been inside (Figure 6.2b). The eviction of the negative ions results in a current from the electrolyte into the yarn, which is by convention a negative current. The reverse happens when the yarn is biased with a negative potential, and thus a positive current is generated upon an increase in tension.

As can be seen in Figure 6.2c, the sign of the sensor current is positive at potentials negative of a certain potential close to 0 V vs. Ag/Ag⁺ reference electrode. The sensor current changes sign and becomes negative at potentials positive of this value. Barisci et al. have measured the potential of zero charge (PZC) for CNTs in acetonitrile medium at ~ 0.005 M tetrabutylammonium hexafluorophosphate [7]. This is the same electrolyte used in our experiments, but at a much lower concentration that enables a reliable measurement of PZC. The PZC was found to be 0.0 V vs. Ag/Ag⁺. This potential matches well with the potential of zero charge for graphite, which is reported to be between -0.3 to 0.15 V vs. Ag/Ag⁺ in similar electrolytes [8-10]. Therefore, it can be expected that the PZC for the yarn in this electrolyte is also near 0 V vs. Ag/Ag⁺.

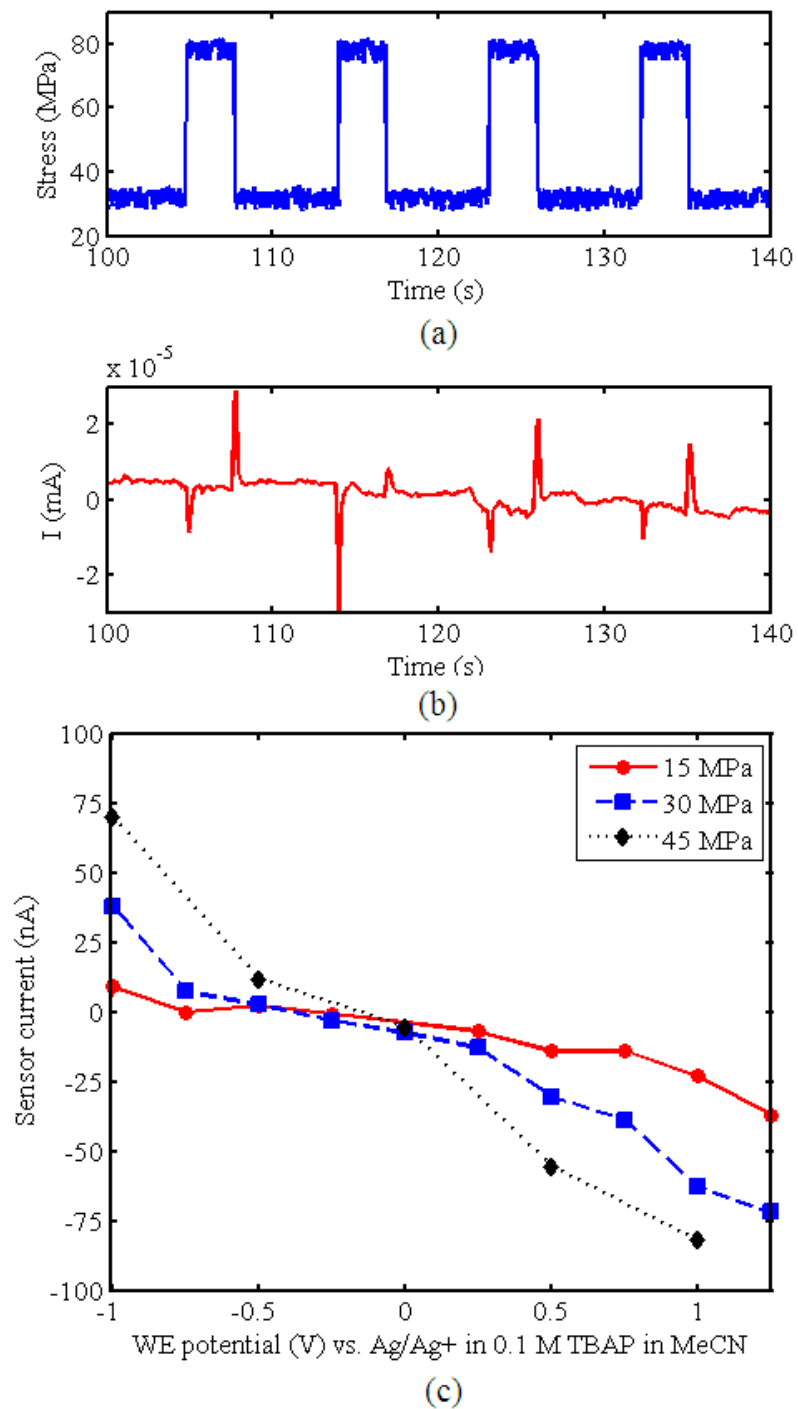
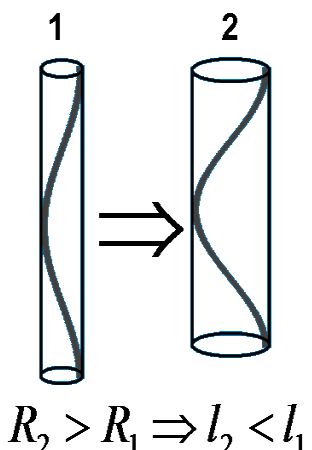


Figure 6.1: (a) Stress profile applied to the yarn under constant potential of 0.50 V vs. RE generates a train of current spikes (a constant background current of 0.08 μ A subtracted) shown in (b). (c) Sensor peak current as a function of the applied bias potential at three different loads. Figure repeated from Chapter 3 for the reader's convenience.



(a)

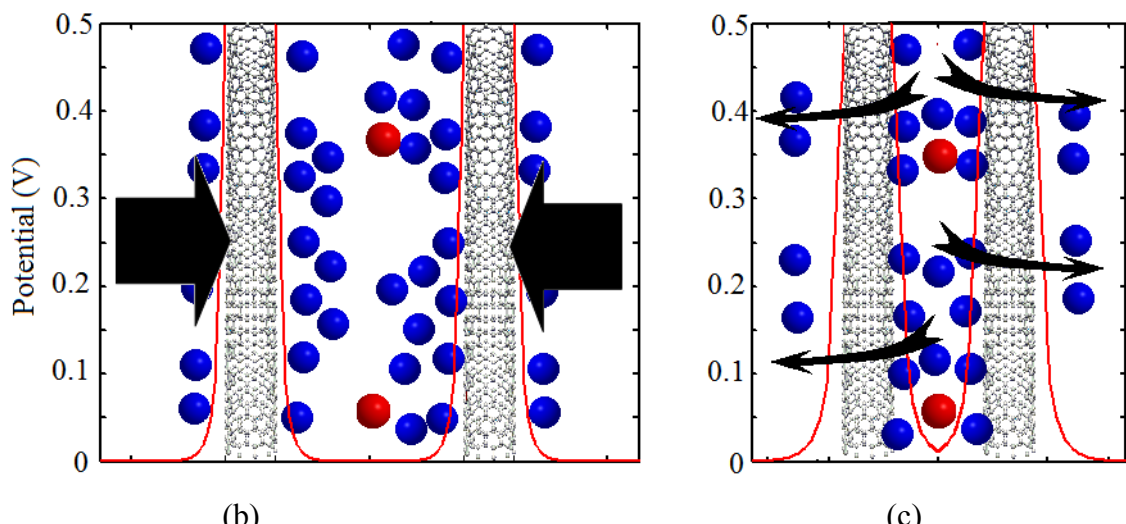
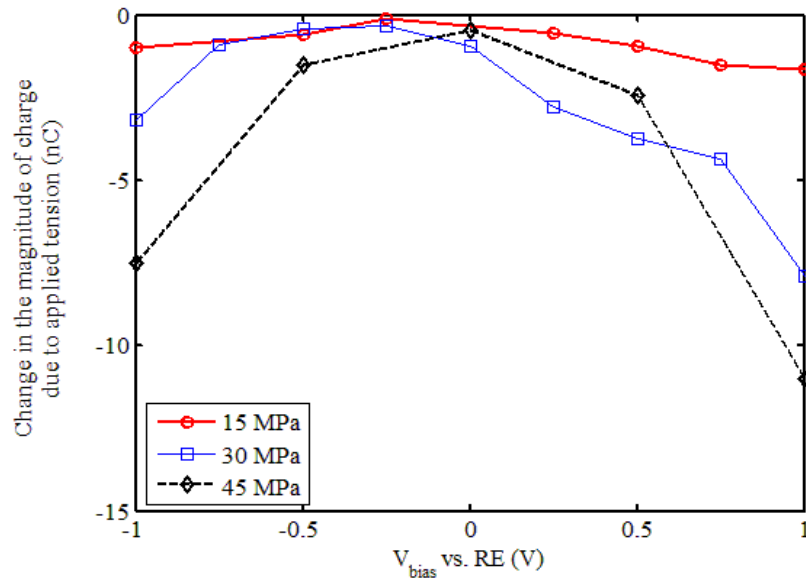
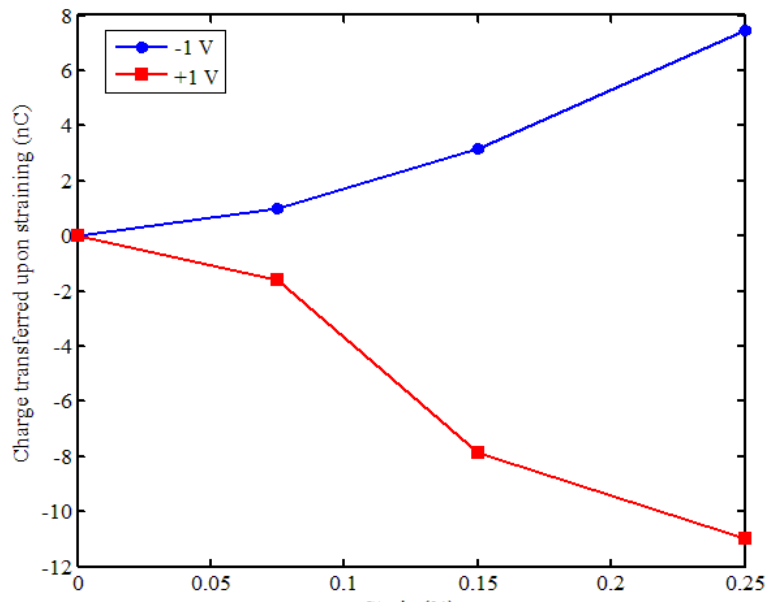


Figure 6.2: Proposed sensing mechanism: (a) stretching a twisted yarn results in radial compaction. (b) the radial compaction brings adjacent MWNTs closer to one another, decreasing the charge storage capacity of the yarn. (c) since the capacitance has decreased and the potential is constant, some ions must leave the yarn, thus generating the sensing current. Blue and red spheres represent negative and positive ions, respectively. The plotted potentials are for demonstration purposes.

By integrating the current impulses generated in response to the input force, one can find the amount of charge transferred in response to stress. Figure 6.3a shows the amount of charge transferred when a tension force is applied to the yarn, found by numerically integrating the currents similar to the one shown in Figure 6.2b over a loading half-cycle. At potentials more negative of the PZC, the ion content of the yarn is expected to mainly consist of positive ions, while at positive potentials, the ion content is expected to mainly consist of negative ions. Since an outflow of positive ions and an inflow of negative ions both constitute a positive current by convention, the positive current at negative potentials can show the eviction of the negative ions that are expected to exist within the yarn at such potentials. By the same argument, the negative current at positive potentials could show the outflow of negative ions that are expected to exist within the yarn at positive potentials. This is reflected in the negative sign of the transferred charges in Figure 6.3a, which means that the total charge stored in the yarn always decreases when the yarn is pulled regardless of the sign of the charge on the CNT backbones. According to our theory, the number of ions inside the yarn is smallest at potentials close to PZC and the number of positive and negative ions is roughly equal. Thus changing the mechanical load will result in the expulsion of roughly equal numbers of positive and negative ions, both in small number. This means that the sensor current response around PZC should be very small, which is in fact confirmed by studying the currents in Figure 6.2, and the corresponding charge values in Figure 6.3a.



(a)

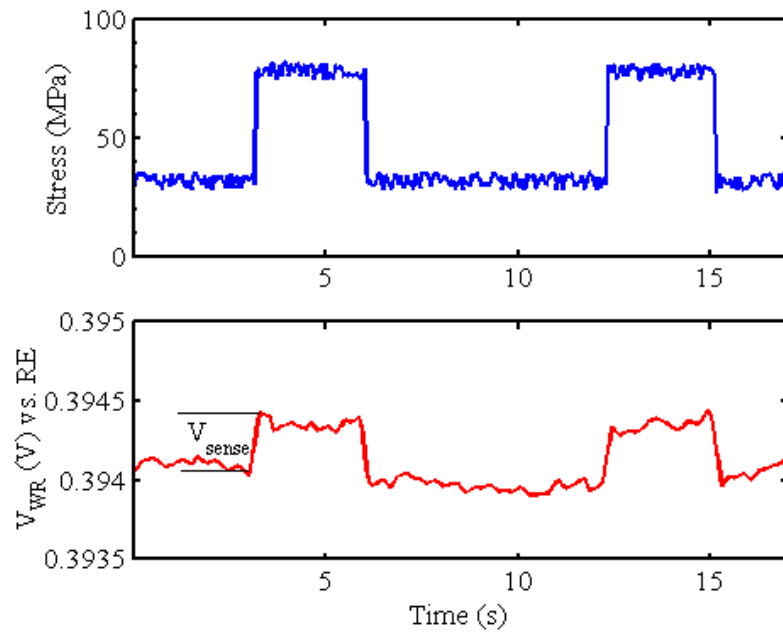


(b)

Figure 6.3: Charge transferred form the yarn in response to tension (a) as a function of the applied bias potential at three loads. (b) Charge transferred at two bias potentials of ± 1 V as a function of the applied strain. The strain values in (b) correspond to the stress values in (a).

A larger charge is transferred when the yarn is pulled at +1 V bias as opposed to -1 V bias (Figure 6.3b). This could be due to the fact that PF_6^- , which is responsible for forming the charge in the double layer at positive potentials, is smaller than TBA^+ , which balances charge at negative potentials. The same change in the volume of the yarn will expel a larger number of ions if the yarn interior is filled with PF_6^- (positive bias, e.g. +1 above).

In open circuit measurements, the magnitude of charge trapped inside the yarn cannot quickly change. When the tension is increased, the overlaps between the diffuse layers of adjacent tubes will increase and the capacitance will therefore decrease. Since at open circuit conditions the stored charge cannot change (or at least not significantly on the timescale of the application of stress), the potential difference across the yarn is expected to increase as the capacitance decreases ($V = Q/C$). The response in Figure 6.4, showing the change in voltage induced in response to a change in stress, qualitatively agrees with the theory.



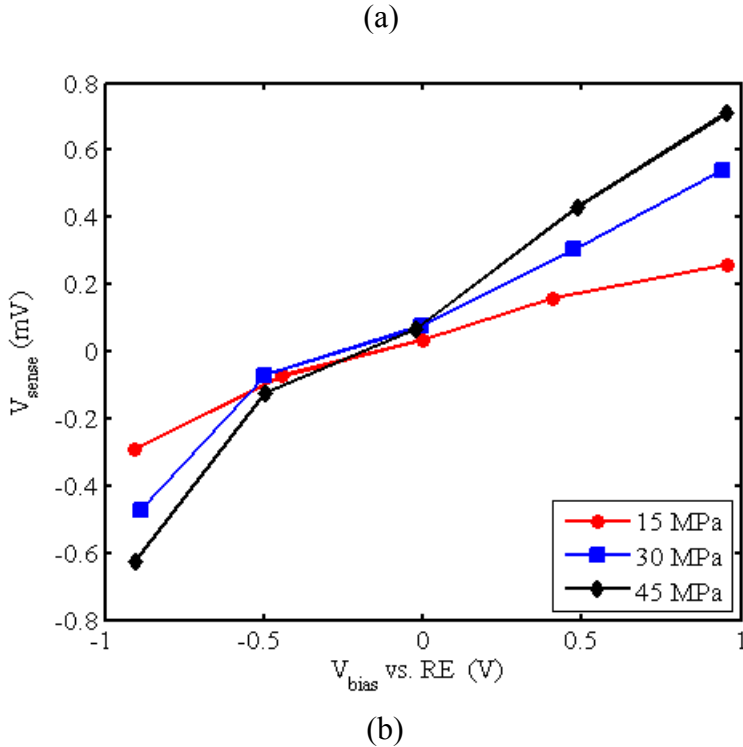


Figure 6.4: (a) Example of the sensor voltage response to the applied stress (b) Sensing voltage as a function of bias at various loads. The lines interconnecting points are to aid with the identification of trends.

Figure 6.5 shows the output sensor voltage as a function of the applied load at various bias potentials. The dependence of the output voltage on load appears to be almost linear. The inset figure in Figure 6.5 shows the slopes of the voltage-load lines plotted as a function of the applied bias potential. This dependency too, turns out to be linear. The maximum sensitivity is achieved at +1 V, with nearly 0.02 mV/MPa sensitivity.

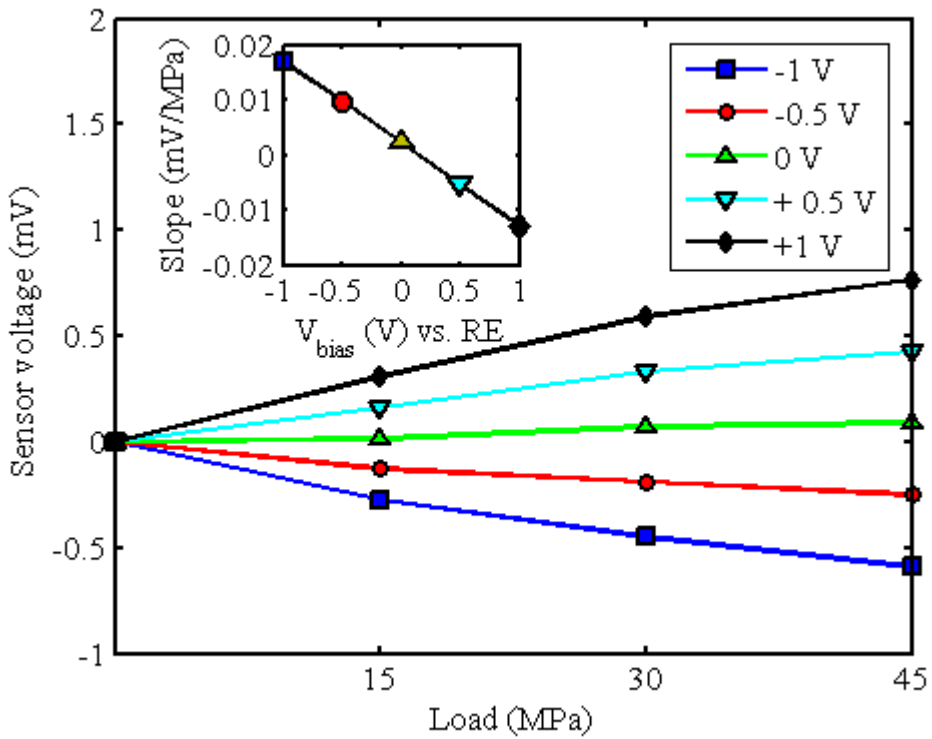


Figure 6.5: Sensor voltage as a function of load at various bias potentials. Inset shows the slopes of fit lines for those five potentials as a function of the applied potential.

In yarn sensors a mechanical input triggers an electrical output. The ratio of electrical output energy to mechanical input energy is one metric by which the effectiveness of the

sensor can be determined. We define this ratio as transduction efficiency, $\eta = \frac{\int_{Q_i}^{Q_f} V.dq}{\int_{x_i}^{x_f} f.dx}$,

integrated over a half cycle. This efficiency is not the same as electromechanical coupling since over a full cycle a significant part of the output energy is provided by the voltage source. Figure 6.6 shows the transduction efficiency in CNT yarn as functions of the change in the mechanical stress and the bias potential. Neglecting the effect of some parasitic currents in the cell, the sensor efficiency can be as high as 22 %. This is due to the fact that the Young's modulus of the yarn is so high and it can withstand relatively

large changes in its load. The creep is two orders of magnitude smaller than the strains induced due to loading. Based on this data, it can be said that higher load does not always lead to higher transduction efficiency. More tests are needed to verify and learn more about this effect.

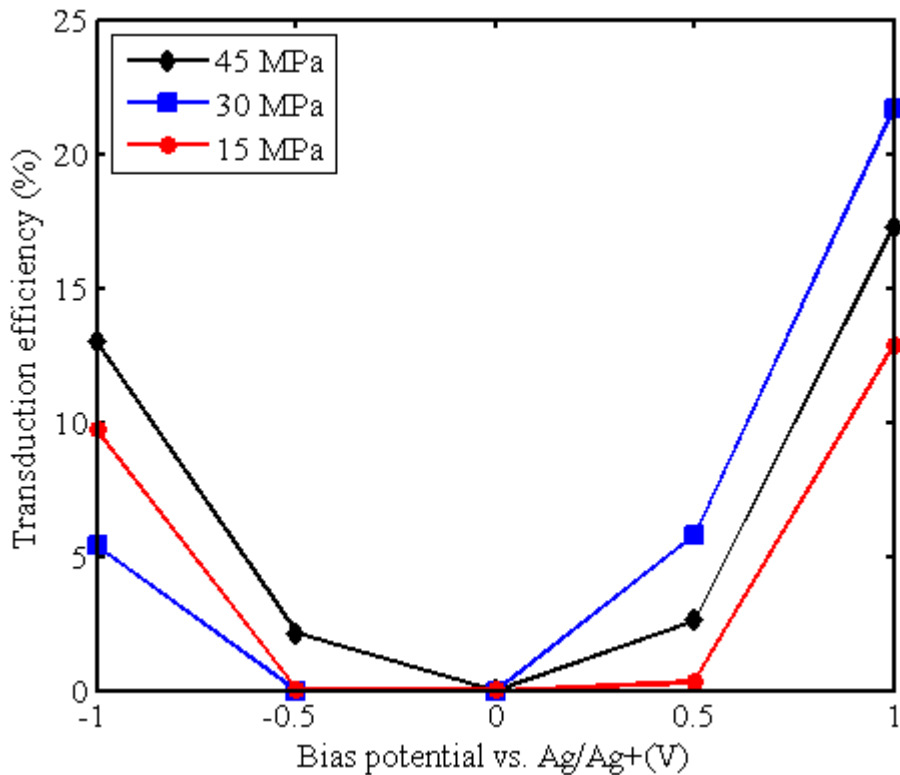


Figure 6.6: Transduction efficiency in charged CNT yarns used as sensors.

6.4. Conclusions

We have shown that twisted yarns of CNTs can be used as mechanical stress sensors and with very high transduction efficiency. The yarns generate a change in current (up to about 1.2 nA/MPa per cm length of the yarn) or the potential difference (up to 0.013 mV/MPa per cm length of the yarn) corresponding to the applied tension force. The transduction efficiency can exceed 20 % in the absence of parasitic currents. Since the

yarns are known to withstand stresses above 800 MPa and temperatures of up to 450 °C in air, they can potentially be used as sensors for high stress and high temperature applications.

References

- [1] M. Zhang, K. R. Atkinson, and R. H. Baughman, "Multifunctional carbon nanotube yarns by downsizing an ancient technology," *Science*, vol. 306, pp. 1358-1361, 2004.
- [2] K. R. Atkinson, S. C. Hawkins, C. Huynh, C. Skourtis, J. Dai, M. Zhang, S. Fang, A. A. Zakhidov, S. B. Lee, A. E. Aliev, C. D. Williams, and R. H. Baughman, "Multifunctional carbon nanotube yarns and transparent sheets: Fabrication, properties, and applications," *Physica B: Condensed Matter*, vol. 394, pp. 339-343, 2007.
- [3] T. Mirfakhrai, J. Oh, M. Kozlov, E. C. W. Fok, M. Zhang, S. Fang, R. H. Baughman, and J. D. W. Madden, "Electrochemical actuation of carbon nanotube yarns," *Smart Materials and Structures*, vol. 16, pp. S243, 2007.
- [4] T. Mirfakhrai, J. Oh, M. Kozlov, E. C. W. Fok, M. Zhang, S. Fang, R. H. Baughman, and J. D. Madden, "Carbon Nanotube Yarns as High Load Actuators and Sensors," *Advances in Science and Technology*, vol. 61, pp. 65-74, 2008.
- [5] Z.-c. Tu and Z.-c. Ou-Yang, "Single-walled and multiwalled carbon nanotubes viewed as elastic tubes with the effective Young's moduli dependent on layer number," *Physical Review B*, vol. 65, pp. 2334071-2334074, 2002.
- [6] J. Hearle, *Mechanics of Yarn*. London, 1966.
- [7] J. N. Barisci, G. G. Wallace, D. Chattopadhyay, F. Papadimitrakopoulos, and R. H. Baughman, "Electrochemical Properties of Single-Wall Carbon Nanotube Electrodes," *Journal of The Electrochemical Society*, vol. 150, pp. E409-E415, 2003.

- [8] Y. Oren and A. Soffer, "The electrical double layer of carbon and graphite electrodes. Part I. Dependence on Electrolyte and concentration," *Journal of Electroanalytical Chemistry*, vol. 162, pp. 87-99, 1984.
- [9] Y. Oren and A. Soffer, "The electrical double layer of carbon and graphite electrodes. Part II. Fast and slow charging processes," *Journal of Electroanalytical Chemistry*, vol. 186, pp. 63-77, 1985.
- [10] H. Gerisher, R. McIntyre, D. Scherson, and W. Storck, "Density of the Electronic States of Graphite: Derivation from Differential Capacitance Measurements," *Journal of Physical Chemistry*, vol. 91, pp. 1930, 1987.

Chapter 7

7 Identification of actuation mechanisms¹

From the results presented in the previous chapters, it was clear that the actuation response contradicted the established theories about the actuation mechanisms in CNTs. Existing theories, which declared the main actuation mechanisms as the expansion of carbon-carbon bond lengths due to charging, predicted an overall expansion for the CNT-based structures due to the expansion of the bonds in the individual CNTs. Although some theories based on quantum calculations predicted contraction in individual CNTs for certain charge levels or charge type, none of them could explain steady contraction in a CNT for both positive and negative charge types. Therefore, the fact that the yarn contracted when it was charged could not be explained by the existing theories.

With no theoretical or experimental evidence for contraction in individual multi-walled carbon nanotubes (MWNTs), the possibility of a structural change in the yarn was investigated as a possible source for actuation. The goal of this chapter is to present analytical and experimental evidence to propose that a change in the structure of the twisted yarn due to the insertion of ion and the interactions between them is the main

¹ A version of this chapter will be submitted for publication: Tissaphern Mirfakhrai et al. “Actuation Mechanisms in Twisted Yarns of Carbon Nanotubes”

cause for actuation. This is shown in section 7.1. Possible mechanisms that can induce this structural change are discussed and evidence is then presented to show that the volume of the ions inserted has a major effect on the magnitude of strain (section 7.2). Based on this assumption, the magnitude of the strain will be calculated and compared with the experimental data (section 7.2.3). It will be shown that the direction, shape, and the order of magnitude of the actuation strain response can be closely predicted using our prepositions. Factors contributing to the deviation of the predicted and experimental responses are discussed in section 7.3. The sensor response, presented in chapter 5, will be also be related to the actuation response following the formalism established in Shoa et al. in section 7.5 [1].

7.1. *Twist effects as mechanism for contractile actuation*

The aim of this section is to establish, based on the literature describing the mechanics of twisted yarns, that a radial swelling in a twisted yarn will lead to change in its twist. If the change of twist is prevented by stopping the yarn from winding or unwinding, the yarn will undergo an axial contraction. Thus if it shown that radial expansion in a charged yarn is plausible, the observed axial actuation can be explained. “The structure of CNT yarns appears to be very different to that of conventional yarns, which is based on classical friction” [2]. On one hand, the yarn is inherently made of CNTs, whose lengths are in the same order of magnitude as that of one turn of twist, and therefore it resembles a staple fibre yarn [3]. On the other hand, it can be argued that due to the interconnectivity among the constituent CNTs, the “effective” fibres forming the yarn are not the individual CNTs, but rather bundles of CNTs. These interconnected bundles can be very long.

Moreover, at about 10000-20000 turns/m, the twist is so high that one can expect to be in the regime where the mechanical behaviour of a staple fibre yarn would resemble that of a continuous filament yarn [3]. For these reasons, it may be justified to use a continuous filament yarn model as a first step in modeling the mechanical and actuation behaviour of CNT yarns. As will be shown in this chapter, there is qualitative agreement of the results predicted using this model with experimental results. Moreover, the fact that only a scaling factor of 4 is needed to make the predicted and experimental results coincide quantitatively, also supports the use of the continuous filament yarn model for the CNT yarns. However, further research and more elaborate models are needed to properly understand the mechanical behaviour of these novel yarns and to fully justify the application of this model to describe actuation.

The first step is to define the nomenclature, after Hearle (1969) [4]:

R = yarn radius (m)

r = radius of the cylinder containing the helical path of a particular fibre (m)

T = yarn twist (turns/m)

h = length of one turn of twist (m)

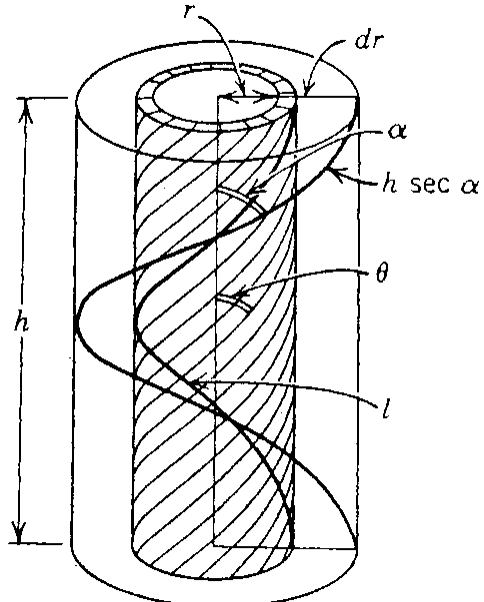
α = surface angle of twist between the axis of a fibre and a line parallel to the yarn axis

θ = the corresponding helical angle at radius r

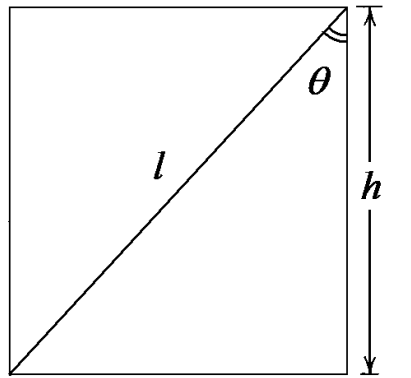
L = length of fibre in one length of twist at radius R

l = length of fibre in one length of twist at radius r

These features are drawn in Figure 7.1a. It should be noted that $h = \frac{1}{T}$.

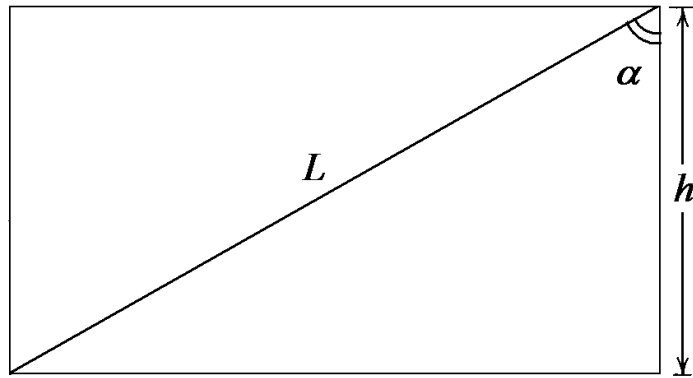


(a)



$2\pi r$

(b)



$2\pi R$

(c)

Figure 7.1: Idealized helical yarn geometry: (a) Idealized geometry (b) “opened-out” diagram of cylinder at radius r , and (c) “opened-out” diagram of the cylinder at radius R (yarn surface)

By cutting the concentric cylinders of Figure 7.1a along a line parallel to the yarn axis,

and then unwinding the cylinders so they lie flat ('opening out' the yarn structure), one can obtain the unwound fibres of lengths l and L shown in Figure 7.1b and c. It then follows that:

$$\begin{cases} l \cos(\theta) = h \\ l \sin(\theta) = 2\pi r \end{cases} \Rightarrow \tan(\theta) = \frac{2\pi r}{h} , \quad \begin{cases} L \cos(\alpha) = h \\ L \sin(\alpha) = 2\pi R \end{cases} \Rightarrow \tan(\alpha) = \frac{2\pi R}{h}$$

Given $R > r$, we can conclude that $\alpha > \theta$.

Therefore a fibre at the surface curls with a larger twist angle compared to a fibre closer to the axis of the yarn.

Now let us assume that for some reason, a yarn with the initial radius of R_0 swells radially (The possible mechanisms for this radial swelling will be discussed in the next section). It means that a fibre that had previously been enclosed in a cylinder with radius R_0 is now at a radius $R > R_0$ (Figure 7.2). If both ends of the yarn are prevented from rotating and changing twist², and assuming that fibres are not going to break away from the yarn, a fibre on the yarn surface must change its twist angle from α_0 to α such that

$\sin(\alpha) = \frac{2\pi R}{L}$. Since $R > R_0$, it follows that $\alpha > \alpha_0$ and therefore $\cos(\alpha) < \cos(\alpha_0)$

(since twist angles are between 0 to 90 degrees). However, the length of the fibre in question is still L (neglecting possible actuation strain in individual MWNT bundles as a result of charging). So the length of a full turn of twist will have to change from h_0 to h , such that $h = L \cos(\alpha) < h_0$.

² We thus assume that the effects of local rotation on yarn length under the explained conditions are small.

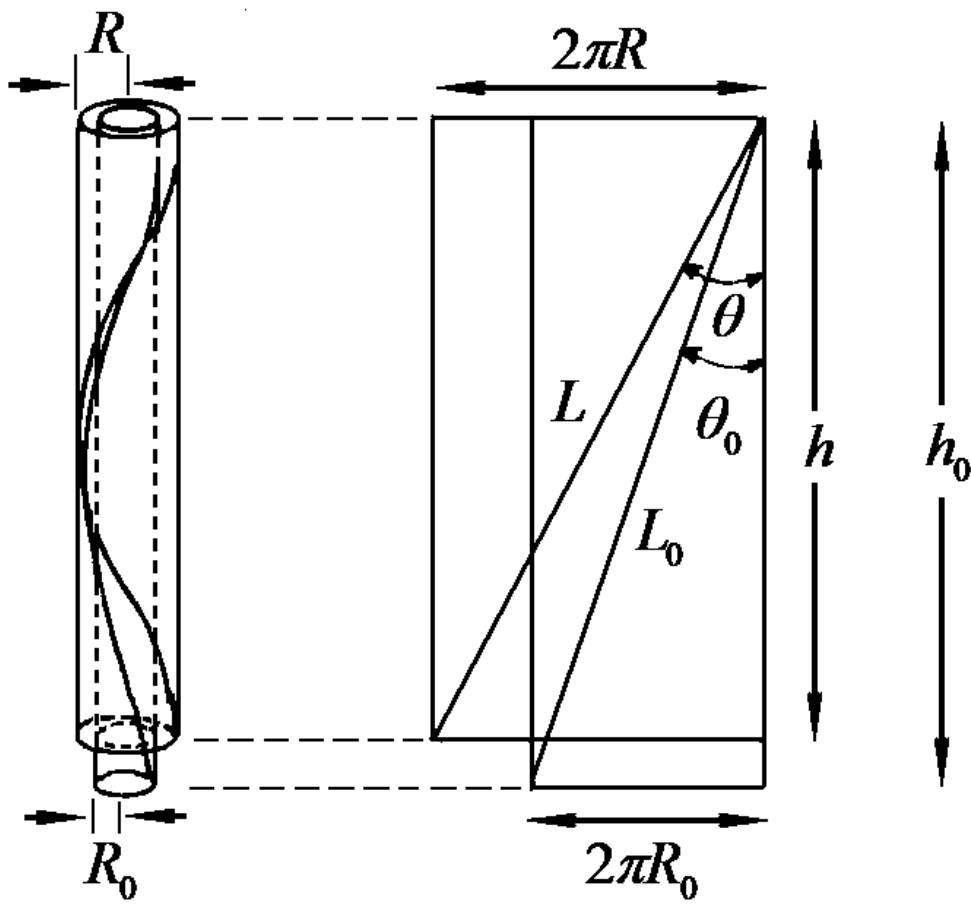


Figure 7.2: axial contraction induced in an idealized twist yarn induced due to radial expansion.

We propose a theory as follows: as a voltage is applied between the yarn and the counter electrode, the ions diffuse into the yarn and cause it to swell radially by a strain of $\varepsilon_R = \frac{R - R_0}{R_0}$. Let us assume that any change in fibre length is negligible such that $L = L_0$, implying

$$\Rightarrow h^2 + (2\pi R)^2 = h_0^2 + (2\pi R')^2 \Rightarrow h_0^2(1 + \varepsilon)^2 + 4\pi^2 R_0^2(1 + \varepsilon_R)^2 = h_0^2 + 4\pi^2 R_0^2.$$

Neglecting higher order terms in strains, we obtain:

$$h_0^2(1+2\varepsilon) + 4\pi^2 R_0^2(1+2\varepsilon_R) = h_0^2 + 4\pi^2 R_0^2.$$

$$\Rightarrow \varepsilon h_0^2 + 4\varepsilon_R \pi^2 R_0^2 = 0$$

Replacing $h_0 = \frac{1}{T_0}$

$$\varepsilon_R = -\frac{\varepsilon}{4\pi^2 R_0^2 T_0^2} \text{ or}$$

$$\varepsilon = -4\pi^2 R_0^2 T_0^2 \varepsilon_R. \quad (7.1)$$

The negative sign means that a radial expansion in the yarn will lead to a contraction in the axial direction. Using typical values of $R_0 = 6 \times 10^{-6} m$, and $T_0 = 15000 \frac{\text{turns}}{m}$, it can be seen that in order to obtain -0.2 % axial strain (as experimentally observed), a radial strain of about 2.9 % is needed.

The above arguments using yarn geometry assumed an idealized continuous-filament twisted yarn, in which well-established equations govern the relationships between the radius and length of the yarn and fibres and the twist. For example, based on Eq. 7.1, the

Poisson's ratio of the yarn is $\nu = \frac{1}{4\pi^2 R_0^2 T_0^2}$. However, SEM measurements of the change in diameter of a dry yarn when axially strained show that Equation 7.1, while qualitatively valid, is quantitatively off by a factor of about 4 [5]. Figure 7.3 shows the experimentally measured Poisson's ratio of the yarn versus what is predicted from equation 7.1. The radial strain is smaller than expected, and shows that the coupling

between the radial and axial directions is about a quarter of what is expected from an ideal yarn. We can therefore speculate that the actuation strain can be expected to be about 4 times smaller than predicted due to this non-ideal coupling. This correction can be added by rewriting equation 7.1 as

$$\varepsilon = -4\pi^2 R_0^2 T_0^2 \lambda \varepsilon_R \quad (7.2),$$

where λ is approximately $\frac{1}{4}$ to account for the non-ideal coupling in the yarn. This approach is equivalent to replacing equation 7.1 with an empirical relationship found from Figure 7.3. The result is a four fold decrease in the predicted actuator strain.

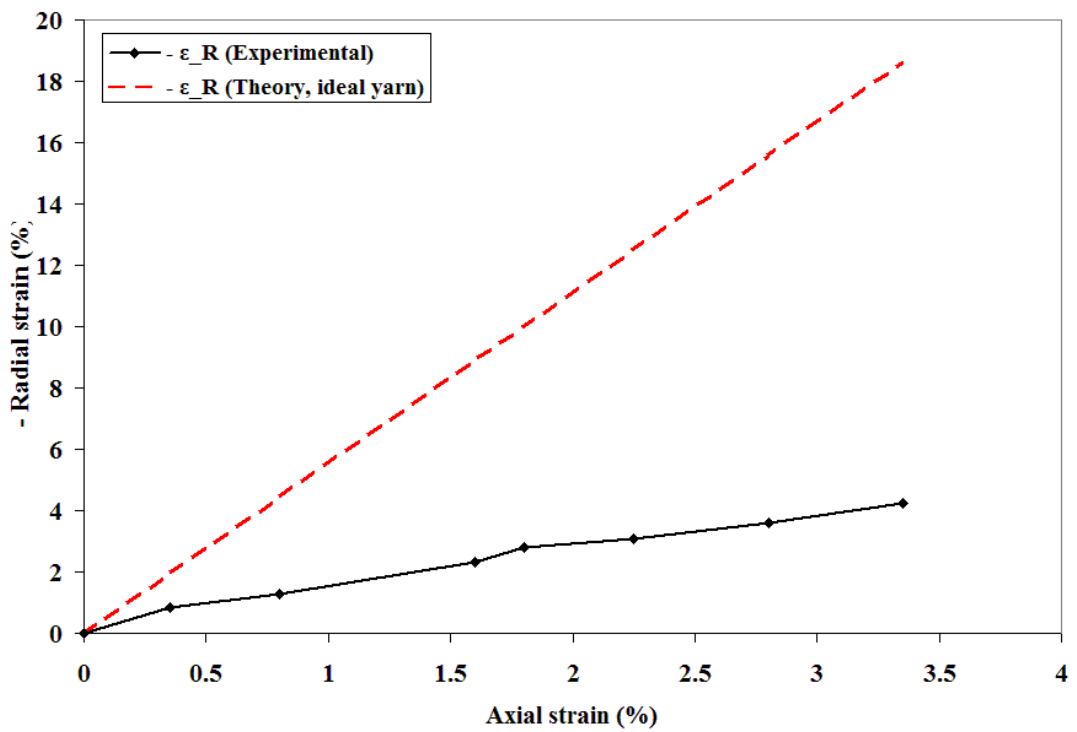


Figure 7.3: The radial-axial Poisson's ratio of the yarn, connected black diamonds show the experimental results from [5] and the red dashed line shows the prediction assuming an idealized twisted fibre yarn.

If at least one end of the yarn is allowed to rotate during this process, the change in twist may take the form of unwinding instead of axial contraction. This effect was recently observed experimentally [6]. As opposed to the experimental setup described in chapters 2 and 3, where both ends of the yarn were clamped and not allowed to rotate, a new setup was designed, such that one end of the yarn was anchored by the “load”, but otherwise allowed to rotate. A 6.5 cm length of yarn was attached to a piece of platinum wire and was suspended in various electrolytes. The load consisted of a rectangular paddle made of MylarTM, glued to a short piece of synthetic thread in a T form (Figure 7.4). This shape was devised to minimize the drag force on the paddle that could be seen affecting the actuation in earlier paddle geometries. The exact T geometry also helped keep the hanging load balanced; it was hard to glue the yarn exactly to the center of the paddle, which meant that the paddle was tilted one way or another, creating an undesired torque on the yarn. The Pt wire was covered in cyanoacrilate to insulate it from the electrically active yarn. Most of the length of the yarn was submersed in the electrolyte to ensure that all of it could contribute to actuation. A few millimetres had to be left out of the electrolyte to make electrical contact through a second piece of Pt wire above the yarn.

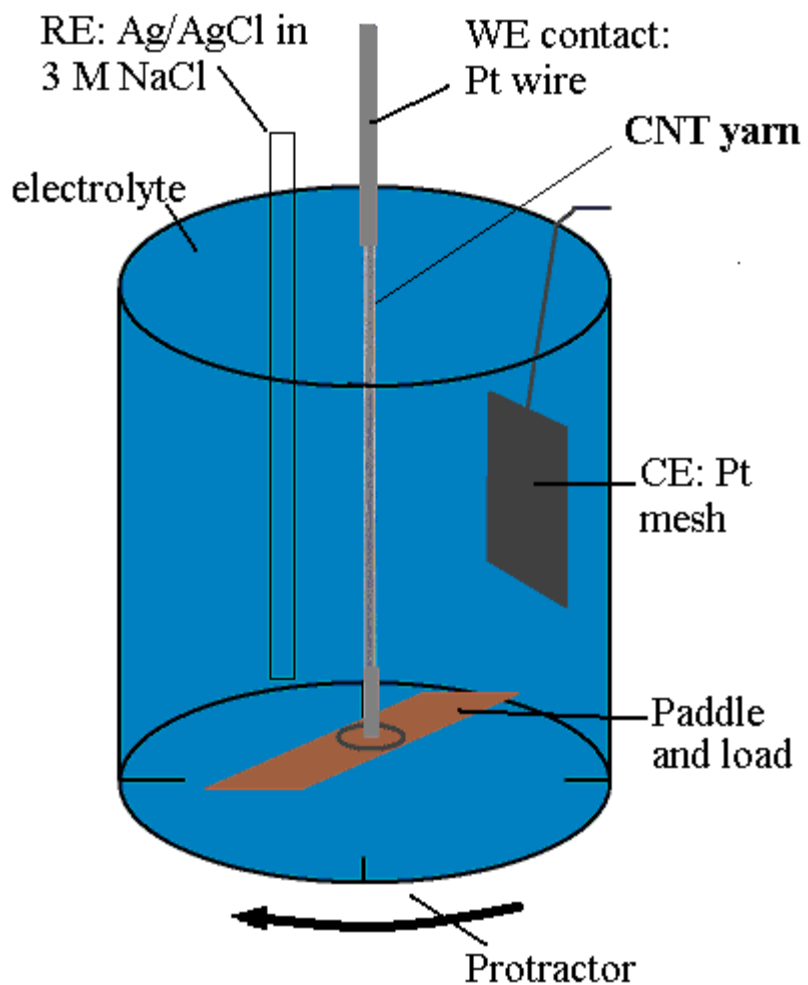


Figure 7.4: Load paddle hanging from the yarn within the experimental cell

A protractor was drawn and attached to the bottom of the vial used for the experiments. A video camera was mounted under the vial to follow the motion of the paddle. A corner of the paddle was painted to facilitate tracking (Figure 7.5). When a potential is applied between the yarn and the counter-electrode, it is observed that the anchor rotates in counterclockwise (CCW) direction, meaning that the yarn is unwinding. The unwinding happens regardless of the sign of the applied potential. When the potential is returned to zero (which is close to the potential of zero charge as discussed in chapter 6), the yarn

rotates in clockwise (CW) direction, although not fully returning to its initial orientation..

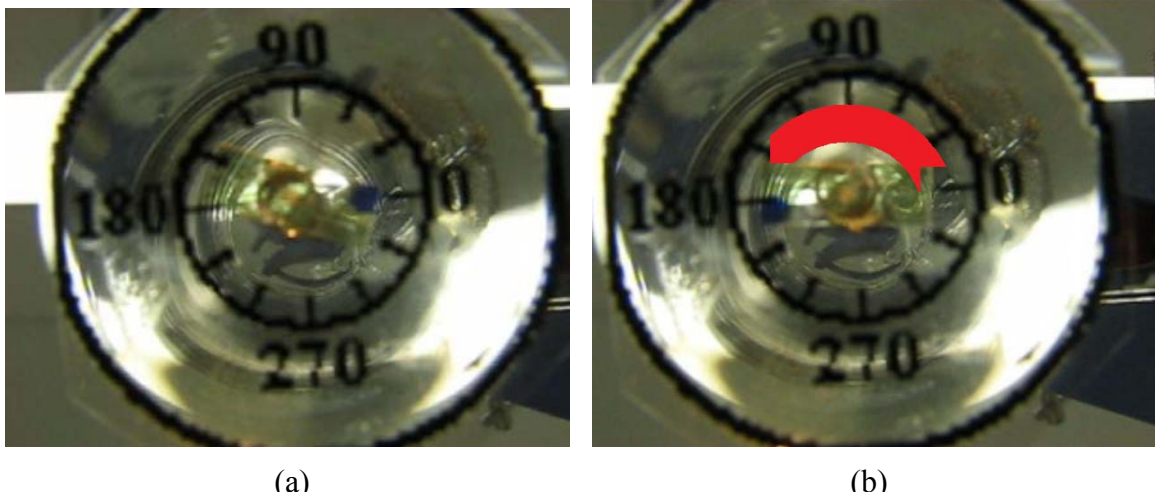


Figure 7.5: the camera view of the cell from underneath, showing the rectangular paddle with its painted corner, and the protractor (a) at the beginning of rotation and (b) during rotation. The painted corner rotates in the CCW direction as the arrow shows.

These effects are exactly consistent with the results reported in chapters 2 and 3. Since the yarn is allowed to rotate in the torsional experiment, the increased twist due to actuation can relax through unwinding; that is the effect that is indeed observed. When the yarn is discharged, it winds back, although usually this rewinding is not complete. This rewinding can be due to the forces between the MWNTs and MWNT bundles forming the yarn, which hold the yarn together. The unwinding and rewinding angles during a few actuation cycles are shown in Figure 7.6. As can be seen in Figure 7.6, the rewinding angle is smaller than the winding angle implying that the restoring forces are not enough to bring the yarn back to its initial state once the actuation force is removed. A possible cause for this effect can be a gradual loss of interconnectivity between the

MWNTs in the yarn that gradually reduces the restoring elastic forces.

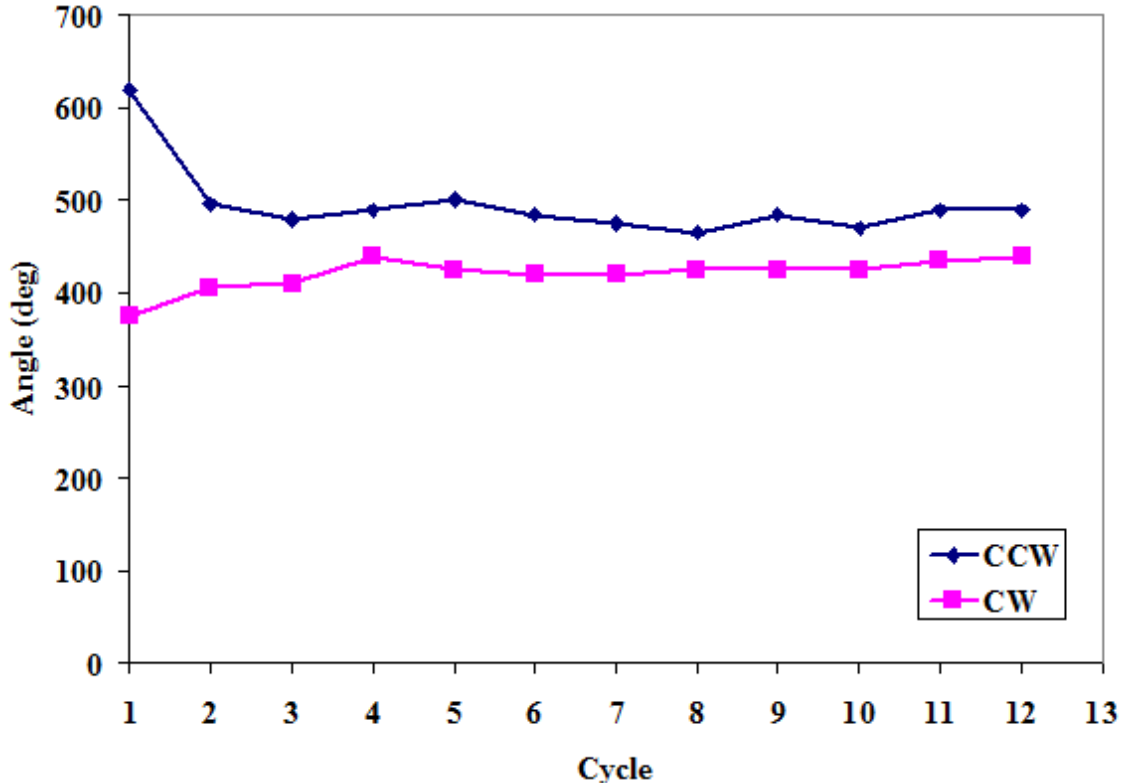


Figure 7.6: Unwinding and rewinding angles for 12 torsional actuation cycles in response to a square wave potential between 0 V and +1 V vs. Ag/AgCl in 3 M NaCl reference electrode, in a 1M aqueous solution of NaCl.

Let us further investigate the quantitative correspondence between the torsional actuation angle and the axial strains reported in previous chapters. As mentioned above, the axial strain in an ideal continuous-filament yarn can be related to the pitch length of the yarn

through $\varepsilon = 100 \times \frac{h - h_0}{h_0}$, where h is the pitch length of the yarn. However, h is nothing

but the inverse of the yarn twist, T . So if ΔT is defined to be the change in twist of the yarn from its original value, T_0 , then:

$$\left. \begin{aligned} \varepsilon &= 100 \times \frac{h - h_0}{h_0} \\ h &= \frac{1}{T} \\ \Delta T &= T - T_0 \end{aligned} \right\} \Rightarrow \varepsilon = 100 \left(\frac{T_0}{T} - 1 \right) \right\} \Rightarrow \varepsilon = -100 \left(\frac{\Delta T}{T_0 + \Delta T} \right) \cong -100 \frac{\Delta T}{T_0}$$

$$\Delta T = \frac{\Delta N}{l_0} \Rightarrow \varepsilon = -100 \frac{\Delta N}{l_0 T_0},$$

where ΔN is the number of times the yarn turns during actuation. If the yarn rotates by an angle of $\Delta\theta$, expressed in degrees, and we replace ΔN by $\frac{\Delta\theta}{360}$ then the equivalent axial strain can be found by:

$$\varepsilon = -100 \times \frac{\Delta\theta}{360^\circ \cdot l_0 \cdot T_0}.$$

For example, as can be seen from Figure 7.6, the average angle of rotational actuation in 1 M NaCl with +1 V pulse is about 450 degrees. This is therefore equivalent to axial strain of

$$\varepsilon = -100 \times \frac{\Delta\theta}{360 l_0 T_0} = -100 \times \frac{450}{360 \times 0.065 \times 20000} \cong -0.09\%,$$

which is of the same order of magnitude as the axial actuation measurement results at similar potentials reported in chapter 2.

The extension of yarn mechanics embodied in equation 7.1 suggests that the observed contraction in the yarn upon charging can be caused by a swelling in the radial direction. Mechanisms that could induce such swelling are now discussed.

7.2. Possible mechanisms for the radial expansion

We have so far shown that a change in the yarn twist takes place during actuation, and argued that if the yarn is prevented from rotating, this change in twist leads to an axial contraction. We have also proposed that a radial swelling in the yarn may explain the aforementioned change of twist. The question, now, is what may be causing this radial strain. In this section, three possible mechanisms will be discussed for this swelling, and based on these discussions, a model will be presented that can reasonably predict the strain-charge and strain-voltage relationships given the mechanical and geometrical properties of the yarn. The three mechanisms are a pneumatic swelling due to gas evolution during electrolysis, double layer repulsion as adjacent nanotubes or bundles in the yarn are charged, or third, swelling that is proportional to the volume of ions and solvent inserted. The latter mechanism agrees best with the observed behaviour.

7.2.1. Pneumatic

Spinks et al. reported a pneumatic mechanism to explain the large actuation strains observed in CNT paper at relatively high potentials in aqueous electrolytes [7]. These strains, which can reach more than 3 % in the longitudinal direction, are explained as being because of swelling in the CNT sheets due to evolution of a gas inside. In the case studied by Spinks et al., this gas was identified as Cl_2 . The potential at which this actuation is observed is consistent with the standard potential of the reactions for forming Cl_2 and O_2 , namely $2\text{Cl}^- \rightarrow \text{Cl}_2 + 2e^-$ at 1.12 V and $2\text{H}_2\text{O} \rightarrow \text{O}_2 + 4e^-$ at 0.99 V vs. Normal Hydrogen Electrode (NHE). In this theory micron-size bubbles are thought to be

formed inside the pores in the actuator, causing it to swell and thus actuate.

As noted by Spinks et al., a signature property of the gas evolution mechanism is the amount of generated gas, and therefore the magnitude of actuation strain, which depends heavily on the concentration of the electrolyte. According to the Nernst equation, the equilibrium half-cell potential of the Cl^-/Cl_2 half-cell reaction decreases with increasing salt concentration. At a given applied potential, a change in the equilibrium potential leads to an increased overpotential at higher electrolyte concentrations. This increase in the over-potential, η , leads to an exponential increase in anodic current from Tafel

equation, $i = i_0 e^{\frac{\eta}{\beta}}$. This leads to larger gas evolution, driving the actuation more strongly. This effect was experimentally observed by Spinks et al., where increasing the concentration of the NaCl electrolyte from 0.1 M to 5 M lead to a 25 fold increase in the size of the actuation strain from 0.1 % to 2.5 %.

To test for this actuation mechanism, the torsional actuation of the yarn was tested in various concentrations of salts. The results for actuation in 0.1 M, 1 M and 5 M aqueous NaCl electrolyte are listed in Table 7.1. This does not show any resemblance to the 25 fold increase observed by Spinks [7]. Also, a dramatic change in strain past the standard potential of the gas evolution reactions was not observed in the torsional actuation experiments. Thus it can be concluded that a pneumatic mechanism is not responsible for the actuation in yarns.

Table 7.1 Rotation angle as a function of electrolyte concentration in torsional actuation experiments

Concentration (M)	Rotation angle (degree)
0.1	400 ± 15
1	700 ± 15
5	700 ± 15

7.2.2. Double-layer forces

It has been known at least since the 1930s that two like-charged objects in close proximity in an electrolyte repel each other despite the screening effect of the surrounding ions [8]. The first comprehensive theory of this repulsion was described in a book by Verwey and Overbeek, based on earlier idea from Landau and Derjaguin [9]. The theory is now known as the DLVO theory after the initials of the four contributors [9, 10]. The classic DLVO theory is a marvel of scientific thinking, which managed to explain many phenomena. In the classic DLVO approach, it is assumed that the concentration of the ions in the electrolyte near a charged planar electrode follows a Boltzmann distribution. Therefore the Poisson equation is solved in conjunction with the Boltzmann equation to find the charge distribution and potential profile in the electrolyte near an electrode. As explained in chapter 1, according to Gouy-Chapman theory a diffuse layer of charge forms at the surface of an electrode submersed in an electrolyte when a potential is applied to the electrode. In this case, the two charged particles act at two electrodes in close proximity. The electrodes will start to interact if they are so close

that their diffuse layers sufficiently overlap. The potentials in the overlapping diffuse layers of the two adjacent electrodes are assumed to linearly superimpose in the region between the electrodes. The CNTs within the yarn act as micro-scale electrodes within close proximity (average distance $\sim 10\text{-}15$ nm). Ions attracted to the charged CNTs store charge in the space between the CNT stands, forming double and diffuse layers. Thus, forces of DLVO nature can repel CNTs away from each other in the radial direction, and thus contribute to radial swelling.

Let us assume that we have two infinite planar electrodes parallel to each other at a distance of d in an electrolyte, with the same potential applied to both (Figure 7.7). Using the above assumptions and based on the DLVO theory, the force per unit area between the two planar electrodes can be shown to be:

$$p = 2n_0kT(\cosh(\frac{ze_0\phi_d}{kT}) - 1), \quad (7.3)$$

where n_0 is the electrolyte concentration in number/m³, k is Boltzmann's constant, T is the temperature, z is the ion valency, e_0 is the fundamental charge, ϕ_d is the potential at the midpoint between the two electrodes, which can be related to the applied potential through numerical computation of some elliptical integrals[10, 11]. The details of this calculation can be found in Appendix 2.

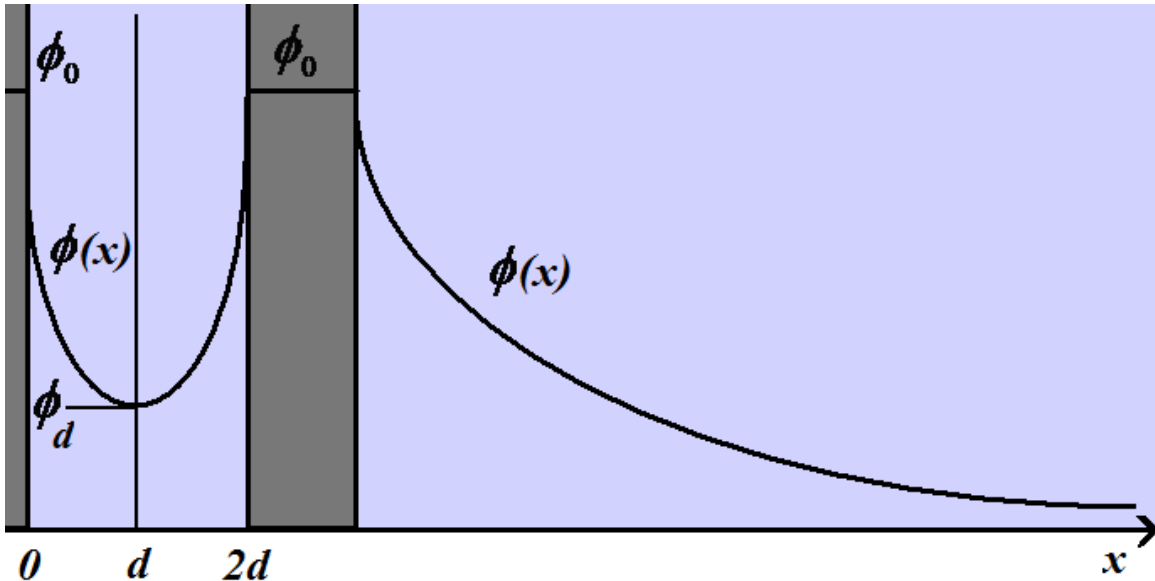


Figure 7.7: Potential profile between and outside two planar electrodes separated by a distance of d in an electrolyte with their double-layers interacting.

Carbon nanotubes do not easily qualify as infinite planes. At the same time, analytically solving for the repulsion force between two cylindrical electrodes using the same principles as above has been shown to be impossible [12]. Considering that the diameter of MWNT bundles forming the yarn is about 50 nm, and the radii of the largest ions involved in our experiments are no more than a 1 nm, it may still be useful to regard the MWNT bundles as planes repelling each other due to charging, and to use equation 7.3 to find stress generated between the bundles. This stress will radially swell the yarn. We have estimated the radial modulus of the yarn to be about 250 MPa³. This was measured using force curves obtained using an atomic force microscope tip pushing on the yarn, immobilized on a glass slide using a thin layer of UV-cured polyurethane. The

³ See Appendix 4

experimental data was interpreted using the method from Butt et al. [13] to find the modulus. Using this information, we can find the strain in the radial direction and therefore find strain in the axial direction using equation 7.2.

Figure 7.8 shows the predicted strain based on the classic DLVO theory. As can be seen in Figure 7.8, the shape of the strain-voltage relationship, although contractile, differs distinctly from Figure 2.9, which shows the experimentally measured strains. The strain-voltage behaviour in Figure 2.9 shows a relatively flat part close to zero, which starts to rise as the potential is increased. This strain reaches 0.5 % (contraction) at higher potentials (-2.5 V vs. Ag/Ag⁺). In contrast, the strain-voltage relationship depicted in Figure 7.8, which is based on the classic DLVO theory, shows a rather sharp V shape in potentials close to zero and saturates as the potential is increased beyond about ±0.3 V. The maximum contractile strain expected based on this model is 1.5×10^{-3} %, more than two orders of magnitude smaller than the maximum strain observed experimentally.

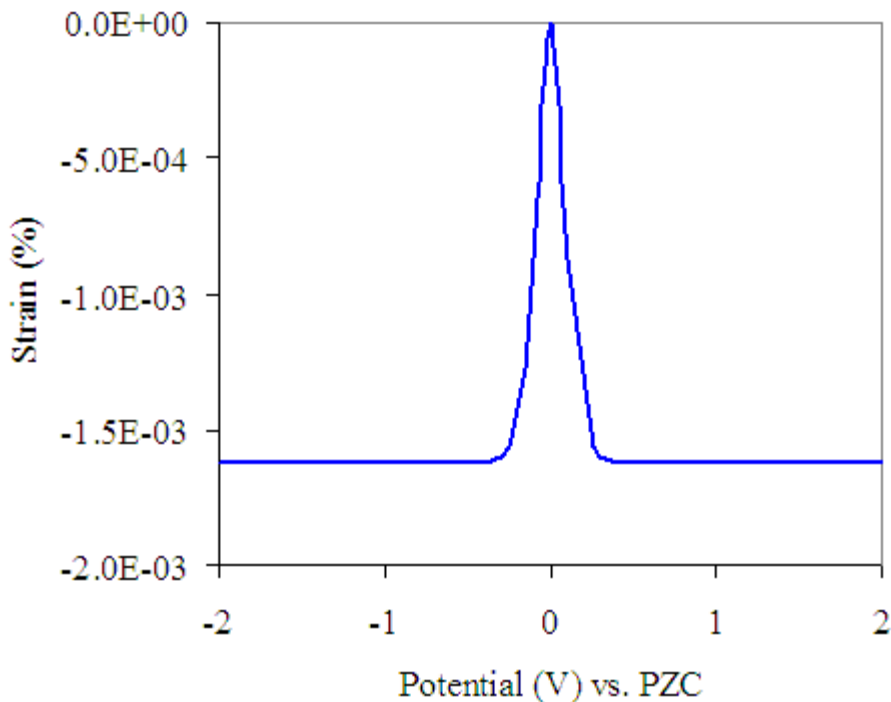


Figure 7.8: Predicted actuation strain in the axial direction as a function of the applied potential based on the classic DLVO theory. The potential of zero charge is taken as zero.

7.2.2.1. Shortcomings of the DLVO theory

The mismatch between predictions of DLVO theory and experimental results is not surprising. It has been known for a long time that the classic DLVO theory has a very limited range of application [14], and in particular the underlying assumptions (including non-interaction of ions, and infinitesimal ion size) make it best suited for low concentrations and voltages. It has also been experimentally observed that there is a high degree of ion specificity, particularly at relatively high concentrations and voltages [9], which is not captured by the DLVO theory. Forces can vary in magnitude by a factor of 50 or more by simply changing the counterion from, e.g., bromide to acetate [11]. Modified DLVO theories that attempt to account for non-idealities struggle to predict the

forces. For example, even with five adjustable parameters, theory often disagrees with experiment at short ranges less than, for instance, 100 Å [17]. The theory does not take into account specific ion effects [8, 9, 11]. Above 0.1 M, the theory “loses all pretence of predictability” [15] [15].

One reason for such mismatch may be because of dispersion forces, i.e. the forces between the solvent and the ions that tend to keep the ions "dispersed" in the solution[15]. The DLVO theory has appeared to work reasonably well for low salt concentrations ($< 5 \times 10^{-2}$ M), where electrostatics dominates. At higher concentrations, however, electrostatic forces that exist between the electrodes at lower potentials are quickly screened by the ions that are abundantly present [15, 16]. Therefore, the dispersion forces on the ions can be expected to dominate electrostatic forces and both the electrostatic and the dispersion forces have to be handled at the same level to obtain a reasonable estimate of the repulsion force[15].

Another shortcoming of the classic DLVO theory is that it assumes ions to be point charges that occupy no space [17]. This assumption is not valid in a system such as our yarn, where the distance between the adjacent electrodes (MWNTs and MWNT bundles) is several nanometres and the radius of an unsolvated TBA⁺ ion is 0.49 nanometres. Therefore, only a few ions can fill in the distance between the CNTs. This no longer complies with the assumptions of the DLVO theory about fitting as many ions as needed to satisfy the Poisson-Boltzmann equations. Yanez and Lange[18] have pointed out that due to the finite size of the counterions, the Debye length cannot decrease to zero as suggested by classical DLVO equations. Feller and McQuarrie have shown that at

small separation distances the double layer repulsion is underestimated when the ions are assumed to be point charges [19]. Their calculations indicate that the additional repulsion is due to the finite size of the ions and might have been the origin of the forces observed that cannot be explained with DLVO theory [20, 21]. The force between charged particles in a solution should not depend on the type of ions involved in the electrolyte, while a clear dependence on ion type has been reported from several experiments, such as the measurements on the viscosity of slurries of various materials such as mica, as well as direct measurements of forces between charged surfaces [19, 22].

These measurements present strong evidence to suggest that the observed repulsion at high concentration is due to counterions acting as a physical barrier to keep the interacting charged particles apart, where the size of the bare ion is the dominant feature that controls the extent of the repulsion at high ionic strength [22]. We propose that in the present case, the charged particles that are the CNTs or CNT bundles. These particles are pushed apart by the ions with forces greater than what is predicted by the DLVO theory, giving rise to the strain-potential behaviour depicted in Figure 2.9. In the next section, we show a relationship exists between the observed actuation strain and the size of the ions, and go on to quantify the relationship between the observed strain and the applied potential using equation 7.2.

7.2.3. Ions as physical barriers

We have shown that the classic DLVO theory fails to predict the magnitude of actuation strain and its dependence on the applied potential in CNT yarns. Based on the literature, we have also indicated that at increasing concentrations and voltages ion size

becomes important. It is possible that ion size is the primary determinant of volume change. Let us now see if the volume of the ion contributing to actuation has any effect on the measured actuation strains. Such correlation between the strain-to-charge ratio and ion size has been reported for conducting polymer actuators. Madden showed that the amount of volumetric strain in polypyrrole actuation is similar in magnitude to the volume of the ions that intercalate into the polymer during charging [23]. Kaneto et al. studied polypyrrole film actuators in a variety of electrolytes and concluded that that actuation stroke depends linearly on the radius of the intercalating ion, except for the case of BF_4^- ion [24].

Our goal is to establish a relationship between the actuation strain and the total volume of the ions that enter the yarn actuators at a given potential. There are values in the literature for the radii and volumes of most of the ions used in our experiments. Because all ions used are monovalent, if we know the amount of charge that enters the yarn at a given potential, we can find the number of ions involved by dividing the total charge by the charge of one ion, i.e. $\pm|e|$, where e is the charge of an electron. In making this statement, we have assumed that at potentials positive of the presumed potential of zero charge, only negative ions are present and move into the yarn, and similarly, that at potentials negative of the presumed potential of zero charge, only positive ions are present and move into the yarn. This is in agreement with Gouy-Chapman theory, which predicts an exponential decrease in the concentration of the ions of the same sign as the charge on the electrode in the vicinity of the electrode surface with increasing applied potential. The Gouy Chapman theory predicts this concentration to become infinitesimally small at potentials

higher than a few tens of millivolts. Although we have argued that the Gouy-Chapman theory may not be strictly valid in our case, it is probably safe to assume that in the absence of specific adsorption the concentration of ions of the same charge type as the electrode charge will drop quickly toward zero as the electrode potential is increased away by e.g. 200 mV from the PZC.

7.2.3.1. Dependence of the stored charge on applied potential

While the transferred charge during actuation at a given potential has been calculated by integrating the experimentally-measured current, this value has the disadvantage of including the charge that may have been consumed due to parasitic reactions at the electrode, and thus not having contributed to the volume change and actuation of the yarn. We therefore believe that using the estimate of the system capacitance using EIS, described in Chapter 6, is a more reliable way to find the charge stored, since the parasitic charge is separately accounted for in that model. This way, the stored charge at every potential can be found by multiplying the capacitance by the applied actuation potential.

As shown in Chapter 6, the capacitance of the yarn in the acetonitrile electrolyte depends on the bias potential at which it has been evaluated. The electrochemical capacitance of the yarn was estimated using two methods in Chapter 6, both using EIS. The results of those estimates were shown in Figure 6.10d, but are reproduced here as the circles and squares in Figure 7.9. As in Figure 6.10d, the squares show the results obtained from the CPE-based model in Figure 6.5a, while the circles show the estimate based on directly fitting the RC circuit in Figure 6.5b. The two sets of capacitance values are quite close at most bias potentials and show identical trends. To simplify the computation, we use

the average of the two values in Figure 6.10d as the true capacitance at each potential.

The average is shown as the triangles in Figure 7.9.

The average capacitance (triangles) seems to increase with the magnitude of potential difference from PZC. This behaviour is independent of the sign of the potential. The possible reasons for such a dependence of capacitance on potential have been discussed in Chapter 6. The triangles lie approximately on two straight lines, intersecting near zero potential, and will be hereafter referred to as the gravimetric capacitance of the yarn.

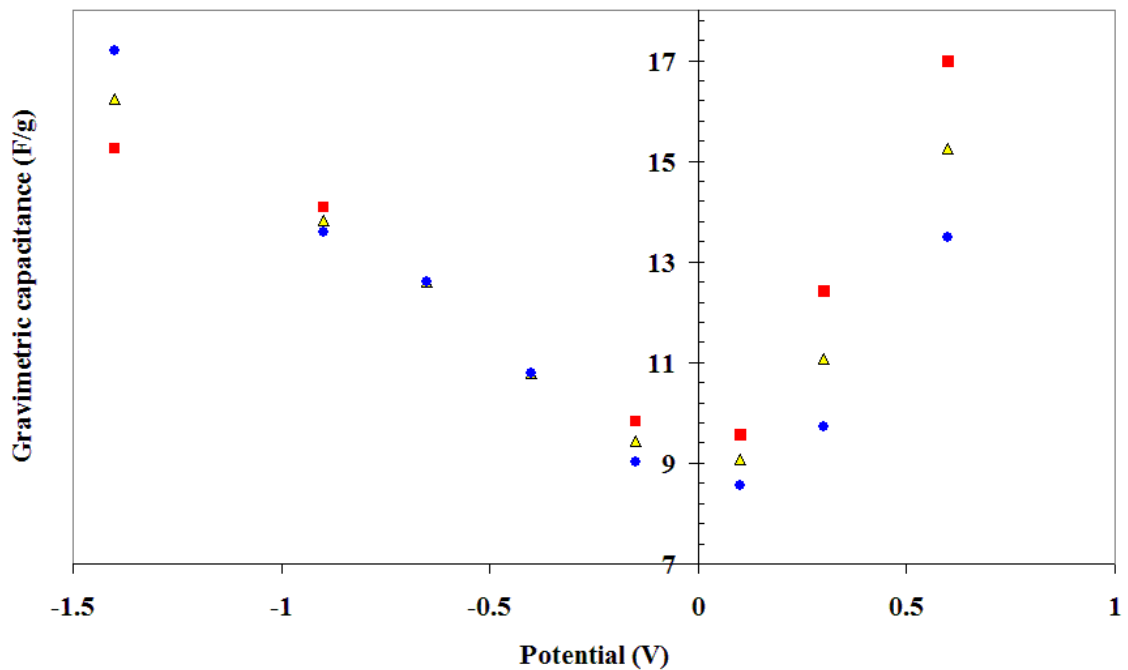


Figure 7.9: Gravimetric capacitance of the yarn sample as a function of the applied bias potential. The red squares and blue circles show the capacitance estimates based on the two methods discussed in chapter 6, and are the same as in Figure 6.10d. The triangles show the averages between the gravimetric capacitances found using the two methods.

The potential range studied in Figure 7.9 is smaller than that employed in actuation

experiments in chapter 2. Let us assume that the linear relationship between capacitance and potential observed in Figure 7.9 extends over the potentials used in experiments in chapter 2 (-2.5 V to +2.5 V). The validity of this extrapolation is supported by the direct measurements of the transferred charge during actuation at higher potentials, after having subtracted the estimated charge due to steady-state parasitic currents. The gravimetric capacitance of the yarn in an aqueous electrolyte was also measured in Chapter 6 and found to be largely independent of the applied bias potential. This information will now be used to find the strain to charge behaviour for Na^+ and Cl^- ions in an aqueous environment and for tetrabutylammonium ion ($(\text{N}(\text{CH}_3)_4)^+$, or TBA^+) and hexafluorophosphate (PF_6^-) ions in acetonitrile.

7.2.3.2. Strain to charge relationship for various ions

By multiplying the capacitance thus estimated by the applied potential, the stored charge in the yarn at each bias potential can be found. Since the strain at every given potential is known, the strain-to-charge relationship for each ion and electrolyte can be found. The axial strain-to-charge relationship shows a linear relationship between charge (and thus ion number) and strain (Figure 7.10). The slope of this line is different for each ion. It should be noted that the measurements with Na^+ and Cl^- ions were performed in water, and those for tetrabutylammonium ion ($(\text{N}(\text{CH}_3)_4)^+$, TBA^+) and PF_6^- in acetonitrile⁴.

⁴ The results from the acetonitrile-based electrolyte are those presented in Chapter 2. The results from the aqueous electrolyte are from similar experiments in water.

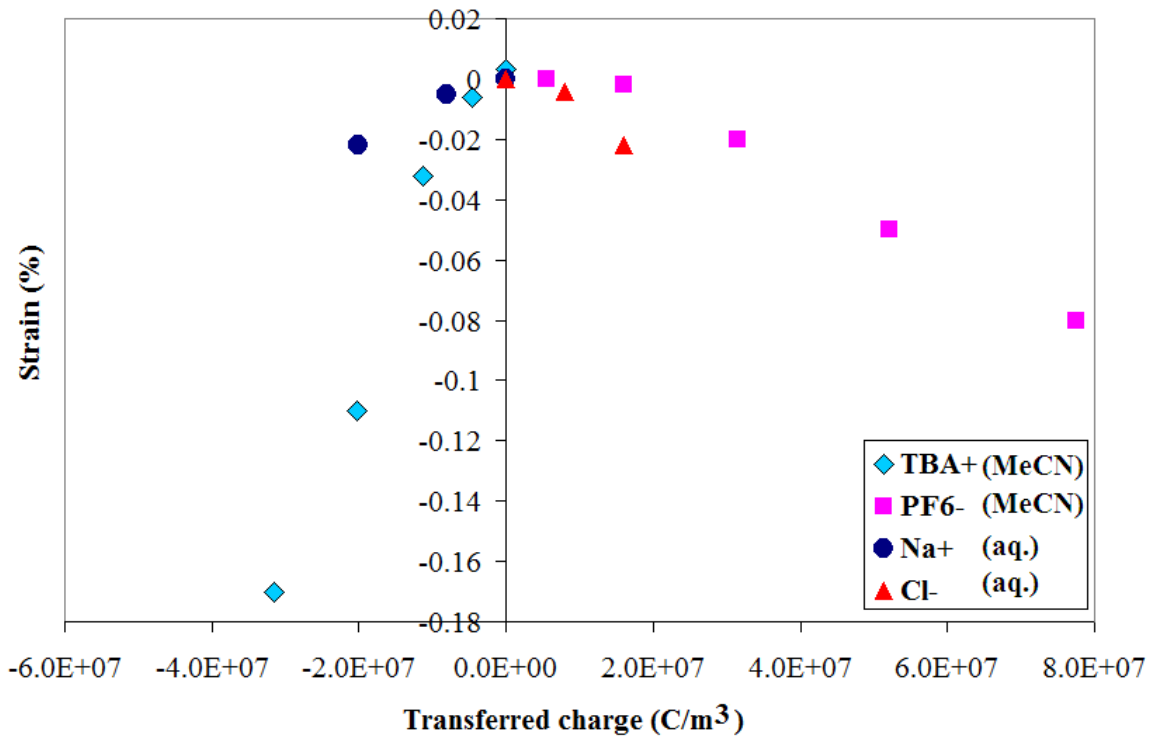


Figure 7.10: Strain to charge relationship in the yarn for various ions. TBA^+ and PF_6^- were measured in acetonitrile as solvent, while Na^+ and Cl^- were measured in water.

7.2.3.3. Strain to volume relationship

It can be seen from Figure 7.10 that the magnitude of the slope of the strain-to-charge line for the tetrabutylammonium ion is larger than the rest. It is also known that the TBA^+ ion is the largest ion among them all. Therefore, it is possible that a relationship exists between the ion size and the strain-charge relationship. All of the above-mentioned ions are monovalent ions. The total number of ions transferred during actuation can be estimated by multiplying the transferred charge by the volume of one ion, and then dividing by the charge of an electron. If the unsolvated ion sizes from the literature are used [25, 26], the strain-volume relationships that result from the above strain-charge relationships are as shown in Figure 7.11.

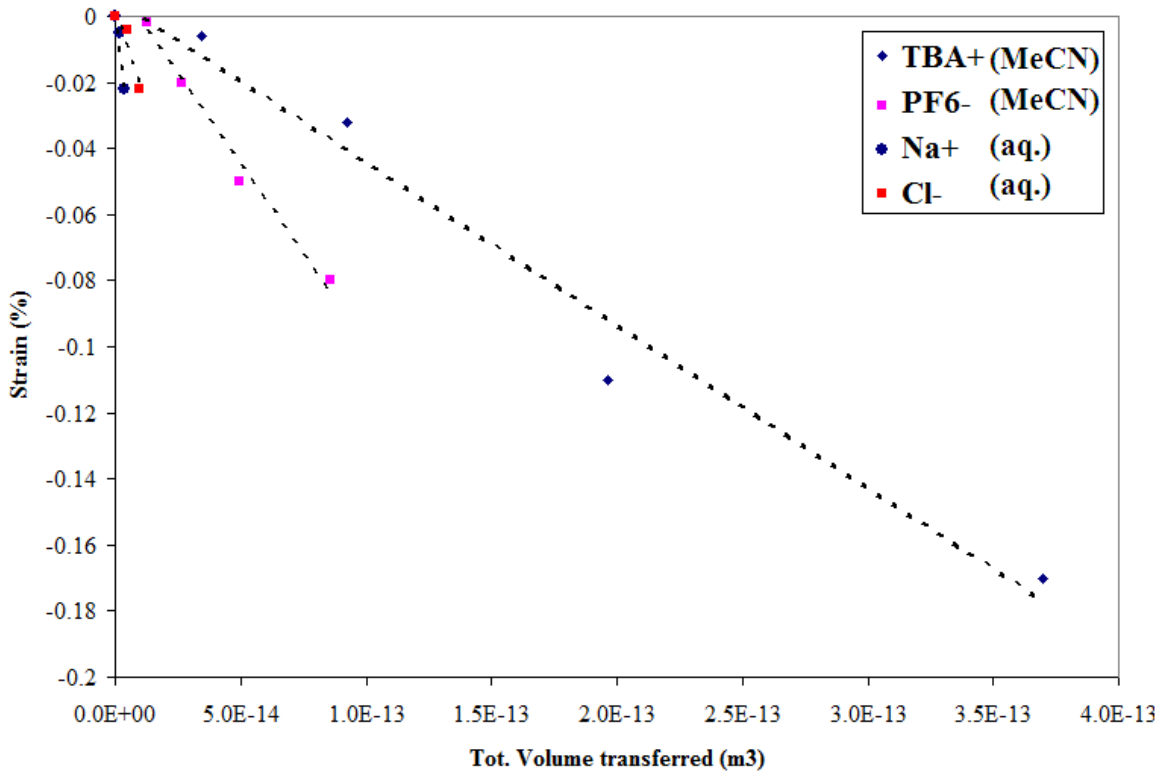


Figure 7.11: Actuation strain versus volume of unsolvated ions transferred during actuation. Dashed lines show linear fits to the data.

If strain is directly proportional to the volume of inserted ions, one would expect all slopes to be the same in Figure 7.11. They clearly are not. However, most ions carry some solvent with them, usually referred to as hydration/solvation sphere. The hydrated radii of Na^+ and Cl^- ions were found from the literature to be 3.58 and 3.31 Å, respectively [27]. The radii of the unsolvated PF_6^- and TBA^+ ions are known to be 2.53 and 4.94 Å, respectively [28]. It is assumed that a large ion like TBA^+ is not solvated in acetonitrile due to its size, and that PF_6^- is also poorly solvated [29]. Thus the solvated and unsolvated radii for TBA^+ are taken to be the same. If we use the solvated volume of ions transferred into the yarn to plot the strain-volume relationship, Figure 7.12 is obtained. This solvated strain-volume plot shows a nearly linear relationship between the

actuation strain and the total transferred volume of ions.

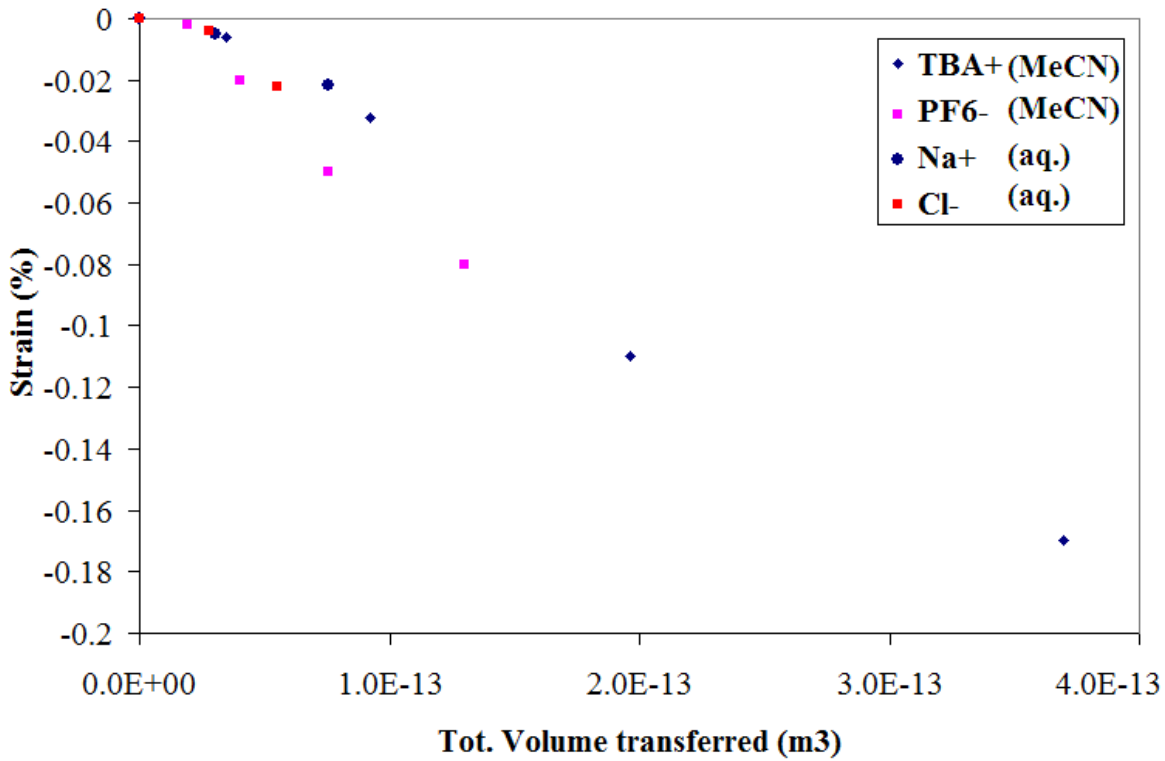


Figure 7.12: Actuation strain versus the volume of solvated ions transferred during actuation.

Let us see if this behaviour can be explained based on yarn geometry. The total volume of the yarn before actuation can be found using $V_{y0} = \pi R_{y0}^2 l_{y0}$, where R_{y0} and l_{y0} are the radius and length of the yarn prior to actuation. The volume of the yarn after actuation can be found as

$$V_y = \pi R_y^2 l_y = \pi R_{y0}^2 l_{y0} + \Delta V, \quad (7.4)$$

where ΔV is the total volume of the ions and solvent added. At the same time, we know that $R_y = R_0(1 + \varepsilon_R)$ and $l_y = l_0(1 + \varepsilon)$. Substituting in 7.4 and neglecting higher order terms leads to the expression

$$\pi R_0^2 l_0 (2\varepsilon_R + \varepsilon) \cong \Delta V. \quad (7.5)$$

Equation 7.2 states that $\varepsilon = -4\pi^2 R_0^2 T_0^2 \lambda \varepsilon_R$ or $\varepsilon_R = \frac{-\varepsilon}{4\pi^2 R_0^2 T_0^2 \lambda}$. Substituting in equation 7.5 to obtain the axial strain as a function of the change in volume yields

$$\varepsilon \cong \frac{\Delta V}{\pi R_0^2 l_0 \left(1 - \frac{1}{2\pi^2 R_0^2 T_0^2 \lambda}\right)}. \quad (7.6)$$

Assuming that the change in volume is directly proportional to the number of ions inserted, then according to equation 7.6, axial strain is also directly proportional to ion number, matching qualitatively at least the observed strain to ion density relationship shown in Figure 7.12.

Equation 7.6 is now used to construct a strain-voltage relationship that is applied to describe actuation in the TBAPF₆ electrolyte. The predicted response is compared to observed actuation results presented in Chapter 2.

7.2.3.4. Strain-bias potential relationship

In order to estimate the total volume transferred during actuation for use in equation 7.6, one should know the total amount of stored charge and the effective size of ions and their solvation spheres. However, the charge measured during actuation experiments in chapter 2 is an overestimate of the total charge stored within the yarn, because it also includes charges lost due to parasitic reactions in addition to the stored charge. The change in stored charge is estimated from the product of the voltage change and the capacitance values extracted using fits to the experimental data presented in Figure 7.9.

Given the potential applied to the yarn, the product of the change in voltage and the capacitance of the yarn is now used to estimate the amount of charge stored in the

yarn during actuation. Knowing the stored charge, it is assumed that only one ion type carries the charge into the yarn, and that the dominant charge carrier is determined by the sign of the voltage relative to the potential of zero charge – i.e. negative ions (PF_6^-) enter at potentials above the PZC, and positive ions ($(\text{N}(\text{CH}_3)_4)^+$) below. This assumption is not accurate, since at the potential of zero charge there are equal numbers of positive and negative ions inside the yarn, assuming monovalent anions and cations. Therefore, at potentials close to PZC, transferring charge to the yarn can happen due to intercalation of ions of one type of charge or the departure of ions of the opposite charge. The strain-charge dependence can be found from Figure 7.10. We can combine the data from those two figures to find the strain-applied potential relationship.

Figure 7.13 shows the strain-potential relationship thus obtained. The blue circles represent the predicted strain, while the red triangles show the experimentally measured values as reported in chapter 2. As can be seen in Figure 7.13, our model correctly predicts the direction, shape, and the order-of-magnitude of the actuation strain. However, the predicted strain is about 7 times larger than the measured strain. There are several likely explanations for this seemingly large discrepancy. These include the inhomogeneous packing of CNTs in the yarn, and mobility of both ions at potentials close to PZC, as are now discussed.

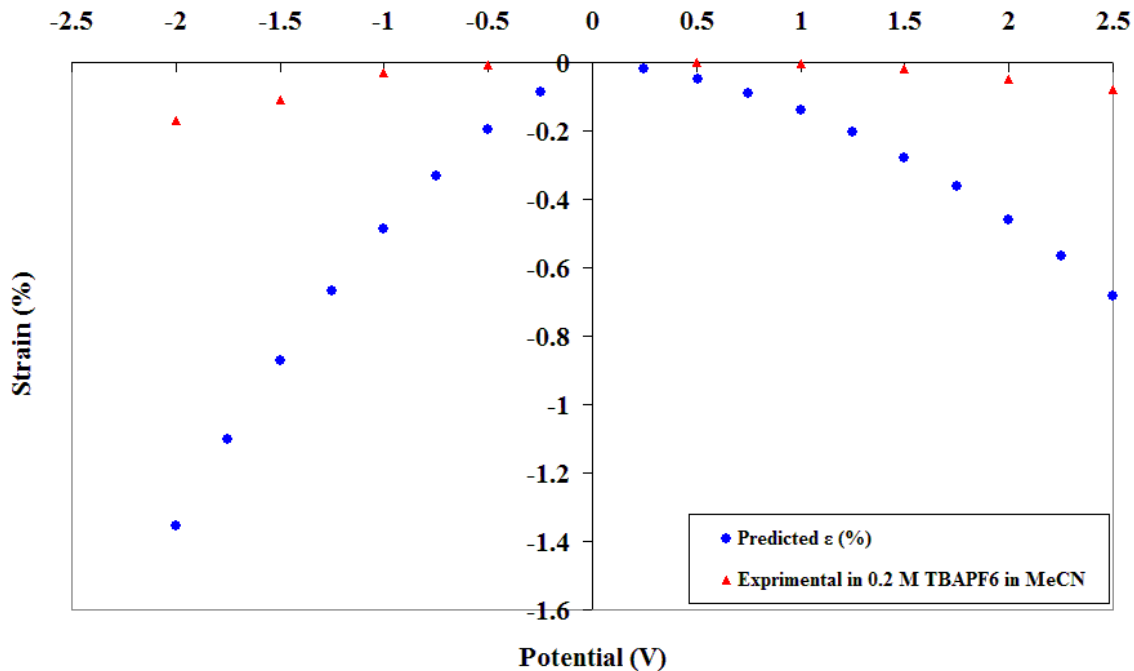


Figure 7.13: Actuation strain as a function of the applied bias potential. The presumed PZC is the zero of the potential axis.

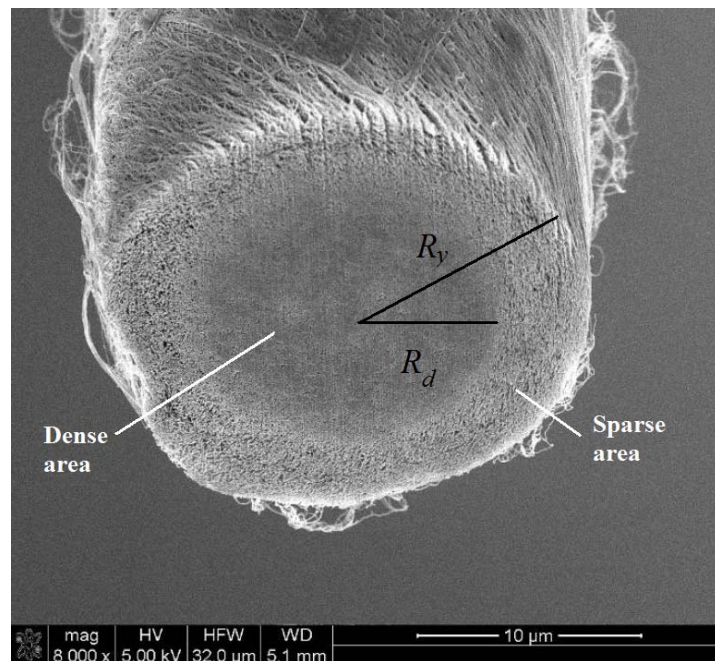
7.3. Possible causes of the overestimation of the actuation strain

7.3.1. Non-uniform packing density and radial structure of the yarn

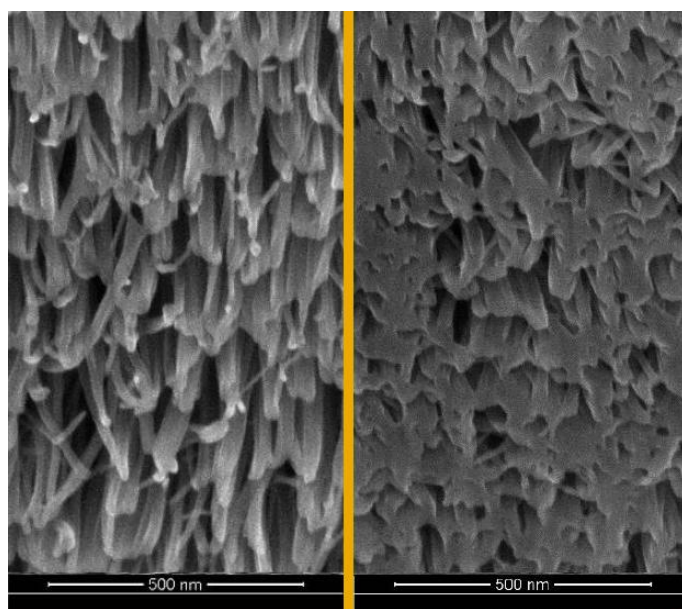
The inhomogeneity of the yarn is a very recent discovery. The packing of the CNTs in the yarn had been a question since the beginning of this research. Based on the measured density of the yarn ($\sim 800 \text{ kg/m}^3$) and the density of the CNTs (estimated to be about 1400 kg/m^3), the average distance between the CNT fibres in the yarn was calculated to be about 15 nm. However, close up SEM images of the yarn surface, such as those shown in chapter 6, showed a much larger distance between the CNTs. Various microtomy techniques were tried to expose and image the cross-section of the yarn with no

success. It seemed that no ordinary cutter could cut through CNTs to expose a clear cross section of the yarn. This enigma of the missing nanotubes was resolved by investigators at the Commonwealth Scientific and Industrial Research Organisation (CISRO) in Australia, who cut the yarn using a focused ion beam (FIB) and image it, as shown in Figure 7.14⁵.

⁵ We thank Mr. Ken Atkinson for permitting to use his SEM images of the yarn cross section.



(a)



(b)

Figure 7.14: (a) Scanning electron micrograph of the cross-section of a twisted CNT yarn with a diameter of about 20 µm, showing a dense core and a sparse outer ring. (b) close-up micrographs of the sparse and dense parts of the same yarn (images courtesy of Ken Atkinson, CISRO).

Figure 7.14a shows the cross-section of a yarn with the diameter of about 20 microns. It can be seen from Figure 7.14 that the yarn consists of a very dense core with a sparse surrounding ring. Figure 7.14b shows close-up images of the dense and sparse areas. Image processing techniques applied to Figure 7.14b suggest that the center of the yarn is about 4 times more densely packed compared to the outer sparse region. This change in the density of packing not only accounts for the discrepancy between the predicted inter-tube distance and the measured distance between the tubes on the yarn surface, but also has implications for actuation. We hereby present evidence that implies that only the outer, sparse, part of the yarn actuates during regular actuation response, with the inner, denser part resisting against the actuation. This effect reduces the resulting actuation strain. The quantitative magnitude of this will be discussed later.

7.3.1.1. Potential dependent ‘creep’ or two-phase actuation response

It had been previously observed that the actuation response of the yarn to a potential step input (Figure 7.15a) is in the form of a sudden contraction upon the application of the step, followed by further contraction at a slower rate (Figure 7.15b). The actuation strain studied throughout this thesis refers to this sudden dimensional change, and not the slow part that follows. The slow dimensional change, that is mostly reversible, has been referred to as ‘potential-dependent creep’, since it resembles dimensional changes due to mechanical creep, but its extent and rate seems to depend on the applied potential⁶. The

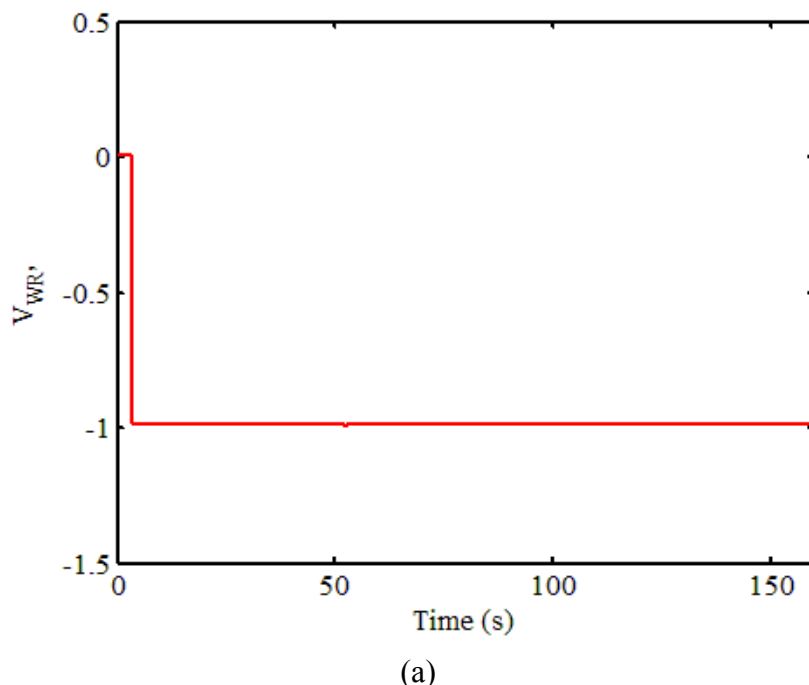
⁶ See chapter 8 about various sources of creep in CNT yarns.

fact that the yarn keeps contracting as opposed to expanding, further confirms that this slow response cannot really be mechanical creep⁷.

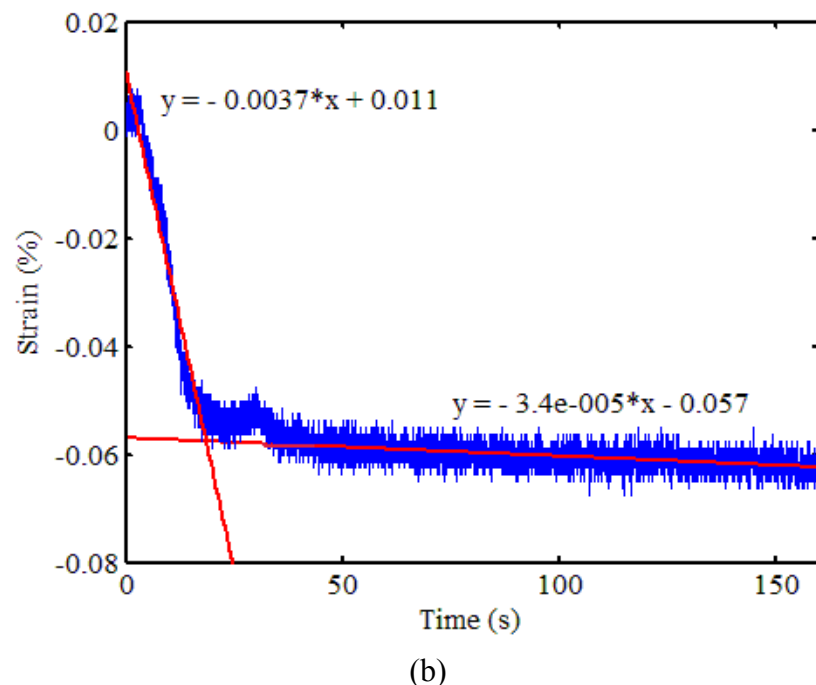
The two-phase radial structure of the yarn provides an explanation for this. When the potential is applied, the outer sparse part of the yarn is charged and contracts due to the yarn geometry as discussed above. However, the middle, denser part of the yarn is not charged, since ions cannot quickly penetrate the structure due to its compact nature. Therefore, the stiffness of the middle core acts against the actuation force, limiting its extent. The slow dimensional change will thus be explained as the gradual diffusion of ions into the dense core of the yarn that causes it to contribute to the actuation.

Assuming that the fibers in the dense and sparse parts of the yarn are generally identical, and considering the quadruple packing density of fibers in the dense part compared to the sparse part, the elastic modulus of the inner dense part will be higher than that of the outer sparse part. Given the elastic modulus of the yarn (from measurements in chapter 2) and using a form of the law of mixtures, we can estimate the elastic moduli and the stiffness values of the dense and sparse parts of the yarn.

⁷ Creep in CNT yarns may have other mechanisms as well, which need further studying. Some of these mechanisms are discussed in Chapter 8 as future directions for research.



(a)



(b)

Figure 7.15: (a) step potential applied to a yarn sample in 0.2 M TBAP in MeCN electrolyte and (b) the yarn actuation strain response to the potential profile in (a), which shows a fast contraction, followed by a slow contraction. The red lines in (b) show linear

fits to the two segments of the strain response, the fit equations for which are presented.

7.3.1.2. Effect of the inhomogeneous yarn packing on actuation

Let us assume that only the sparse part of the yarn actuates. Let us define Y_s and Y_y as the elastic moduli of the sparse part of the yarn and the overall yarn, respectively, and R_d is the radius of the dense core. Following arguments based on the volumetric change similar to the above, but this time only applied to the outer sparse part of the yarn, the actuation strain can be calculated as:

$$\varepsilon_{act} = \frac{Y_s}{Y_y} \frac{\Delta V}{\pi R_{y0}^2 l_0 \left(1 - \frac{2}{4\pi^2 (R_{y0}^2 - R_d^2) \lambda T_0^2}\right)} . \quad (7.7)$$

For the derivation of this formula, please see the appendix. The predicted strain is plotted in Figure 7.16, along with the experimentally measured strain. The agreement between predicted and experimental results is now excellent, especially at higher potentials. We shall now try to address the possible cause of the small discrepancy at lower potentials.

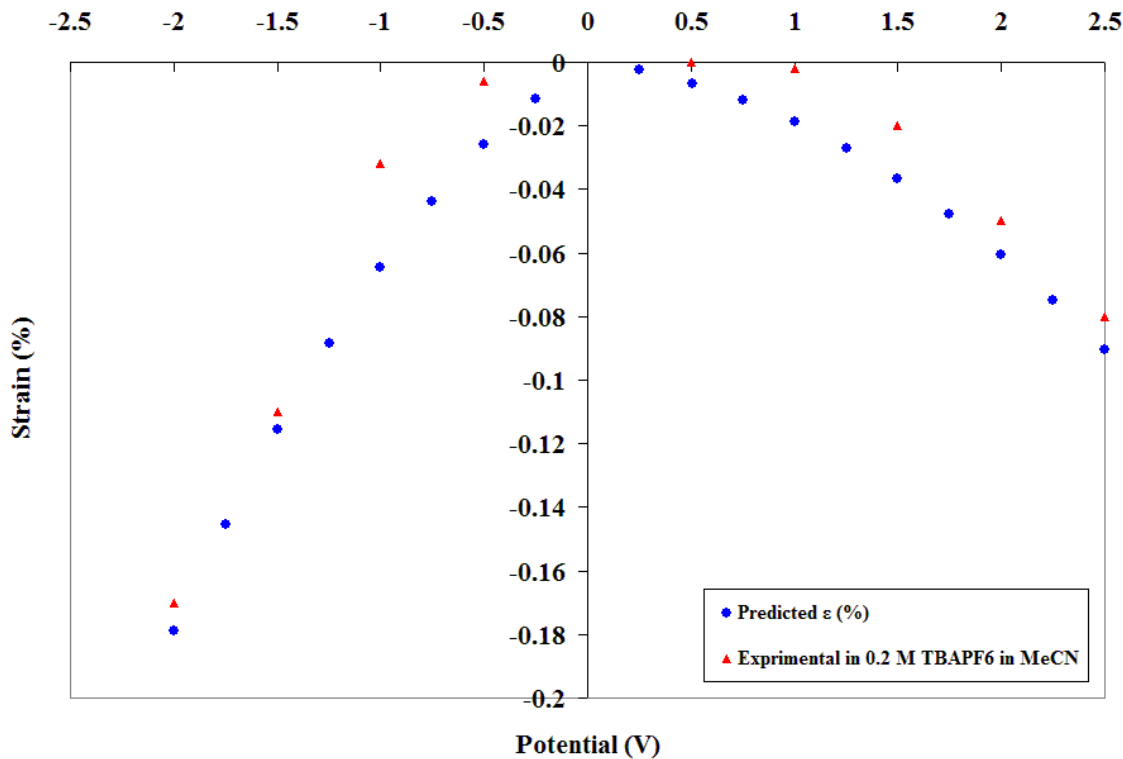


Figure 7.16: Actuation strain vs. applied potential after the dense-sparse radial structure of the yarn are taken into account (blue circles), compared with experimentally measured response (red triangles), from chapter 2.

7.3.2. Other possible causes of discrepancy

There is still some discrepancy between the predicted and measured actuation strains, especially at potentials close to the middle of the plot. It is in this range of potentials that the potential of zero charge is found. Since both anions and cations are mobile and can enter and exit the yarn, we can predict that equal number of cations and anions would be present in the yarn around PZC. When the potential applied to the yarn is changed around PZC, the extra charge on the yarn can be balanced both by bringing in ions of opposite charge or expelling ions of the like charge, until there are few ions of the like charge

left within the yarn. The removal of the ions of like charge from the yarn results in the removal of ions and solvent and a decrease in the volume of the yarn. This decrease of volume has to be subtracted from the increase in the volume due to intercalation of ions of opposite charge, which happens simultaneously. Therefore, the change in the yarn volume and the real actuation strain would be smaller than what is predicted by the model. Expulsion of some solvent due to elastic forces within the yarn as the yarn swells during actuation may be another source of overestimating the actuation strain in the model.

7.4. Full model for the actuator

To arrive at a full model for the actuation behaviour, we can start from equation 7.7:

$$\varepsilon_{act} = \frac{Y_s}{Y_y} \frac{\Delta V}{\pi R_y^2 l_0 \left(1 - \frac{2}{4\pi^2 (R_y^2 - R_d^2) \lambda T_0^2}\right)}$$

But ΔV is the total ion and solvent volume transferred during the actuation, which can be expressed as $\Delta V = N_{ion} \cdot V_{ion} = \frac{Q}{ze} \cdot V_{ion}$, where Q is the total charged transferred into the yarn during actuation, z is the valancy of the ion contributing to actuation, e is the fundamental charge and V_{ion} is the solvated volume of the ion in question. Therefore,

$$\varepsilon_{act} = \frac{Y_s}{Y_y} \frac{Q \cdot V_{ion}}{ze \pi R_{y0}^2 l_0 \left(1 - \frac{2}{4\pi^2 (R_{y0}^2 - R_d^2) \lambda T_0^2}\right)} = \frac{Y_s}{Y_y} \frac{\rho \cdot V_{ion}}{ze \left(1 - \frac{2}{4\pi^2 (R_{y0}^2 - R_d^2) \lambda T_0^2}\right)} ,$$

where ρ is the volumetric charge density in the yarn.

The strain-to-charge ratio for actuation from a certain type of ion can be found as

$$\alpha = \frac{\varepsilon_{act}}{\rho} = \frac{Y_s}{Y_y} \frac{V_{ion}}{ze(1 - \frac{2}{4\pi^2(R_{y0}^2 - R_d^2)\lambda T_0^2})}. \quad (7.8)$$

The total strain; i.e. the combination of active and passive strains can be found as

$$\varepsilon = \varepsilon_{pass} + \varepsilon_{act} = \frac{\sigma}{Y_y(\rho)} + \alpha \cdot \rho, \quad (7.9)$$

where σ is the applied load. The Young's modulus of the yarn may itself depend on the applied potential and stored charge, as discussed in chapter 2.

7.5. Comparison with sensor

Let us see if the properties observed from the actuator are consistent with those measured for the sensor experiments in chapter 5. As an alternative to the variable capacitance model proposed in chapter 5 to explain the sensor response, Shoa et al. [1] proposed that for a conducting polymer force sensor, the generated sense voltage follows $V_{sensor} = -\alpha \cdot \sigma$, where α is the strain-to-charge ratio for the actuator, and σ is the variation in the mechanical stress. Does the same relationship govern the mechanical force sensing behaviour in CNT yarns? We have proposed that ion insertion leads to swelling. In a similar way, Shoa et al. have proposed that the stress applied to a sheet of Polypyrrole helps or inhibits insertion/removal of ions, and therefore has an effect on open-circuit potential of the cell. Proof of the existence of a similar behaviour in the CNT yarns, and the same governing rules for the constant of proportionality (e.g. its dependence on the strain-to-charge ratios), would support the charge insertion model for actuation.

If there is a path for the charge to flow, the generated sense voltage will lead to a charge transfer. The change in the charge density transferred in response to an induced sensor voltage is expected to be

$$\rho_{sensor} = C_{V_{eff}} V_{sensor},$$

where $C_{V_{eff}}$ is the effective volumetric capacitance of the sample as described in [1].

Strain can be re-expressed in terms of charge via the following steps:

$$V_{sensor} = -\alpha \cdot \sigma = -\alpha \cdot Y \cdot \varepsilon_{passive}$$

The charge displaced during sensing can be found by multiplying the volumetric capacitance by the change in potential due to sensor mechanical input:

$$\Rightarrow \rho_{sensor} = C_{V_{eff}} \cdot V_{sensor} = -C_{V_{eff}} \cdot \alpha \cdot Y \cdot \varepsilon_{passive}$$

Substituting from the equations above for V_{sensor} , we have,

$$\Rightarrow \rho_{sensor} = -C_{V_{eff}} \cdot \alpha \cdot Y \cdot \varepsilon_{passive}$$

Similar to the definition of the strain-to-charge ratio for the actuator, let us define the charge-to-strain ratio for the sensor as the amount charge moved per unit applied passive strain:

$$\Rightarrow \frac{\rho_{sensor}}{\varepsilon_{passive}} = -C_{V_{eff}} \alpha \cdot Y \quad (7.10)$$

From Figure 7.10, we know that the strain to charge ratio with TBA^+ and PF_6^- ions is about $5.03 \times 10^{-11} \frac{m^3}{C}$ and $-1.29 \times 10^{-11} \frac{m^3}{C}$, respectively. These values are found by

multiplying the slopes of the fit lines in Figure 7.10 by the volume of the yarn sample. The Young's modulus of the yarn was found to be about 15 GPa (Chapter 2). For $C_{V_{eff}}$, we can use the values of the capacitance at +1 V and -1V found in chapter 6. Substituting in equation 7.10, the charge-to-strain ratio for the sensor is found to be $6.2 \times 10^6 \frac{C}{m^3}$ and $-2.9 \times 10^6 \frac{C}{m^3}$ for the TBA^+ and PF_6^- ions, respectively. Figure 7.17 shows the experimental sensor strain-charge data. The squares and circles are the same data as in Figure 5.4, normalized by the volume of the yarn, while the lines show model predictions from the above discussion. As can be seen, the trends and the order of magnitude of the charge transferred as a result of a certain change in passive strain are predicted correctly in case of both ion types. While the model also predicts the transferred charge for the PF_6^- ion relatively accurately, the magnitude of the transferred charge is overestimated for the TBA^+ ion by about a factor of about 2. A possible cause for the discrepancy between predicted and measured sensor data is the variation in the gravimetric capacitance in various batches of yarn spun at different times, which have occasionally varied by up to 300 %. Since the capacitance is found from the sample used in chapter 6, and the sensor data is from a sample used for the experiments in chapter 5, the two samples may have had different capacitances. Given the limitations of our knowledge about the specific yarn properties employed in the sensor, the sensor data appears to be consistent with the actuator measurements within the framework of the proposed models. Another possibility is that the TBA^+ ion is in fact solvated to some extent, thus straining the yarn by a certain amount results in the expulsions of fewer TBA^+ ions than expected from the calculations.

This would mean some adjustments are needed in the actuator calculations, still within the uncertainties of the data.

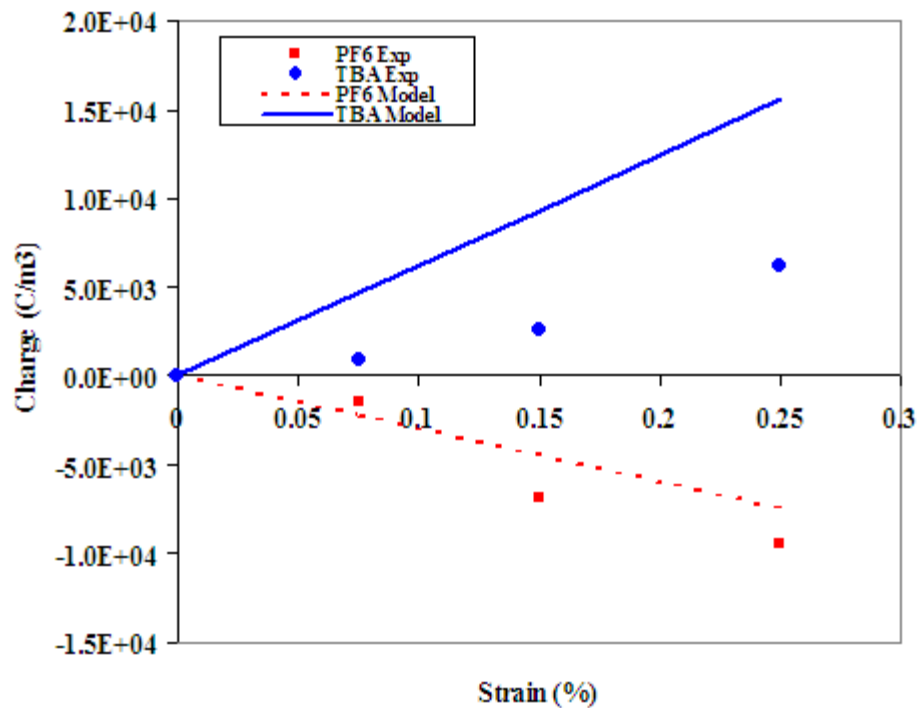


Figure 7.17: A reproduction of Figure 5.4b (squares and circles), with the results of the model prediction (lines) superimposed. The blue circles indicate the experimental results using the TBA^+ ion at -1 V bias and the red squares are experimental results for PF_6^- ion at +1 V bias.

7.6. Conclusions

A model was presented to explain the actuation of twisted yarns of carbon nanotubes, based on the changes in the volume of the yarn as a result of electrochemical charging. It was proposed that the double-layer forces from ions that occupy significantly large amount of space, and thus cannot be thought of as point charges, result in a force in the radial direction that pushes the CNTs in the yarn apart. Based on the geometry of a

twisted yarn, it is shown that a radial expansion will lead to an axial contraction in the yarn. That information was combined with the capacitance results from chapter 6 to create a quantitative model to relate the axial contraction in the yarn to the applied actuation potentials. The predictions of the model generally agree with experimental results for actuation. It was shown that the actuation data and the sensor data presented in chapter 5 are consistent within the framework of the present actuation model and that of Shoa et al. [1].

References

- [1] T. Shoa, J. D. W. Madden, T. Mirfakhrai, G. Alici, G. M. Spinks, and G. G. Wallace, "Electromechanical coupling in polypyrrole sensors and actuators," *Submitted to Sensors and Actuators A*, 2009.
- [2] K. Atkinson, "Production, Properties, and Prospects of Dry-Spun Carbon Nanotube Yarns for Textile Applications," presented at Techtextil North America Symposium 2009 Las Vegas, NV, 2009.
- [3] J. W. S. Hearle, P. Grossberg, and S. Backer, *Structural mechanics of fibers, yarns and fabrics*. New York: Wiley-Interscience., 1969.
- [4] J. W. S. Hearle, P. Grossberg, and S. Backer, *Structural Mechanics of Fibers, Yarns and Fabrics*, vol. 1. New York: Wiley-Interscience, 1969.
- [5] L. J. Hall, V. R. Coluci, D. S. Galvão, M. Zhang, M. Kozlov, A. A. Zakhidov, S. R. Shah, R. Raj, A. B. Dalton, J. D. W. Madden, T. Mirfakhrai, G. M. Spinks, G. G. Wallace, J. N. Barisci, S. O. Dantas, E. Muñoz, K. Atkinson, and R. H. Baughman, "Strain Amplification for Artificial Muscles and Sensors Using Giant Poisson Ratios and

Giant Linear Compressibilities," presented at Materials Research Society Fall meeting 2006., 2006.

- [6] J. Foroughi, T. Mirfakhrai, R. H. Baughman, S. Fang, M. M. Kozlov, J. D. W., G. M. Spinks, and G. G. Wallace, "Carbon nanotube yarn as a microscale rotational actuator," presented at SPIE Smart Structures / NDE 2010, San Diego, CA, 2010.
- [7] G. M. Spinks, G. G. Wallace, L. S. Fifield, L. R. Dalton, A. Mazzoldi, D. De Rossi, Khayrullin, II, and R. H. Baughman, "Pneumatic carbon nanotube actuators," *Advanced Materials*, vol. 14, pp. 1728-1732, 2002.
- [8] I. Langmuir, "The Role of Attractive and Repulsive Forces in the Formation of Tactoids, Thisotropic Gels, Protein Crystals and Coacrevates," *Journal of Chemical Physics*, vol. 6, pp. 873-896, 1938.
- [9] B. V. Derjaguin and L. D. Landau, "Theory of stability of strongly charged lyophobic sols and of the adhesion of strongly charged particles in solutions of electrolytes," *Acta Physicochimica URSS*, vol. 14, pp. 633-662, 1941.
- [10] E. J. W. Verwey and J. T. G. Overbeek, *Theory of the stability of lyophobic colloids: The interaction of sol particles having an electric double layer*. Amsterdam: Elsevier Publishing Company, 1948.
- [11] J. Israelachvili, *Intermolecular & Surface Forces*, 2nd ed: Academic Press, 1991.
- [12] R. J. Hunter, *Foundations of Colloid Science* 2ed. USA: Oxford University Press, 2001.
- [13] H.-J. r. Butt, B. Cappella, and M. Kappl, "Force measurements with the atomic force microscope: Technique, interpretation and applications," *Surface Science Reports*, vol. 59, pp. 1-152, 2005.

- [14] J. T. G. Overbeek, "Strong and Weak Points in the Interpretation of Colloid Stability," *Advances in Colloid and Interface Science*, vol. 16 pp. 17-30, 1982.
- [15] M. Boström, D. R. M. Williams, and B. W. Ninham, "Specific Ion Effects: Why DLVO Theory Fails for Biology and Colloid Systems," *Physical Review Letters*, vol. 87, pp. 168103-1-4, 2001.
- [16] B. W. Ninham and V. Yaminsky, "Ion Binding and Ion Specificity: The Hofmeister Effect and Onsager and Lifshitz Theories," *Langmuir*, vol. 13, pp. 2097-2108, 1997.
- [17] E. Darmois, "The theory of concentrated electrolyte solutions," *Journal de Physique et le Radium*, vol. 1, pp. Suppl. 41-2, 1940.
- [18] F. F. Lange, "Shape forming of ceramic powders by manipulating the interparticle pair potential," *Chemical Engineering Science*, vol. 56, pp. 3011-3020, 2001.
- [19] S. E. Feller and D. A. McQuarrie, "Ionic Size Effects on the Force between Planar Electrical Double Layers," *Journal of Physical Chemistry*, vol. 97, pp. 12083-12086, 1993.
- [20] R. M. Pashley, "Hydration Forces Between Mica Surfaces in Electrolyte Solutions," *Advances in Colloid and Interface Science*, vol. 16, pp. 57, 1982.
- [21] J. N. Israelachvili, "Forces between surfaces in liquids," *Advances in Colloid and Interface Science*, vol. 16, pp. 31-47, 1982.
- [22] M. Colic, G. V. Franks, M. L. Fisher, and F. F. Lange, "Effect of Counterion Size on Short Range Repulsive Forces at High Ionic Strengths," *Langmuir*, vol. 13 pp. 3129-3135, 1997.

- [23] J. D. Madden, Conducting Polymer Actuators, Ph.D. Thesis, 2000, Massachusetts Institute of Technology, Cambridge, MA
- [24] K. Kaneto, Y. Sonoda, and W. Takashima, "Direct Measurement and Mechanism of Electro-Chemomechanical Expansion and Contraction in Polypyrrole Films," *Japanese Journal of Applied Physics*, vol. 39, pp. 5918-5922, 2000.
- [25] G. Sutra, "The dimension of ions of electrolytes. I. Aqueous solutions. Hydration of ions" *Journal de Chimie Physique et de Physico-Chimie Biologique*, vol. 43, pp. 189-204, 1946.
- [26] G. Sutra, "The dimension of electrolytic ions. III. Solvents other than water," *Journal de Chimie Physique et de Physico-Chimie Biologique*, vol. 43, pp. 279-289, 1946.
- [27] H.-H. Jung, S.-W. Hwang, S.-H. Hyun, K.-H. Lee, and G.-T. Kim, "Capacitive deionization characteristics of nanostructured carbon aerogel electrodes synthesized via ambient drying," *Desalination* vol. 216 pp. 377–385, 2007.
- [28] S.-H. Yeon, K.-S. Kim, S. Choi, H. Lee, H. S. Kim, and H. Kim, "Physical and electrochemical properties of 1-(2-hydroxyethyl)-3-methyl imidazolium and N-(2-hydroxyethyl)-N-methyl morpholinium ionic liquids," *Electrochimica Acta*, vol. 50, pp. 5399-5407, 2005.
- [29] H. L. Yeager and B. Kratochvil, "Conductance Study of Ion Pairing of Alkali Metal Tetrafluoroborates and Hexafluorophosphates in Acetonitrile," *Canadian Journal of Chemistry*, vol. 53, pp. 3448 1975.

Chapter 8

8 Contributions, concluding discussions and future directions

This Chapter summarizes the contributions of this work, provides a discussion of the actuation properties of CNT yarns, and ends with conclusions.

8.1. Contributions

1. We have shown that twist-spun yarns of carbon nanotubes can act as electromechanical actuators and sensors when charged in an electrolyte. The present work is the first characterization of CNT yarns (or any yarn) as actuators.
2. Basic properties of the yarn important for actuation were determined. These include:
 - a. active stress and strain as actuator,
 - b. tensile modulus, (15 ± 2 GPa)
 - c. work density, (between 40 and 528 kJ/m³, depending on conditions)
 - d. electromechanical coupling

Also determined are the working limits of the yarn, such as potential range and load range within which the actuator can be operated.

3. The yarns were shown to actuate under a load of $2.0 \pm 0.6 \times 10^8$ Pa (with 0.4 % strain), two orders of magnitude higher than had previously been reported in CNT actuators [1, 2], and only matched by shape memory alloys among artificial muscle technologies [3]. This achievement is made possible by:
 - a. The actuation of highly aligned carbon nanotubes that feature high tensile strength and
 - b. The use of an ionic liquid electrolyte, which allows operation at high voltages and with little creep.
4. The capability of the yarns to act as mechanical force sensors was also demonstrated, and it was shown that they can generate a change in the cell current or open-circuit cell potential in response to external applied change in tensile load (0.02 mV/Pa).
5. Actuation mechanisms were investigated and it was shown that actuation is the result of interactions between nanotubes, rather than changes in length of charged nanotubes, as had previously been suggested. A correspondence between ion size and actuation strain was shown, and increased repulsion between nanotubes as they are charged is due at least in part to the physical insertion of ions. This new mechanism may also explain the observed actuation in other nanotubes actuators, and be used in the design of new actuating materials.

6. A model was developed to relate the mechanical and electrical properties, such as stress, strain, voltage and charge, and geometric properties of the yarn, such as the diameter and twist. Literature from widely varied fields was studied and information combined to provide the full model. These fields include mechanics, electromagnetism, electrochemistry, textile mechanics, surface science, biophysics (double-layer interactions literature), circuit theory, quantum chemistry (single CNT actuation), etc.
7. The electrochemical charge storage properties of the yarns were investigated using cyclic voltammetry (CV) and electrochemical impedance spectroscopy (EIS), showing that the yarn behaves like a constant phase element (CPE), with resistance of solution and contact modeled as a resistor in series with the CPE. Any reactions leading to charge loss can be modeled by a resistor in parallel with the CPE. If the operation frequency range of interest is small, the CPE can be approximated by a pure capacitor. The capacitance was found to depend on the applied potential, rising at higher potentials. This effect was found to be more pronounced in acetonitrile than in water. The gravimetric capacitance of the equivalent capacitor was measured to be about 10 F/g for aqueous electrolytes and between 10-50 F/g in acetonitrile.
8. For the first time, nonlinear equivalent circuit models were presented to describe the charge storage behaviour and the large-signal current-potential relationship in the yarns.

Below is a summary discussion of the most important points.

8.2. Advantages and challenges as actuators

8.2.1. Actuation stress and strain

As actuators, CNT yarns operate at low applied potentials, (less than 10 V) and are capable of actuating against loads of up to at least 200 MPa, about 1000 times the stresses sustainable by human skeletal muscle. Only shape memory alloys are known to match this stress level [3]; and when normalized by density the yarns could come out ahead, providing electrolyte and packaging masses can be kept small. Since the tensile strength of the yarns has been measured to be about 1 GPa, it is conceivable that the actuation load can be increased even further.

The actuation strains that yarns can generate reach 0.6 %. To put this value into context, piezoelectric actuators used commercially in many precision applications generate about 0.1-0.2 %, at stresses that are generally 10 MPa or less, while needing voltages of 100 V or higher [4]. Although the strains are larger than in piezoelectrics, they are much lower than in muscle. Much as piezoelectrics often make use of mechanical amplification or a stepping motion in order to move lenses or provide nanopositioning, so might yarn actuators. Their advantages of larger strain and higher stress may be offset by lower bandwidth, as high bandwidth helps enable the stepping motion that is often employed in piezoelectric devices. Thus far the fastest nanotubes actuators respond in about 5 ms, whereas piezoelectrics operate in the kilohertz frequency range.

8.2.2. Tensile modulus

Although the modulus of a dry yarn had been measured by Zhang et al. [5], the dependence of this modulus on the charge content of an active yarn has not been studied

before. The first wet measurement of the tensile modulus of the yarn as a function of the applied potential was presented (Chapter 2). The Young's modulus of the yarn seems to decrease at higher charge levels. This is consistent with what is observed in conducting polymer actuators and has been attributed to the increased solvent content in the actuator that results in a softer, more viscous artificial muscle [6]. In the case of the twisted yarn the change in effective twist angle can also contribute to decreasing the yarn modulus, although this contribution should be small.

8.2.3. Strain rate and band width

How quickly can a yarn actuator respond? This question has not been directly investigated in the present work. Since actuation depends on the charging of the yarn the speed of actuation and the response time are also determined by the speed with which the yarn can be charged. The yarn behaves roughly like a capacitor (Chapters 4, 5). In the simplest case, there is also the resistance of the electrolyte and contact resistance that are in series with the yarn capacitance. Thus, on the first level of approximation, the time constant of charging can be found from $\tau = R_s \cdot C$, where R_s is solution and contact resistance and C is the capacitance of the yarn. Thus the speed of actuation clearly depends on the geometry of the actuator and the cell. Carbon nanotubes papers have been shown to actuate at 19 %/s [7], and, with careful attention to minimize cell resistances, such actuation speeds should be possible in nanotubes yarns.

8.2.4. Work density and blocking load

Following Spinks and Truong [8], we calculate the work density for the yarn actuator in three ways. The first scenario to compute the work density starts with a non-activated,

unloaded yarn, and follows it through stages of loading it with a constant stress and actuating it. The second scenario is to start with a yarn that is already under constant mechanical load, but is not actuated, and then following through a constant load actuation half cycle. The third scenario is to compute the work density, assuming that the yarn is working against a spring with a stiffness of k_e , that is equal in stiffness to the yarn actuator. We start by computing the actuator strain under load and the blocking load.

8.2.4.1. Actuator strain

Let us assume that an artificial muscle is under constant tensile load and is caused to contract when stimulated by an applied voltage. The length changes occurring are shown in Figure 8.1 for the case of a CNT yarn actuator that is contracting against an attached load. Applying a force ($\Delta f = f$) produces an initial elastic deformation (ΔL_{AB}). The length change produced by the applied voltage can be separated into two parts: ΔL_{BC} and ΔL_{CD} , which are due to actuation and to a change in elastic modulus, respectively.

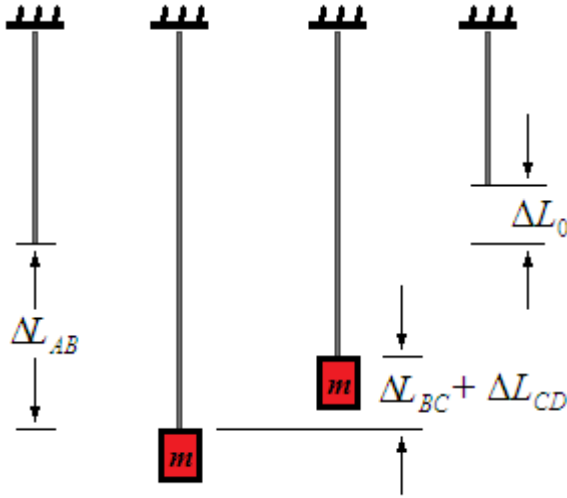


Figure 8.1: CNT yarn actuator (represented by the gray line) work cycle under a constant load: ΔL_{AB} , effect of initial loading; ΔL_{BC} , (contractile) effect of actuation; ΔL_{CD} (expansive) effect of the (decreasing) change in the Young's modulus of the yarn; ΔL_0 free stroke strain of the actuator.

As shown by Spinks and Truong, if the modulus of the actuator does not change, the total strain stroke as a function of applied mechanical load can be found as

$$\varepsilon_f = \varepsilon_0 - \frac{\sigma}{Y}, \quad (8.1)$$

where ε is now the actuator strain and σ is the load stress. This means that the actuator stroke decreases linearly from the free stroke at zero load to zero at a load known as the *blocking load or stress*. If the effect of a changing elastic modulus is included, it is shown that

$$\varepsilon_f = \varepsilon_0 - \frac{\sigma}{Y'} . \quad (8.2)$$

It can be seen that the modulus *after* application of the drive voltage (Y') determines the net effect of the applied load. In general, the larger the decrease in modulus, the more rapidly the strain decreases. This leads to smaller blocking load.

In the second scenario, where load is constant and already applied, there is still a blocking force when the drop in modulus fully counteracts the strain (i.e. $\Delta L_{BC} = -\Delta L_{CD}$ in Figure 8.1). This isotonic blocking load is:

$$\sigma_{blocking} = \frac{\varepsilon_0 Y Y'}{Y - Y'} \quad (8.3).$$

For example, in a yarn¹ the modulus was shown to change from about 20.5 GPa at $V = 0$ V to 18 GPa at $V = +2$ V. So $\beta = \frac{20.5}{18} = 1.14$

A peak-to-peak strain of 4×10^{-4} (absolute) was measured at a load of 10 MPa. Therefore, the strain at no load can be estimated to be about 5×10^{-4} (absolute). Therefore the blocking load according to equation 8.3 will be

$$\sigma_{blocking} = \frac{\varepsilon_0 Y Y'}{Y - Y'} = 73.2 \text{ MPa}$$

The value from the experimental plot (Figure 8.2) is approximately 89 MPa by extrapolation ($\sim 15\%$ deviation from equation 8.3 above).

¹ 060726 experiments

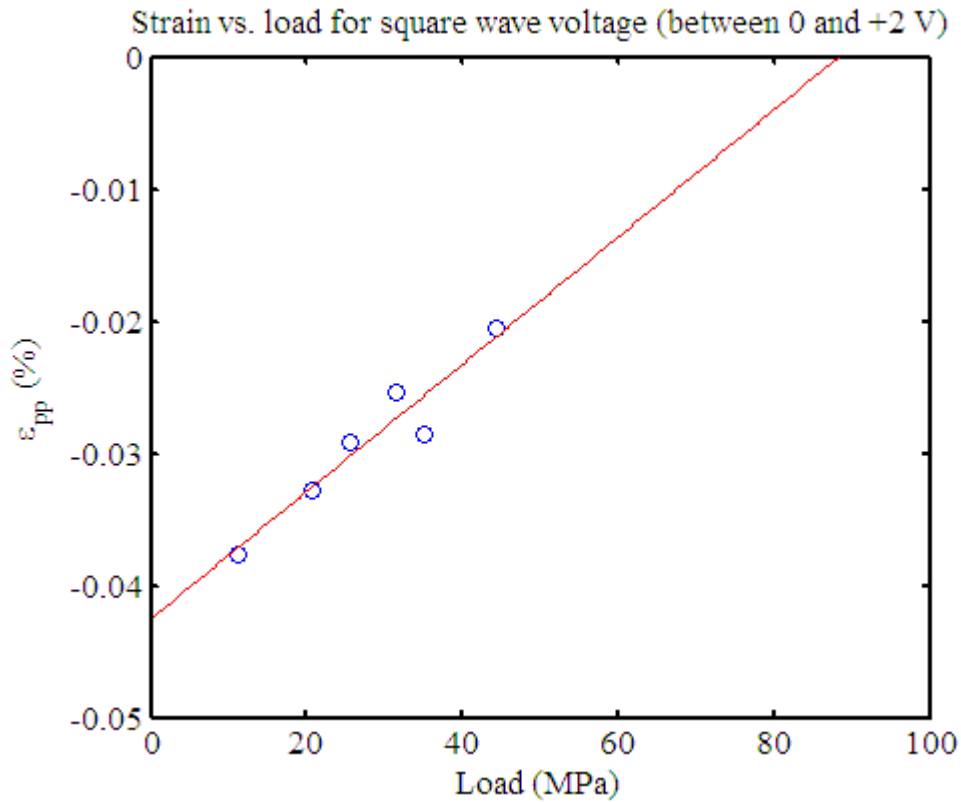


Figure 8.2: Strain generated as a function of load for actuation of a yarn with a 18 μm diameter and a length of 12.9 mm in a 0.2 M solution of tetrabutylammonium hexafluorophosphate in response to a step voltage between 0 and 2 V vs. Ag/Ag⁺.

8.2.4.2. Actuator work-per-cycle

8.2.4.2.1 *Actuator works against a constant load, starting in the unloaded state*

As mentioned above, the calculation of the work density of the actuator depends upon the definition of the work cycle and the scenario that is adopted. For the work cycle that includes steps A–D as shown in Figure 8.1 [9], the actuator stroke is given by equation (8.2) and the work done is given by:

$$W = f\Delta L_f \text{ or } W_V = \sigma \cdot \varepsilon_0 - \frac{\sigma^2}{Y'}$$

If V is the sample volume and $V = AL_0$, differentiating with respect to stress we can find the stress at which work density is maximum. The maximum volumetric (W_v) and gravimetric (W_g) work densities can then be found to be

$$W_{V_{\max}} = \frac{1}{4} \varepsilon_0^2 Y' \quad (\text{J/m}^3) \quad \text{and} \quad W_{g_{\max}} = \frac{1}{4\rho} \varepsilon_0^2 Y', \quad (\text{J/kg}) \quad (8.4)$$

where ρ is the actuator material density. The maximum work density can be found when the load is $\sigma_{\max} = \frac{1}{2} Y \varepsilon_0$.

As the modulus decreases, the maximum work occurs at a smaller applied force and gives a significantly smaller work-per-cycle. For the yarn the maximum work density under these conditions can be found:

$$W_{\max} = \frac{1}{4} \varepsilon_0^2 Y' = \frac{1}{4} 25 \times 10^{-6} \cdot 13 \times 10^9 = 8 \times 10^4 \text{ (J/m}^3), \text{ or } 1 \times 10^2 \text{ J/kg.}$$

The work capacities of various actuators, calculated using equation 8.4, are included in Table 8.1.

8.2.4.2.2 Actuator works against a constant load, starting in the loaded state

The analysis by Baughman [10] includes the work-per-cycle calculations for steps B-D only (constant load), where the work-per-cycle depends on the applied load:

$$W = f \Delta L_0 - \frac{f^2 L_0}{A} \left(\frac{1}{Y'} - \frac{1}{Y} \right).$$

Once again, we can differentiate with respect to stress to find the stress (σ_{\max}) at which the work density is maximized. The analysis can then be extended to show that the maximum volumetric work and gravimetric work are given by

$$W_{V_{\max}} = \frac{1}{4} \varepsilon_0^2 \frac{YY'}{Y-Y'} \text{ (J/m}^3\text{)} \quad \text{and} \quad W_{g_{\max}} = \frac{1}{4\rho} \varepsilon_0^2 \frac{YY'}{Y-Y'} \text{ (J/kg)} . \quad (8.5)$$

It should be noted that if the modulus does not change ($Y = Y'$), the value of σ_{\max} increases to infinity and therefore an infinite work per cycle can be obtained. In reality, the maximum load that can be applied is limited by the tensile strength of the material. Baughman [8] has suggested that the practical maximum applied load is 50% of the breaking or yield force (σ_b), so that $W_{V_{\max}} = \varepsilon_0 \sigma_b$.

For the CNT yarns, typical values are: $Y = 15 \text{ GPa}$, $Y' = 13 \text{ GPa}$, $\varepsilon_0 = 0.5 \% = 5 \times 10^{-3}$.

Thus:

$$W_v = \frac{1}{4} \varepsilon_0^2 \frac{YY'}{Y-Y'} = 528 \text{ kJ/m}^3 \text{ or } 660 \text{ J/kg} . \text{ The work densities for this scenario are also}$$

listed in Table 8.1 and compared with other types of artificial muscles.

8.2.4.2.3 Actuator works against a restoring spring

In many applications using commercially available actuators (electrostrictive ceramics or shape-memory alloys) the actuator works against a restoring spring, as schematically illustrated in Figure 8.3.

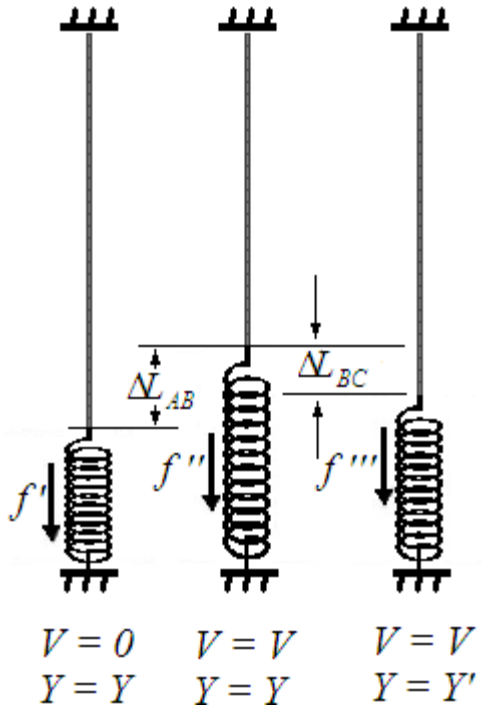


Figure 8.3: Actuator work cycle when working against a spring.

Let us assume that the yarn actuator is at rest but under a pre-stress caused by the external spring (initial force of f'). When a voltage is applied, the actuator contracts and the spring extends by ΔL_{AB} . Therefore, the restoring force increases from f' to f'' because of the extension of the spring. However, the voltage also changes the Young's modulus of the actuator so that the external spring extends by ΔL_{BC} , and the spring force is therefore reduced to f''' . Spinks and Truong give the actuator stroke as $\Delta L_f = \frac{\Delta L_0}{1+r}$, where r is the ratio of the external spring stiffness (k_e) to the internal stiffness of the actuator material (k_i). They also show that when $r = 1$ (the so-called “impedance matching” point when the spring stiffness equals the yarn stiffness) and assuming no change in the Young's modulus of the actuator, the maximum volumetric and gravimetric work density is

achieved. The maximum volumetric and gravimetric work density can be shown to be equal to:

$$W_v = \frac{1}{4} \left(\frac{1}{2} Y \varepsilon_0^2 \right) \text{ (J/m}^3\text{)} \quad \text{and} \quad W_g = \frac{1}{4\rho} \left(\frac{1}{2} Y \varepsilon_0^2 \right). \quad \text{(J/kg)}$$

The analysis can be extended to include the changing internal modulus of the actuator during actuation, and gives a maximum volumetric and gravimetric work capacity of

$$W_v = \frac{1}{4} \left(\frac{1}{2} Y' \varepsilon_0^2 \right) \text{ (J/m}^3\text{)} \quad \text{and} \quad W_g = \frac{1}{4\rho} \left(\frac{1}{2} Y' \varepsilon_0^2 \right), \quad \text{(J/kg)} \quad (8.6)$$

where Y' is the Young's modulus of the actuator at the new potential.

If the CNT yarn works against a spring, we can estimate using typical properties that:

$$W_v = \frac{1}{4} \left(\frac{1}{2} Y' \varepsilon_0^2 \right) = \frac{1}{4} \left(\frac{1}{2} 13 \times 10^9 \cdot 25 \times 10^{-6} \right) = 40 \text{ kJ/m}^3.$$

Table 8.1 includes the predicted maximum work-per-cycle for various actuator materials operating against a restoring spring. The table shows that CNT yarns compare very favourably with other contractile materials.

Table 8.1: Calculated work capacity for various actuator materials using different theoretical approaches (Table adopted with minor changes from [8], with the data for the yarn added)

Material	ε_0 (%)	Y (GPa)	Y/Y'	ρ (g/cm ³)	Isotonic (A–D)		Isotonic (B–D)		Against spring	
					W_v (kJ/m ³)	W_g (J/kg)	W_v (kJ/m ³)	W_g (J/kg)	W_v (kJ/m ³)	W_g (J/kg)
CNT yarn	0.6	15	1.15	0.8	81	100	530	660	40	51
Piezoelectric ceramic [11]	0.2	64	1.1	7.5	58	8	640	85	29	4
Electrostrictive polymer [11]	5	0.4	1.2	1.8	208	116	1250	694	104	58
Conducting polymer 1 [8]	2	0.11	1.16	1.5	9	6	66	44	5	3
Conducting polymer 2 [8]	5	0.1	5	1.5	13	8	16	10	6	4
CNT (Bucky paper)[8]	0.5	5	1	0.3	31	104	125	417	16	52
Electrostatic elastomer [12-14]	63	0.001	1	1.4	99	71	7875	5625	50	35

8.2.5. Coupling

There are several ways to define and measure electromechanical coupling [8]. One way is defining the work cycle of interest as moving a fixed mass back and forth². If the actuator is just moving a fixed mass back and forth, the coupling can be extremely high; rising in proportion to the maximum load that can be handled providing that strain is not affected by load.

Another way to view coupling is to determine the amount of electrical energy converted to internal mechanical work. In this case the actuator is charged in an unloaded state. The

² Other definitions, such as measuring coupling when the actuator is working against a spring can be used.

strain is measured, and is assumed to have been achieved by working against the elastic modulus of the actuator material. The ratio of mechanical work done on the actuator material itself to electrical work in then represents coupling.

This would be equivalent to defining coupling as the ratio of the mechanical work out of the actuator to the electrical work that has gone in during a half-cycle of actuation³. A typical value for the electrical work per unit volume going in to the actuator can be found from:

$$W_{in} = \frac{1}{2} C_v V^2,$$

where C_v is the volumetric capacitance of the yarn, and V is the applied voltage. The volumetric capacitance of the yarn is $C_v = C_g \cdot \rho$, where ρ is the density of the yarn, with a typical value of about $800 \frac{kg}{m^3}$. Thus the electrical energy going into the unit volume of the actuator can be found to be:

$$W_{in} = \frac{1}{2} C_g \cdot \rho \cdot V^2 = \frac{1}{2} 20000 \frac{F}{kg} \cdot 800 \frac{kg}{m^3} \cdot 3^2 V^2 = 72 \frac{MJ}{m^3}.$$

Values for the gravimetric capacitance and applied potential are taken to be typically $20 F/g$ and $3 V$, as demonstrated in the previous Chapters. Thus the coupling is between 1.4 % to 6.9 % based on the values for output mechanical work density estimated above. Spinning yarns using longer CNTs with more interconnectivity can lead into yarns

³ If the actuator goes back to its initial length at the end of the full cycle, the work per cycle would be zero due to zero displacement. Thus work per *cycle* is not a useful measure of the actuation performance.

actuators that can operate at higher loads and thus have higher couplings. For example, if the tensile strength of the yarn can reach 5 GPa, which is the strength of the strongest commercially-available steel wires, and if it can be actuated at close to its tensile strength, the coupling can reach 35 %. This value would be unsurpassed among ionic artificial muscles, and is close to the maximum achieved among artificial muscles (in dielectric elastomer actuators, $\sim 50\%$ [3]).

8.2.6. Creep

Another issue of prime importance is creep during actuation. The so-called creep in the yarns is likely to be a combination of several phenomena, including:

- a. Mechanical creep due to sliding of CNTs past each other upon application of mechanical load,,
- b. Acceleration in the mechanical creep during the active (charged) half-cycle. The presence of the ions between the CNTs, may reduce the interactions between the adjacent CNTs that hold them together, leading to easier slipping and expedited creep during the active half-cycle. This is exacerbated if the potentials are high.
- c. A slow actuation due to the gradual intercalation of ions in the inner, denser, part of the yarn that can be mistaken for creep due to its slow time constant, as discussed in Chapter 7. This part can actually be reversed.

In some cases, and especially during fast actuation, creep can be significant compared to the actuation strain. We have shown that creep is much slower when actuation takes place

in viscous ionic liquids. This may be due to higher stability of these electrolytes, such that the effect of parasitic reactions is reduced.

8.2.7. Encapsulation and handling

The need to contain an electrolyte around the yarn is a challenge - as it is for all ionic artificial muscles. Using more viscous electrolytes, such as ionic gels, can be a solution since a fluid electrolyte such as acetonitrile is hard to contain in an encapsulated actuator while still allow the actuator to move.

Handling issues can be significant. The diameters of the yarns are typically under 20 μm , meaning that a force of a few grams can exceed their tensile strengths and break the yarn with slightest human error during handling. Although yarns have been spun with diameters of up to 100 μm by our collaborators in UT Dallas and CISRO [15], actuation response of those has not been studied yet.

8.2.8. Repeatability

Yarn samples from seven batches were used in the experiments mentioned in this thesis. Each batch was spun separately at the Nanotech Institute at the University of Texas at Dallas. The length of yarn in each batch ranged from less than 10 cm in early batches, to one meter in later batches. Some yarn properties can vary significantly from batch to batch. For example, the gravimetric capacitance of the yarn for the samples from the batch used for the experiments in Chapter 4 showed a gravimetric capacitance of about 55 F/g, while the gravimetric capacitance for the yarn samples used in Chapter 6 were less than 20 F/g. These differences may be due to different inner structure of the yarn; for example due to the existence of a smaller or larger dense core in a batch due to spinning

conditions, or differences in the growth conditions of the CNT forest used to spin the yarn batch. These variations can be attributed to our collaborators attempts to improve the mechanical properties of the yarn, which may have lead to changing steps in growth and spinning process. More consistent growth and processing can decrease these issues.

Variations of properties within one batch are smaller, and can be mainly attributed to the variation of the yarn diameter within the batch, which can be about 10 % according to SEM measurements. Results obtained from each sample are usually repeatable within experimental measurement uncertainties if cell conditions are unchanged. To avoid degradation processes that lead to change in cell conditions, the yarn should not be kept at potentials that have shown to result in Faradaic currents for long periods of time.

8.3. Advantages and challenges as mechanical force sensor:

8.3.1. Measurable stress levels

We have shown that the yarn can measure stresses up to 80 MPa. However, since the tensile strength of the yarn is about 1 GPa, there seems to be no reason why it shouldn't be able to measure stresses up to close to that limit – apart from the increased creep that may be induced. Considering that the density of the yarn is much lower than those of the materials used for other types of sensors, such as metallic membranes, piezoelectrics, and silicon-based materials, this may put the yarn sensors at an advantage and make them competitive with other rival technologies.

8.3.2. Issues with parasitic currents and charges

Higher sense currents are generated from the yarn charging levels are increased. However, at and near the limits of the operating potential range, parasitic currents transfer significant charge in the cell, making it difficult to clearly measure the charge passed through the cell due to the applied force and the charge passed due to parasitic currents. These background currents exist at all potentials, and their magnitude fluctuates during an experiment by up to 20 %. This fluctuation may be due to changes in temperature, mechanical vibrations in the room, or the possible presence of micro-bubbles around the electrodes at higher potentials. The fluctuations in the background current make it difficult to clearly differentiate between the change in current due to load and the change due to the fluctuations. This is especially true if the change in load is gradual, such that the rate of change in the load is comparable to the rate of change in the background current.

8.3.3. Issues with variable open-circuit cell potential

When measuring the open-circuit cell potential as the sensor output, higher sense voltages can be generated at higher bias. However, the same processes that result in parasitic currents can now lead to a drift in the open-circuit potential of the cell, making it difficult to differentiate between the change in open-circuit potential due to an applied force and a change due to electrochemical effects in the cell.

8.4. Future work

8.4.1. Effect of load

Understanding the effect of the load on actuation strain is important to understanding actuation. Work on this has already started, but the results need further analysis. Effect of load on actuation strain and charge storage capacitance of the yarn was studied in acetonitrile and ionic liquids. These experiments included the study of the actuation and electrochemical responses during cyclic voltammetry under various loads. In general actuation strain seems to decrease slightly at higher loads; e.g. decreasing from 0.5 % to 0.44 % when the load was increased from 100 MPa to 200 MPa, but this effect is not very significant considering the doubling of the load. Part of that decrease in stain may also be due to history of the sample, since the load was increased in stages during the experiment. No clear relationship was found between the load and the charge storage capacitance of the yarn found using CV. This relative independence of the actuation strain from load is good news, since it implies that the yarn may be able to actuate at loads close to its tensile strength of 1 GPa. If doubling the load from 100 MPa to 200 MPa results in only 11 % decrease in the actuation strain, as implied from our results mentioned above, we could still expect to have about 0.3 % actuation strain at a load of 800 MPa by extrapolation.

8.4.2. Viscoelastic modeling of the yarn

If the yarns are to be fully utilized as sensors and actuators, it is important to properly characterize their mechanical properties. Knowing the tensile strength and strain at break of the yarn is important to set the limit for their applications as actuators and sensors. Knowing how they respond to stretches and impacts may also help determine their

passive mechanical response and the types of applications they can be used for. We had long noticed that the mechanical response of the yarns looked different when they were stretched at different strain rates. We therefore designed and performed a set of experiments to study the viscoelastic properties of the yarns as well as their tensile limits. The results of those studies will be the subject of a future publication.

That work will summarize the experiments performed on the tensile behaviour of the twist-spun MWNT yarns. The results presented belong to static tests in which the yarn sample was stretched to break and dynamic tests which consisted of several consecutive cycles of stretching and relaxation. The samples have been imaged after the experiments using a scanning electron microscope (SEM) to study the fracture patterns and their possible relationship with the strain rates and other yarn properties. The analysis presented consists of fitting some possible viscoelastic models (e.g. Kelvin-Voigt model) to both the static and dynamic curves and a discussion of energetics of the yarn during the dynamic tests.

8.4.3. Characterizing the actuation as a function of twist

An important experiment that can help improve our present theories is characterization of actuation as a function of initial twist. If yarns of various initial twists are actuated under identical conditions, the actuation strain can be characterized as a function of the twist and compared with equation 7.6. While the lengths of the fibres in the CNT yarn are thousands of times larger than the effective fibre diameter and hundreds of times larger than the yarn diameter, the CNT yarn is not exactly a “continuous filament” yarn as presumed in the analysis presented in Chapter 7. This means that other empirical

correction factors, similar to α in equation 7.6, or more complicated models may be necessary to quantitatively explain the actuation behaviour of the yarn.

8.4.4. Studying the radial actuation under an atomic force microscope

While all evidence points to a radial swelling of the yarn being the main cause of actuation in yarns, this effect hasn't been independently and directly observed yet. The reason is that, as shown in Chapter 7, less than 3 % swelling in the radial direction is needed to create the axial strains measured. The diameter of the yarn is 10 μm , and 3 % of that is only 300 nm of displacement. This is below what can be detected by an optical microscope. An instrument capable of measuring such small displacements in an electrolyte is an atomic force microscope (AFM). AFM imaging in a liquid is challenging on its own [16]. Moreover, since a change in twist and diameter is expected to happen in the yarn, the yarn must be free to move and rotate to some extent for its actuation response to be observed. This directly contradicts a basic requirement of AFM imaging, which is having the sample firmly fixed to avoid vibration during imaging.

Several methods were tried to attach the yarn to a substrate for this purpose. The best method found so far is immobilization using UV-cured polyurethane. Uncured precursor was spread thin across a glass slide. The yarn was lowered from above and laid on the spread surface. Polymerization was then performed using a UV light. The sample was then imaged by a profilometer (Veeco) and was found to be well immobilized, while showing a height of about 12 μm above the polymer surface, implying that it was not fully submersed in the polymer. An optical microscope image also shows the yarn resting on top of the polymer surface. The yarn was then imaged using AFM (JPK Instruments AG) in tapping mode. A 3D version of the height signal image can be seen in Appendix 4

in Figure A4.3. No electrochemistry or actuation tests have so far been attempted under the AFM. The image of the surface is clear, and it can be seen that the immobilization is enough to hold the yarn from vibrating during imaging. It can be hoped that the yarn still has enough freedom to actuate and that this actuation can be measured by the AFM. For further discussion of AFM measurements on the yarns, see Appendix 4.

8.5. Potential applications:

8.5.1. High-load, high-temperature, light-weight actuator/sensor

As discussed previously, the yarn can withstand loads of 1 GPa. The tensile strength is being improved by using longer CNT forests to spin the yarn, and is expected to reach and surpass the strength of steel wires at 5 GPa [17]. We have shown actuation under loads of up to 200 MPa (Chapter 3), and we have seen minimal effect from load on actuation (see the previous section). Thus, it is perceivable that the yarn can still actuate at such high loads, making it an actuator/sensor capable of operating under immense loads. This property becomes more important when other related properties of the yarn are taken into account. CNTs are known to be stable up to temperatures above 1000 °C, if protected from oxygen, and the density of the yarns is $0.8 \frac{g}{cm^3}$, by far smaller than those of metallic actuators and sensors. These properties together make the yarns interesting possibilities to be used in applications where high temperatures are involved, or applications where the mass of actuator is a concern, such as aerospace applications.

8.5.2. Non-muscle application

8.5.2.1. Dye or drug release

It has been shown that CNT-based sheets fabricated similar to our yarns can store ions in them after having been charged, even when the electrolyte has been drained [18]. Similar effects have been observed in yarns. The stored ions can then be expelled by applying a sufficiently large potential of the same sign as the ions to the yarn. This implies that if the ions in the electrolyte carry a medicine, or are chromatic, by discharging the yarn at the desired time and place, the drug or the dye can be released into the environment simply by controlling the applied potential and actuating the yarn *in situ*. Similar applications in drug delivery have been shown for conducting polymers like polypyrrole [19-21].

8.6. Concluding remarks

Carbon nanotube yarns are composed of highly aligned, conductive tubes that are closely spaced ($\sim 10\text{-}20\text{ nm}$). This unusual and probably unique morphology creates conditions under which charging in an electrolyte leads to an axial contraction by half a percent, and a radial swelling. Although radial swelling has yet to be directly observed, it is predicted by yarn mechanics. The degree of actuation is proportional to charge density, and to the size of the ions inserted. The nano-structured morphology of the CNT yarns is of prime scientific interest. Scientists have been studying the forces between charged surfaces in electrolytes for decades. However, a conductive and continuous material with nanostructured spacing seems to have never existed. The scientists have therefore been limited to studying the forces between individual particles (e.g. mica) suspended in an electrolyte. Charging those particles usually happened by changing the pH of the

environment and allowing hydrogen adsorption on their surfaces. Never before has there been a structure of almost aligned cylindrical and conductive particle with diameters and average spacing distance of circa 10-20 nm, with enough continuity and bulk conductivity to allow charging just by applying a potential to one end. The anisotropic elastic properties of the yarn also contribute to these interesting properties. The elastic modulus of the yarn in the axial direction is about 15-20 GPa (Chapter 2) and in the radial direction about 250 MPa (Appendix 4). These figures differ by about 100 times. Similarly, while the tensile strength of the yarn in the axial direction is very high (~ 1 GPa), there is very little interconnectivity in the radial direction due to the mostly axial alignment of the CNT fibres and bundles. The yarn can withstand huge forces in the axial direction, which are coupled into radial expansions resulting from electrically driven forces, while allowing for radial displacements of the constituent CNT fibres due to either DLVO or non-DLVO forces. These interactions manifest themselves in the form of the actuation strains due to the twisted structure of the yarn. Despite modest strains, the large stresses enable high work densities to be achieved (528 kJ/m³), greatly exceeding muscle and piezoceramic actuators. These properties may lead to useful engineering applications, and they make the yarn an interesting crucible in which surface interaction phenomena in an electrolyte can be studied. Further studies of such effects, possibly on the microscopic scale using devices such as atomic force microscopes, can lead into better understandings of surface interaction forces that still pose open questions to scientists [22-24].

References

- [1] R. H. Baughman, C. X. Cui, A. A. Zakhidov, Z. Iqbal, J. N. Barisci, G. M. Spinks, G. G. Wallace, A. Mazzoldi, D. De Rossi, A. G. Rinzler, O. Jaschinski, S. Roth, and M. Kertesz, "Carbon nanotube actuators," *Science*, vol. 284, pp. 1340-1344, 1999.
- [2] M. Hughes and G. M. Spinks, "Multiwalled carbon-nanotube actuators," *Advanced Materials* vol. 17, pp. 443-46, 2005.
- [3] J. D. W. Madden, N. A. Vandesteeg, P. A. Anquetil, P. G. A. Madden, A. Takshi, R. Z. Pytel, S. R. Lafontaine, P. A. Wieringa, and I. W. Hunter, "Artificial muscle technology: Physical principles and naval prospects," *IEEE Journal of Oceanic Engineering*, vol. 29, pp. 706-728, 2004.
- [4] I. Hunter and S. LaFontaine, "A comparison of muscle with artificial actuators," *Technical Digest IEEE Solid-State Sensor Actuator Workshop*, pp. 178-185, 1992.
- [5] M. Zhang, K. R. Atkinson, and R. H. Baughman, "Multifunctional carbon nanotube yarns by downsizing an ancient technology," *Science*, vol. 306, pp. 1358-1361, 2004.
- [6] R. Z. Pytel, E. L. Thomas, Y. Chen, and I. W. Hunter, "Anisotropic actuation of mechanically textured polypyrrole films," *Polymer* vol. 49, pp. 1338-1349, 2008.
- [7] J. D. W. Madden, J. N. Barisci, P. A. Anquetil, G. M. Spinks, G. G. Wallace, R. H. Baughnan, and I. W. Hunter, "Fast carbon nanotube charging and actuation," *Advanced Materials*, vol. 18, pp. 870-+, 2006.
- [8] G. M. Spinks and V.-T. Truong, "Work-per-cycle analysis for electromechanical actuators," *Sensors and Actuators A* vol. 119 pp. 455–461, 2005.

- [9] V. Giurgiutiu, C. A. Rogers, A. Rogers, and Z. Chaudhry, "Energy-based comparison of solid-state induced-strain actuators," *Journal of Intelligent Materials, Systems, and Structures*, vol. 7, pp. 4-14, 1996.
- [10] R. H. Baughman, "Conducting polymer artificial muscles," *Synthetic Metals*, vol. 78, pp. 339-353, 1996.
- [11] Z.-Y. Cheng, V. Bharti, T.-B. Xu, H. Xu, T. Mai, and Q. M. Zhang, "Electrostrictive poly(vinylidene fluoride-trifluoroethylene) copolymers," *Sensors and Actuators A*, vol. 90, pp. 138-147, 2001.
- [12] R. Pelrine, R. Kornbluh, and G. Kofod, "High-strain actuator materials based on dielectric elastomers," *Advanced Materials*, vol. 12, pp. 1223-1225, 2000.
- [13] R. Kornbluh, R. Pelrine, J. Joseph, R. Heydt, Q. Pei, and S. Chiba, "Highfield electrostriction of elastomeric polymer dielectrics for actuation," *SPIE Electroactive Polymer Actuators*, vol. 3669, pp. 149-161, 1999.
- [14] S. M. Ha, I. S. Park, M. Wissler, R. Pelrine, S. Stanford, K. J. Kim, G. Kovacs, and Q. Pei, "High Electromechanical Performance of Electroelastomers Based on Interpenetrating Polymer Networks," presented at Electroactive Polymer Actuators and Devices (EAPAD) San Diego, CA, 2008.
- [15] K. R. Atkinson, S. C. Hawkins, C. Huynh, C. Skourtis, J. Dai, M. Zhang, S. Fang, A. A. Zakhidov, S. B. Lee, A. E. Aliev, C. D. Williams, and R. H. Baughman, "Multifunctional carbon nanotube yarns and transparent sheets: Fabrication, properties, and applications," *Physica B: Condensed Matter*, vol. 394, pp. 339-343, 2007.

- [16] M. J. Higgins, S. T. McGovern, and G. G. Wallace, "Visualizing Dynamic Actuation of Ultrathin Polypyrrole Films," *Langmuir*, vol. 25, pp. 3627-3633, 2009.
- [17] G. Gao, T. Cagin, and W. Goddard, A. III, "Energetics, structure, mechanical and vibrational properties of single-walled carbon nanotubes," *Nanotechnology*, pp. 184, 1998.
- [18] A. A. Zakhidov, D.-S. Suh, A. A. Kuznetsov, J. N. Barisci, E. Munoz, A. B. Dalton, S. Collins, V. H. Ebron, M. Zhang, J. P. Ferraris, A. A. Zakhidov, and R. H. Baughman, "Electrochemically Tuned Properties for Electrolyte-Free Carbon Nanotube Sheets," *Advanced Functional Materials*, vol. 19, pp. 2266–2272, 2009.
- [19] R. T. Richardson, A. K. Wise, B. C. Thompson, B. O. Flynn, P. J. Atkinson, N. J. Fretwell, J. B. Fallon, G. G. Wallace, R. K. Shepherd, G. M. Clark, and S. J. O'Leary, "Polypyrrole-coated electrodes for the delivery of charge and neurotrophins to cochlear neurons.,," *Biomaterials*, vol. 30, pp. 2614-24, 2009.
- [20] R. Wadhwa, C. F. Lagenaur, and X. T. Cui, "Electrochemically controlled release of dexamethasone from conducting polymer polypyrrole coated electrode," *Journal of Controlled Release*, vol. 110, pp. 531-41, 2006.
- [21] M. A. Moses, H. Brem, and R. Langer, "Novel Delivery Systems in Cancer Chemotherapy," *Science & Medicine*, vol. 9, pp. 264-273, 2003.
- [22] J. Israelachvili, *Intermolecular & Surface Forces*, 2nd ed: Academic Press, 1991.
- [23] K.-L. Yang, S. Yiacoumia, and C. Tsouris, "Monte Carlo simulations of electrical double-layer formation in nanopores," *Journal of Chemical Physics*, vol. 117, pp. 8499-8507, 2002.

- [24] M. Kinoshita, "Structure of aqueous electrolyte solutions near a hydrophobic surface," *Condensed Matter Physics*, vol. 10, pp. 387-396, 2007.

Appendix 1 : Impedance of a pore

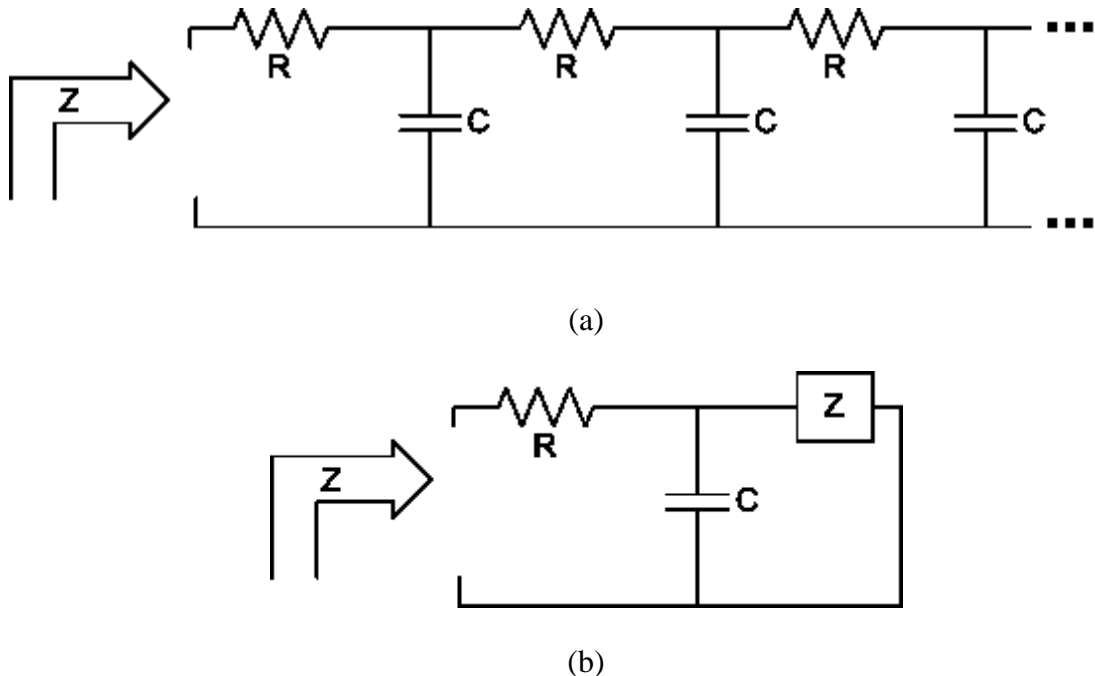


Figure A1.1: (a) An infinite RC ladder network with the impedance, Z and (b) its circuit equivalent.

In order to find the input impedance of the infinite RC ladder circuit in Figure A1.1, we can observe that this circuit can be redrawn as in Figure A1.1b [1, 2]. Based on the latter, the impedance can be easily determined as:

$$Z = \frac{R}{2} \left(1 + \sqrt{1 + \frac{4}{j\omega CR}} \right). \quad (\text{A1.1})$$

Now let us assume that $R = R_0\Delta x$ and $C = C_0\Delta x$, where R_0 and C_0 are the resistance and capacitance per unit length of the material and Δx is a small length along the pore direction. Substituting in Eqn. A1.1, we obtain:

$$\begin{aligned} Z &= \frac{R_0\Delta x}{2} \left(1 + \sqrt{1 + \frac{4}{R_0 C_0 \Delta x^2 j\omega}}\right) = \frac{R_0\Delta x}{2} + \sqrt{\left(\frac{R_0\Delta x}{2}\right)^2 + \left(\frac{R_0\Delta x}{2}\right)^2 \frac{4}{R_0 C_0 \Delta x^2 j\omega}} . \\ &= \frac{R_0\Delta x}{2} + \sqrt{\left(\frac{R_0\Delta x}{2}\right)^2 + \frac{R_0}{C_0 j\omega}} \end{aligned} \quad (\text{A1.2})$$

In the limit, as $\Delta x \rightarrow 0$:

$$\lim_{\Delta x \rightarrow 0} Z = \sqrt{\frac{R_0}{j\omega C_0}} \quad (\text{A1.3})$$

Therefore, the impedance of such an RC network can be calculated as:

$$Z = \sqrt{\frac{R_0}{j\omega C_0}} \quad (\text{A1.4})$$

References

- [1] J. R. Macdonald and W. R. Kenan, *Impedance Spectroscopy: Emphasizing Solid Materials and Systems*: Wiley-Interscience 1987.
- [2] W. Scheider, "Theory of Frequency Dispersion of Electrode Polarization. Topology of Networks with Fractional Power Frequency Dependence," *Journal of Physical Chemistry*, vol. 79, pp. 127-136, 1975.

Appendix 2 : Calculation of the repulsion between two parallel planar electrodes in an electrolyte

A2.1. Calculation of the potential between the electrodes

Imagine two planar electrodes separated by a distance of d submersed in an electrolyte, with a potential of ϕ_0 applied to both. We would like to first find the distribution of charges if the double layers interact and influence each other. A few works have looked into this problem [1-3].

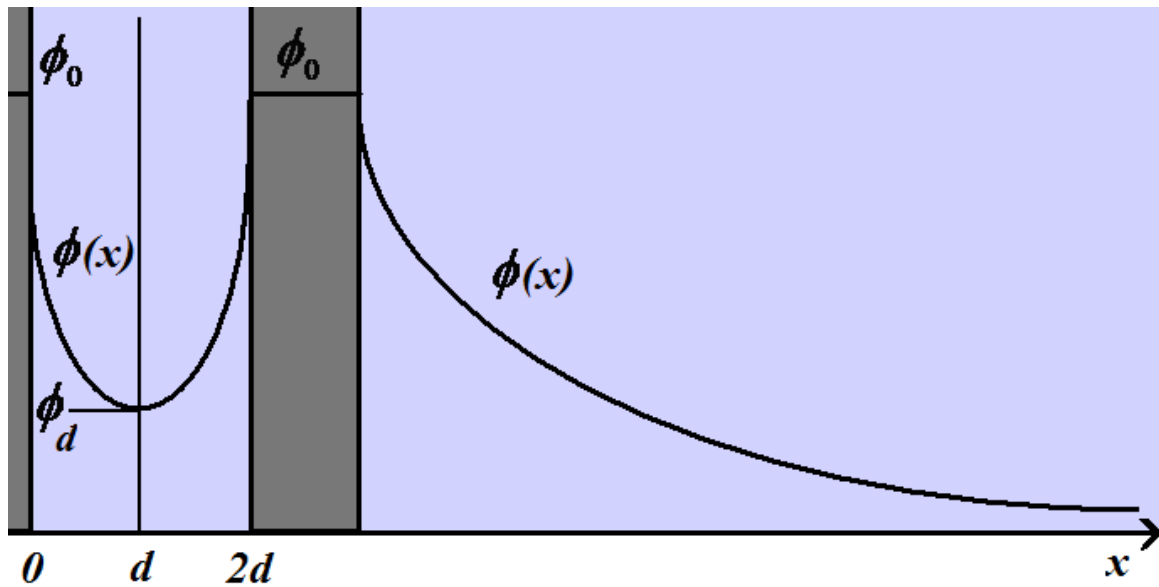


Figure A2.1: Potential profile between and outside two planar electrodes separated by a distance of d in an electrolyte with their double-layers interacting.

Poisson's equation can be written in electrostatic units as

$$\nabla^2 \phi = \frac{4\pi\rho}{\epsilon}, \text{ (SI: } \nabla^2 \phi = \frac{\rho}{\epsilon\epsilon_0} \text{)}$$

where ϕ is the electric potential, ρ is the spatial charge density and ε is the dielectric constant of the electrolyte. Assuming we have both positive and negative ions with same valencies in the electrolyte, the volumetric charge density can be determined from the number of positive and negative ions as

$$\rho = ze_0(n^+ - n^-),$$

where z is valency of the ions and e_0 is the fundamental charge. If the electrode surface charge is thought to be positive, negative ions will be attracted to the surface and positive ions will be repelled. The effect of these electric forces is counteracted by the thermal motion of the ions, which gives the charge layer its spatial ‘diffuse’ character. Here, similar to Bard and Faulkner [4], we assume that the average concentration of the ions at a given point in the electrolyte can be found from the value of the electric potential at the same point with the aid of Boltzmann’s equation:

$$\begin{cases} n^+ = n_0 e^{-\frac{ze_0\phi}{kT}} \\ n^- = n_0 e^{\frac{ze_0\phi}{kT}} \end{cases}$$

Here ϕ is the electric potential, n_0 is the number of ions per volume unit far from the surface where $\phi = 0$, k is Boltzmann’s constant and T is the absolute temperature. The main assumptions made are the following:

- I. The work required to move an ion from the bulk to a position inside the diffuse layer is electrostatic (no friction etc.)
- II. The ions are treated as point charges

III. The solvent is treated as a dielectric having a fixed dielectric constant
Substituting, we have:

$$\rho = ze_0(n^+ - n^-) = ze_0(n_0 e^{-\frac{ze_0\phi}{kT}} - n_0 e^{\frac{ze_0\phi}{kT}}) = -2n_0 ze_0 \sinh(\frac{ze_0\phi}{kT})$$

Now if we substitute this value for ρ into Poisson's equation, we obtain

$$\nabla^2 \phi = -\frac{8\pi n_0 ze_0}{\epsilon} \sinh(\frac{ze_0\phi}{kT}), (\text{SI: } \nabla^2 \phi = -\frac{2n_0 ze_0}{\epsilon \epsilon_0} \sinh(\frac{ze_0\phi}{kT})) \quad (1)$$

Following Verwey and Overbeek [3] and considering only one dimension x in Poisson's equation, we introduce the new variables

$$y = \frac{ze_0\phi}{kT} \text{ and } \xi = \sqrt{\frac{8\pi n_0}{\epsilon kT}} e_0 z x$$

(In SI: $\xi = \sqrt{\frac{2n_0 e_0^2 z^2}{\epsilon \epsilon_0 kT}} x$, where $\kappa = \sqrt{\frac{2n_0 e_0^2 z^2}{\epsilon \epsilon_0 kT}}$ is the inverse of the Debye length).

This way the fundamental differential equation (1) above can be written as

$$\frac{d^2 y}{d\xi^2} = \sinh(y)$$

Integrating once, we obtain

$$(\frac{dy}{d\xi})^2 = 2 \cosh(y) + c$$

The boundary conditions are $y = \frac{ze_0\phi_d}{kT}$ and $\frac{dy}{d\xi} = 0$ both at $x = d$.

Therefore $c = -2 \cosh(\frac{ze_0\phi_d}{kT})$ and $(\frac{dy}{d\xi})^2 = 2 \cosh(y) - 2 \cosh(\frac{ze_0\phi_d}{kT})$

In other words

$$\frac{d\phi}{dx} = \sqrt{\frac{8\pi n_0 kT}{\varepsilon}} \sqrt{2 \cosh(\frac{ze_0\phi}{kT}) - 2 \cosh(\frac{ze_0\phi_d}{kT})},$$

$$(\text{In SI: } \frac{d\phi}{dx} = \sqrt{\frac{2n_0 kT}{\varepsilon\varepsilon_0}} \sqrt{2 \cosh(\frac{ze_0\phi}{kT}) - 2 \cosh(\frac{ze_0\phi_d}{kT})}) \quad (2)$$

If necessary, this equation can be numerically integrated to find the potential at any desired point in the electrolyte between the electrodes. Outside the electrodes, the potential and the charge distribution are similar to those found in [4] for a single planar electrode.

A2.2. *Calculation of the repulsion force between the planar electrodes*

Because of the electrostatic force on the ions in the double-layer, there is a stress applied on them which will compress the ions in the double-layer towards the electrode. This stress can be identified with Maxwell stress, $\frac{1}{2}\varepsilon E^2$. Using electrostatic units

(statcoulombs, etc.) this equation will appear as $\frac{\varepsilon}{8\pi}E^2 = \frac{\varepsilon}{8\pi}(\frac{d\phi}{dx})^2$, (SI:

$\frac{1}{2}\varepsilon\varepsilon_0 E^2 = \frac{\varepsilon\varepsilon_0}{2}(\frac{d\phi}{dx})^2$) [5]. This force is equal to zero in the middle of the gap between

the two electrodes ($x = d$), because there $\frac{d\phi}{dx} = 0$ (Figure A2.1). The maximum stress is

at $x = 0$, where the electric field has its largest value and $\frac{\epsilon}{8\pi} \left(\frac{d\phi}{dx} \right)^2 \Big|_{x=0}$, (SI:

$\frac{1}{2} \epsilon \epsilon_0 \left(\frac{d\phi}{dx} \right)^2 \Big|_{x=0}$). This can be seen from Figure A2.1 for $x = 0$, because there the

potential ϕ changes most rapidly as a function of x . A stress equal and opposite to the latter stress is applied directly on to the electrode surface. Therefore for two plates at distance d_0 the stress pushing the planar electrodes together will be:

$$\sigma_{attractive} = \frac{\epsilon}{8\pi} \left(\frac{d\phi}{dx} \Big|_{x=0, d=d_0} \right)^2, \text{ SI: } \sigma_{attractive} = \frac{1}{2} \epsilon \epsilon_0 \left(\frac{d\phi}{dx} \Big|_{x=0, d=d_0} \right)^2$$

However, there is one more force to be taken into the account. The double-layer on the other face of the electrode will similarly apply a stress onto the electrode surface. Since this force is in the opposite direction to the first force, it will push the electrode planes together. This stress component can be computed by assuming a third parallel planar electrode very far away and computing the repulsive force between the two electrodes with a distance of $d \rightarrow \infty$. Therefore the stress pushing the electrodes apart can be written as:

$$\sigma_{repulsive} = \frac{\epsilon}{8\pi} \left(\frac{d\phi}{dx} \Big|_{x=0, d \rightarrow \infty} \right)^2, \text{ (SI: } \sigma_{repulsive} = \frac{1}{2} \epsilon \epsilon_0 \left(\frac{d\phi}{dx} \Big|_{x=0, d \rightarrow \infty} \right)^2)$$

The net repulsive stress can be found to be

$$p = \frac{\epsilon}{8\pi} \left\{ \left(\frac{d\phi}{dx} \Big|_{x=0, d \rightarrow \infty} \right)^2 - \left(\frac{d\phi}{dx} \Big|_{x=0, d=d_0} \right)^2 \right\}, \text{ (SI: } p = \frac{1}{2} \epsilon \epsilon_0 \left\{ \left(\frac{d\phi}{dx} \Big|_{x=0, d \rightarrow \infty} \right)^2 - \left(\frac{d\phi}{dx} \Big|_{x=0, d=d_0} \right)^2 \right\})$$

Using equation (2) above:

$$\frac{d\phi}{dx} = \sqrt{\frac{8\pi n_0 kT}{\varepsilon}} \sqrt{2 \cosh(\frac{ze_0\phi}{kT}) - 2 \cosh(\frac{ze_0\phi_d}{kT})}, \text{ (SI: } \frac{d\phi}{dx} = \sqrt{\frac{2n_0 kT}{\varepsilon\varepsilon_0}} \sqrt{2 \cosh(\frac{ze_0\phi}{kT}) - 2 \cosh(\frac{ze_0\phi_d}{kT})})$$

When $d \rightarrow \infty$, $\phi_d \rightarrow 0$. Therefore:

$$(\frac{d\phi}{dx}) \Big|_{\substack{x=0, \\ d \rightarrow \infty}} = \sqrt{\frac{8\pi n_0 kT}{\varepsilon}} \sqrt{2 \cosh(\frac{ze_0\phi_0}{kT}) - 2},$$

$$\text{SI: } (\frac{d\phi}{dx}) \Big|_{\substack{x=0, \\ d \rightarrow \infty}} = \sqrt{\frac{2n_0 kT}{\varepsilon\varepsilon_0}} \sqrt{2 \cosh(\frac{ze_0\phi_0}{kT}) - 2}$$

$$(\frac{d\phi}{dx}) \Big|_{\substack{x=0, \\ d=d_0}} = \sqrt{\frac{8\pi n_0 kT}{\varepsilon}} \sqrt{2 \cosh(\frac{ze_0\phi_0}{kT}) - 2 \cosh(\frac{ze_0\phi_d}{kT})}$$

$$\text{SI: } (\frac{d\phi}{dx}) \Big|_{\substack{x=0, \\ d=d_0}} = \sqrt{\frac{2n_0 kT}{\varepsilon\varepsilon_0}} \sqrt{2 \cosh(\frac{ze_0\phi_0}{kT}) - 2 \cosh(\frac{ze_0\phi_d}{kT})}$$

So the repulsive stress will be

$$p = 2n_0 kT (\cosh(\frac{ze_0\phi_d}{kT}) - 1)$$

Interestingly, Langmuir [6] arrives at the exact same conclusion using only osmotic pressure concepts. His approach can be summarized as follows:

When a potential is applied to the planar electrodes, oppositely-charged ions are accumulated around them, resulting in an excess of ions in the space between. Assuming a positive potential is applied to the parallel planar electrodes, the increase in the number

of the negative ions at $x = d$ is $n_0 e^{\frac{ze_0\phi_d}{kT}} - n_0$. This quantity will always be larger than the

decrease in the number of the positive ions at the same plane, which is $n_0 - n_0 e^{-\frac{ze_0\phi_d}{kT}}$.

Therefore the total increase in the concentration of ions at $x = d$ will be

$$n_0 e^{\frac{ze_0\phi_d}{kT}} - n_0 - (n_0 - n_0 e^{-\frac{ze_0\phi_d}{kT}}) = 2n_0 (\cosh(\frac{ze_0\phi_d}{kT}) - 1)$$

The force pushing the electrodes apart can be found as the difference between the osmotic pressures in the middle of the distance between the planes ($x = d$) and the osmotic pressure far away from the electrodes. Therefore, the repulsive stress is

$$p = 2n_0 kT (\cosh(\frac{ze_0\phi_d}{kT}) - 1)$$

It seems that the equivalence of the two methods results from the fact that both are based on a double layer theory involving the equilibrium between the electric and osmotic (thermal diffusion) forces acting on the ions in the solution [3].

A2.3. *Finding the repulsive stress at low and high*

potentials:

We have so far found a quantitative relationship between the repulsive stress and the potential at the midpoint plane between the electrodes. We now need to find a relationship that relates the repulsive stress to the potential applied to the electrodes. We shall here study two cases, namely low applied potentials and high applied potentials. If the potential applied to the electrodes is low, the electric potential of one electrode at the other electrode can be assumed to be negligible. Therefore, as an approximation, one can assume that the potential at the midpoint can be found simply by adding the potentials from the two electrodes.

Therefore we have $\phi_d = 2\phi'_d$, where ϕ'_d is the potential that would exist at a distance of d from a single double-layer. The potential of a single double-layer at a distance of x from the surface is found using Gouy-Chapman theory as

$$y = 2 \ln \frac{1 + \gamma e^{-\xi}}{1 - \gamma e^{-\xi}}, \text{ with } \gamma = \frac{e^{\frac{z}{2}} - 1}{e^{\frac{z}{2}} + 1} \quad (\text{SI: } \phi = 2 \frac{kT}{ze_0} \ln \frac{1 + \gamma e^{-\kappa x}}{1 - \gamma e^{-\kappa x}}, \text{ with } \gamma = \frac{e^{\frac{ze_0\phi_0}{2kT}} - 1}{e^{\frac{ze_0\phi_0}{2kT}} + 1}).$$

If $\kappa x \gg 1$ (meaning that we are far enough from the electrode), then the above expression(s) can be simplified to yield

$$y = 2 \ln \frac{1 + \gamma e^{-\xi}}{1 - \gamma e^{-\xi}} \cong 2 \ln(1 + 2\gamma e^{-\xi}), \text{ for } \frac{1+x}{1-x} \cong 1 + 2x \text{ when } x \text{ is small. Moreover,}$$

$$y \cong 2 \ln(1 + 2\gamma e^{-\xi}) \cong 4\gamma e^{-\xi}.$$

In SI units this will look as

$$\phi \cong 4 \frac{\frac{ze_0\phi_0}{2kT} - 1}{\frac{ze_0\phi_0}{2kT} + 1} e^{-\kappa x}$$

This equation gives the potential at any point in the diffuse layer as a function of the potential applied to the electrode and the distance from it. So the potential from one of the

two electrodes at a distance of d from it will be: $\phi'_d \cong 4 \frac{\frac{ze_0\phi_0}{2kT} - 1}{\frac{ze_0\phi_0}{2kT} + 1} e^{-\kappa d}$ and

$\phi_d \cong 8 \frac{\frac{ze_0\phi_0}{2kT} - 1}{\frac{ze_0\phi_0}{2kT} + 1} e^{-\kappa d}$. The repulsive force can be found from $p = 2nkT(\cosh(\frac{ze_0\phi_d}{kT}) - 1)$ as

before. At very high applied potentials (See Verwey, P.72),

$$\kappa d = 2e^{-\frac{ze_0\phi_d}{2kT}} \text{arcCos}(e^{-\frac{ze_0(\phi_0-\phi_d)}{2kT}})$$

References

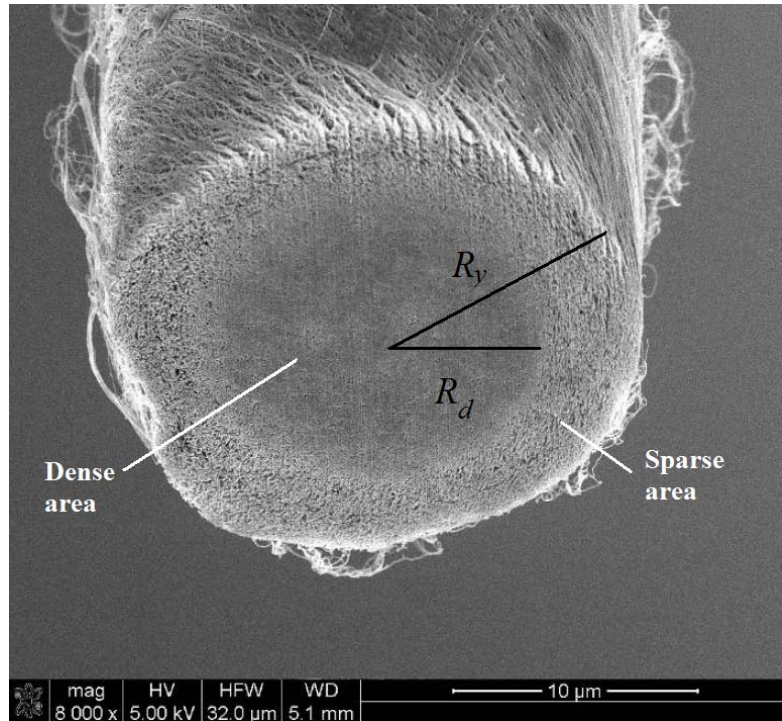
- [1] J. J. Bikerman, *Physical Surfaces*. U.S.: Academic Press Inc., 1970.
- [2] B. V. Derjaguin, N. V. Churaev, and V. M. Muller, *Surface Forces*. New York: Consultants Bureau 1987.
- [3] E. J. W. Verwey and J. T. G. Overbeek, *Theory of the stability of lyophobic colloids: The interaction of sol particles having an electric double layer*. Amsterdam: Elsevier Publishing Company, 1948.
- [4] A. J. Bard and L. R. Faulkner, *Electrochemical Methods, Fundamentals and Applications*. New York: Wiley, 1980.
- [5] B. V. Derjaguin, "On the repulsive forces between charged colloid particles and on the theory of slow coagulation and stability of lyophobe sols," *Transactions of the Faraday Society* vol. 35, pp. 203-215, 1940.
- [6] I. Langmuir, "The Role of Attractive and Repulsive Forces in the Formation of Tactoids, Thisotropic Gels, Protein Crystals and Coacrevates," *Journal of Chemical Physics*, vol. 6, pp. 873-896, 1938.

Appendix 3 : The tensile moduli of the dense and sparse parts

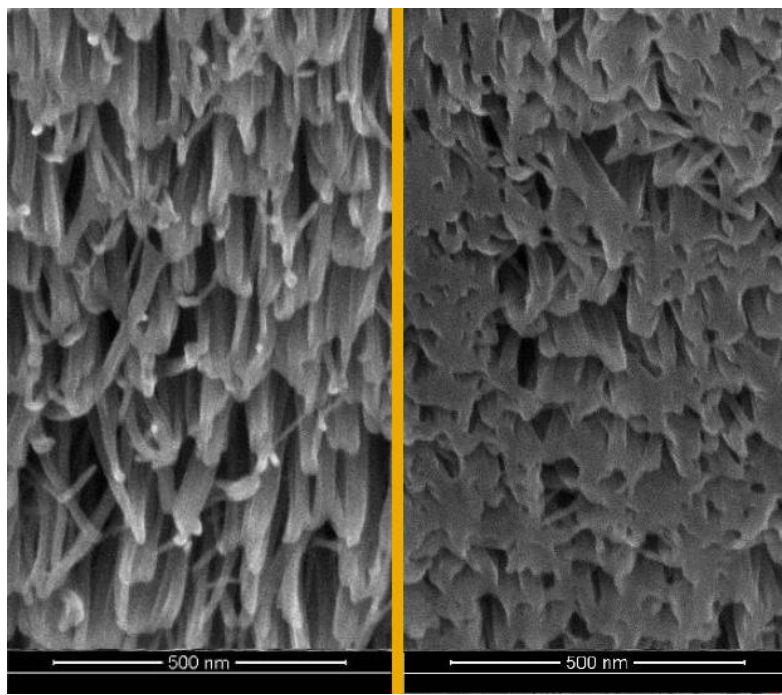
A3.1. Actuation stress and strain from the sparse part of the yarn

Assume that all the ions and solvent volume is added into the sparse part of the yarn, and the dense part only changes length under the actuation forces generated by the actuation of the sparse part. In this case, both the radius and the length of the sparse part vary, changing to R_o and l from their initial values of R_y and l_0 . Meanwhile, but the radius of the dense core R_i stays relatively constant:

$$\begin{aligned}
 \Delta V = V - V_0 &= \underbrace{\pi R_o^2 l - \pi R_i^2 l}_{\text{volume of sparse part after actuation}} - \underbrace{(\pi R_y^2 l_0 - \pi R_i^2 l_0)}_{\text{volume of sparse part before actuation}} \\
 &= \pi R_o^2 l - \pi R_i^2 l - \pi R_y^2 l_0 + \pi R_i^2 l_0 \\
 &= \pi R_y^2 (1 + \varepsilon_R)^2 l_0 (1 + \varepsilon) - \pi R_i^2 l_0 (1 + \varepsilon) - \pi R_y^2 l_0 + \pi R_i^2 l_0 \\
 &\cong \pi R_y^2 l_0 [(1 + 2\varepsilon_R)(1 + \varepsilon) - 1] - \pi R_i^2 l_0 \varepsilon \\
 &= \pi R_y^2 l_0 [2\varepsilon_R + \varepsilon] - \pi R_i^2 l_0 \varepsilon \\
 &= 2\pi R_y^2 l_0 \varepsilon_R + \pi l_0 \varepsilon (R_y^2 - R_i^2)
 \end{aligned}$$



(a)



(b)

Figure A3.1: (a) scanning electron micrograph of the cross section of the yarn, showing its dense core and sparse outer ring and (b) close up SEMs of the sparse and dense parts; repeated from Chapter 7 for the reader's convenience.

We know that $\varepsilon_R = -\frac{\varepsilon}{4\pi^2 \alpha R_y^2 T_0^2}$

$$\Delta V = -2\pi R_y^2 l_0 \frac{\varepsilon}{4\pi^2 \alpha R_y^2 T_0^2} + \pi l_0 \varepsilon (R_y^2 - R_i^2)$$

$$= [(1 - \frac{R_i^2}{R_y^2}) - \frac{2}{4\pi^2 R_y^2 \alpha T_0^2}] \pi R_y^2 l_0 \varepsilon$$

$$\varepsilon = \frac{\Delta V}{\pi R_y^2 l_0 ((1 - (\frac{R_i}{R_y})^2) - \frac{2}{4\pi^2 R_y^2 \alpha T_0^2})}$$

This actuation strain would exert a force, which can be found by multiplying the above strain by the modulus of the sparse part of the yarn, Y_s . So we temporarily turn our attention to finding this modulus.

A3.2. Tensile moduli of the sparse and dense sections of the yarn

The modulus of the yarn itself is about 15 GPa [1]. According to Hearle [2], the modulus of a twisted yarn varies with $\cos^2 \theta$, where θ is the twist angle on the surface of the yarn. The dense part of the yarn forms a yarn of smaller diameter within the main yarn. The effective twist angle on the surface of this yarn is smaller than the twist angle on the surface of the real yarn. The relationship between the twist angle and the radius of a yarn can be found through:

$$\tan \theta_y = 2\pi R_y T, \tan \theta_d = 2\pi R_d T \Rightarrow \frac{\tan \theta_y}{\tan \theta_d} = \frac{R_y}{R_d}$$

$$\tan \theta_d = \frac{R_d \tan \theta_y}{R_y}$$

$$\cos^2 \theta_d = \frac{1}{1 + \tan^2 \theta_d} = \frac{1}{1 + (\frac{R_d \tan \theta_y}{R_y})^2}$$

$$\frac{Y_d}{Y_y} = \frac{\cos^2 \theta_d}{\cos^2 \theta_y} = \frac{1 + \tan^2 \theta_y}{1 + (\frac{R_d}{R_y})^2 \tan^2 \theta_y}$$

$$Y_d = Y_y \frac{1 + 4\pi^2 R_y^2 T^2}{1 + 4\pi^2 R_d^2 T^2}$$

$$f = f_d + f_u = \varepsilon Y_d S_d + \varepsilon Y_u S_u$$

$$\sigma = \frac{f}{S_y} = \frac{\varepsilon Y_d S_d + \varepsilon Y_u S_u}{S_y}$$

$$Y = \frac{\sigma}{\varepsilon} = \frac{Y_d S_d + Y_u (S_y - S_d)}{S_y}$$

$$YS_y = Y_d S_d + Y_s (S_y - S_d)^1$$

¹ One possibility is to say that $Y_d = n Y_s$, so $Y_s = \frac{Y}{(n-1)(\frac{R_d}{R_y})^2 + 1}$

Remember

that,

$$\rho_y = \frac{m_d + m_s}{v_y} = \frac{\rho_d v_d + \rho_s v_s}{\pi R_y^2 l_y} = \frac{\rho_d \pi R_d^2 l_y + \rho_s \pi (R_y^2 - R_d^2) l_y}{\pi R_y^2 l_y} = \frac{\rho_d R_d^2 + \rho_s (R_y^2 - R_d^2)}{R_y^2}$$

and, assume $\rho_d = n\rho_s$:

$$\rho_y = \frac{n\rho_s R_d^2 + \rho_s (R_y^2 - R_d^2)}{R_y^2} = \frac{(n-1)R_d^2 + R_y^2}{R_y^2} \rho_s = ((n-1)\frac{R_d^2}{R_y^2} + 1)\rho_s$$

$$\rho_s = \frac{\rho_y}{(n-1)\frac{R_d^2}{R_y^2} + 1}, \quad \rho_d = \frac{n\rho_y}{(n-1)\frac{R_d^2}{R_y^2} + 1} \text{ so } \frac{\rho_d}{\rho_y} = \frac{n}{(n-1)\frac{R_{dense}^2}{R_y^2} + 1}.$$

The effective fibre densities are also scaled by the same factor, i.e.

$$\frac{E_{fd}}{E_{fy}} = \frac{n}{(n-1)\frac{R_{dense}^2}{R_y^2} + 1}$$

$$YS_y = Y \frac{n}{(n-1)\frac{R_{dense}^2}{R_y^2} + 1} \frac{\cos^2 \theta}{\cos^2 \alpha} S_d + Y_s (S_y - S_d)$$

$$S_y - \frac{n}{(n-1)\frac{R_{dense}^2}{R_y^2} + 1} \frac{\cos^2 \theta}{\cos^2 \alpha} S_d = 1 - \frac{n}{(n-1)\frac{R_d^2}{R_y^2} + 1} \frac{\cos^2 \theta}{\cos^2 \alpha} S_y$$

$$Y_s = Y \frac{S_y - \frac{n}{(n-1)\frac{R_{dense}^2}{R_y^2} + 1} \frac{\cos^2 \theta}{\cos^2 \alpha} S_d}{S_y - S_d} = Y \frac{1 - \frac{n}{(n-1)\frac{R_d^2}{R_y^2} + 1} \frac{\cos^2 \theta}{\cos^2 \alpha} S_y}{1 - \frac{S_d}{S_y}}$$

$$Y_s = Y \frac{\frac{1}{(n-1) + \frac{R_y^2}{R_{dense}^2}} \frac{\cos^2 \theta}{\cos^2 \alpha}}{\frac{1 - \frac{R_d^2}{R_y^2}}{1 - \frac{R_d^2}{R_y^2}}} = Y \frac{\frac{n}{(n-1) + \frac{R_y^2}{R_d^2}} \frac{1 + 4\pi^2 R_y^2 T^2}{1 + 4\pi^2 R_d^2 T^2}}{\frac{1 - \frac{R_d^2}{R_y^2}}{1 - \frac{R_d^2}{R_y^2}}}^2$$

$$Y_s = Y \frac{\frac{n R_d^2 (1 + 4\pi^2 R_y^2 T^2)}{(n-1) R_d^2 + R_y^2 + 4\pi^2 R_d^4 T^2 (n-1) + 4\pi^2 R_y^2 R_d^2 T^2}}{\frac{1 - \frac{R_d^2}{R_y^2}}{1 - \frac{R_d^2}{R_y^2}}}$$

$$Y_s = Y \frac{\frac{(n-1) R_d^2 + R_y^2 + 4\pi^2 R_d^4 T^2 (n-1) + 4\pi^2 R_y^2 R_d^2 T^2 - n R_d^2 (1 + 4\pi^2 R_y^2 T^2)}{(n-1) R_d^2 + R_y^2 + 4\pi^2 R_d^4 T^2 (n-1) + 4\pi^2 R_y^2 R_d^2 T^2}}{\frac{1 - \frac{R_d^2}{R_y^2}}{1 - \frac{R_d^2}{R_y^2}}}$$

$$Y_s = Y \frac{\frac{(-1 + 4\pi^2 R_d^2 T^2 (n-1)) (R_d^2 - R_y^2)}{(1 - \frac{R_d^2}{R_y^2}) ((n-1) R_d^2 + R_y^2 + 4\pi^2 R_d^4 T^2 (n-1) + 4\pi^2 R_y^2 R_d^2 T^2)}}{1 - \frac{R_d^2}{R_y^2}}$$

$$Y_s = Y \frac{\frac{(-1 + 4\pi^2 R_d^2 T^2 (n-1)) (R_d^2 - R_y^2)}{(1 - \frac{R_d^2}{R_y^2}) ((n-1) R_d^2 + R_y^2 + 4\pi^2 R_d^4 T^2 (n-1) + 4\pi^2 R_y^2 R_d^2 T^2)}}{1 - \frac{R_d^2}{R_y^2}}$$

$$^2 \text{ In case } n = 1: Y_s = Y \frac{\frac{1 - \frac{1}{(1-1) + \frac{R_y^2}{R_d^2}} \frac{1 + 4\pi^2 R_y^2 T^2}{1 + 4\pi^2 R_d^2 T^2}}{1 - \frac{R_d^2}{R_y^2}}}{1 - \frac{R_d^2}{R_y^2}} = Y \frac{\frac{1 - \frac{R_d^2}{R_y^2} \frac{1 + 4\pi^2 R_y^2 T^2}{1 + 4\pi^2 R_d^2 T^2}}{1 - \frac{R_d^2}{R_y^2}}}{1 - \frac{R_d^2}{R_y^2}}$$

$$Y_s = Y \frac{\frac{R_y^2 (1 + 4\pi^2 R_d^2 T^2) - R_d^2 (1 + 4\pi^2 R_y^2 T^2)}{R_y^2 (1 + 4\pi^2 R_d^2 T^2)}}{1 - \frac{R_d^2}{R_y^2}} = Y \frac{\frac{R_y^2 + 4\pi^2 R_d^2 R_y^2 T^2 - R_d^2 - 4\pi^2 R_d^2 R_y^2 T^2}{(1 + 4\pi^2 R_d^2 T^2) (R_y^2 - R_d^2)}}{1 - \frac{R_d^2}{R_y^2}} = Y \frac{1}{1 + 4\pi^2 R_d^2 T^2}$$

$$Y_s = Y \frac{R_y^2(1 - 4\pi^2 R_d^2 T^2(n-1))}{((n-1)R_d^2 + R_y^2 + 4\pi^2 R_d^4 T^2(n-1) + 4\pi^2 R_y^2 R_d^2 T^2)}$$

$$Y_s = Y \frac{R_y^2(1 - 4\pi^2 R_d^2 T^2(n-1))}{((n-1)R_d^2(1 + 4\pi^2 R_d^2 T^2) + R_y^2(1 + 4\pi^2 R_d^2 T^2))} = Y \frac{1 - 4\pi^2 R_d^2 T^2(n-1)}{((n-1)(\frac{R_d}{R_y})^2 + 1)(1 + 4\pi^2 R_d^2 T^2)}$$

If a tension force, f , is applied to the yarn, part of it will be born by the dense part of the yarn (f_d) and part of it will be born by the outer sparse part (f_s). In that case

$$f = f_d + f_s$$

$$\sigma = \frac{f}{A} = \frac{f_d + f_s}{A} = \frac{\sigma_d A_d + \sigma_s A_s}{A} = \frac{Y_d \varepsilon A_d + Y_s \varepsilon (A - A_d)}{A}$$

$$Y_y = \frac{\sigma}{\varepsilon} = \frac{Y_d A_d + Y_s (A - A_d)}{A}$$

$$Y_y = \frac{Y_d \pi R_d^2 + Y_s \pi (R_y^2 - R_d^2)}{\pi R_y^2} = Y_d (\frac{R_d}{R_y})^2 + Y_s (1 - (\frac{R_d}{R_y})^2)$$

and knowing that $Y_d = Y_y \frac{1 + 4\pi^2 R_y^2 T^2}{1 + 4\pi^2 R_d^2 T^2}$, we obtain:

$$Y_s = Y_y \frac{1 - \frac{1 + 4\pi^2 R_y^2 T^2}{1 + 4\pi^2 R_d^2 T^2} (\frac{R_d}{R_y})^2}{1 - (\frac{R_d}{R_y})^2} = Y_y \frac{1 - \frac{R_d^2 + 4\pi^2 R_d^2 R_y^2 T^2}{R_y^2 + 4\pi^2 R_d^2 R_y^2 T^2}}{1 - (\frac{R_d}{R_y})^2} = Y_y \frac{1}{1 + 4\pi^2 R_d^2 T^2}$$

$$Y_s = Y_y \frac{1}{1 + 4\pi^2 R_d^2 T^2}$$

The force generated from the actuation of the sparse part of the yarn can be found by multiplying this modulus by the expected actuation strain and by the cross sectional area of the sparse part,

$$\varepsilon = \frac{\Delta V}{\pi R_y^2 l_0 ((1 - (\frac{R_d}{R_y})^2) - \frac{2}{4\pi^2 R_y^2 \alpha T_0^2})}.$$

$$f_s = Y_s A_s \frac{\Delta V}{\pi R_y^2 l_0 ((1 - (\frac{R_d}{R_y})^2) - \frac{2}{4\pi^2 R_y^2 \alpha T_0^2})}$$

This force now acts on the whole yarn, while the stiffness of the dense part in the middle of the yarn works against it.

$$\varepsilon_{act} = \frac{f_s}{A_y Y_y} = \frac{Y_s}{Y_y} \frac{\Delta V}{\pi R_y^2 l_0 (1 - \frac{2}{4\pi^2 (R_y^2 - R_d^2) \alpha T_0^2})}$$

This is equation 7.7 in chapter 7

References

1. Mirfakhrai, T., et al., *Electrochemical actuation of carbon nanotube yarns*. Smart Materials and Structures, 2007. **16**(2): p. S243.
2. Hearle, J.W.S., P. Grossberg, and S. Backer, *Structural Mechanics of Fibers, Yarns and Fabrics*. Vol. 1. 1969, New York: Wiley-Interscience.

Appendix 4 Atomic Force Microscopy on the yarn surface

A4.1. Immobilization of the yarn for microscopy

In order to measure the Young's modulus of the yarn in the radial direction, or to detect radial actuation of the yarn using an AFM, or even to image the surface of the yarn with one, it is important that the yarn is properly immobilized and does not move as the AFM tip is scanned across its surface. However, since we believe that the actuation in the yarn is mainly due to rearrangement of the MWNTs and MWNT bundles in the yarn, firmly immobilizing the yarn will probably result in stopping or at least limiting its actuation as well. It is therefore necessary to devise a method to immobilize the yarn for imaging that allows for some reconfiguration.

For this purpose several methods were tried. It was suggested that interactions between the yarn and a surface would be enough to hold the yarn down during imaging. Since no immobilization on a regular glass substrate was observed, and because MWNTs are known to be hydrophobic, it was proposed to try to immobilize it on a glass slide whose surface is functionalized with a hydrophobic group. A glass slide functionalized with octadecyltrichlorosilane (ODTS) resulting in a hydrophobic surface¹. The yarn was placed on this surface and a droplet of water was placed over it. The yarn at first seemed

¹ We acknowledge the assistance of Mr. Adrian Gestos of the IPRI in functionalizing the glass surfaces with various groups.

immobilized on the surface after the water had evaporated, but it was separated from the substrate in a few hours, floating in the container. Functionalizing the glass substrate with (3-aminopropyl) triethoxysilane (APTES), which is a hydrophilic group, had a similar result.

The next immobilization method attempted was electrodepositing a thin layer of gold (Figure A4.1). The yarn was placed on an indium tin oxide (ITO) slide substrate (1) and electrical contact was made to the yarn to the ITO surface (2). The assembly was placed in an electrodeposition bath and a voltage was applied to electrodeposit a thin layer of gold on the assembly (3). It was hoped that little gold would be deposited on the yarn itself due to large potential drop across the contact resistance between the ITO slide and the yarn, while the deposited layer of gold between the ITO and the yarn would be enough to immobilize the yarn on the ITO surface².

² Dr. Scott McGovern has substantially contributed to this part in developing immobilization methods and performing the electrodeposition.

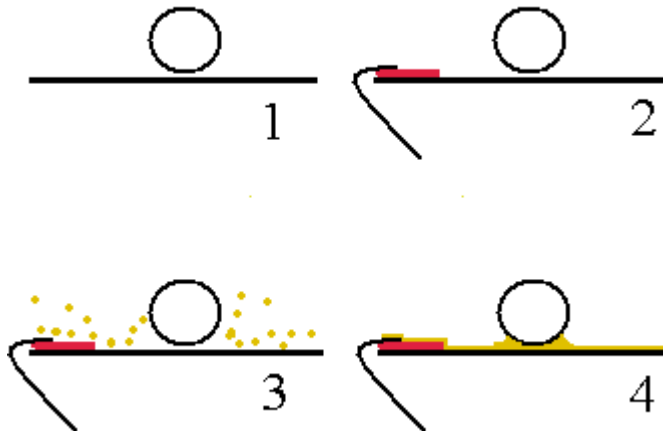


Figure A4.1: Schematic drawing of immobilization of the yarn on a glass slide by gold electrodedeposition

Several samples were made this way using electrodeposition potentials between 3-3.2 V and with various deposition durations between 5 to 20 s. All deposited films were thin enough to see through them. While most samples looked well immobilized to the naked eye (e.g. while shaken or blown on), none remained fix under the AFM and the tip could move them around during scanning.

Finally, immobilization was attempted using UV-cured polyurethane. Uncured precursor was spread thin across a glass slide. The yarn was lowered from above and laid on the spread surface. Polymerization was then performed using a UV light. The sample was then imaged by a profilometer (Veeco) and was found to be well immobilized, while showing a height of about 12 μm above the polymer surface, implying that it was not fully submersed in the polymer. An optical microscope image also shows the yarn resting on top of the polymer surface (Figure A4.2).

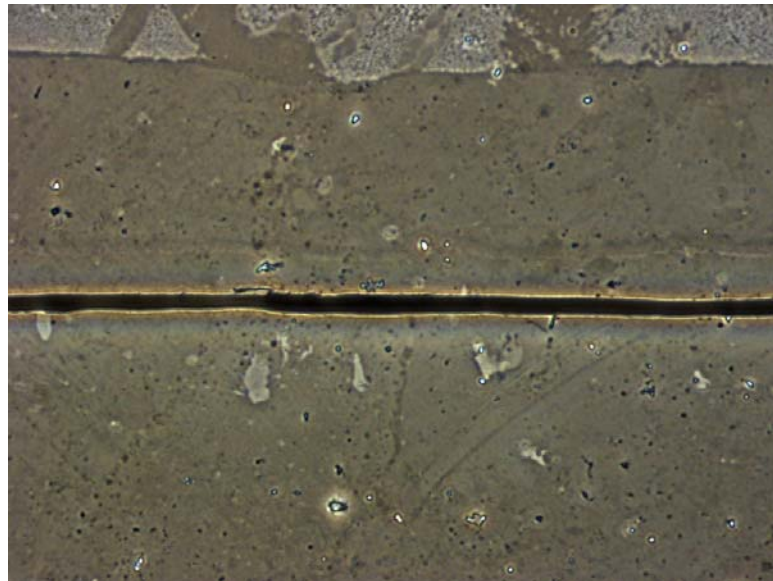


Figure A4.2: Optical microscope image of the yarn, immobilized on a glass slide using a thin layer of UV-cured polyurethane as adhesive.

A4.2. AFM imaging

The yarn was then imaged using AFM (JPK) in tapping mode. A 3D version of the height signal image can be seen in Figure A4.3³

³ Dr. Michael Higgins has made substantial contribution in AFM imaging.

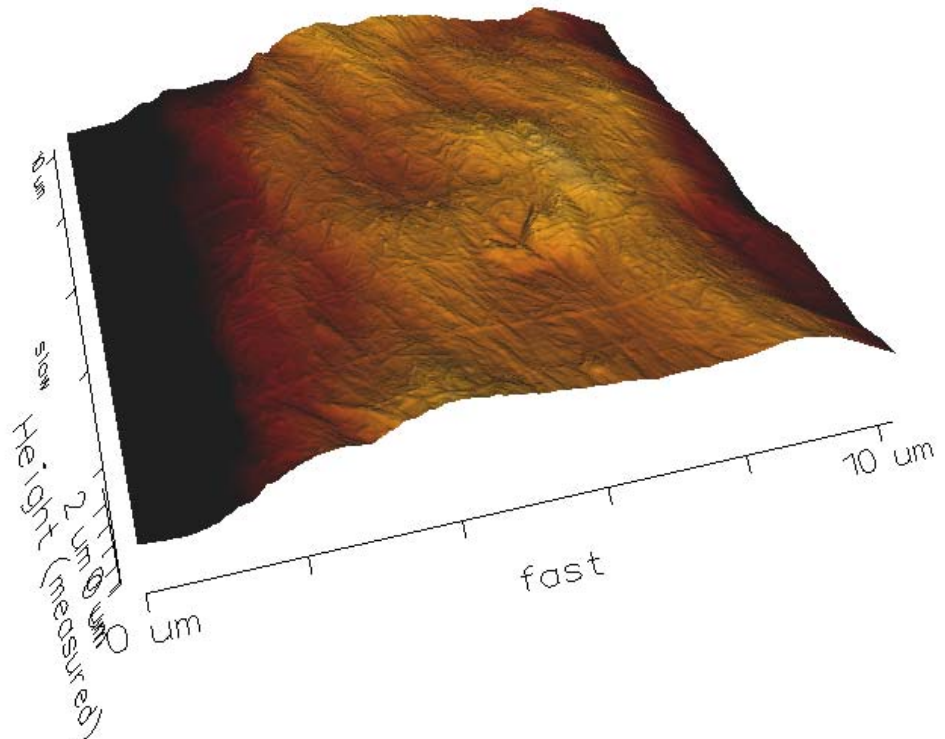


Figure A4.3: A three dimensional rendition of the surface of the yarn, imaged using an atomic force microscope.

The general twist of the fibres can be seen in the height image and was estimated at 20 degrees twist angle using the AFM, well complying with the value measured using the SEM. The amplitude signal shows individual MWNTs or bundles of MWNTs, while still showing the general directionality. Figure A4.4 shows a top view of the same sample. As

can be seen on the edges of this image, the sides of the yarn look smoother. We think this is where the polyurethane has diffused into the yarn and makes the surface look smoother.

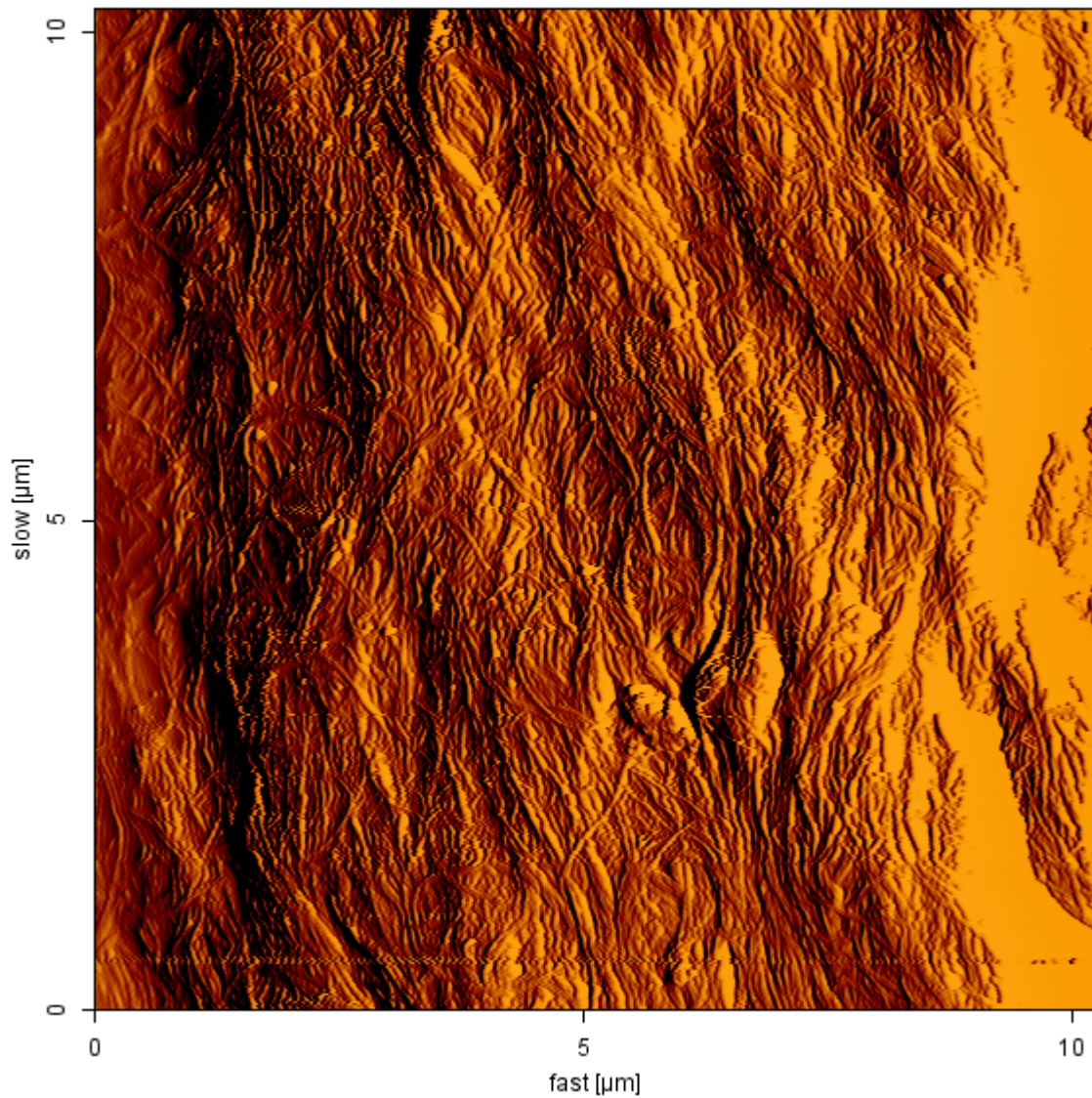


Figure A4.4: Atomic force microscope image of the yarn surface, showing areas to the right and left extremes, smoothed possibly due to the diffusion of polyurethane into the yarn.

A4.3. Force curves

Due to the limited time, no electrochemistry has yet been performed under the AFM on the yarn to see if the polymer allows for any radial expansion. Instead, we decided to use contact mode AFM to estimate the Young's modulus of the yarn in the *radial* direction. It is known that the modulus for MWNT sheets, drawn similar to these yarns from forests, is substantially lower in the transverse direction than in the direction along the length of the MWNTs. No knowledge about the radial modulus of these yarns exists. Mechanical forces between the MWNTs that contribute to the radial stiffness of the yarn can be the same forces that restore the yarn once the electrical stimulus has been removed. Therefore gaining any knowledge about the radial stiffness is essential to finding the restoring force in the yarn and the reversibility of the actuation. Such information can also be used in modeling of the actuation.

Force curves were performed at 3 different points on the yarn surface (Figure A4.5). The curves, shown in Figure A4.6, show a consistent behaviour. The source of noise on the force curves at point 1 is unknown. Another interesting phenomenon is the “dip” observed when the tip makes contact with the yarn surface on the extend curve. Such dips are expected on hydrophilic surfaces, where the surface is usually covered by a thin layer of moisture from air. The water on the surface attracts the tip, resulting in a downward force and the dip. However, since MWNTs are believed to be hydrophobic, the source of the dip in the present case is not known and can be subject to further study.

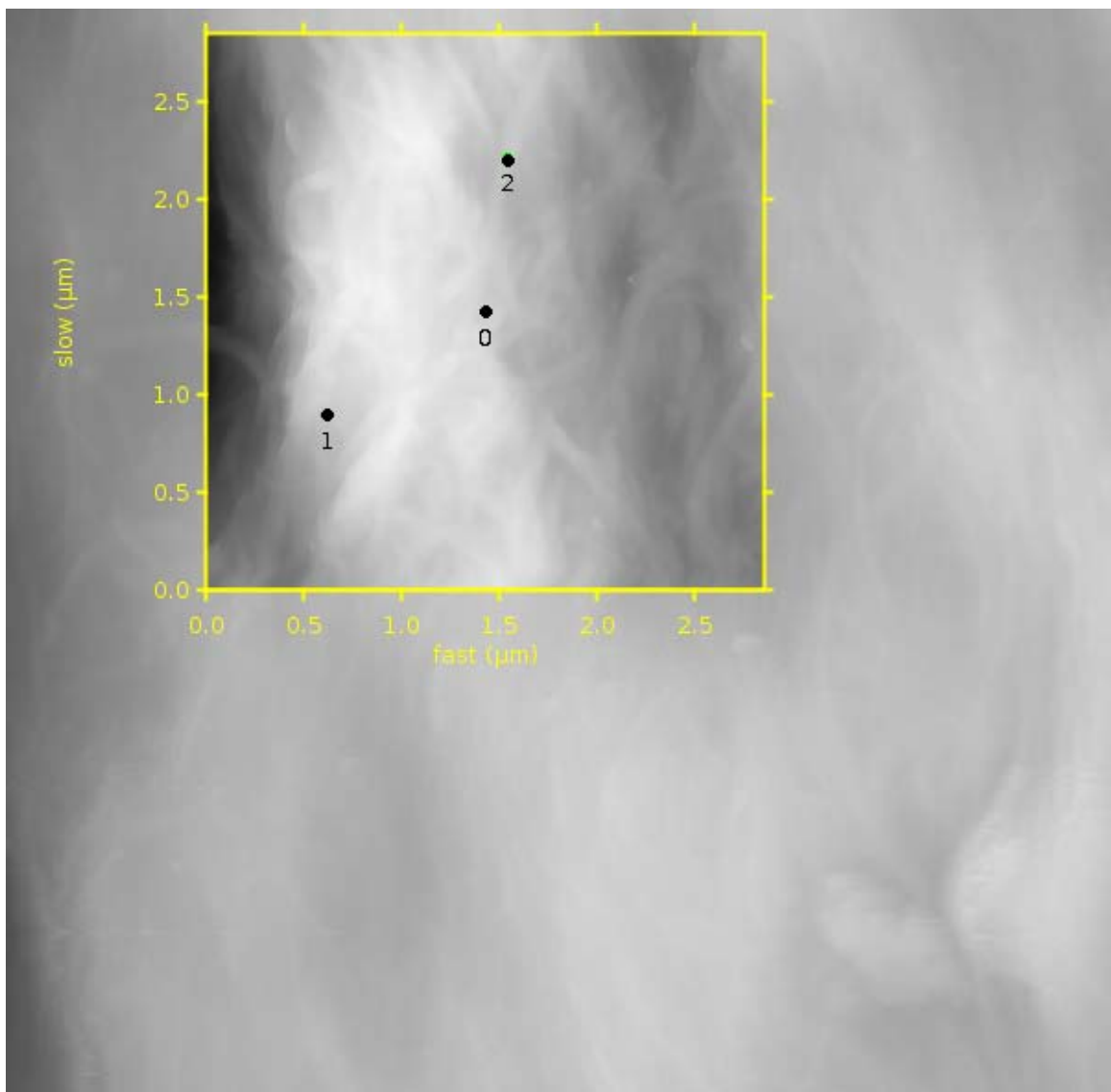


Figure A4.5: Position of the three points selected for force-curve measurements on the yarn, indicated on an AFM image of the yarn surface.

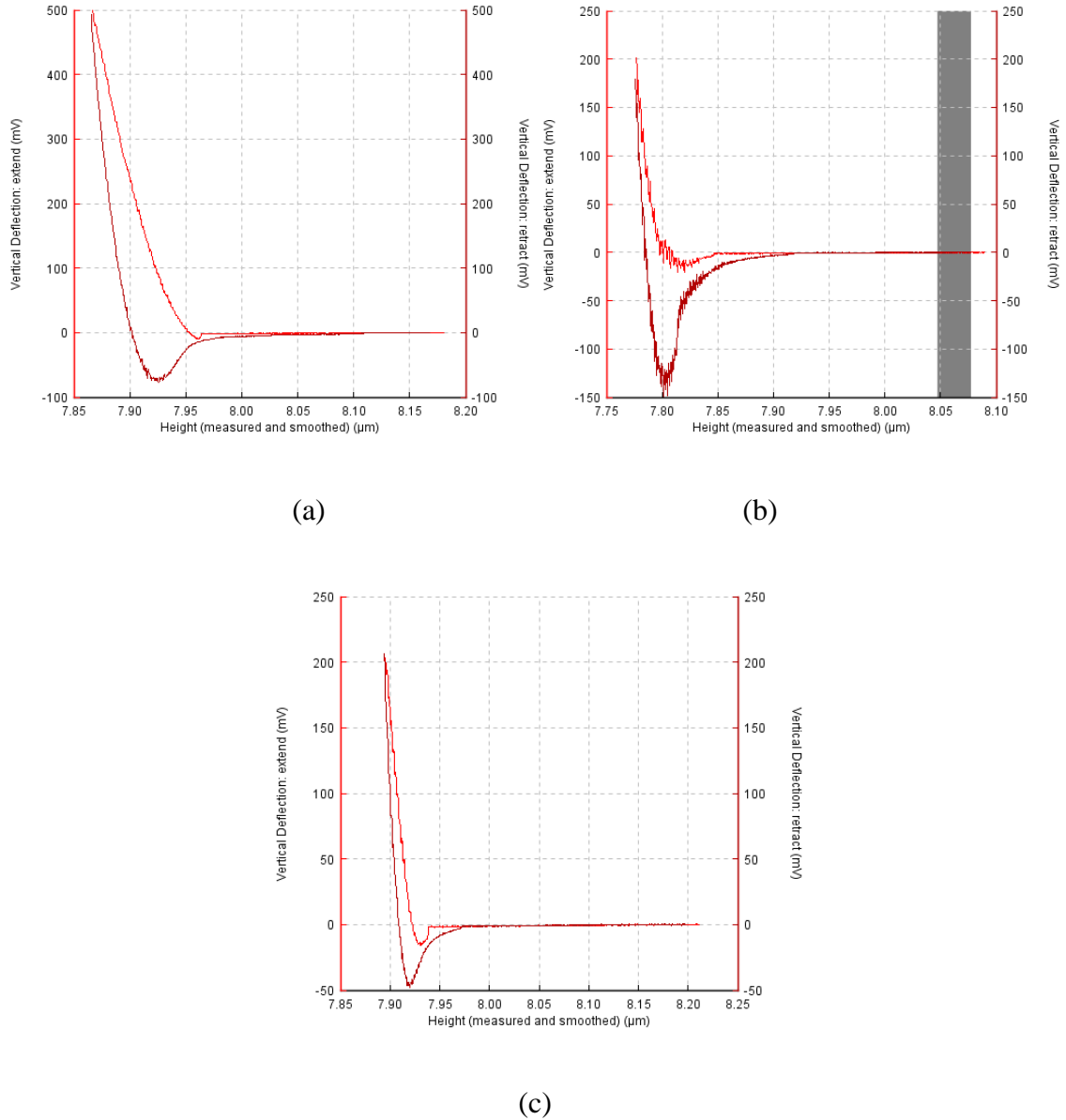


Figure A4.6: Force curve at (a) point 0, (b) point 1, and (c) point 2

A4.4. ***Estimating the radial Young's modulus***

The data was interpreted to estimate the modulus of the yarn in the radial direction both using the method described in [1], and using a fitting routine included in the JPK

processing software that is used to run the atomic force microscope⁴. The former method employs a Hertz model (Figure A4.7). Both methods give results in similar ranges. The tip was assumed to have a spherical shape with a radius of between 10-20 nm. The spring constant of the cantilever was 43 N/m R_{tip} . The fitting parameters were, tip radius, R_{tip} , Poisson's ratio of the yarn, ν , and the Indenter exponent, N . The values thus obtained for the Young's modulus are:

$$Y_{Radial} = 200 - 290 \text{ MPa } (\nu = 0.8, N = 1.5, R_{tip} = 10-20 \text{ nm}, \text{ and } \nu = 0.8)$$

or

$$Y_{Radial} = 420 - 590 \text{ MPa } (\nu = 0.5, N = 1.5, R_{tip} = 10-20 \text{ nm}).$$

The range given for the modulus is due to the range used for R_{tip} . The assumptions and limitations of this estimation method must be further studied before a value can be assigned to the modulus with enough certainty. However, the fact both methods result in similar values, and that the order of magnitude of the estimated modulus above does not seem to depend on the values of tip radius and Poisson's ratio of the yarn within the acceptable ranges show that these values should be in the correct order of magnitude.

⁴ The interpretation of the data and the Hertz model are done by Dr. Michael Higgins.

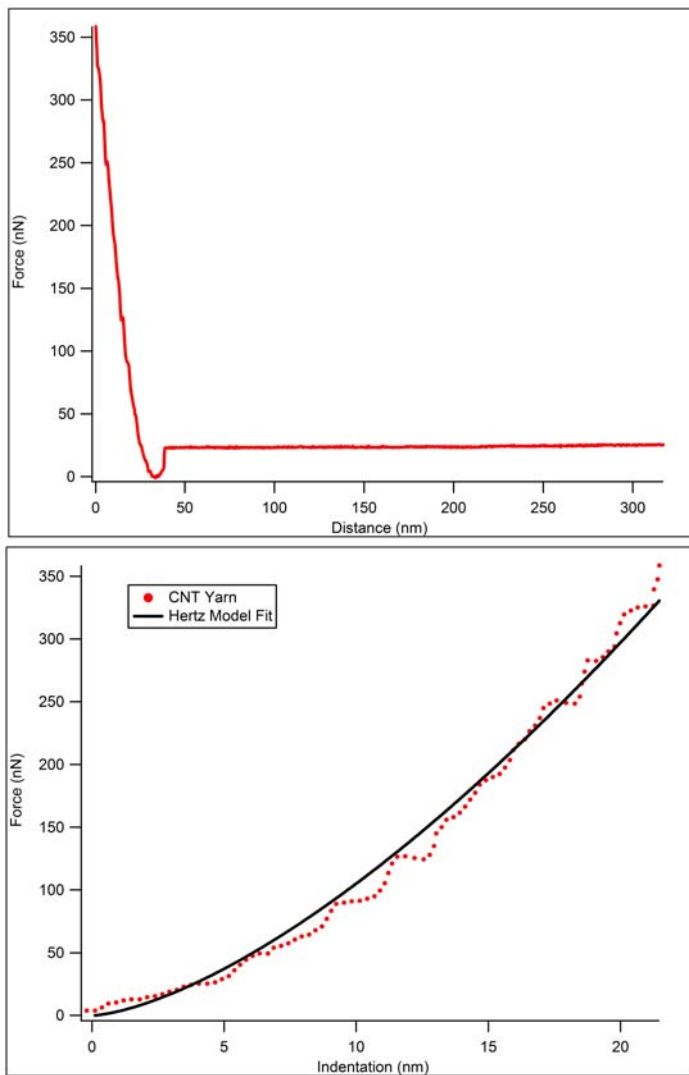


Figure A4.7: Hertz model fit to a force curve data to estimate the radial modulus

A4.5. Future direction

It has been suggested that if the yarn is immobilized on a glass slide such that short length of it sticks out of the glass slide edge, and if the length sticking out is not much larger than the diameter of the yarn, then it may be possible to apply a potential to the yarn while imaging the free end of the yarn with an AFM, thus observing the radial actuation unhindered.

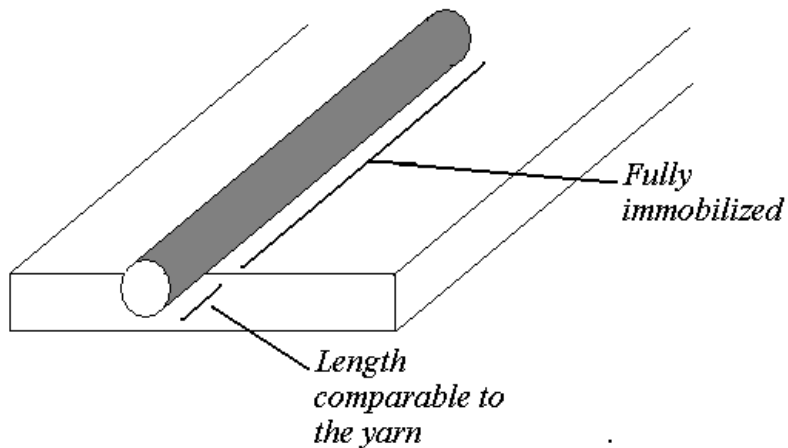


Figure A4.8: Schematic design for a suggested setup to measure radial actuation of the yarn while it is immobilized

References

- [1] H.-J. r. Butt, B. Cappella, and M. Kappl, "Force measurements with the atomic force microscope: Technique, interpretation and applications," *Surface Science Reports*, vol. 59, pp. 1-152, 2005.

Appendix 5 : Undersampled Sensor current

Analysis

It was shown in chapter 6 that an impulse-like current is generated by the yarn when the mechanical tensile load on the yarn is abruptly changed. However, while in those experiments the magnitude of change in tensile load was fixed for every cycle (Figure 6.2a), the magnitude of the observed sensor current was not the same for every cycle (Figure 6.2b). The main reason for this discrepancy is that the current is undersampled, and a sampling frequency of 5-10 Hz is not enough to capture the full shape of such sharp, impulse-like peaks. As a result, most of the spikes measured consist of 1-3 points. However, we believe the magnitude of the largest peak, which happens more than once, can still be taken as a good measure of the actual magnitude of the sensor current spike. A statistical analysis of the data, shown in the histogram in figure A5.1 supports this hypothesis. This histogram shows the statistical distribution of the magnitude of the current peaks observed in the experiments in Figure 6.2a and b. A number is counted in a particular bin if it is equal to or less than the bin number down to the last bin. All values below the first bin value are counted together, as are the values above the last bin value.

As can be seen the histogram has its peak at lower currents (15 nA bin), then it almost goes to zero at intermediate currents (45, 55 nA bins), then there is a larger concentration of samples in the highest bin (65 nA bin). No current spikes larger than 65 nA were measured and the distribution is seen to cut off above that bin, supporting the suggestion that the real magnitude of the current spike is about 60 nA. Taking into account the negative direction of the current at the rising edge of the force signal, this is the value

assigned to the magnitude of the measured current spike in the plot in Figure 6.2c at point +0.5 V vs. Ag/Ag+.

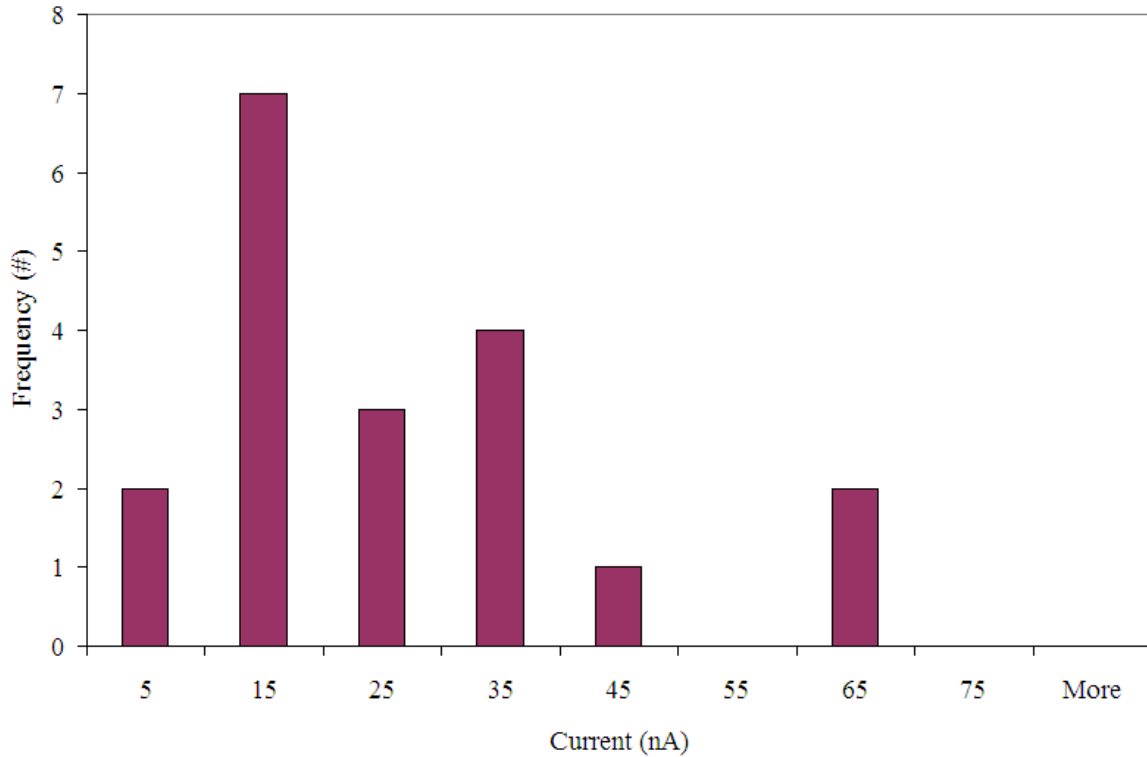


Figure A5.1: Histogram of the magnitude of the current peaks at a load of 45 MPa and bias potential of +0.5 V vs. Ag/Ag+. It cuts-off above the 65 nA bin, implying the value of the peak to fall in that bin.

The number of spikes measured in the experiment in Figure A5.1 is about 20. It is desirable to have a larger number of samples to further verify the validity of our assumption that the largest peak magnitude recorded can indeed represent the true magnitude of the current peak. For this purpose the histogram for a similar experiment (not reported in the thesis) is presented in Figure A5.2, in which about 60 peaks were measured. The high preload of about 120 MPa and the larger change in the load (~ 100

MPa) mean that the magnitude of the currents in this experiment are as large as up to 600 nA. The bias potential has been 0.75 V vs. Ag/Ag+. This histogram more clearly shows the trends observed above in Figure A5.1. Here about 20 of the 60 samples fall in the highest two bins before the histogram cuts off beyond the 600 nA bin, clearly establishing that the true value of the bin is most likely to fall in this bin. Repeating the experiments with an instrument capable of sampling at a faster rate can provide more details about the shape and size of the sensor current peaks.

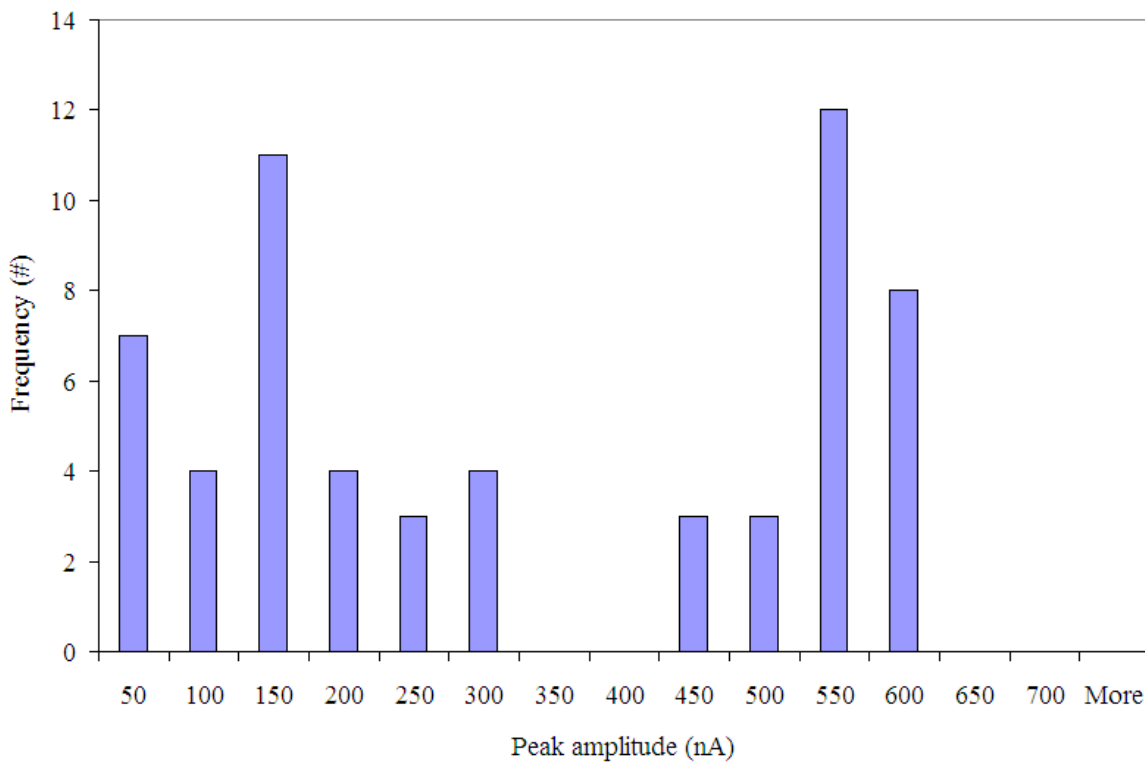


Figure A5.2: Histogram for a force sensing experiment at a preload of about 120 MPa and a change in the load of about 100 MPa in the form of a square-wave. The bias potential was +0.75 V vs. Ag/Ag+.

Another piece of evidence supporting using the magnitude of the current spikes as done in this thesis is the consistency of the load dependence of the results found this way. If the sense currents plotted in Figure 6.2c are normalized by their respective loads, the normalized currents virtually coincide within measurement error at almost all applied potentials (Figure A5.3). This would have been unlikely to happen if these currents were not real. Moreover, the experimental data seems to show that although of various amplitudes, all current spikes decay with the same time constant, implying that all of them are undersampled versions of the same spike.

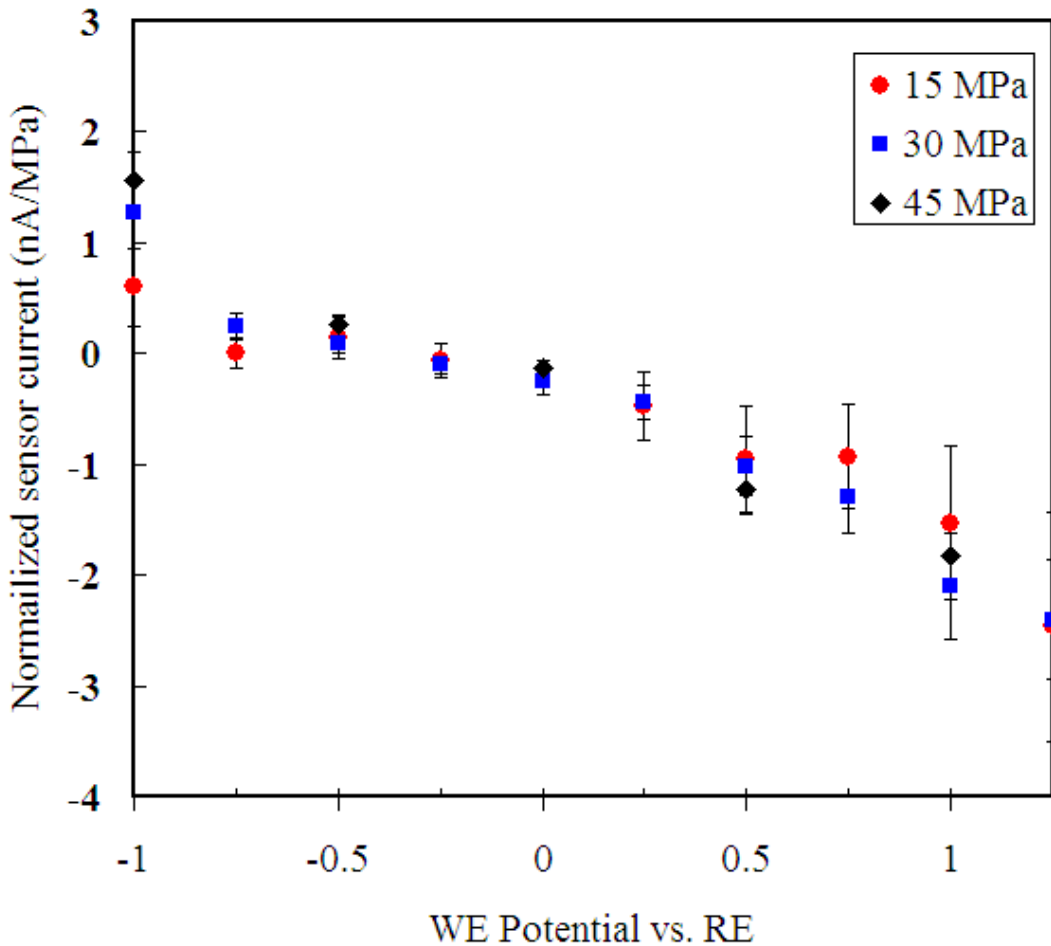


Figure A5.3: Sensor currents from Figure 6.2c, normalized by load, at various bias potentials.